HIGH TEMPERATURE CORROSION BEHAVIOR OF ALLOYS IN MIXED-GAS ENVIRONMENTS

by

Satia Soltanattar

B.S. in Materials Science and Engineering, Isfahan University of Technology, 2008

M.S. in Materials Science and Engineering, Isfahan University of Technology, 2011

Submitted to the Graduate Faculty of

Swanson School of Engineering in partial fulfillment

of the requirements for the degree of

Doctor of Philosophy

University of Pittsburgh

2018

UNIVERSITY OF PITTSBURGH

SWANSON SCHOOL OF ENGINEERING

This dissertation was presented

by

Satia Soltanattar

It was defended on

February 2, 2018

and approved by

Gerald H. Meier, Ph.D., Professor, Department of Mechanical Engineering and Materials Science

Anthony J. Deardo, Ph.D., Professor, Department of Mechanical Engineering and Materials Science

Badie I. Morsi, Ph.D., Professor, Department of Chemical and Petroleum Engineering

Dissertation Director: Brian M. Gleeson, Harry S. Tack Chair Professor, Department Chairman, Department of Mechanical Engineering and Materials Science

HIGH TEMPERATURE CORROSION BEHAVIOR OF ALLOYS IN MIXED-GAS ENVIRONMENTS

Satia Soltanattar, Ph.D.

University of Pittsburgh, 2018

Recent efforts to increase the efficiency of and reduce NO_x emissions from coal-fired boilers have led to higher operating temperatures and localized reducing conditions that favor sulfidation and carburization, together with possible formation of only the most stable oxides (e.g., Al_2O_3, SiO_2 and Cr_2O_3). Under such conditions, the ability of a given alloy to develop a protective oxide scale is crucial for achieving extended corrosion resistance. This study assessed the effects of different major and minor alloying components on the corrosion resistance of several commercial alloys (all supplied by Haynes International), pure chromium and model alloys in environments having a relatively low oxygen, but high sulfur and carbon potentials. Such environments are relevant to low-NO_x burner and coal gasification systems. Isothermal exposures were done for up to 100 h at 871°C (1600°F) and the exposed alloys were characterized in detail using some combination of XRD, SEM, EPMA, XPS, GDOES, EBSD and TEM.

It was found that the mode of growth and kinetics of chromia formation are affected by the presence of water vapor, sulfur and carbon in the atmosphere. The presence of these species was inferred to affect the grain-boundary diffusion. Under such conditions, chromia scales can grow much faster and have a finer grain structure than those formed in dry air. It was also shown

that Ni-Co-base alloys exhibit much better sulfidation and carburization resistance to the mixed-gas environments studied compared to Ni- and Fe-Ni-base alloys. An optimum in sulfidation resistance can be achieved when the Ni:Co mass ratio is close to unity, due to the reduced risk of formation of relatively low-temperature metal/metal-sulfide eutectics. Resistance to carburization, however, could only be achieved by formation of a continuous alumina scale. The effect of Cr concentration on corrosion resistance of Ni-Co-base alloys was also studied. It was found that in the presence of specific minor alloying elements, higher Cr concentration is not necessarily better for sulfidation resistance. A combination of lower Cr and minor alloying elements can provide better resistance. Silicon additions, in combination with Al, Ti, and Mo, were found to be the most effective in providing the resistance to mixed gases owing to the establishment of a complex inner layer at the alloy surface.

TABLE OF CONTENTS

LIST OF TABLES

LIST OF FIGURES

ACKNOWLEDGEMENTS

Foremost, I would like to express my profound appreciation for my advisor Prof. Brian Gleeson and his continuous support, patience, motivation, enthusiasm, and immense knowledge. I could not have imagined having a better mentor for my Ph.D. research. I would like to express my gratitude to Prof. Gerald Meier for his guidance and expertise. My sincere thanks also goes to my other committee members: Prof. Anthony DeArdo and Prof. Badie Morsi, for their insightful comments.

I would also like to thank my fellow labmates: Dr. Thomas Gheno, Dr. Juan Manuel Alvarado Orozco, Dr. Nathaniel Bohna, and other members of the group for all of their guidance, stimulating discussions, and the enjoyable moments that we shared in the past several years.

To my family: my parents Farzaneh and Anoushirvan Soltanattar, and my brother Ardeshir, for all of their love and support throughout my life.

Last but not the least, to my husband Steven, none of these would be possible without your love, patience, and support.

1.0 INTRODUCTION

Attention towards coal-fired steam power plants is mainly due to the worldwide availability and low cost of coal. However, coal combustion generates a very harsh environment characterized by high temperatures and corrosive gases, which cause severe wastage of the exposed boiler components. When fossil fuels are burned in air, nitric oxide and nitrogen dioxide are produced. These pollutants can result in the production of ozone and acid rain. The nitrous oxides (NO_x) are produced through high-temperature combustion and in most cases, can be reduced by lowering flame temperature. However, reducing the flame temperature will reduce the overall efficiency of the boiler. Another method to reduce these emissions while also improving boiler efficiency is to control the air-fuel ratio for the combustion. Specifically, combustion at high temperature and low oxygen partial pressure reduces NO_x emissions. However, these conditions may also have negative effects of enhancing the propensity for corrosion and consequently increasing materials wastage in boilers [1, 2].

Many power plant operators are moving toward the staged combustion process in order to reduce the boiler emissions in accordance with recent environmental regulations. In this process, NO_x emissions are reduced in the by-product of combustion by delaying the mixing of fuel and oxygen, and therefore, creating a reducing environment in the boiler. A low-NO_x atmosphere usually contains about 15% carbon monoxide, 3% hydrogen, 0.12% hydrogen sulfide and 3% steam and nitrogen in which the equilibrium oxygen partial pressure is very low, about 10^{-20} atm,

which is “reducing” from the standpoint of iron and nickel oxidation (i.e., FeO_x and NiO formation is thermodynamically not possible) [3].

Prior to using staged combustion, most boiler atmospheres were oxidizing and component degradation by sulfidation and/or carburization was not a major problem. Formation of a protective oxide scale on waterwall tubes under the oxidizing conditions prevented their failure and increased their service life [2]. On the other hand, in the staged combustion boilers the atmosphere is very reducing to the extent that the highly corrosive H_2S gas is stable. Reaction of H_2S, as well as SO_2 and SO_3, with waterwall tubing materials leads to the formation of metal sulfides, excessive wastage of the tube, and unsatisfactory service life of the low alloy steel tubes [4]. For instance, waterwall tubing materials in low-NO_x burner plants have experienced wastage between two times to an order of magnitude higher than conventional oxidative atmosphere plants [5]. One of the best approaches to solve this problem has been to use a weld overlay cladding of more resistant alloys, such as nickel base superalloys, on the tubes. These alloys can provide more protection in reducing environments than standard steels, and in some cases have exceeded 10 years of service. However, they contain expensive alloying elements such as niobium and titanium, and most of them are susceptible to circumferential cracking [3].

The purpose of this study is to systematically determine the corrosion behavior of nickel-, cobalt- and iron-base alloys containing different levels of chromium and minor alloying elements, such as aluminum, molybdenum and silicon, in mixed-gas environments that are carburizing, oxidizing-sulfidizing, and oxidizing-sulfidizing-carburizing. A thorough understanding of the behavior of these alloys in mixed gases can significantly aid in the design of more corrosion-resistant alloys for extended service at higher temperatures.

2.0 BACKGROUND

2.1 SULFIDATION OF ALLOYS

In many technical processes, in particular low-NO_x burners, the structural components are exposed to atmospheres with low oxygen and high sulfur partial pressures. Sulfur is a relatively strong oxidant and can cause aggressive forms of corrosion depending on its concentration. In general, corrosion by sulfur is much more rapid than the corresponding oxides [6]. Figure 2-1 shows an Arrhenius plot comparing parabolic rate constants for sulfidation and oxidation of Fe, Ni and Cr.

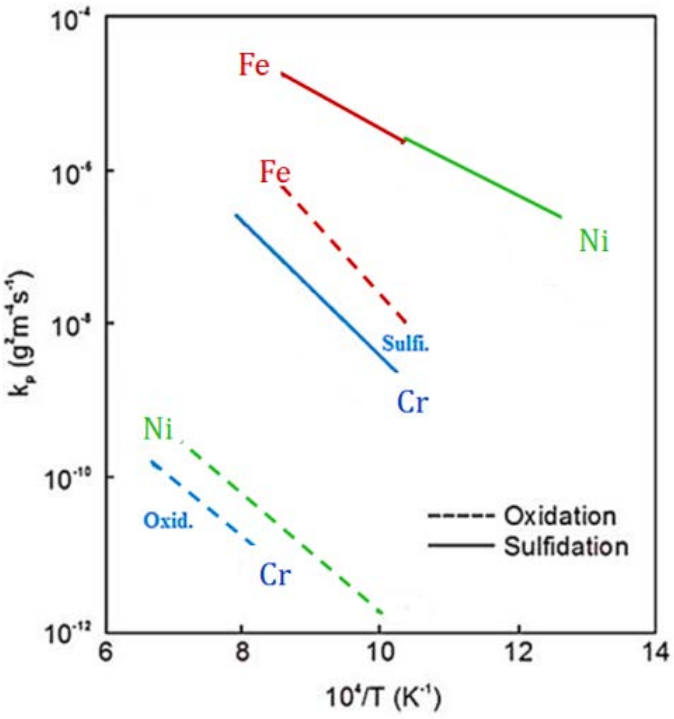

Figure 2-1 Collective plot of the temperature dependence of the sulfidation and oxidation rates of some metals [6]

Previous studies [7, 8, 9] have shown that all Ni-, Co-, and Fe-base alloys in reducing environments exhibit a transition from oxidation with low oxide-scale growth rates to sulfidation with much higher sulfide-scale growth rates. This transition is often referred to as a "kinetic boundary," and it will be reviewed in detail in the next chapter. The aim of this section is to define general concepts of high-temperature sulfidation in the environments having a low P_{O2} and high P_{S2}. Thermodynamics and mechanistic aspects are presented. Then the effects of alloying elements are briefly described.

2.1.1 Thermodynamics of sulfidation

In laboratory studies of metals and alloys under sulfidizing conditions, the environment is characterized by a certain sulfur partial pressure (P_{S2}). A commonly used gas mixture for sulfidation studies is H_2/H_2S and the important gas-phase equilibrium to consider in such an atmosphere follows:

$$H_2S = H_2 + \frac{1}{2}S_2 \tag{2-1}$$

$$K_1 = \frac{P_{H_2}\sqrt{P_{S_2}}}{P_{H_2S}} = exp\left[\frac{-\Delta G_1^o}{RT}\right] \tag{2-2}$$

where $\Delta G_1°$ is the standard Gibbs free energy change for reaction ((2-1) in J/mol, R the gas constant and T the temperature. In sulfidizing atmospheres with relatively high sulfur potentials, sulfides of nickel, cobalt, iron, and chromium are likely to form if the sulfur potential is sufficiently high. The equilibrium reaction for sulfidation is:

$$xM + \frac{1}{2}yS_2 = M_xS_y \tag{2-3}$$

The standard free energy for metal sulfidation is given by:

$$\Delta G_T^o = RTln(P_{S_2})^{1/2} \tag{2-4}$$

and thus,

$$(P_{S_2})^{1/2} = \exp(\frac{\Delta G_T^o}{RT}) \tag{2-5}$$

where P_{S2} is the equilibrium sulfur partial pressure between metal and metal sulfide and it is called the sulfide dissociation pressure. When the sulfur partial pressure in the environment is higher than the sulfide dissociation pressure, sulfide formation is thermodynamically stable. The sulfur partial pressure in equilibrium with a sulfide can be read from the Ellingham diagram

(Figure 2-2) by drawing a straight line from point "S" to the P_{S2} through the temperature of interest and crossing the free-energy line of a given sulfide [10].

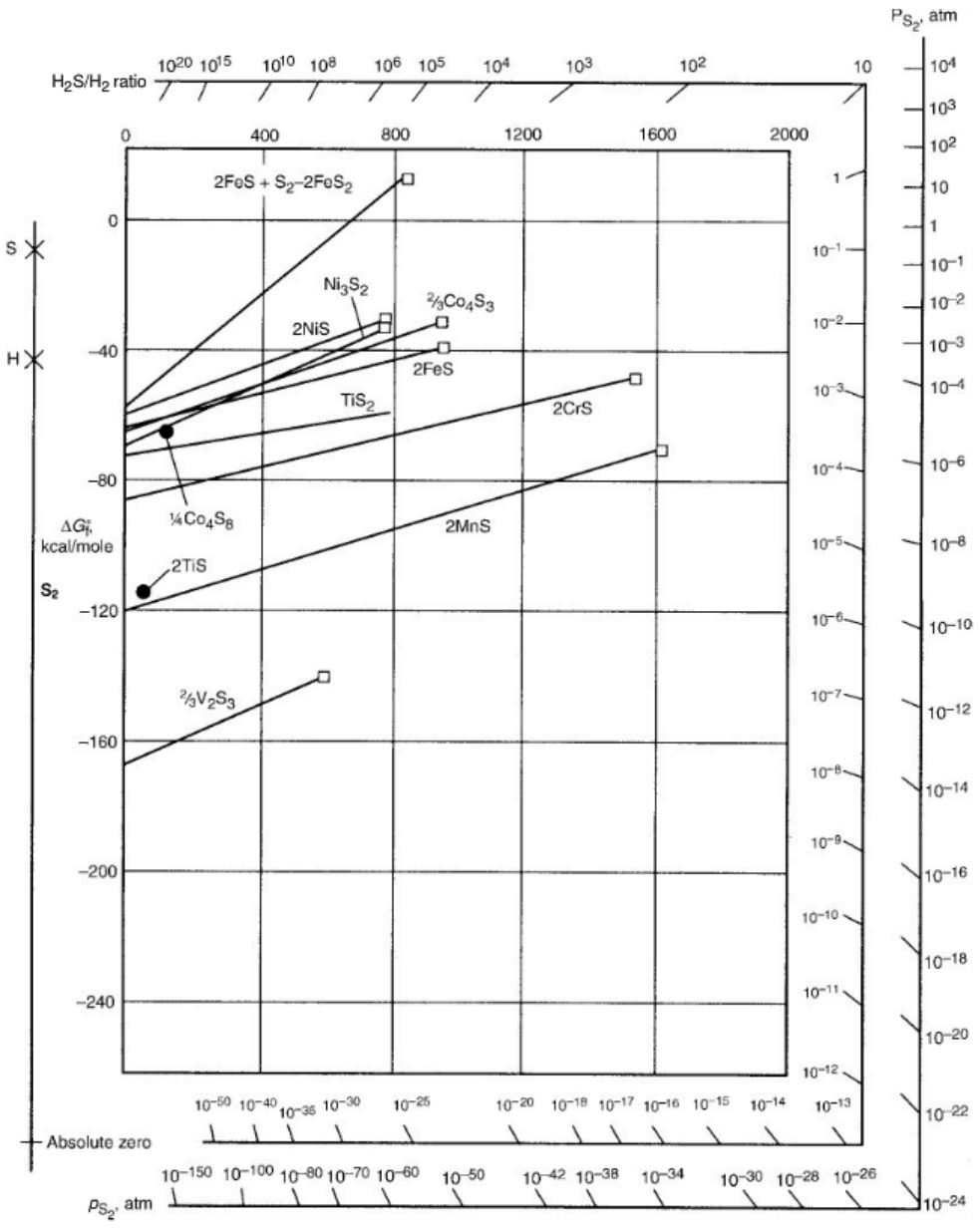

Figure 2-2 Standard free energies of formation of selected sulfides [10]

Less research has been published on sulfidation compared to oxidation, mainly due to the much greater ease in conducting oxidation experiments. Sulfidation is more complex than oxidation mainly due to the large number of stable sulfides compared to oxides. The standard free energies of the formation of sulfides are generally less negative than that for the corresponding oxide (Table 2-1). The differences in anion sizes in sulfides and oxides, leads to the longer M-S bond lengths compared to M-O and, thus, smaller lattice energies. This will reflect in lower free energies of sulfide formation and, therefore, lower melting points of sulfides. Another major concern in sulfidation of metals at elevated temperatures is the liquid product formation due to the low melting point metal-metal sulfide eutectics. Liquid corrosion products tend to rapidly consume the alloy and are, therefore, highly undesirable. Alloys containing above about 20% nickel are often susceptible to liquid formation. Table 2-2 shows the melting points of sulfides of several metals compared to their oxides and also several important metal-sulfide eutectics. As it can be seen, Ni-Ni_3S_2 eutectic forms at about 645 °C [9].

Table 2-1 Free energies of formation of several metal sulfides and oxides in kJ of oxidant at 1200 °C [9]

Sulfide	**ΔG°**	**Oxide**	**ΔG°**	**$\Delta G^\circ_{(Oxide)} - \Delta G^\circ_{(Sulfide)}$**
FeS	-21,11	FeO	-43,84	23,73
CoS	-16,20	CoO	-34,90	19,70
CrS	-33,09	Cr_2O_3	-64,88	31,79
MnS	-47,83	MnO	-70,97	23,14
Al_2S_3	-47,17	Al_2O_3	-103,13	55,96
ZnS	-39,16	ZnO	-53,26	14,10
TiS	-55,91	TiO	-101,53	45,62
ZrS_2	-58,13	ZrO_2	-104,02	45,89
ReS_2	-8,60	ReO_2	-26,91	18,31
InS	-19,63	In_2O_3	-43,44	23,81
ThS	-63,52	ThO_2	-119,59	56,07

Table 2-2 Melting points of several sulfides, oxides and metal-sulfide eutectics [9]

Sulfide	Melting point (K)	Oxide	Melting point (K)	Metal-Sulfide Eutectics	Melting point (K)
TiS	2373	TiO	2023	Mn-MnS	1513
Y_2S_3	1873	Y_2O_3	2683	Cu-Cu_2S	1343
CrS	1823	-	-	Fe-FeS	1258
Cr_2S_3	?	Cr_2O_3	2607	Co-Co_4S_3	1153
MoS_2	1431	MoO_2	2200	Ni-Ni_3S_2	918
MnS	1598	MnO	2058		
FeS	1468	FeO	1697		
CoS	1373	CoO	2083		
Al_2S_3	1373	Al_2O_3	2319		
NiS	1083	NiO	2230		
Ni_3S_2	1067	-	-		
Cu_2S	1403	Cu_2O	1515		

2.1.2 Mechanisms and kinetics of sulfidation

The mechanisms of sulfidation is fundamentally similar to these of oxidation. However, they can differ in complexity and, more importantly, rate of attack. Metal sulfide scales generally grow according to parabolic kinetics as a result of solid-state diffusion control. However, according to previous studies [9, 6, 8], sulfidation rates of most metals are orders of magnitude higher than their oxidation rates (Figure 2-1). This increase in sulfidation rate is primarily due to the higher degree of non-stoichiometry in sulfides compared to oxides. This section is aimed to briefly define the defect structures in sulfides, transport properties and kinetic rate laws.

2.1.2.1 Defect structures and diffusion mechanisms

In general, sulfides of common-metals, such as chromium, nickel and cobalt, show greater deviation from stoichiometry, and therefore, higher defect concentrations than their oxides. This

deviation from stoichiometry occurs mainly in sulfides due to their smaller lattice energy, which makes the formation of point defects much easier. Higher concentrations of point defects will cause higher diffusion rates and, correspondingly, higher growth rates in sulfides [11, 9].

Defect structures

There are three main pathways for transport of metal or sulfur species in sulfide scales: macroscopic defects, grain boundaries and lattice defects. The predominant lattice defects in the stoichiometric ionic compounds are Schottky and Frenkel defects. Schottky defect is an equivalent number or concentration of vacancies on both cationic and anionic sub-lattices and both anions and cations can therefore be mobile. Frenkel defect, on the other hand, is when the anion lattice is assumed to be perfect but cation lattice contains cation vacancies and interstitials in equivalent concentrations and thus, only cations are mobile. However, simultaneous migration of ions and electrons is necessary to be considered in order to explain the materials transport and neither of these defect structures provides a mechanism by which electrons can migrate. As was mentioned before, sulfides of common metals show deviations from stoichiometry and it is necessary to consider them as non-stoichiometric compounds. Under such conditions, the ratio of metal to non-metal atoms is not exactly as it appears from the chemical formula and it should be assumed that cations or anions exhibit variable valency in their sub-lattices in order for the compound to be electrically neutral. These non-stoichiometric compounds can be classified into two main categories: n-type (metal excess or non-metal deficit), where the charge is transferred by negative carriers and p-type (metal deficit or non-metal excess), where charge is transferred by positive carrier [12]. The deviation from stoichiometry in some of these sulfides can be seen in Table 2-3.

Table 2-3 Metal/metal sulfide eutectic temperatures and sulfide non-stoichiometry ranges [13]

System	T_E(°C)	Sulfide (T (°C))	δ
Fe/FeS	988	$Fe_{1-\delta}S$ (800)	0 to 0.20
Co/Co_4S_3	880	$CoS_{1+\delta}$ (800)	0 to 0.07
Ni/Ni_3S_2	645	$Ni_3S_{2\pm\delta}$ (645)	−0.188 to 0.222
Mn/MnS	1,242	$Mn_{1-\delta}S$ (800)	0 to 1×10^{-4}
		$Cr_{1-\delta}S$ (700)	0.032 to 0.205
		$Cr_{3\pm\delta}S_4$ (700)	−0.10 to 0.11
		$Cr_{2+\delta}S_3$ (700)	0.054 to 0.11 (tr)
			0.033- (rh)

In addition, sulfide scales formed on high temperature alloys inevitably contain some forms of macroscopic defects (such as cracks or voids), mainly due to the stresses induced during growth, poor adhesion to the substrate or porosity due to rapid or incomplete growth. These defects can act as one rapid transport path for sulfur or other oxidants in the environment.

The third pathway for transport of metal and sulfur in the sulfide scales is the grain boundaries. In these polycrystalline scales, grain size can vary considerably. Grain boundary diffusion, in general, is more important than lattice diffusion; especially at lower temperatures due to the lower activation energy and more disordered structures. Boundary diffusion is an important component in scale growth [13, 14].

Diffusion mechanisms

According to Wagner's theory of oxidation [15], mass transport through oxides (or sulfides) results from two distinct driving forces: charged species migrating in an electrical field and of chemical species diffusing along chemical potential gradients. Metal and sulfur ions tend to migrate across the scale in the opposite directions and since they are charged particles, their

migration will cause the formation of an electrical field across the scale. As a result, electrons can transport in this electrical gradient across the scale from metal to the atmosphere.

Sulfides of common metals (nickel, cobalt, iron …), in general, grow by outward diffusion of cations [9]. It should be noted that the solid state diffusion in these sulfides proceeds mainly through the defects which can be point defects, grain boundaries, or macroscopic defect as discussed before. Transport through the lattice can be described by self- and chemical-diffusion coefficients. Previous studies showed that the self-diffusion rates of cations in common-metal sulfides are generally much higher than in their corresponding oxides [16, 17]. Self-diffusion coefficient is the product of defect concentration and mobility. It has been shown that in majority of cases, higher self-diffusion rates in sulfides compared to oxides results from higher defect concentrations and not from greater defect mobility since the defect mobility in sulfides and oxides do not differ significantly [9, 6]. However, it has become clear that in most cases short-circuit paths predominate during the mass transport [14]. Diffusion through grain boundaries and defects such as cracks or pores is called short-circuit diffusion. The relative contributions to scale growth from lattice and grain boundary diffusion depend on temperature and the grain size of the scale (sulfide or oxide).

In the case of refractory-metal sulfides (Mo, W, Ta, and etc.), the situation is much different. Refractory-metal sulfides show very little deviation from the stoichiometry. As opposed to other common-metal sulfides, anion defects are predominant defects in these sulfides. These sulfides (such as MoS_2) have a layered crystal structure which allows the intercalation of ions of the common base metals (such as Co or Ni). These transition metal ions can diffuse through the octahedral holes within the Van der Waals gap separating the S-Mo-S layers as illustrated in Figure 2-3. They can diffuse between these layers at a relatively fast speed.

However, in sulfidation of pure Mo, diffusion of molybdenum and sulfur do not occur through these Van der Waals gaps. Thus, MoS_2 can be very protective on pure Mo and in the absence of Ni or Co [18]. Sulfidation rates of most of the refractory-metals are comparable to the oxidation rate of chromium [19].

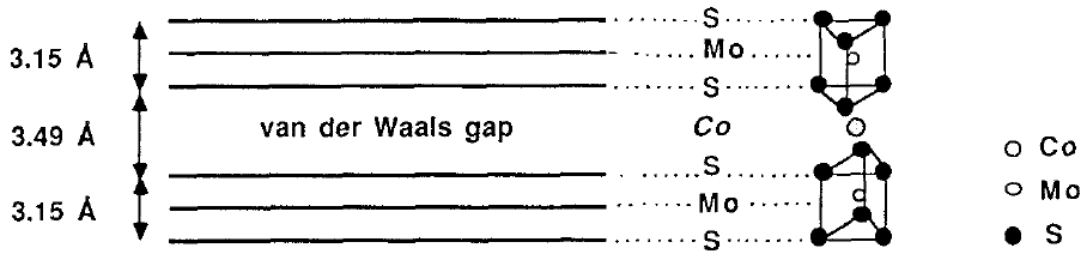

Figure 2-3 Schematic of the layered structure of MoS_2 showing the Van der Waals gap between the loosely bound S-Mo-S sandwiches. As depicted, cobalt intercalates in the Van der Waals gap. Also shown is the perspective structure of MoS_2 [18]

Knowing the transport mechanisms, the kinetics of sulfidation (similar to oxidation) can be determined by the rate of the slowest step of the process. Rate laws associated with the most common rate-controlling steps are presented next.

2.1.2.2 Rate laws

Sulfidation and oxidation are very similar processes and in general, sulfides of common metals contain the same type of cation defects as found in oxides. This will cause the sulfide scales to grow predominantly by outward cationic diffusion. Thus, the principles of Wagner theory can equally well be applied to sulfidation and oxidation.

Linear kinetics

If the rate-controlling step proceeds at a constant rate, oxidation kinetics follow a linear law

$$x = k_l t \tag{2-6}$$

where "x" is the scale thickness, "k_l" the linear rate constant and "t" the oxidation time. A linear rate law may result when a phase boundary reaction controls the kinetics rather than a transport process through the scale. As an example, it can be observed at the early or transient stage of oxidation or sulfidation, when the scale is sufficiently thin to support rapid diffusion. In addition, if the reaction product is volatile or if the scale spalls or cracks, the substrate metal or alloy can be consumed in a very short time. Under such conditions, the scale formed does not provide a barrier separating the alloy from the atmosphere, and the condition of fast metal supply is fulfilled throughout the process, which results in continued linear kinetics [12].

Parabolic kinetics

After the rapid initial scale growth stage, the reaction rate will eventually decrease when the scale reaches a specific thickness. In other words, when the scale is thin the activity of metal at the scale-gas interface is high and the rate of the oxidation is controlled by the surface reaction. As the scale thickens, the flux of ions through the scale must be equivalent to the surface reaction and as a result, the activity of metal at the scale-gas interface drops to approach the value in equilibrium with the atmosphere. At this stage, the transport of reactant species may become the rate-controlling step. Thus, the scaling kinetics will follow the "parabolic rate law". In parabolic kinetics the scale thickness, x, increases with time, t, and by increasing the diffusion distance over time the oxidation rate decreases [12]. Thus, the oxidation rate is inversely proportional to the scale thickness,

$$\frac{dx}{dt} = \frac{k'_P}{x} \tag{2-7}$$

$$x^2 = 2k'_P t \tag{2-8}$$

This can also be shown as a function of weight gain ($g.cm^{-2}$):

$$\Delta m^2 = k_P t \tag{2-9}$$

k_P is directly related to the diffusivities within the scale, so that

$$k_P \propto \exp(\frac{-Q_d}{RT}) \tag{2-10}$$

Here, Q_d is the activation energy for the oxide scale growth. The dependence of the parabolic rate constant k_P on temperature for the oxides of several major components of high temperature alloys (Ni, Co, Fe, Cr, Al, and Si) is shown in Figure 2-4. As can be seen from this diagram, the growth rates of oxides of Si, Al, and Cr are much lower compared to Ni, Co, and Fe [20]. Thus, in development of corrosion resistant alloys for high temperature applications, formation of one of these slow growing oxides as the scale is always considered.

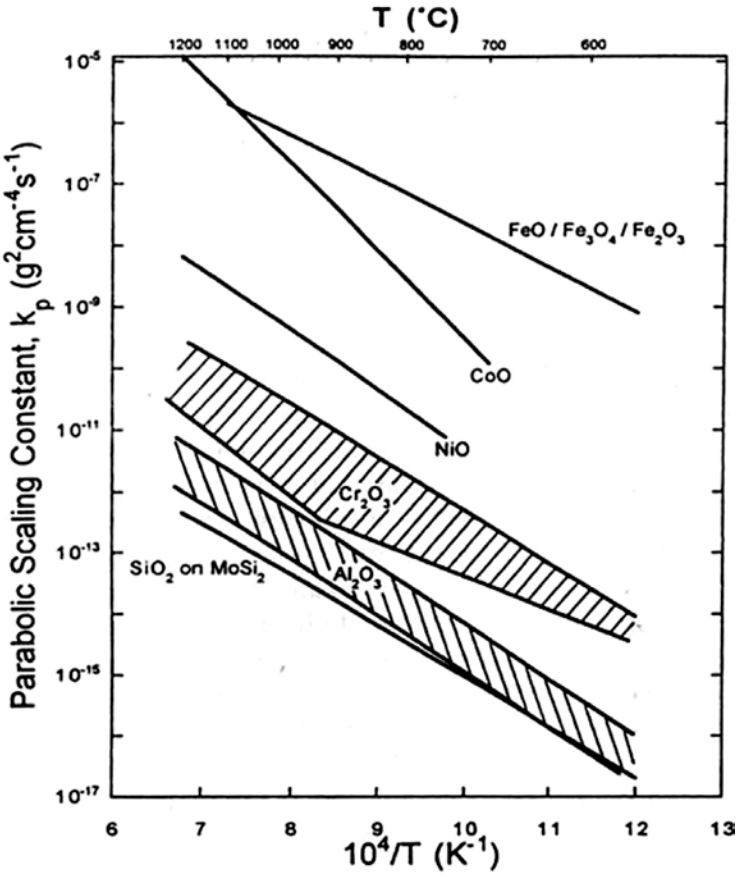

Figure 2-4 Parabolic oxidation rate constant for various oxide scales as a function of temperature [20]

Sulfidation of Ni, Co, and Fe in H_2-H_2S gas mixtures were investigated and summarized by Mrowec and Przybylski previously [16]. Sulfidation of all these metals was found to follow parabolic behavior. They also showed that binary Ni-Cr, Co-Cr, and Fe-Cr alloys exhibit parabolic behavior with no significant difference among them. All three alloy systems showed a similar trend of decreasing sulfidation rate by increasing chromium content. Alloys with less than 40% Cr showed improved resistance to sulfidation mainly due to the formation of an inner chromium sulfide or $Fe(Fe_{2-x}Cr_x)S_4$ layer. The sulfidation resistance for these alloys can be improved through addition of other alloying elements such as Al and Mo which will be discussed next.

2.1.3 Alloying effect on sulfidation resistance

As previously mentioned, large deviations from stoichiometry occur in sulfides since point defects can easily be created. As a result of high defect concentrations in sulfides, they have high diffusion rates and therefore, high corrosion rates. The sulfidation rates of most of the major metallic components in conventional high temperature alloys are 10^4-10^6 times higher than their oxidation rates (Figure 2-1). Resistance to sulfidation comes from the ability to form a continuous and adherent slow-growing oxide scale which has sufficient mechanical properties to withstand the effects of both growth and thermal stresses. Thus, elements such as Cr, Al and Si are mainly added to these alloys for the purpose of forming a continuous oxide scale with a very low growth rate. But in the absence of oxygen, it is known that these elements alone do not seem to be very promising in designing novel materials for high temperature applications. In this section the effect of some of the important elements in conventional high temperature alloys on their sulfidation resistance will be reviewed briefly.

Effect of nickel- High nickel contents in chromia forming alloys can make them susceptible to rapid sulfidation attack at temperatures higher than 645 °C, since according to the Ni-S phase diagram (Figure 2-5) a low melting point eutectic for Ni-Ni_3S_2 exists at 645 °C. Molten sulfide can easily destroy the chromium oxide scale and cause catastrophic sulfidation attack. Figure 2-6 shows the influence of nickel, iron and chromium contents on the melting temperature of the sulfides formed on these alloys. According to this diagram the melting temperature of the sulfide increases with increasing iron and chromium contents and alloys with ≥25Cr and ≤20Ni are safe from liquid sulfide formation under most practical conditions [21].

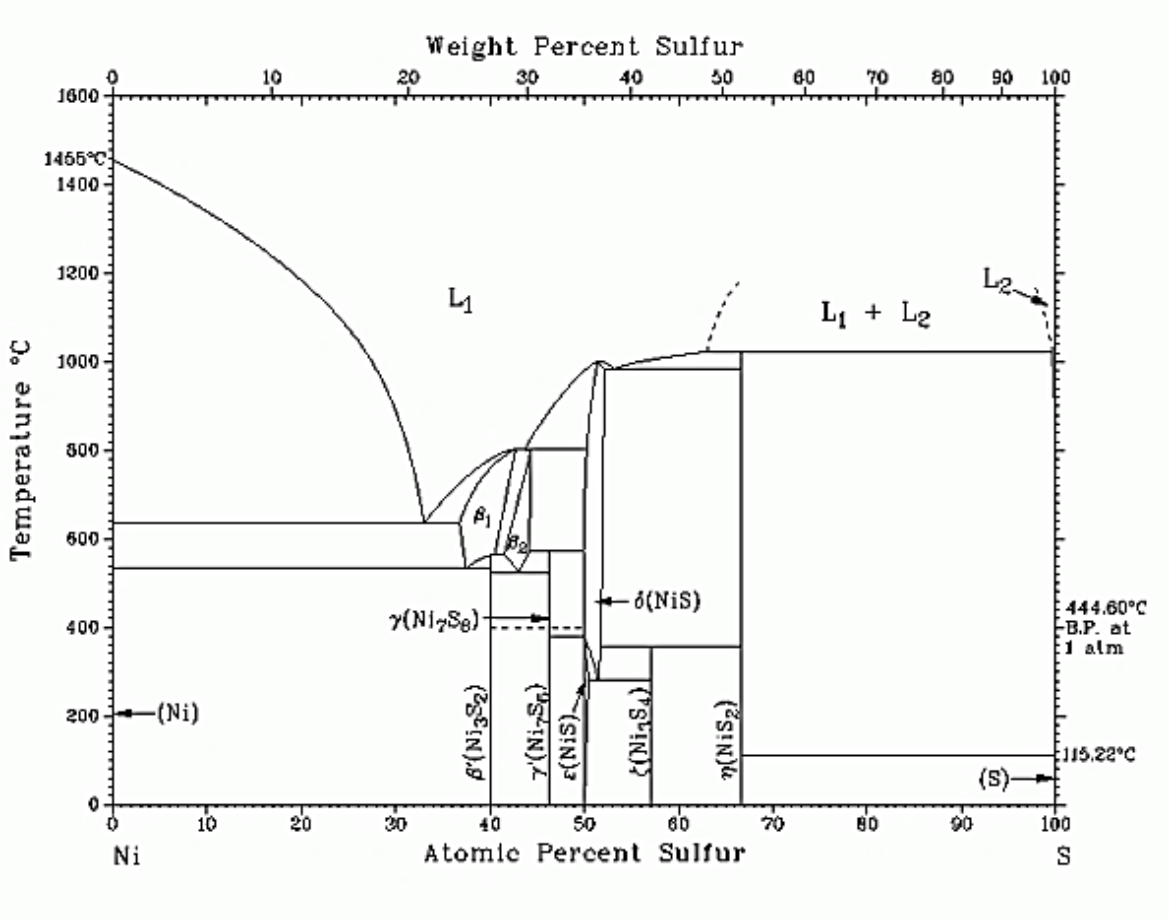

Figure 2-5 Ni-S binary phase diagram

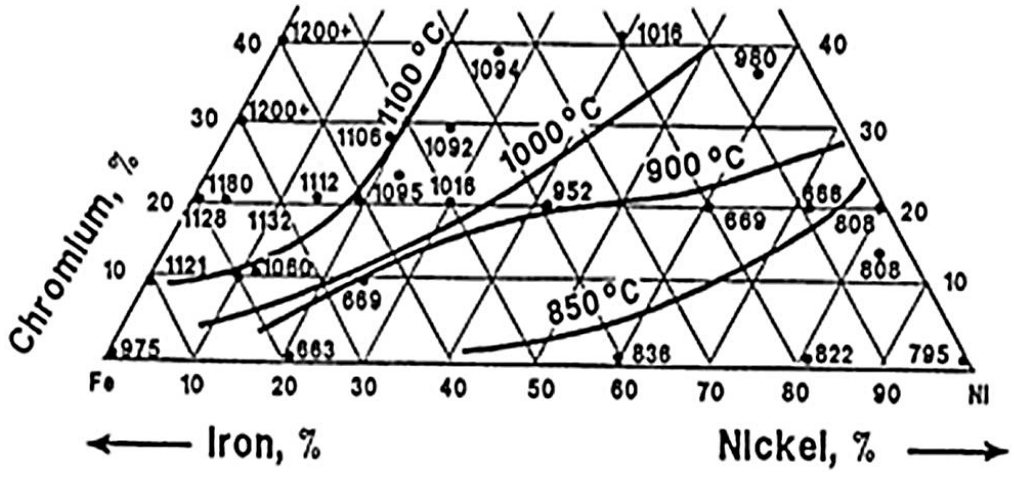

Figure 2-6 The melting points of sulfide scales that form on Fe-Ni-Cr alloys [21]

Effect of Cobalt- Cobalt-base alloys or, in general, cobalt-containing alloys have better sulfidation resistance than nickel- or iron-nickel-base alloys with similar chromium contents. These alloys have higher temperature capabilities and are more resistant to breakaway corrosion. High cobalt concentrations can reduce the rate of sulfur diffusion in the alloy and also decrease the risk of Ni-Ni_3S_2 eutectic formation. Previous studies [10, 22, 23, 24] on pure cobalt in H_2-H_2S environments showed that under similar conditions, the rate of sulfidation attack for cobalt is lower than nickel and iron. Also in 1985, Lai [25] showed that Co-based alloys were more resistant than Ni and Ni-Fe-based alloys when they are exposed to atmospheres having $P_{O2} \leq 3 \times 10^{-17}$ atm and $P_{S2} \leq 4 \times 10^{-6}$ atm at 760, 870, and 980°C.

Effect of chromium- In 1971 Rau [26] showed that the sulfides of chromium are highly non-stoichiometric and so the protection from sulfidation achieved by addition of chromium is less than that observed for oxidation. Figure 2-7 shows the dependence of the sulfidation and oxidation rate of Fe-Cr alloys on their chromium content. According to this diagram, at compositions around 40% Cr the oxidation rate of the alloys is much lower than their sulfidation rate when a homogeneous Cr_2S_3 scale was formed.

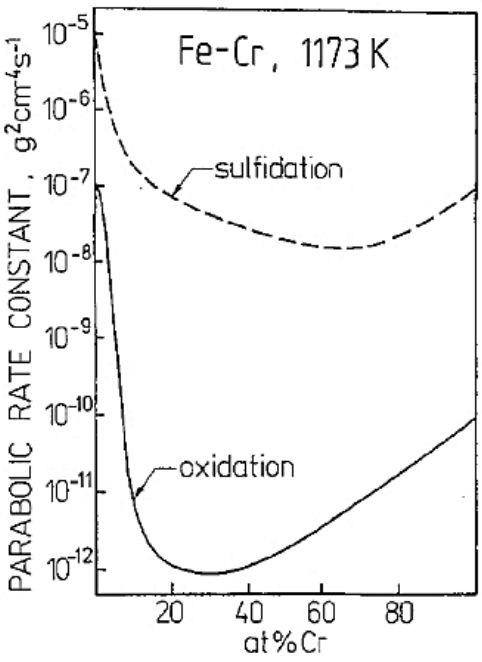

Figure 2-7 The dependence of the sulfidation and oxidation rates of Fe-Cr alloys on composition [6]

However, addition of chromium to some level can still decrease the sulfidation rate in pure sulfidizing environments. The sulfidation rate of Fe-Cr, Co-Cr and Ni-Cr alloys have been studied previously by Mrowec [6, 9]. His results are demonstrated in Figure 2-8 which shows that the sulfidation resistance of all these alloys performs similar to each other with increasing chromium content. According to this study (Figure 2-9), addition of chromium to about 2% does not affect the sulfidation rate of the base metal. The scale formed on the alloy at this stage is a single phase scale of base metal sulfide doped with chromium. By increasing chromium content to about 20%, the sulfidation rate decreases rapidly due to the formation of an inner barrier layer of: $Fe(Fe_{2-x}Cr_x)S_4$ for Fe-Cr alloys and chromium sulfide with nickel and cobalt for Ni-Cr and Co-Cr alloys, respectively. Addition of more chromium to the alloy will cause the scale to transform to a homogenous layer of chromium sulfide doped with base metal which has a

sulfidation rate lower than that of pure chromium. Eventually, when the chromium is depleted, the remaining base metal will be attacked rapidly [27].

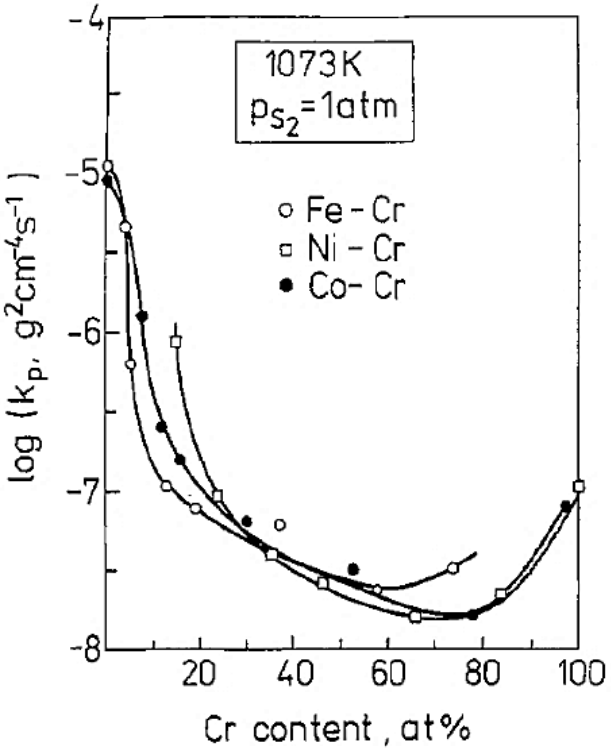

Figure 2-8 The dependence of sulfidation rate of Fe-Cr, Co-Cr and Ni-Cr alloys on composition [6]

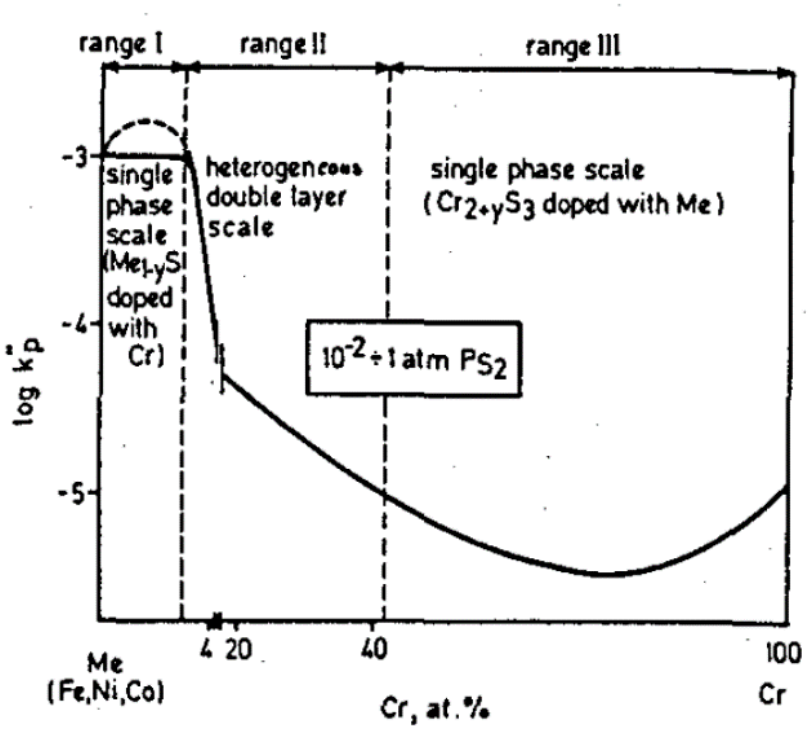

Figure 2-9 Schematic of the composition dependence of the sulfidation rate of Fe-Cr, Ni-Cr and Co-Cr alloys [6]

Effect of Mo- Another important alloying element would be molybdenum since Mo is added to most of the high temperature Ni-based alloys for solid solution strengthening purposes. Therefore, the effects of different Mo contents in these alloys on their sulfidation resistance in environments containing high sulfur and low oxygen partial pressures would be of interest. Mo, and more generally, refractory metals (mainly Mo and Nb) seem to be very promising candidates in sulfidizing atmospheres as they show excellent resistance to sulfidation. The reason for the remarkably low rate of sulfidation of these metals is shown to be the low defect concentration in their sulfide structures. It is also assumed that, as refractory metal sulfide and oxide scales grow by inward diffusion of sulfur and oxygen respectively, anionic, as opposed to cationic, defects predominate, as in the case in common metal sulfides [28]. As was mentioned in a previous section, Mo shows an excellent resistance to sulfidation by formation of MoS_2, which sulfidizes

at a rate comparable to oxidation of chromium. However, it can only provide moderate protection on common-base-metal alloys due to the layered structure and rapid diffusion of transition metal ions through these weakly bonded Van der Waals gaps [18, 29]. Therefore, addition of refractory metals, such as Mo, cannot provide a satisfactory resistance to sulfidation alone.

Effect of Al- Aluminum is also a beneficial alloying element in improving sulfidation resistance, especially for Fe-Cr and Co-Cr alloys. The beneficial effect of aluminum additions was previously reported by Mrowec and Przybylski [16] and it was attributed to the formation of an inner layer of $Fe(Fe_xAl_yCr_{z-x-y})S_4$ for Fe-Cr alloys with an outer layer of $Fe_{1-y}S$. Similar behavior was also observed for Co-25Cr alloys with aluminum content up to 22% (at.%) [30].

According to the results by Douglass et al. [18, 31] on the combined effect of aluminum and molybdenum, Fe-30Mo-5Al alloy shows excellent protective properties with the formation of an outer scale mainly composed of $Al_{0.5}Mo_2S_4$. The sulfidation rate of this alloy is comparable to oxidation rate of chromium. However, due to the two phase nature of this alloy consisting of a Fe-rich α phase and Mo-rich β-intermetallic phase, numerous cracks have been observed. In addition, the low aluminum activity at the alloy-scale interface cannot suppress the formation of the highly volatile molybdenum oxide (MoO_3). As a result, further modifications are required for this alloy.

In 1998, Yakuwa et al. [32] studied the effects of the above mentioned alloying elements on sulfidation behavior in H_2-H_2S environments at 600°C in comparison with alloy AISI685 ((18-21 wt. % Cr)-(12-15 wt. % Co)-(3.5-5 wt. % Mo)-(2.75-3.25 wt. % Ti)-(1.2-1.6 wt. % Al)-(0.02-0.08 wt. % Zr)-(0.003-0.1 wt. % B)-(≤2 wt. % Fe)-(≤0.15 wt. %Si)-bal. Ni). Alloy AISI685 is a γ′ (Ni_3(Al,Ti))-precipitation hardening alloy where the strength is determined by the

quantity of γ′. Low γ′ quantities provide inadequate strength while high quantities affect the hot workability and make the forging process difficult. Thus, the amount of Al and Ti needed to be controlled in order to have the same mechanical properties but with better sulfidation resistance. The summary of their results is shown in Figure 2-10. They showed that by increasing Al and Ti contents up to 2.5%, sulfur penetration into the alloy and internal sulfidation can be controlled to great extents. However, they showed that in the alloys with similar chemical composition to alloy AISI685, increasing the Al content to 3.5% and decreasing the Ti content to 1.5% will result in the best balanced composition overall with reasonable mechanical properties and high temperature sulfidation resistance.

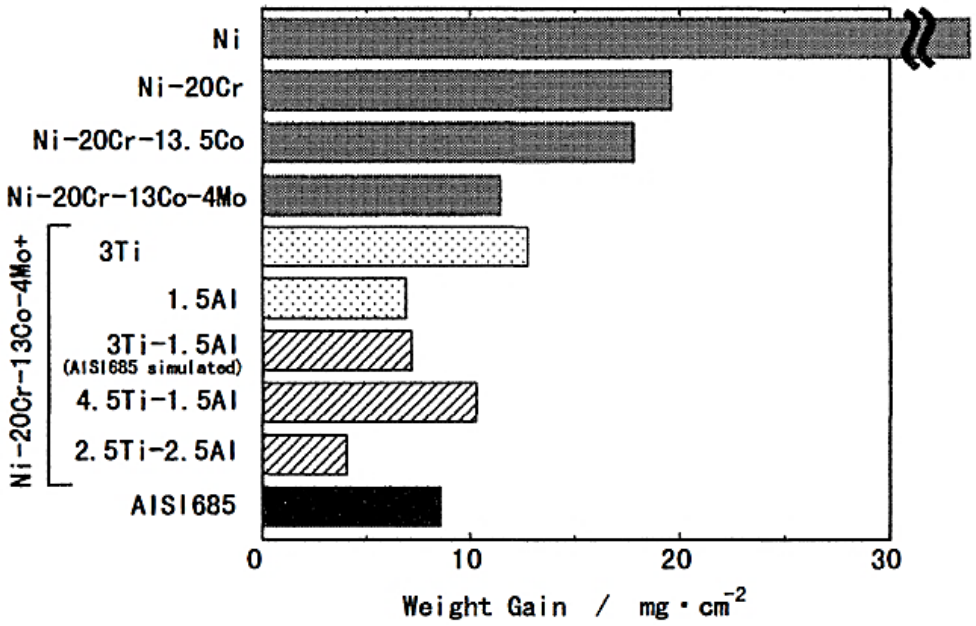

Figure 2-10 Weight gain of Ni-base alloys sulfidized in H_2-H_2S mixture [32] (Sulfur partial pressure is $10^{-10.5}$ atm, at 600°C for 49 hours)

The above mentioned results by previous researchers on the effects of alloying elements on improving the sulfidation resistance of high temperature alloys can be used in this study to

better understand the behavior of alloys in multi-oxidant environments and to design model alloy systems with better resistance in these environments.

2.2 CARBURIZATION OF ALLOYS

Strongly carburizing gases are encountered in different process environments using fossil fuels (coal and natural gas) as their feedstock. The combustion reactions such as synthesis gas reaction

$$CO(g) + H_2(g) = H_2O(g) + C(s) \quad (2\text{-}11)$$

the Boudouard reaction

$$2CO(g) = CO_2(g) + C(s) \quad (2\text{-}12)$$

and the hydrocarbon cracking

$$C_nH_m(g) = nC(s) + \frac{m}{2}H_2(g) \quad (2\text{-}13)$$

are the main carburization reactions when the environment contains CH_4, CO, or H_2 and CO. If the oxygen partial pressure in the environment is high enough to form an oxide scale (Cr_2O_3, Al_2O_3, and SiO_2), carbon ingress into the alloy can be prevented. The main concern is then the stability of these oxides at high temperatures, their ability to prevent the carbon ingress into the alloy, and the consequences of their failure. The ingress of carbon in chromia forming alloys causes precipitation of chromium-rich carbides and therefore, a loss of ductility and oxidation resistance.

Carburization has been studied by several authors in different environments with different carbon activities [33, 34, 35, 36]. In general, carburizing environments are characterized by a carbon activity and an oxygen partial pressure. However, as discussed

previously, in order to reduce the emission of greenhouse gases (CO_x and NO_x) a number of high temperature processes are now carried out under reducing conditions. When carbon activity is lower than 1, but large enough to stabilize a metal carbide and oxygen partial pressure is lower than the equilibrium partial pressure for the oxide formation, carbon can easily diffuse in and severe carbon pick-up can occur which is described as carburization. In this case the rate of carburization depends on the solubility and diffusivity of carbon into the alloy. When carbon activity is lower than 1 and oxygen partial pressure is relatively higher than the equilibrium partial pressure needed for the formation of a stable oxide scale such as chromia ($\sim 10^{-20}$ bar), oxide will be formed and carburization cannot take place. Under these conditions, carburization can occur only if carbon diffuses along the grain boundaries or cracks in the oxide scale and reaches the surface of the alloy. Although stainless steels are stable under these conditions, nickel-based alloys are often preferred since they have higher carburization resistance [37].

At carbon activities higher than 1, so-called metal dusting is frequently observed. Metal dusting results from oversaturation of alloys with carbon which can cause the disintegration of the alloy in a dust of metal particles, graphite, oxides or carbides.

This section is aimed to define the general concepts of the high-temperature carburization. Thermodynamics and kinetics aspects are discussed. Then the effects of alloying elements on carburization resistance are reviewed. In the last section, carburization of nickel-base alloys is described.

2.2.1 Mechanisms and kinetics of carburization

High temperature carburization kinetics can be divided into three main steps: first, adsorption of carbon containing species in the gas phase on alloy surfaces, second, diffusion of the adsorbed

carbon into the alloy and third, reaction of carbon with carbide forming elements, most importantly Cr, and formation of internal carbides. The kinetics of surface reaction (step 1) are mainly controlled by a linear rate law, whereas the kinetics related to the carbon diffusion into the alloy obeys a parabolic rate law. The latter can be described using Fick's second law. In the one-dimensional case if we assume that carbon diffusivity is much higher than other elements, the change in concentration of carbon N(C) with time is given by

$$\frac{\partial N(C)}{\partial t} = D_C \frac{\partial^2 N(C)}{\partial x^2} + D_C Z \frac{\partial N(C)}{x \partial x} \tag{2-14}$$

where N(C) is the carbon concentration, D_C the diffusion coefficient of carbon, x the penetration depth, t the time and Z is the geometrical constant of the sample which can be considered zero for plane geometry. According to Wagner's theory for internal oxidation [38], the carbon penetration depth can be calculated as

$$x = \left[\frac{2 D_C N_S(C) t}{\nu_{eff} N_B^0}\right]^{1/2} \tag{2-15}$$

where $N_s(C)$ is the mole fraction of carbon at the surface, ν_{eff} is the stoichiometric factor of $B_\nu C$ and D_C is the diffusion coefficient of carbon in the metal. As can be seen from this model, the carbon penetration depth has parabolic time dependence [39].

$$x^2 = 2 k_P t \tag{2-16}$$

As Eq. 2-15 shows the carburization rate is determined by the inward diffusion of carbon which depends on carbon diffusivity D_C and solubility $N_s(C)$. The product of these two factors is known as the permeability and depends on the composition of the substrate alloy. According to previous studies [33, 39, 40], carbon permeability shows a minimum at the ratio Ni/Fe=4/1. The solubility and diffusivity of carbon in Fe-Ni alloys has also been investigated and both decrease by increasing Ni content in the alloy up to about 70-80 wt. % nickel and after that a small

increase with increasing Ni content to 100 wt. % (Figure 2-11). This is mainly due to the fact that nickel reduces the chromium activity coefficient and is less soluble in $M_{23}C_6$ carbide compared to iron. A previous study by Forseth and Kofstad [39] shows that Eq. 2-15 can describe carburization kinetics only approximately. Since the carbon activity in the substrate alloy increases as the carburization process proceeds, the stability of the internal carbide phases formed in the alloy changes. This fact has been neglected in the above mentioned model. The quantity N_B in the above equation, which is mainly related to chromium concentration, will be changed during the process since some amount of chromium will precipitate as carbides. On the other hand, B can contain substantial levels of iron as well as chromium and therefore the value of N_B is an underestimate.

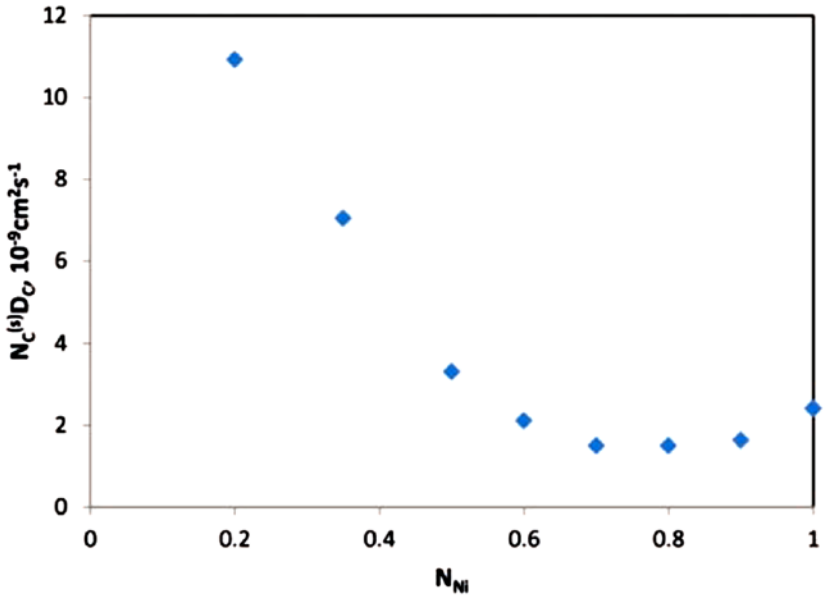

Figure 2-11 Carbon permeability as a function of alloy composition for Fe-Ni alloys at 1000°C with unit carbon activity

Internal carburization of the high temperature alloys is the result of the competition between the rapid diffusion of carbon into the alloy and chromium to the surface of the alloy. Therefore, high temperature alloys are unlikely to form external carbide scales, since the inward diffusion coefficient of carbon is so high. In most of the iron-, nickel- and cobalt-base alloys, carbon diffusion will result in formation of chromium carbides of Cr_3C_2, Cr_7C_3 and $Cr_{23}C_6$ or for combined metal elements in the carbide are then represented as M_3C_2, M_7C_3 and $M_{23}C_6$. The stabilities of these carbides can be described through stability diagrams, which will be discussed in the next chapter.

2.2.2 Thermodynamics of carburization

The most important parameter in carburization of an alloy is the carbon activity in the environment and the carbon activity in the alloy. Carburization occurs when carbon activity in the environment is higher than the carbon activity in the alloy. Other than that, decarburization will occur. Carbon activity of the environment (a_C) can be calculated from the reaction that will produce C from the carbon containing specie in the gas. As an example, in most reducing environment when there is no oxygen in the environment this reaction can be written as previously mentioned hydrocarbon cracking reaction (2-2). Under these conditions the carbon activity in the environment can be calculated by

$$\Delta G^{\circ} = -RTln\frac{a_C^n \cdot P_{H_2}^{m/2}}{P_{C_nH_m}} \tag{2-17}$$

$$a_C = e^{-\Delta G^{\circ}/RT}\left(\frac{P_{C_nH_m}}{P_{H_2}^{m/2}}\right) \tag{2-18}$$

In many high temperature alloys (ferritic and austenitic stainless steels and nickel- and cobalt-base alloys) carbon can diffuse into the alloy rapidly which results in the formation of mainly chromium carbides. The morphology of the precipitates is the result of a competition between nucleation and growth. Depending on alloy microstructure, more rapid carbon diffusion will lead to a quicker supersaturation and the nucleation will tend to be homogeneously distributed. On the other hand, the presence of grain boundaries will cause a rapid chromium supply to the precipitates and favor their continued growth.

There are three different types of chromium carbides of: Cr_3C_2, Cr_7C_3 and $Cr_{23}C_6$. In general, higher carbon activities will favor the formation of Cr_3C_2 carbide in the alloy. However, as the carbon diffuses into the alloy, the activity of carbon will be reduced and Cr_7C_3 and after that $Cr_{23}C_6$ carbides will be formed respectively. Until now, the assumption was that these chromium carbides are pure phases. This is only true in the systems such as Ni-Cr-C. However, these carbides can incorporate other alloying elements such as Fe in Fe-Cr-C or Ni-Fe-Cr-C systems. Therefore, for combined metal elements, carbides can be represented as M_3C_2, M_7C_3 and $M_{23}C_6$. In 1974, Benz et al. [41] studied the phase relations in the Fe-Cr-C system in temperature range of 900 to 1150°C. Figure 2-12 shows the isothermal section of this system at 1000°C. It can be clearly seen that the iron solubility in carbides is high and cannot be neglected.

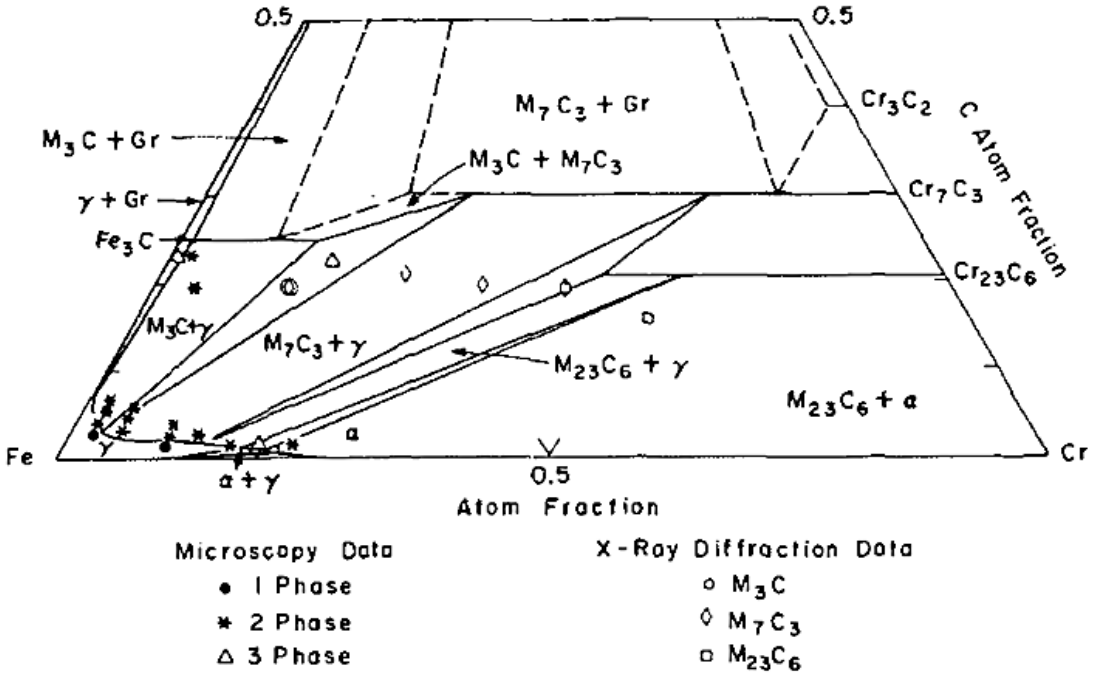

Figure 2-12 Isothermal section of the Fe-Cr-C system at 1000°C [41]

Other alloying elements such as Mo, Ti, Ta, Nb and W, which are strong carbide formers, also have been added to many high-temperature alloys for an important strengthening mechanism by forming carbides. The stability of some of these binary carbides are shown in Figure 2-13. The next chapter is focused on the effect of several important alloying elements on carburization behavior of high temperature alloys. Several studies on the effect of these alloying elements on carburization behavior will be briefly reviewed.

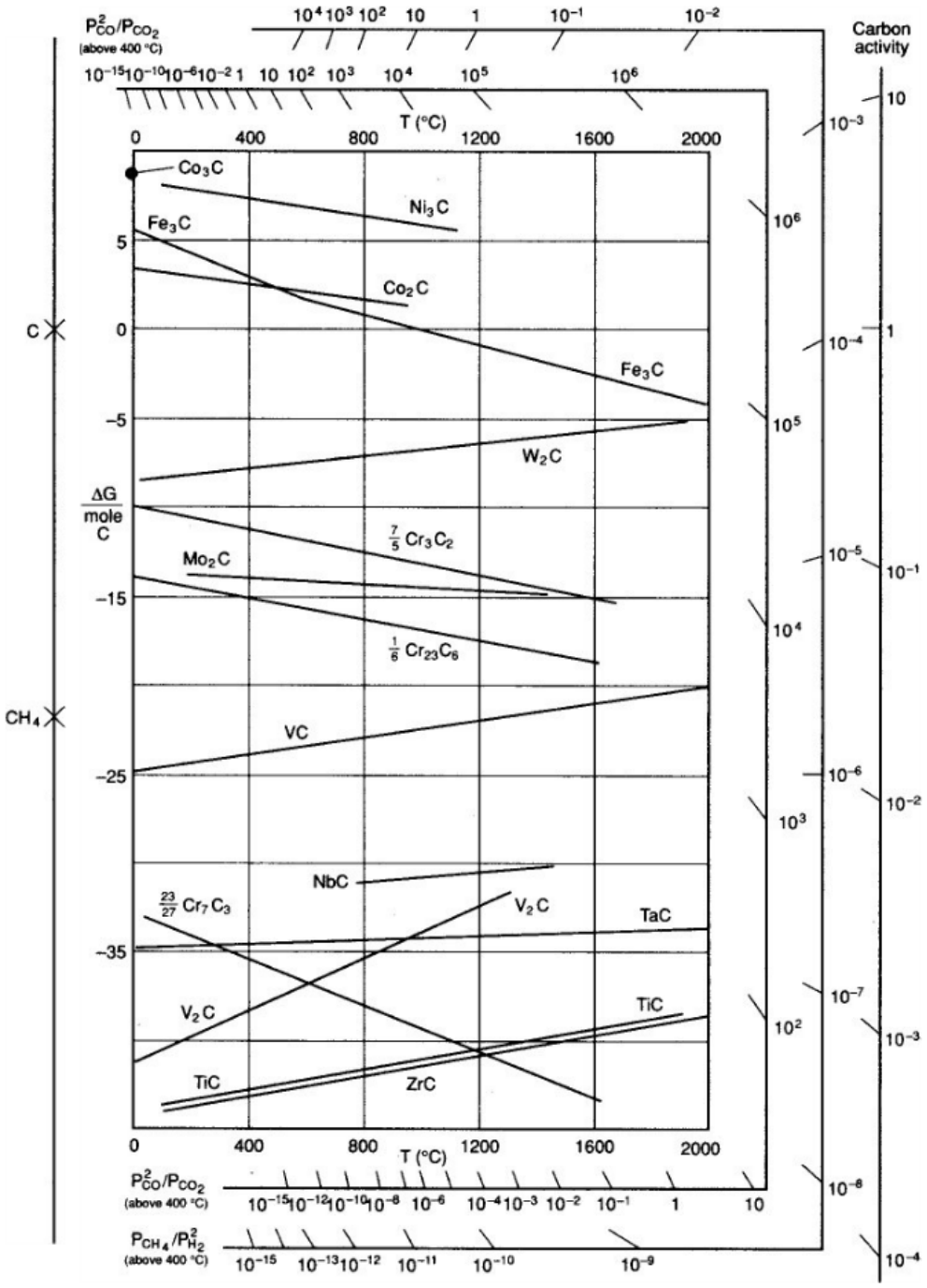

Figure 2-13 Standard free energies of formation for selected binary metallic carbides [25]

2.2.3 Alloying for carburization resistance

Effect of nickel- Traditional materials used in carburizing environments such as steam cracking furnaces were either cast (HK40) or wrought (Incoloy 800 or type 310 stainless steel). In order to increase the efficiency, tube wall thicknesses are being decreased and as a result, higher levels of major (Ni, Cr) or minor (Mo, Si, Ti, Al, Nb) alloying elements are being used to increase the tube lifetime [42]. Previous studies show that high-nickel alloys are generally more resistant to carburization compared to Fe-Ni-Cr alloys. In 1976, Grabke et al. [43] observed that carburization resistance of the Fe-Ni-Cr alloys increases with increasing nickel content and the maximum resistance is achieved when Ni/(Fe+Cr) ratio is 4:1. In 1970s, Demel et al. [44] showed that the diffusivity of carbon in Fe-15Cr-Ni alloys decreases by almost two orders of magnitude when the nickel content increases from 26 to 50%. In addition, nickel reduces chromium activity coefficient and it's also less soluble in $M_{23}C_6$ carbide than iron.

Effect of silicon- Oxide scale formation is one of the most effective ways to reduce the carbon diffusion into the alloy. As a result, elements such as aluminum, silicon and chromium have been added to high temperature alloys to form a protective oxide scale at the surface. The diffusion of carbon in such cases mainly depends on the nature of the oxide scale and the oxygen partial pressure of the environment. Under reducing conditions, where the partial pressure of the oxygen is not enough to form this oxide layer at the surface, these oxides cannot be formed due to their lower thermodynamic stability in comparison with the carbides [45]. Under such conditions, carburization is mainly controlled by diffusivity and solubility of carbon. It has long been known that silicon additions to these alloys can reduce the carburization attack. In addition, the stability of silicon carbide (SiC) is much less than chromium carbides. Therefore, no SiC will be formed and addition of silicon does not affect the value of N_B in Eq. 2-15. The effect of

silicon addition has been studied by Roy et al. [46], Mitchell et al. [47] and Smith et al. [42]. According to their studies, silicon has been known to reduce both solubility and diffusivity of carbon into the alloy. In 1982, Mitchell et al. [47] showed that addition of silicon decreased the solubility more than diffusivity. However, since the addition of silicon reduces the creep strength and weldability of the austenitic alloys, the maximum limit of silicon content in cast HP and HK grades are approximately 2%.

Effect of aluminum- The beneficial effect of aluminum additions has also been demonstrated previously. Aluminum has been known as the most effective element in improving the carburization resistance since the Al_2O_3 layer is thermodynamically stable at the impurity levels of water vapor which are unavoidable in reaction gases. In most of the cases, this oxide layer is so thin which cannot be seen by scanning electron microscopy. Smith et al. [42] have shown that addition of aluminum up to 3.3 wt. % is effective against carburization. In addition, Ando et al. [48] have reported the existence of a critical concentration of ~2.7 wt. % aluminium for good carburization resistance. They showed that for aluminum concentrations less than the critical value, protective oxide scale cannot be formed. Clearly an aluminum content of 4.5 wt. % is sufficient to maintain a protective oxide film, even under strongly reducing conditions [49].

Effect of molybdenum- Molybdenum, which is strong carbide former, has been added to high temperature alloys for the purpose of solution strengthening. According to previous study by Mitchell et al. [49], the carbides of Mo_3C and Cr_7C_3 have similar stabilities and can coexist at similar activity levels. As a result, presence of this carbide can increase the value of N_B in Eq. 2-15.

Effect of niobium and titanium- Niobium and titanium have similar effect on carburization resistance. Both of these elements are strong carbide formers and their precipitation

can decrease the reaction rate by consuming some of the carbon flux. The effect of Nb and Ti on increasing the carburization resistance and decreasing the k_P have been reported previously by Smith et al. [42]. However, since these elements are usually added in low concentrations (typically around 0.1-1.2 wt. %), their effect on the value of N_B in Eq. 2-15 is much less than the reductions observed on k_P. It was observed that increasing the Ti level from 0.4 wt. % in alloy 800H to 1.2 wt. % in alloy 801 can cause a decrease of about 90% in k_P. This was much higher than the predicted value of about 10% at 1000°C. Therefore, it is possible that carbides of these elements show some blocking effect on carbon diffusion and, thus, decrease the $N_C D_C/N_B$ in Eq. 2-15.

2.2.4 Protection by adsorbed sulfur

Carburization attack can also be reduced by adjusting the composition of the environment, most importantly, introducing sulfur containing compounds such as H_2S into the environment. As was mentioned previously, there are three different kinetic steps in the high temperature carburization of an alloy:

1- Transfer of carbon from gas phase to the alloy surface (linear rate law)

2- Diffusion of carbon into the alloy (parabolic time dependence)

3- Reaction of carbon with chromium to form chromium carbides

At lower temperatures and in the absence of sulfur, kinetics are controlled by diffusional processes and have parabolic time dependence; but upon sulfur additions or at higher temperatures step 1 in the aforementioned sequence of steps becomes very important and becomes the slowest step. When sulfur is introduced to the environment, it can preferentially be adsorbed by the alloy surface and therefore, blocks the adsorption sites for carbon and prevent

the transfer of carbon into the alloy. Figure 2-14 shows a schematic of the mechanism of inhibition of carburization by sulfur [50].

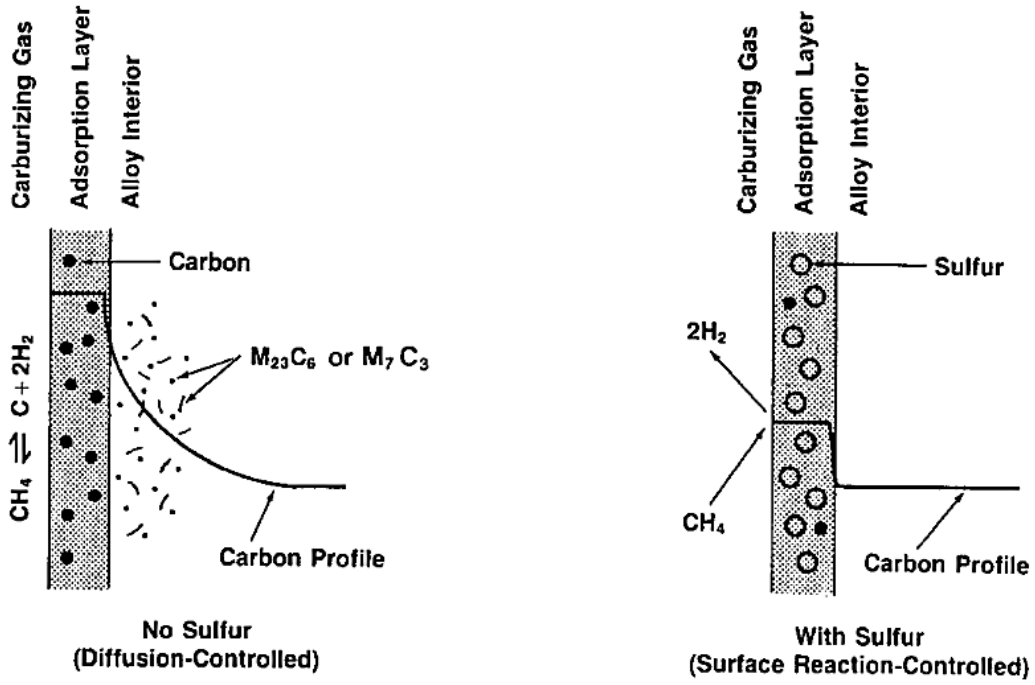

Figure 2-14 Schematic mechanism of inhibition of carburization by sulfur [50]

In a1998, Ramanarayanan et al. [34] conducted an experiment to show the effect of H_2S on carburization kinetics. In their experiment, H_2S was introduced at a concentration level of 100 ppm after the surface chromium oxide was completely converted to the carbide and carburization had set in. A dramatic reduction in carburization rate was observed according to the thermogravimetric regime in Figure 2-15. When the H_2S turned off, rapid carburization happened almost immediately. These results show that sulfur has no memory effect. The precise mechanism of sulfur interaction with carbide surface in carburizing environments still needs further study.

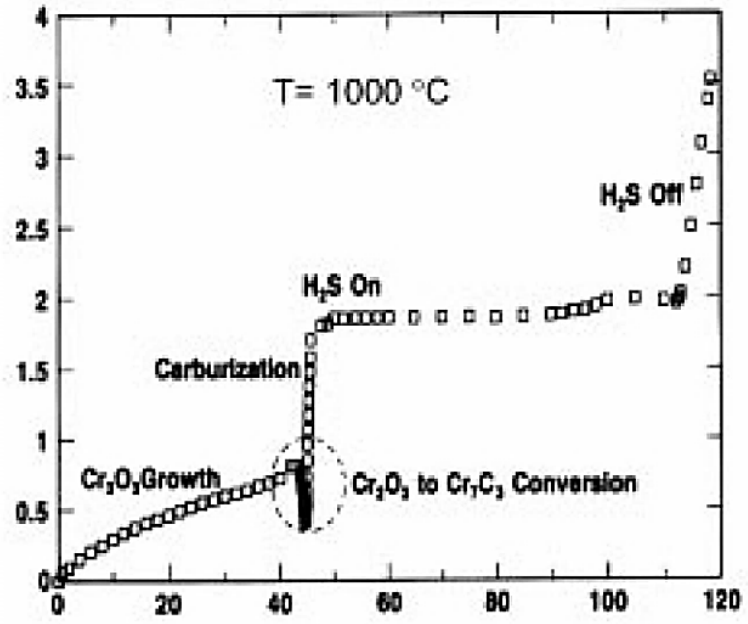

Figure 2-15 Effect of H_2S addition on kinetics of carburization [34]

Up until now, thermodynamics and kinetics of the reactions in single-oxidant environments of sulfidizing and carburizing and the effect of alloying elements on the high temperature resistance of alloys in these environments were discussed separately. The following section is focused on the reaction of these alloys in multi-oxidant environments.

2.3 CORROSION IN MIXED-GAS ENVIRONMENTS

Earlier in this chapter the reaction of metals and alloys in single-reactant environments containing sulfur or carbon was discussed. As was mentioned before, in some process environments such as coal conversion systems or certain petrochemical processes, alloys are exposed to multi-oxidant gas atmospheres containing low oxygen and high sulfur and carbon

activities. The product of high temperature reactions with these environments can be very complex and the rate of formation is difficult to predict.

Although laboratory testing can never simulate the exact conditions existing in powerplants, the results obtained over the years of testing can be very helpful in providing the technical basis for alloy design. Having an understanding of individual corrosion processes, such as oxidizing, sulfidizing or carburizing, can be very helpful but definitely do not provide synergistic effects that might occur in the plant. In order to understand how alloys behave in different corrosion environments containing several oxidants, it is important to understand the fundamentals of the thermodynamic phase stability of the metal-gas system.

2.3.1 Sulfidizing-oxidizing

Most common gas mixtures used in sulfidation-oxidation studies are H_2-H_2O-H_2S which has relatively low oxygen partial pressures and SO_2-containing atmospheres with higher oxygen partial pressures. Since the focus of this research is on the atmospheres with low oxygen and high sulfur potentials, the atmospheres containing H_2, H_2S, and H_2O will be studied in more detail in this chapter.

2.3.1.1 Thermodynamic considerations

Up until the 1990's, many laboratory studies in sulfidizing-oxidizing conditions have been concerned with relatively high temperatures, 700-1000°C, using equilibrated gas. However, in the 1990's emphasis moved to lower temperatures of about 400-700°C since no alloy could resist such atmospheres at those temperatures. Under these reducing environments, the most relevant reactions in order to determine the equilibrium P_{O2} and P_{S2} are:

$$H_2(g) + \frac{1}{2}O_2\,(g) \rightarrow\ H_2O(\mathrm{g}) \tag{2-19}$$

$$H_2(g) + \frac{1}{2}S_2\,(g) \rightarrow\ H_2S(g) \tag{2-20}$$

From these reactions the equilibrium constant, K, can be written as:

$$K_1 = \frac{P_{H_2O}}{P_{H_2}\sqrt{P_{O_2}}} = exp\left[\frac{-\Delta G_1^o}{RT}\right] \tag{2-21}$$

$$K_2 = \frac{P_{H_2S}}{P_{H_2}\sqrt{P_{S_2}}} = exp\left[\frac{-\Delta G_2^o}{RT}\right] \tag{2-22}$$

where ΔGs are the standard Gibbs free energy change for reaction (2-19) and (2-20) in typical units of J/mole, R is the gas constant and T the absolute temperature. By combining these two equations it is found that:

$$\frac{P_{O_2}}{P_{S_2}} = \left[\frac{K_2}{K_1}.\frac{P_{H_2O}}{P_{H_2S}}\right] \tag{2-23}$$

$$\frac{K_2}{K_1} = exp\left[\frac{-155{,}710 + 5.41T}{RT}\right] \tag{2-24}$$

According to equations (2-23) and (2-24), by increasing temperature the P_{O2}/P_{S2} ratio increases (for a fixed P_{H2O}/P_{H2S} ratio). Same thing happens with increasing P_{H2O} (at a fixed temperature and P_{H2S}). Increasing the P_{O2}/P_{S2} ratio increases the oxidizing potential of the gas mixture and therefore, increases the resistance to sulfidation by promoting the formation of a protective oxide layer.

In general, sulfidizing-oxidizing atmospheres are characterized in terms of both sulfur and oxygen partial pressures. This can be presented through metal-sulfur-oxygen stability diagrams. Hemmings and Perkins [51] previously discussed how these stability diagrams can be used in order to understand the corrosion behavior of various metals in these environments. For a given atmosphere there exist equilibrium values of P_{O2} and P_{S2} which represent a point on the

stability diagram and identify the phase that is in equilibrium with that particular atmosphere. Figure 2-16 shows the stability range of Ni and Cr and their oxides and sulfides as a function of P_{O2} and P_{S2}.

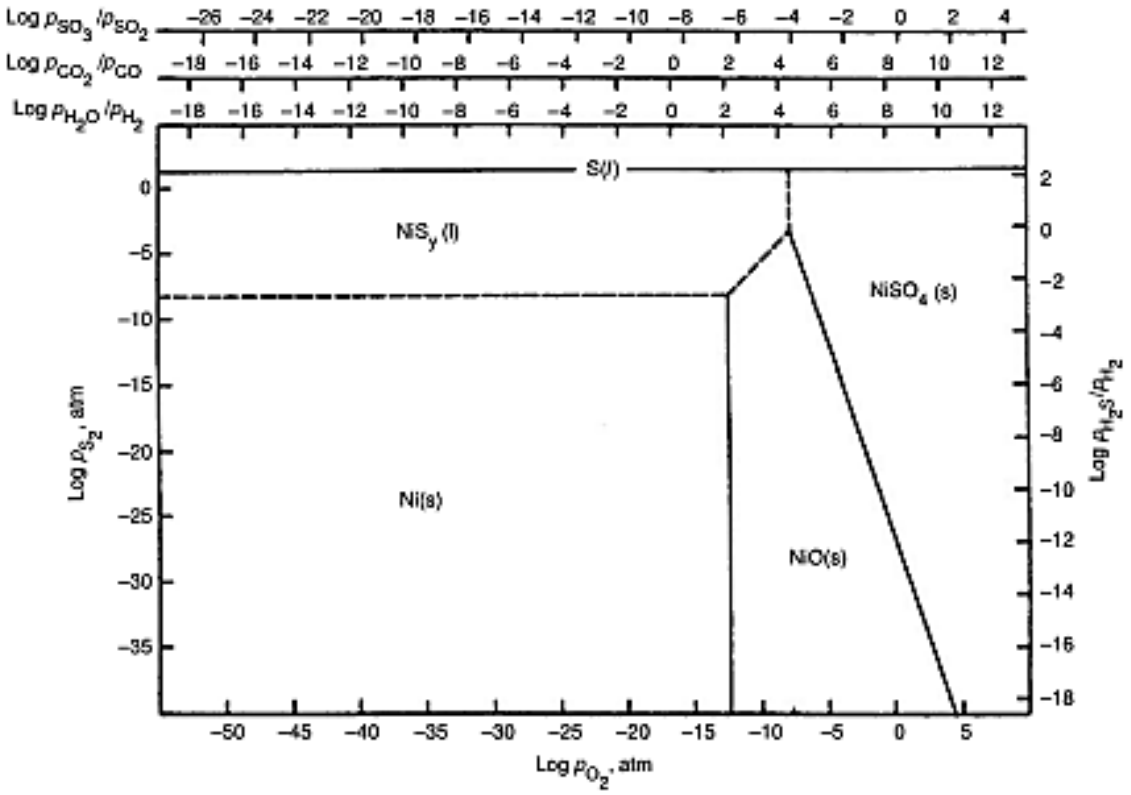

(a)

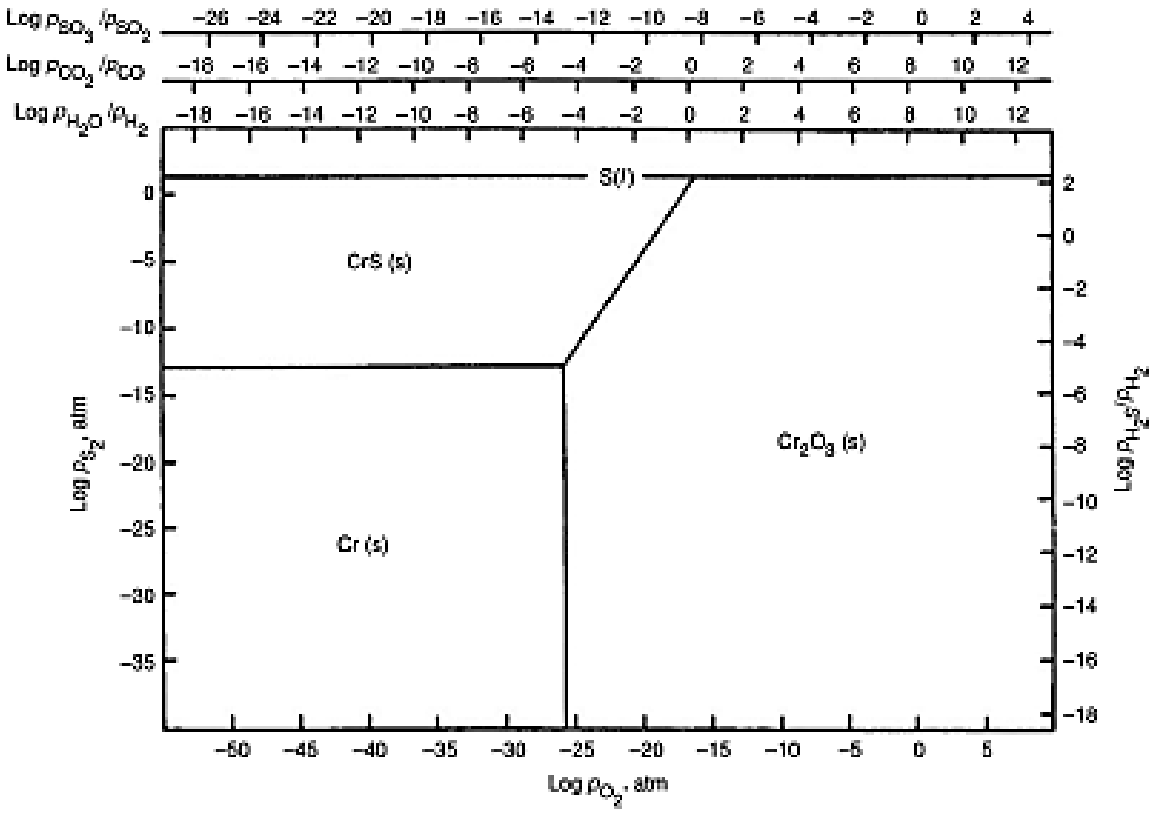

(b)

Figure 2-16 Stability diagram of a) Ni-S-O and b) Cr-S-O at 870°C (1600°F) [51]

These stability diagrams can be determined considering the equilibrium reactions between metal and oxide and metal and sulfide as follow

$$M + \frac{1}{2}O_2\,(g) \rightarrow\ MO \tag{2-25}$$

$$M + \frac{1}{2}S_2\,(g) \rightarrow\ MS \tag{2-26}$$

$$MO + \frac{1}{2}S_2\,(g) \rightarrow\ MS + \frac{1}{2}S_2\,(g) \tag{2-27}$$

These diagrams allow us to predict the phases that are likely to form on pure metals when they are exposed to the multi-oxidant environments.

2.3.1.2 Kinetic boundary

According to reaction (2-27), the thermodynamic boundary separating the sulfide and oxide stable regions can be determined through

$$\left[\frac{P_{O_2}}{P_{S_2}}\right]^{\frac{1}{2}} = K \tag{2-28}$$

However, many studies previously showed that transition from sulfide to oxide actually occurs at higher P_{O2} values compared to the calculated values. It has been shown [52] that the experimentally-determined boundary of sulfide/oxide in these diagrams, is affected by the kinetic factors and accordingly, is referred to as “kinetic boundary”. The location of this boundary depends on many factors, such as: alloy composition, surface finish of the specimen, composition of the gaseous environment, etc. It has been observed [52] that the oxygen pressure of about two orders of magnitude is necessary for oxide formation and to suppress sulfidation (see Figure 2-17). In the case of alloys, superposition of different diagrams for pure metals can aid us in interpreting the reaction products. However, the practice of superposition is not so accurate since it neglects the formation energies due to the mutual solubility of metals and their products.

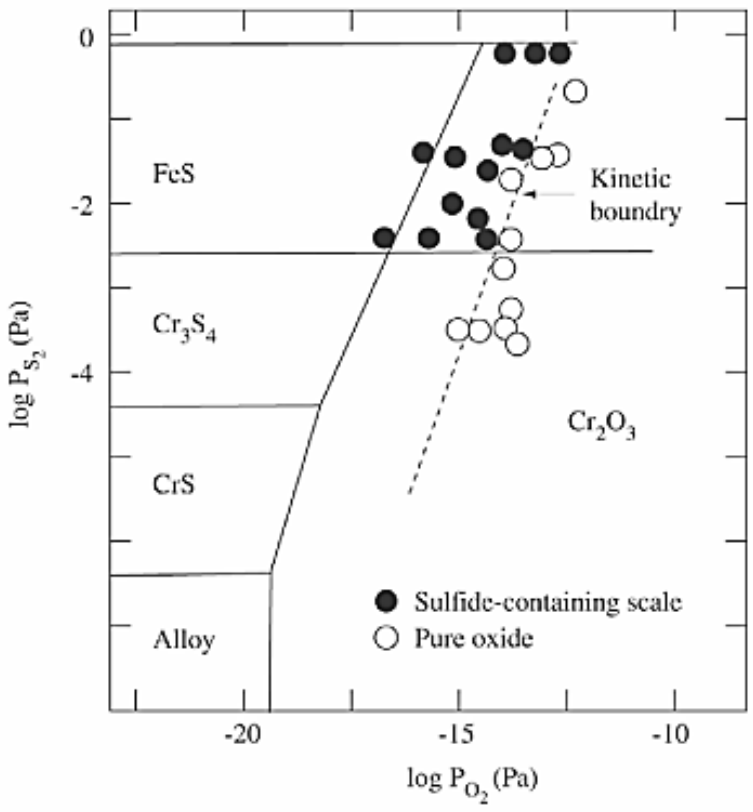

Figure 2-17 Thermodynamic phase-stability diagram for type 310 stainless steel at 875°C, showing the experimentally-determined kinetic boundary [7]

2.3.1.3 Protection by formation of an oxide scale

The protection against sulfidation mainly comes from the ability of the alloy to form a protective, slow growing oxide scale at the surface, which protects the substrate alloy from further attack. Most commercial high temperature alloys consist of a base of Ni, Co, or Fe, which forms very stable sulfides and moderately stable oxides. On the other hand, they also consist of alloying elements Cr, Al, or Si, which form highly stable oxides. The selective oxidation (oxidation of solute preferentially to the parent element) of these elements is the basis for the protection of all alloys used at high temperatures. The concentration of these alloying elements plays an important role in protective behavior of the scale. However, Al and Si tend to embrittle the metallic materials and therefore, there is a limit on their content in the alloy. Thus, for

applications in coal fired boilers or gasification plants, chromia forming alloys are the usual choice.

The oxidation of these elements can occur by either one of two mechanisms depending on their concentrations in the alloy and oxygen potential in the gas. If the concentration of the oxidizing element is low, oxygen will diffuse inward, causing the formation of an internal oxidation zone. If the concentration is sufficiently high, solute atoms can diffuse outward and oxide will be formed as an external layer. The minimum required concentration of these elements for the formation of an external, protective oxide scale can be calculated through the Wagner's theory;

$$N_B^{(0)} > \left[\frac{\pi g^*}{2\nu} N_O^{(S)} \frac{D_O V_m}{D_B V_{ox}}\right] \tag{2-29}$$

where g* is the critical volume ratio necessary to form a continuous BO_v scale (typically $g* = 0.3$), $N_O^{(s)}$ the oxygen solubility in the alloy, D_O and D_B diffusivity of oxygen and the oxide forming element B in the alloy, V_m and V_{ox} the molar volumes of alloy and oxide. It is seen that according to this equation, the exposure conditions can affect the minimum concentration of the solute to be able to form a protective external oxide scale.

Continued growth of oxide scale depends on the transport of metal and oxygen species through the existing layer. Wagner (1952) also determined the minimum required concentration of the oxide-forming element B necessary to maintain the growth of the external oxide scale of BO_v on an A-B alloy. Several assumptions were made: D_B is independent of concentration, the growth of this oxide scale obeys the parabolic rate law, solvent metal A is insoluble in BO_v, and that the moving boundary of alloy/scale can be neglected; Wagner derived the following criterion:

$$N_{B,min}^{(0)} > \frac{V_m}{32}\left(\frac{\pi k_P}{D_B}\right)^{1/2} \quad (2\text{-}30)$$

where it shows the molar flux of solute B to that being required for oxide growth. The actual concentration of oxide-forming element B necessary for both the establishment and sustained growth of a BO_v scale will probably be higher than due to the kinetic reasons [53].

2.3.1.4 Transport properties of the scale

In the presence of a secondary oxidant, chromia scale has been found to behave in different ways. Under such conditions, a Cr_2O_3 layer might not form or even when it forms, it might not be completely protective. Previous studies [54, 55], clearly show the formation of other phases (carbides, sulfides, and nitrides) beneath or above the initially formed chromia scale after certain amount of time into the reaction, which shows the existence of an incubation period for the oxide layer. This incubation period last longer for the more adherent oxide scales.

During the initial period of the reaction in sulfidizing-oxidizing atmospheres, there is no equilibrium with the gas phase and both sulfide and oxide can be formed as long as their formation pressure is exceeded. In other words, the transient stage is mainly governed by kinetics. In 1987, LaBranche et al. [8] showed that oxides and sulfides can both nucleate on the surface of the alloys during the heating stage and can continue to grow when the sample reaches the reaction temperature. Continued growth of oxides and sulfides depends on both kinetic and thermodynamic factors. If oxide is more stable than sulfide, sulfide that formed initially is quickly overgrown by oxide and trapped as separate sulfide particles at the alloy/scale interface. Later, diffusion of sulfur through the oxide layer causes the growth of initially formed sulfide particles, which will further cause the breakdown of the oxide scale and rapid corrosion. This phenomenon is known as “breakaway corrosion” which is shown schematically in Figure 2-18.

The penetration of sulfur through the oxide scale may be possible in two ways: 1. Dissolution of sulfur in the oxide scale and diffusion to the scale/alloy interface, and 2. Transport of sulfur or sulfur containing species (H_2S) through physical defects in the scale such as cracks or pores or through grain boundaries. However, the solubility of sulfur in chromia scales is negligible. Thus, it is generally accepted that sulfur transport occurs mainly through physical defects (cracks or pores) and other internal surfaces such as grain boundaries in the oxide scale.

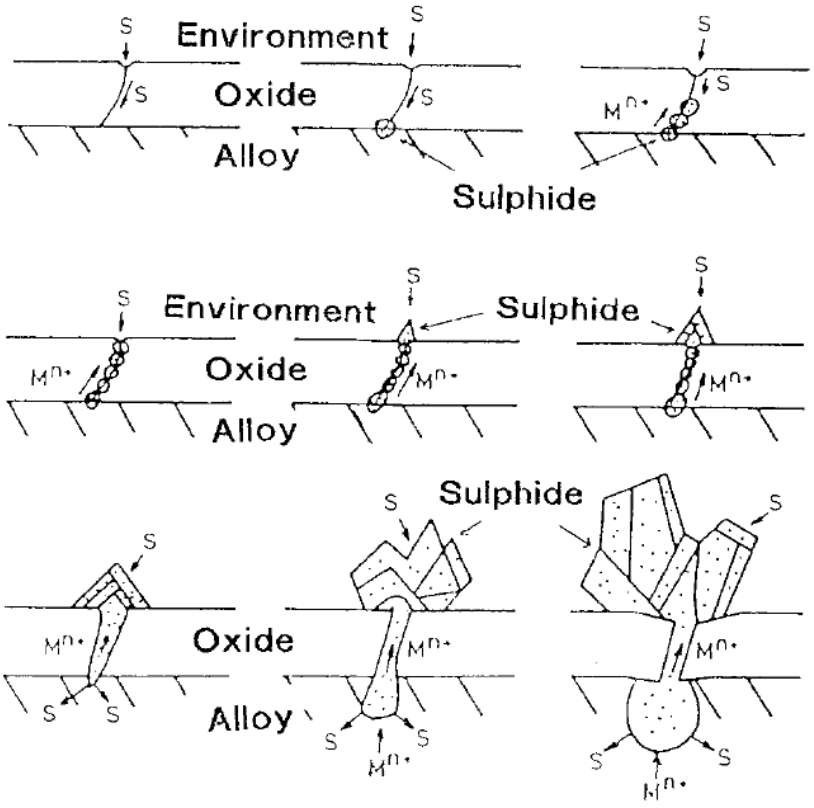

Figure 2-18 Schematic of the degradation sequence leading to breakaway corrosion under oxidizing-sulfidizing conditions [6]

The presence of other species in the gas can affect the transport properties of the chromia scale. The preferential adsorption of one particular gas molecule on internal surfaces of the oxide scale can greatly influence the permeation of other species. As an example, Young et al. [54, 55]

observed that the presence of water vapor can prevent the inward transport of nitrogen and formation of internal nitrides or at as was discussed in the previous chapter, preferential adsorption of sulfur on the internal surfaces of the oxide can decrease the permeability to carbon.

When oxide scale breaks down, fast growing sulfides can form on the surface of the oxide scale. Considering a typical scale formed on the surface of an alloy, the activity of the reactants will decrease from a maximum value at the scale/gas interface to a minimum in the alloy while the activity of the metallic elements increases. Figure 2-19 (a) shows a typical scale formed on a Ni-Cr alloy in sulfidizing-oxidizing environment. This concept is the basis of the "reaction path" concept which was introduced by Stringer et al. in 1977 [56]. This can be explained by the dashed line in the phase stability diagram shown in Figure 2-19 (b) as a path from point A to D.

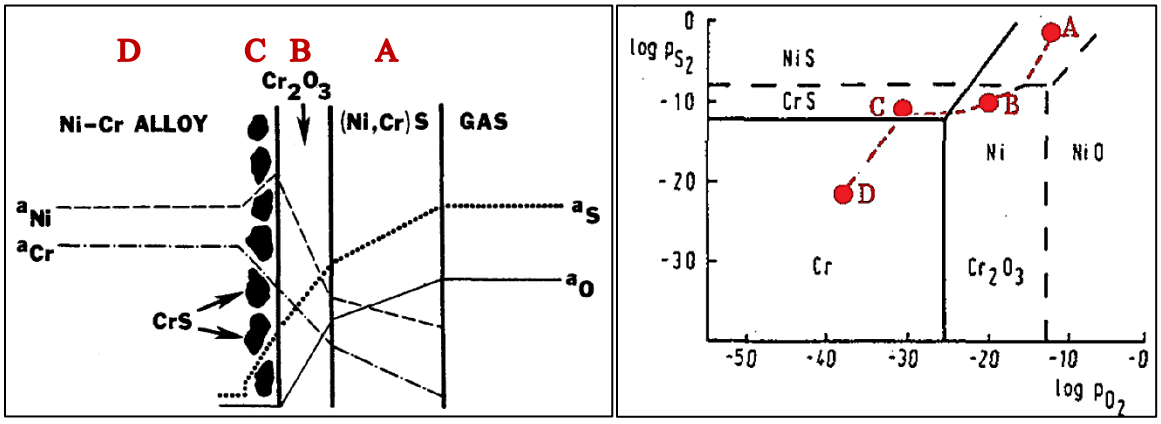

(a) (b)

Figure 2-19 a) Schematic model to compare sequence of reaction products in sulfidizing-oxidizing environment, b) Superimposed phase stability diagram and reaction path depicting the change of sulfur and oxygen activities in the reaction products [57]

At the scale/gas interface (point A), NiS is in equilibrium with the gas. As the local values of P_{O2} and P_{S2} decrease through the scale, a point B is reached where the value of P_{S2} is below the Ni/NiS boundary but the value of P_{O2} is still sufficiently high for Cr_2O_3 to form and this explains the presence of the Cr_2O_3 layer beneath the NiS layer. At position C the P_{O2} value has become too low for Cr_2O_3 to be stable but the P_{S2} is still sufficient for CrS to form, hence explaining the presence of CrS precipitates in the alloy. Finally position D is reached where only the alloy is stable [28].

2.3.1.5 Alloying for protection in sulfidizing-oxidizing environments

The effect of different alloying elements in sulfidizing environments was previously discussed at the beginning of this chapter. As was mentioned, common metals and their corresponding sulfides can form low melting point eutectics (Table 2-3) which will cause the formation of liquid sulfide over the oxide scale. As a result, high nickel containing alloys are susceptible to sulfidation and liquid attack at temperatures higher than 645°C. It has been known that increasing Fe content of the alloy can decrease the risk of liquid sulfide formation. For more severe conditions, Co-containing alloys can be a good alternative, such as alloy HR-160 (~37Ni-30Co-28Cr-2.75Si). High cobalt content in Ni-base alloys is generally known to reduce the risk of Ni-Ni_3S_2 eutectic formation and also can decrease the rate of sulfur diffusion in the alloy matrix.

Most high temperature alloys used in these environments are chromia former alloys, which mainly rely on chromia formation for protection against corrosion. In general, increasing the chromium content causes better sulfidation resistance in most iron- and nickel-base alloys [58]. Figure 2-20 shows the effect of chromium concentration in several commercial alloys on the time to breakaway corrosion [59].

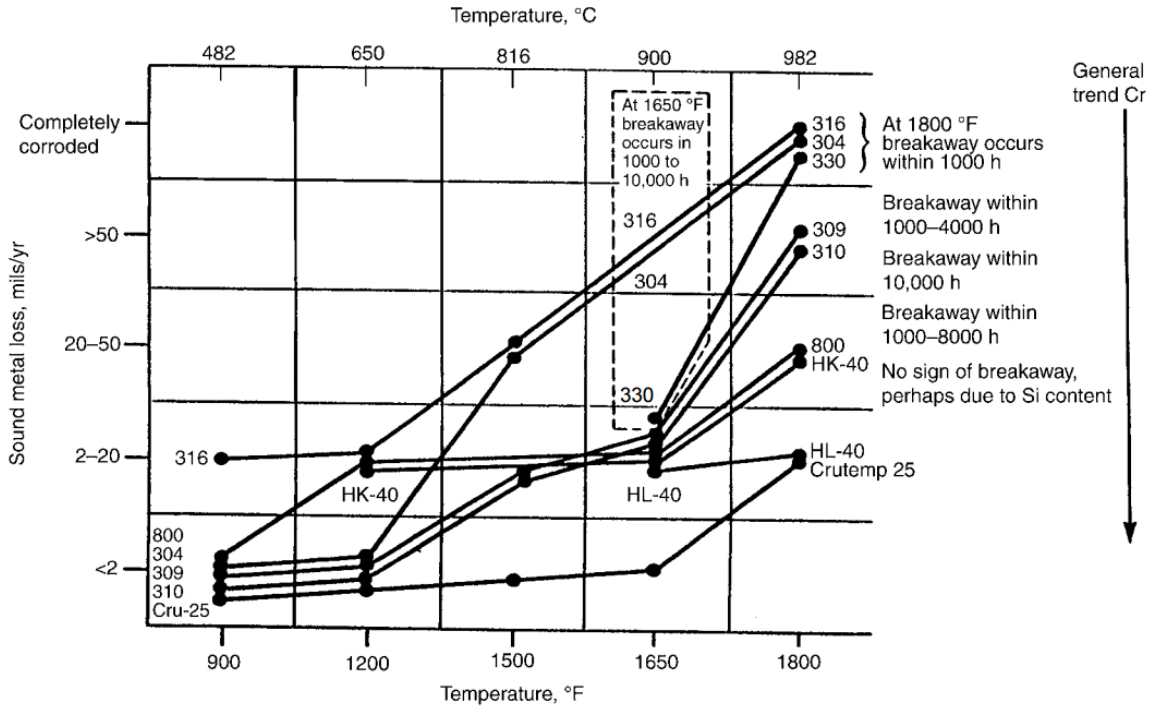

Figure 2-20 Effect of chromium concentration on the time to breakaway corrosion of Fe-Cr-Ni alloys in coal gasification atmospheres with 1 and 1.5% H_2S [59]

Based on the previous studies on alumina forming alloys, it is clear that these alloys provide the best resistance to sulfidation by formation of an alumina layer. However, formation of a protective and continuous alumina scale requires high concentrations of Al. Effect of Si on sulfidation resistance of alloy HR-160 was also investigated by Lai [10]. Addition of about 2.75% Si to this alloy provided a good sulfidation resistance by formation of a chromium oxide layer followed by a SiO_2 layer in the subscale region. However, Al and Si tend to embrittle the metallic materials and therefore, there is a limit on their concentrations in the alloy.

2.3.2 Carburizing-oxidizing

Many commercial carburizing atmospheres often contain both C- and O-containing gas species, and the oxygen partial pressure is usually enough to cause simultaneous oxidation and carburization. The oxidizing species are usually present in the form of carbon dioxide or water vapor and the common equilibria are the synthesis gas reaction

$$CO + H_2 = H_2O + C \tag{2-31}$$

or the Boudouard reaction

$$2CO = CO_2 + C \tag{2-32}$$

2.3.2.1 Thermodynamic considerations

Carburizing environments can also be characterized using two terms of a_C and P_{O2}. The carbon activity at the alloy surface can be calculated by:

$$a_C = e^{-\frac{\Delta G}{RT}}\left(\frac{P_{CO}.P_{H_2}}{P_{H_2O}}\right) \tag{2-33}$$

$$a_C = e^{-\frac{\Delta G}{RT}}\left(\frac{P_{CO}^2}{P_{CO_2}}\right) \tag{2-34}$$

which shows the carbon activity as a function of gas compositions. Similar to sulfidizing-oxidizing environments, stability diagrams can be plotted for M-C-O systems, M being different metallic components. Figure 2-21 shows the stability diagram for the Cr-C-O system at 870°C. As it was mentioned before in the carburization chapter, chromium is one of the most important elements in carburizing environments by forming stable carbides.

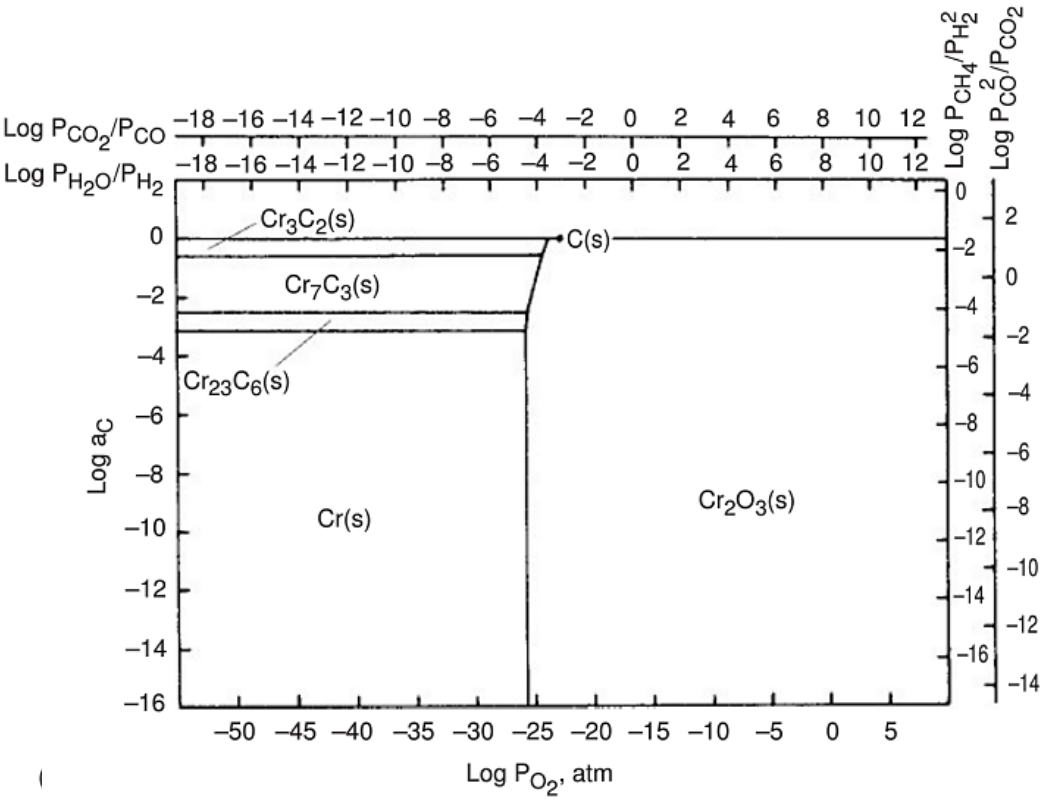

Figure 2-21 Stability diagram of Cr-C-O system at 870°C [25]

Another important reaction in carburizing-oxidizing conditions for chromia-forming alloys is:

$$3Cr_2O_3 + 4C = 2Cr_3C_2 + \frac{9}{2}O_2 \quad (2\text{-}35)$$

$$\Delta G° = 3{,}192{,}100 - 797.3\,T\;J.mol^{-1} \quad (2\text{-}36)$$

which can be used to determine the thermodynamic boundary between Cr_3C_2/Cr_2O_3. According to this reaction, chromium carbide is stable when P_{O2} of the environment is lower than the equilibrium P_{O2} from above reaction. On the other hand, if P_{O2} is higher than the equilibrium P_{O2} chromium oxide will be stable. This reaction is temperature dependent and, thus, temperature can significantly affect the carburization behavior of an alloy. Accordingly, higher temperatures favor carburization and lower temperatures favor oxidation [13].

2.3.2.2 Kinetic considerations

As it was mentioned before in the carburization section, carburization is generally the result of a competition between internal precipitation due to the rapid inward carbon diffusion and external scale formation by chromium outward diffusion. Internal carburization obeys parabolic kinetics, similar to internal oxidation. Parabolic rate constant and depth of carbon penetration is directly proportional to carbon permeability which consists of carbon diffusivity and solubility.

However, under carburizing-oxidizing environments, the presence of water vapor or CO_2 can help the formation of an oxide layer, which can prevent or slow down the carbon penetration into the substrate alloy. Carbon ingress can be greatly reduced by formation of a dense oxide layer such as Cr_2O_3 or, more importantly, Al_2O_3 and SiO_2. Carburization kinetics under such conditions, are then controlled by carbon diffusion through the oxide scale. Previous studies [60] showed that there is no detectable solubility for carbon in these oxide scales. Thus, carbon cannot diffuse through a perfectly dense oxide scale, unless the scale exhibits some kind of defect such as pores or cracks or even possibly through the grain boundaries. Carbon transport mechanisms through oxide scale will be discussed next.

2.3.2.3 Transport properties of the scale

Under carburizing-oxidizing conditions, when the partial pressure of oxygen is high enough, the chromium oxide scale forms at the surface. However, it has been reported that the expected protection against carbon penetration was not achieved in the case of chromia forming alloys. Carbides can still form beneath the oxide layer and continue to grow as the oxide scale thickens. Figure 2-22 shows a schematic of the microstructure that can form under these conditions and also oxygen and carbon activity profiles across different layers. The observed sequence of reaction products are in accord with their thermodynamic stability with the most stable phase

(oxide) at scale surface, where the Cr activity is the lowest, and the least stable phase (carbide) at the scale/metal interface where Cr activity is the highest. In 1986, Grabke et al. [61] conducted experiments to investigate the mechanism of carbon transport through the oxide layer. In this study, several Fe-Cr alloys were pre-oxidized in H_2-H_2O gas mixtures (at 900 or 1000°C) and then exposed to the H_2-H_2O-CO-CO_2 atmospheres with carbon activity of 0.2 and oxygen partial pressure of 10^{-20}, tagged with radiotracer carbon. They observed that carburizing specie can slowly permeate through the preformed oxide scale.

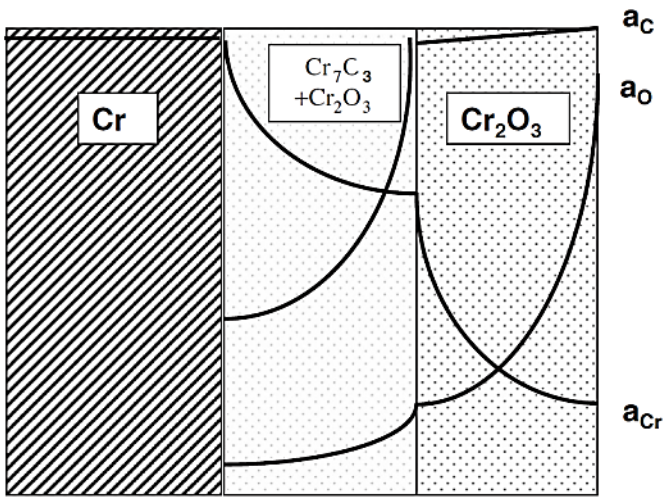

Figure 2-22 Schematic activity profile representing the penetration of carbon through a Cr_2O_3 layer [13]

Now, the important question is: How does carbon penetrates an otherwise protective chromia scale? It has been known that solubility of carbon in chromia scale is too low and lattice diffusion is therefore unimportant [60]. Thus, carbon penetration occurs either by gaseous diffusion through large defects such as cracks or pores in the scale or through much smaller defects such as internal surfaces. However, the gaseous transport through macro cracks cannot be the main mechanism here since the oxygen and carbon activities at the alloy/scale interface

would then be similar to those in the external gas atmosphere, and carburization is thermodynamically impossible. Therefore, transport of molecular species through oxide grain boundaries or nanoscale pores has been proposed [62].

In a recent study by Nguyen et al. [63], it was clearly shown that chromia scales are not completely protective against carburization attack and carbon can still transport through the chromia grain boundaries. A two-stage test was performed, where a sample of Fe-20Cr was first exposed to Ar-20O_2 gas, followed by exposure to Ar-20CO_2 gas at 650 °C. Formation of internal carbides beneath the oxide scale showed that carbon or carbon-containing specie can transport through the oxide scale. Further atom probe tomography confirmed the enrichment of carbon on some of the grain boundaries of the oxide. It was then concluded that grain boundary transport is the main mechanism, where carbon penetrates the oxide scale and enters the substrate alloy. In addition, it was observed that the presence of carbon can lead to the refinement in grain size of the oxide scale which might be due to the presence of carbon on grain boundaries and limiting their mobility.

2.3.2.4 Alloying for protection in carburizing-oxidizing environments

As noted earlier, most industrial gas atmospheres almost always contain oxidizing species with partial pressures high enough to form the stable oxides such as chromia, and therefore alumina and silica. The resistance to carburization comes from the ability of alloys to form one of these oxides and the protective nature of this scale.

Aluminum has been known as the most effective alloying element in increasing carburization resistance [45]. Alumina scale is thermodynamically stable at impurity levels of water vapor which are unavoidable in reaction gases. However, sufficient Al content in the alloy is necessary to form an external scale (see Eq. 2-29). A minimum Al content of 4 wt. % is

required to achieve complete protection. Figure 2-23 shows the results of the study by Lai [25] on two commercial alloys of 214 (alumina former) and 601 (chromia former) in the environment characterized by unit carbon activity and oxygen partial pressures such that chromia was not expected to form. No internal carburization was detected in alloy 214 due to the formation of alumina scale.

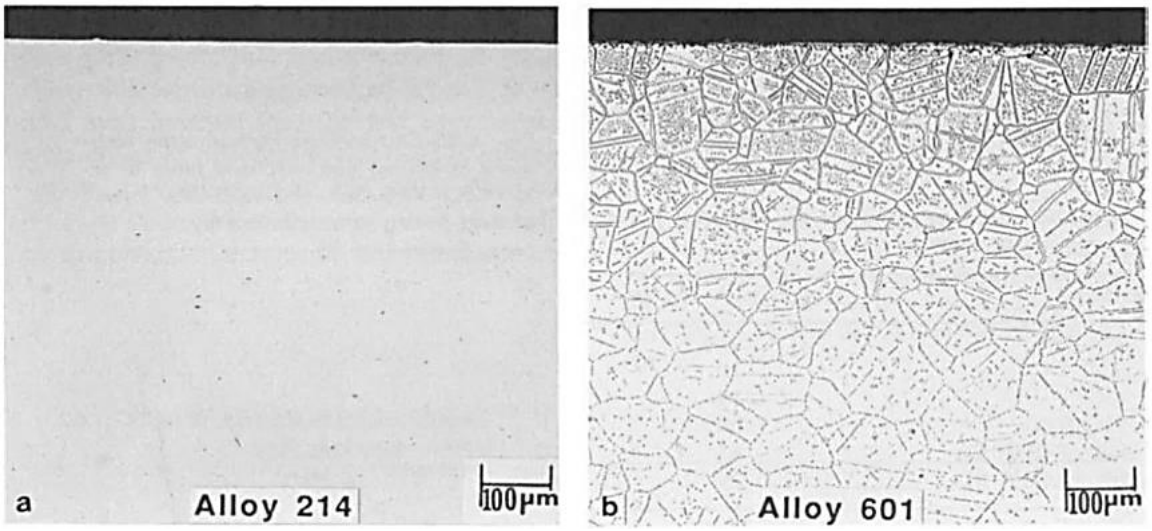

Figure 2-23 Optical micrographs showing the microstructures of (a) alumina-former alloy 214 (Ni-16Cr-3Fe-4.5Al-Y), and (b) chromia-former alloy 601 (Ni-23Cr-14Fe-1.4Al) [25]

It has long been known that silicon is beneficial in providing carburization resistance. Silicon addition is known to reduce the solubility and diffusivity of carbon into the alloy. In addition, chromia forming alloys containing sufficient silicon tend to develop silica layers beneath their chromia scales, which greatly improve the carburization resistance. Kane [64] previously showed that the best corrosion resistance is achieved at silicon contents above 2%.

2.4 SUMMARY

To conclude this literature survey, the main aspects regarding the reaction of high-temperature alloys in sulfur and carbon-containing environments are summarized here.

The reaction of metals and alloys in sulfur-containing environments has been reviewed by many researchers. It has been found that austenitic Fe-Ni-Cr steels have the most resistance in sulfur containing environments. High-Ni alloys, however, have been shown to be susceptible to sulfidation attack, especially at high temperatures due to the formation of the low melting eutectics. It has also been shown that resistance to these environments can only be achieved by formation of a stable, slow-growing, and dense oxide layer. Alumina-scale forming alloys show a very good sulfidation resistance at high temperatures. However, in order to form a protective alumina layer high Al contents are needed, but that also tends to embrittle the alloy. Therefore, chromia-scale forming alloys are the usual choice for such applications.

Carburization of high-temperature alloys occurs in many industrial environments containing CO, CH_4, or other hydrocarbon gases at elevated temperatures. In the absence of a protective layer, carbon can diffuse into the substrate alloy at relatively high rates and form internal carbides, which will cause embrittlement of the alloy and an overall degradation of its original mechanical properties. The effect of various alloying elements on carburization resistance was discussed in previous sections. It was found that Ni-base alloys generally exhibit better carburization resistance over Fe-base alloys. Nickel reduces the diffusivity of carbon in Fe–15Cr–Ni alloys and at a Ni/Fe ratio of 4:1, a maximum of carburization resistance can be achieved. It was also shown that Al and Si are the most effective alloying elements in providing carburization resistance by forming Al_2O_3 and SiO_2 scales. In addition, silicon tends to reduce the carbon diffusivity in the substrate alloy.

The environments of certain high-temperature commercial processes can be even more complex by having low oxygen and high sulfur and carbon activities at the same time. Under such conditions, the composition of these alloys becomes more important since they not only need to have high sulfidation resistance, which implies low Ni-content chromia former alloys, but also high carburization resistance, which implies high Ni-content silica or alumina former alloys. Thus, it is very important study the behavior of these alloys in more realistic conditions containing both sulfur and carbon activities.

3.0 RESEARCH OBJECTIVES

In Chapter 2, the kinetics and thermodynamics of reactions in single and multi-oxidant environments were reviewed and some of the important results from previous studies were highlighted. According to those results, protection of the alloys is always dependent on their ability to form a continuous and slow-growing oxide scale with good adherence to the substrate alloy. The most important oxides for this purpose are Al_2O_3, SiO_2 and Cr_2O_3, which have much lower growth rates compared to the oxides of relevant base-metal elements such as Ni, Co and Fe. However, by moving toward more reducing environments and increasing the temperature in a staged combustion process, the environment becomes more reducing and highly corrosive. The environments of certain high-temperature commercial processes can be even further complicated by having carburization as an additional degradation mode. Such conditions require materials that have higher resistance to different corrosive species and high temperature strength. Thus, the effect of alloy composition becomes very important in reducing the rates of component degradation. Under such conditions, protection depends on the effect of both major and minor alloying elements to retard the process of sulfide formation or carbon penetration into the alloy and promote the formation of a protective oxide scale under reducing conditions.

The corrosion mechanism of unalloyed chromium and chromia-forming alloys in different environments of H_2-C_3H_6 [33, 55], CO-CO_2 [63, 57, 55], H_2-H_2S [65, 66, 8], O_2-SO_2 [67, 68, 55] or other mixtures of these gases [65, 69, 28, 54, 55] has been studied. Although

understanding the corrosion mechanisms in environments containing one or two oxidants can be very useful, such environments do not provide the synergistic effect that occur under actual conditions. As a result, fundamental understanding of corrosion mechanisms in complex atmospheres is quite limited. Consequently, it is important to identify and analyze a number of unresolved questions in this area of research.

Accordingly, the general aim of this study is to better understand the effects of alloying components and their amounts on the high-temperature corrosion behavior of commercial and model alloys in sulfur and carbon-rich atmospheres. This study will discuss laboratory-scale efforts to better understand the effects of compositional and environmental factors on the corrosion behavior of model and commercial alloys in sulfidizing, carburizing and mixed (sulfidizing-carburizing-oxidizing) atmospheres at temperatures above 650°C, which is the current temperature of the most efficient fossil-fueled power plants. Thus, the main aims of this research are to:

1- Determine the degradation behavior of several commercial Ni-, Ni-Fe, Ni-Co-base alloys in mixed sulfidizing-oxidizing conditions with low oxygen and high sulfur partial pressures, and also in a carburizing environment with high carbon activity. The temperature of study will be mainly 871°C (1600°F), based on the temperature of interest in collaboration with Haynes International (our industry collaborator), for which very little published data exist.

2- Investigate the effect of different oxidants in the mixed gas environments on corrosion mechanism and morphological development of reaction products on pure Cr in strongly reducing sulfidizing and sulfidizing/carburizing environments.

3- Determine the effects of gas composition on surface reaction pathways, using three different environments of sulfidizing-oxidizing, carburizing and sulfidizng-carburizing-oxidizing.

4- Determine the influence of compositional factors on reaction kinetics by designing model alloys that introduce minor additions (Al, Mo, Ti, and Si) at different levels and studying their behavior in similar environments.

5- Ultimately guide alloy selection and design for use in advanced combustion systems.

4.0 MATERIALS AND EXPERIMENTS

4.1 MATERIALS

4.1.1 Commercial alloys

The first part of this study is concerned with the behavior of wrought commercial alloys in mixed gas environments. Thus, several commercial Ni-, Ni-Fe-, and Ni-Co-base alloys (supplied by Haynes International, collaborated on project) were selected for the investigation. Nominal alloy compositions are presented in Table 4-1. Rectangular specimens were cut to approximate dimensions of $10 \times 8 \times 2$ mm^3. A 1mm diameter hole was drilled near the edge of a given sample so that it could be suspended in the furnace. Samples were then polished to 320-grit finish using SiC paper, ultrasonically cleaned and degreased in ethanol and then weighed prior to testing.

Table 4-1 Commercial alloys chemical compositions

Alloy		wt%										
		Ni	Co	Cr	Fe	Al	Si	Mo	W	Mn	C	Other
HR-160	Ni-Co based	37[a]	29	28	2*	-	2.75	1*	1*	0.5	0.05	0.5 Ti- 1* Nb
617		54[a]	12.5	22	1	1.2	-	9	-	-	0.07	0.3 Ti
HR-120	Ni-Fe based	37	3	25	33	0.1	0.6	2.5	2.5	0.7	0.05	0.7 Nb- 0.004 B- 0.2 N
HR-224		47	2*	20	27.5	3.8	0.3	0.5*	0.5	0.5*	-	0.3Ti-0.004*B-0.15*Nb-0.01*La-0.025*Zr
214	Ni based	75[a]	-	16	3	4.5	0.2*	-	-	0.5*	0.05	0.01* B- 0.01 Y- 0.1* Zr
625		62[a]	1*	21	5*	0.4*	-	9	-	0.5*	0.1*	0.4* Ti- 3.7 (Nb+Ta)

4.1.2 Model alloys

To better understand the interaction among different species in the gas and their effect on the modes of degradation, the first set of experiments were done on pure chromium system. Pure chromium of 99.99% purity, procured from Goodfellow Corporation, was used in this study. Based on recent observations by Wu [70], it was shown that Ni-Co-based commercial alloys showed the better corrosion resistance compared to Ni- and Ni-Fe-based alloys. It was also confirmed that when the Ni:Co ratio in these alloys is near unity, the alloy has optimum sulfidation resistance. Based on this study, two Ni-Co-base chromia-scale forming model alloys 38Ni-40Co-22Cr and 32Ni-40Co-28Cr (compositions in at.%) were designed to study the effect of chromium content on their corrosion behavior. All model alloys were made by the Materials Preparation Center at the Ames Laboratory [71]. The alloys were prepared by arc melting of the 99.95% purity constituent elements on a water-cooled copper hearth in an atmosphere of high purity argon. After that, the alloy was drop-cast into a 10 mm diameter chilled copper mold. The alloy was then annealed at 1100°C for 24 hours in vacuum.

In the next set of experiments, eight different model alloys were designed to study the effect of minor alloying element additions. The nominal compositions of these alloys are

presented in Table 4-2. These model alloys have different levels of Ni, Co and Cr and are modified with minor alloying elements of Al, Ti, Mo, and Si. Model alloys 1, 2, and 3 were previously tested in similar environments but at lower temperature of 750°C and showed exceptional sulfidation resistance [70]. It is noted that the average grain size of the cast model alloys are much larger than those of the wrought commercial alloys mentioned in the previous section. The average grain sizes for commercial alloys and the first three model alloys are compared in Figure 4-1. The first three model alloys have a single-phase γ structure, with precipitation of σ-phases in the alloy 2 after exposure at 871 °C. However, precipitation of other phases (not identified) were observed in the as-received structures of the modified model alloys 4, 5, 6, 7, and 8 with addition of Si or increasing the Al and Cr chromium concentrations. The as-received SEM microstructure of these alloys and measured EDS analyses of these phases can be seen in Figure 4-2.

Round specimens were cut from model alloys with diameter of approxiamtely 10 mm and thickness of 1mm. A 1mm diameter hole was drilled near the edge of a given sample so that it could be suspended in the furnace. Samples were then polished to 320-grit finish using SiC paper, ultrasonically cleaned and degreased in ethanol and then weighed prior testing.

Table 4-2 Chemical composition of model alloys

Alloy	Composition (wt. %)							Alloy structure
	Ni	Co	Cr	Al	Mo	Ti	Si	
1	50.6	17.4	22	2.5	5	2.5	-	Single phase γ
2	44.8	17.2	28	2.5	5	2.5	-	γ + σ
3	33.1	34.9	22	2.5	5	2.5	-	Single phase γ
4	31.6	33.4	22	2.5	5	2.5	3	γ 20Ni-24Co-16Cr-18Si-13Mo-9Ti 32Ni-21Co-6Cr-24Si-1Mo-16Ti
5	30.2	31.8	28	2.5	5	2.5	-	γ + σ
6	31.9	33.6	22	5	5	2.5	-	γ 34Ni-21Co-9Cr-6Ti-30Al
7	30.4	32.1	22	5	5	2.5	3	γ 36Ni-21Co-10Cr-4Si-4Ti-25Al 17Ni-29Co-30Cr-11Si-8Mo-3Ti-2Al
8	29.0	30.5	28	5	5	2.5	-	γ 36Ni-19Co-10Cr-6Ti-29Al 13Ni-27Co-48Cr-8Mo-1Ti-3Al

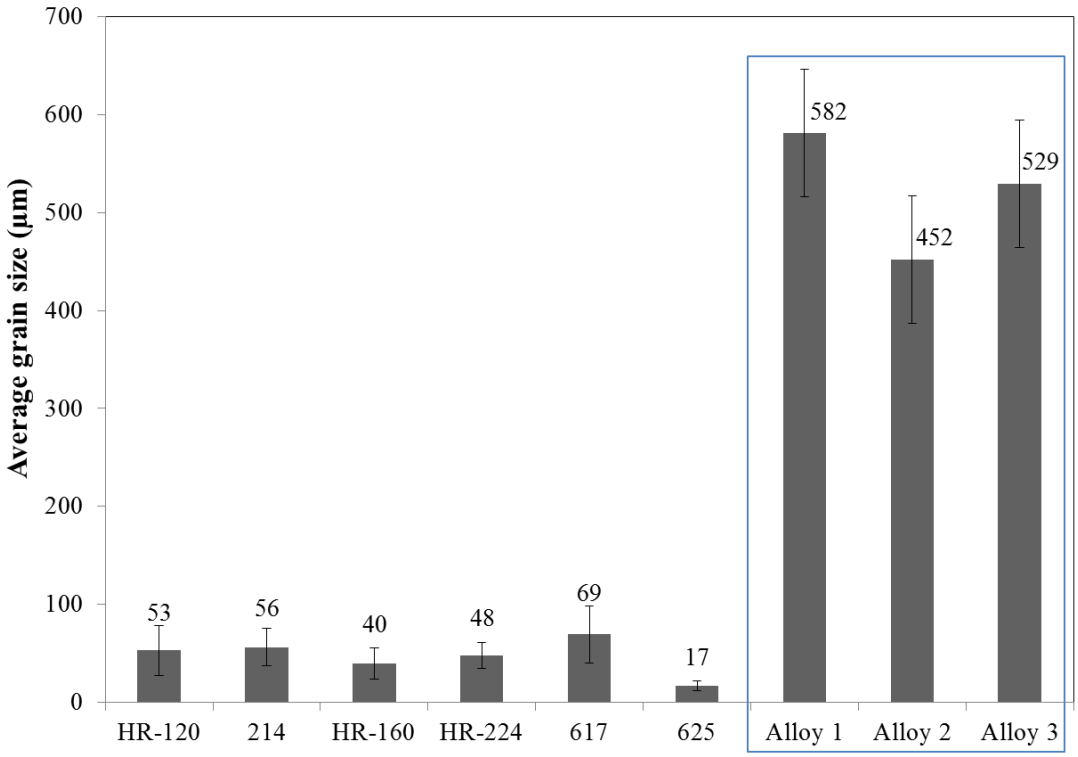

Figure 4-1 Average grain size base on at least 10 measurements for commercial alloys and the first three model alloys

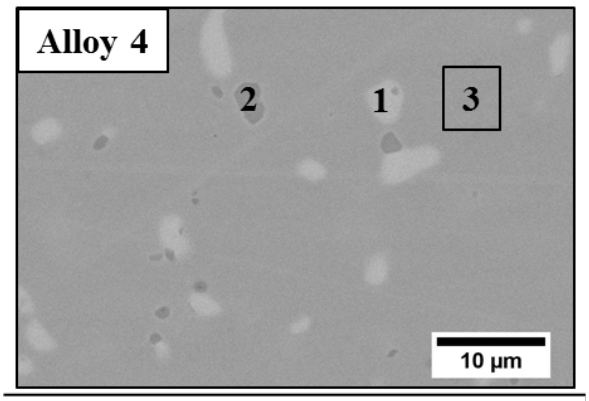

	Al	Si	Ti	Cr	Co	Ni	Mo
1	0.7	17.9	8.8	16.0	24.3	19.4	12.9
2	0.6	23.4	15.7	5.9	20.8	32.2	1.4
3	5.6	6.4	2.7	23.8	31.0	28.7	1.9

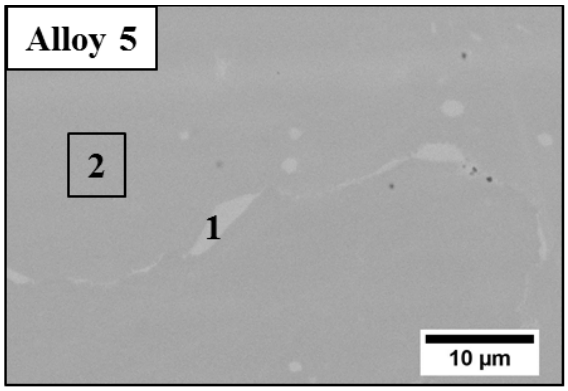

	Al	Ti	Cr	Co	Ni	Mo
1	2.0	1.9	47.6	26.4	14.3	7.8
2	5.6	3.1	30.9	29.6	28.0	2.7

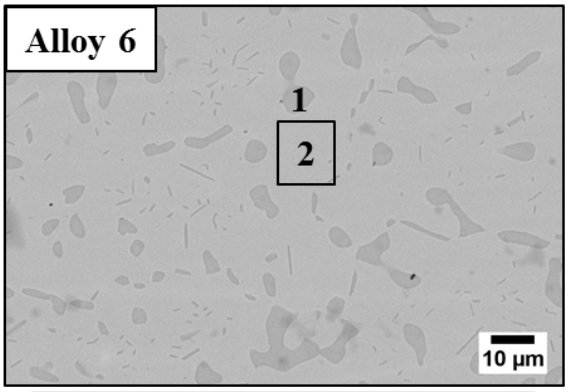

	Al	Ti	Cr	Co	Ni	Mo
1	29.0	6.0	9.5	21.3	34.2	
2	8.8	2.7	26.0	31.0	28.4	3.1

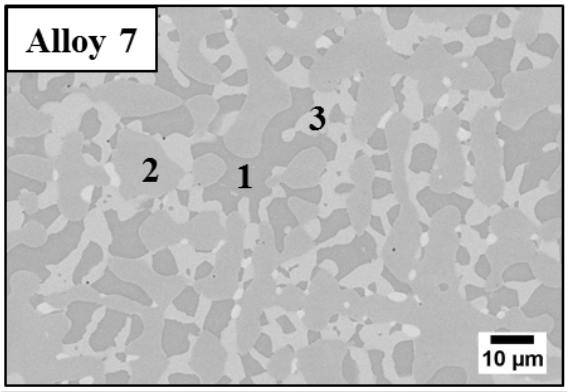

	Al	Si	Ti	Cr	Co	Ni	Mo
1	24.7	4.5	4.4	9.7	21.1	35.6	
2	6.2	4.6	1.8	26.5	32.1	26.7	2.3
3	2.2	10.6	3.6	30.2	29.0	16.6	7.7

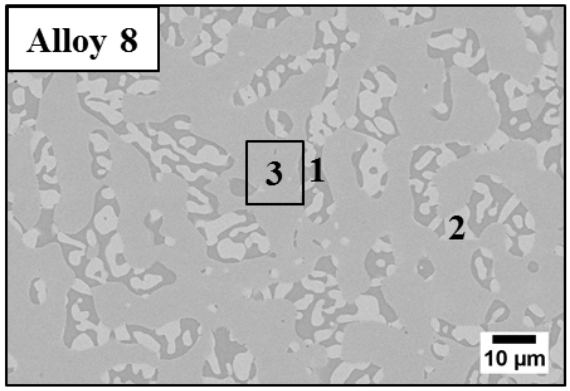

	Al	Ti	Cr	Co	Ni	Mo
1	29.2	6.6	9.6	19.1	35.6	
2	3.1	1.5	48.4	27.0	12.6	7.4
3	7.0	2.4	30.1	30.0	27.8	2.6

Figure 4-2 As-received microstructures of model alloys 4, 5, 6, 7, and 8 and EDS analyses of the different phases

4.2 GAS MIXTURES

Tests were carried out at 871°C (1600°F) in gas mixtures summarized in Table 1. Water vapor was obtained by flowing the gas through distilled water at a controlled temperature of 0°C, room temperature and 46°C to obtain 0.6, 3, and 10% water vapor, respectively. The pH of the water was stabilized via saturation to ensure achievement of the nominal gas compositions. Average pH values of 4.73 and 4.63 after 6 and 30 hours of flushing with the reaction gas, respectively, confirmed the stability of the pH of the water in the times studied. The calculated partial pressures of the gases by using the HSC software are presented in the Table 1 and shown on the super-imposed stability diagrams of Ni-O-S and Cr-O-S in Figure 4-3. It can be seen that the first four mixed gases are in the oxide stable region with respect to chromium and sulfide stable region with Ni. Gas 5, on the other hand, is very reducing and has the carbon activity of unity. Although there was no oxygen in the premixed gas, there still exists an impurity level of water vapor in the system, even after flushing the system for 24 hours.

Table 4-3 Equilibrium gas compositions and corresponding equilibrium oxidants potentials at 871°C (1600°F)

Gas No.	Gas Composition (Vol%)	P_{S2} (atm)	P_{O2} (atm)	a_C
1	N_2-15%CO-3%H_2-0.6%CO_2-0.12%H_2S [72]	1.3×10^{-6}	8.0×10^{-22}	0.2
2	N_2-15%CO-3%H_2-0.6%CO_2-0.12%H_2S + 0.6% H_2O	9.2×10^{-7}	2.1×10^{-20}	0.2
3	H_2-25%CH_4-14.8%N_2-4%CO-0.6%CO_2-0.6%H_2S + 3% H_2O [69]	2.57×10^{-8}	1.35×10^{-22}	~1
4	H_2-25%CH_4-14.8%N_2-4%CO-0.6%CO_2-0.6%H_2S + 10% H_2O	2.25×10^{-8}	4.14×10^{-22}	~1
5	Ar-5%H_2-2%C_3H_6	-	-	1

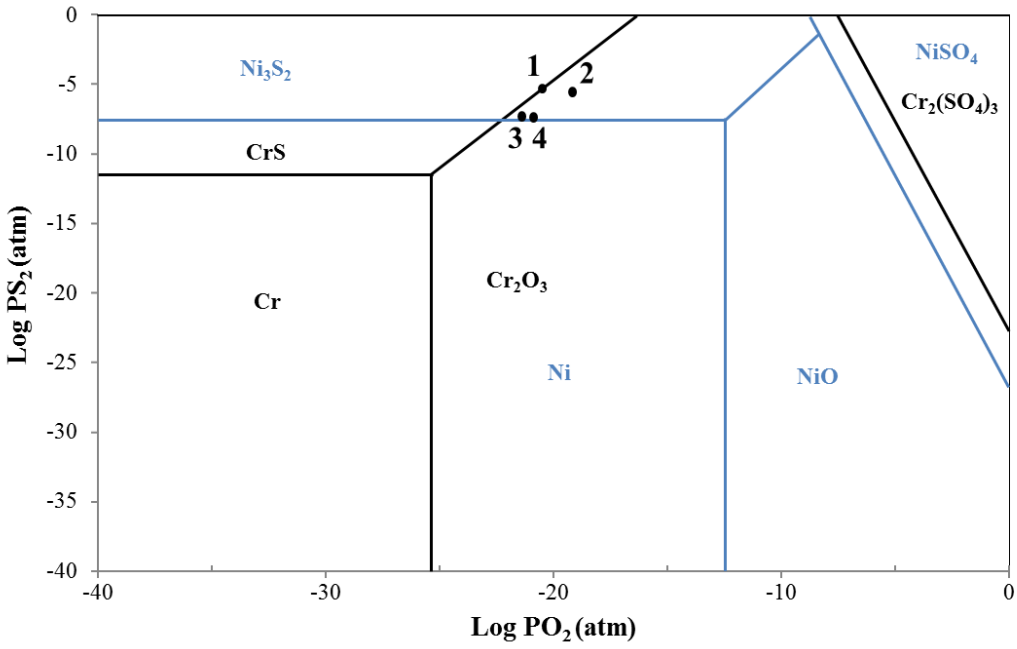

Figure 4-3 Superimposed phase stability diagram for three systems of Ni-, Cr- and Co-O-S at 871°C

4.3 EXPERIMENTAL PROCEDURE

A schematic of the testing system used is shown in Figure 4-4. The main part of the system is a horizontal furnace. Samples were suspended from the sample holder in the furnace using kanthal wires. The system was first purged with argon gas for about 20 hours to remove oxygen prior to exposing samples to the reaction gas. All corrosion tests were carried out at 871°C (1600°F). With a given gas mixture flowing through the pre-heated system at a rate of 50 ml/min, a test was initiated by pushing the samples from a position outside the furnace to inside the hot zone. Thus, sample heating to 871°C was less than 60 s. Since the calculated gas compositions are really close to the thermodynamic boundary, a Pt catalyst was positioned at the front (i.e., upstream position) of the hot zone to ensure gas-phase equilibrium. However, due to the presence of high levels of sulfur in the reaction gases, sulfur poisoning of the surface of the

catalyst after some time is still a possibility. It is inferred that, based on agreement of the experimental observations of the reaction products formed on pure chromium after exposure to these environments (Chapter 5.2.1) with the calculated equilibrium partial pressures in Figure 4-3, the environments were at least near equilibrium in the tests conducted.

After thermal exposure, samples were removed from the hot zone, cooled to room temperature under argon gas flow and then removed from the system and weighed. The weight change for each sample caused by oxygen, sulfur or carbon pick-up was determined. Additional tests were also carried out in dry-air atmosphere using a Setaram symmetrical thermogravimetric analyzer (TGA) with heating and cooling rates of 99 and 50°C/min, respectively.

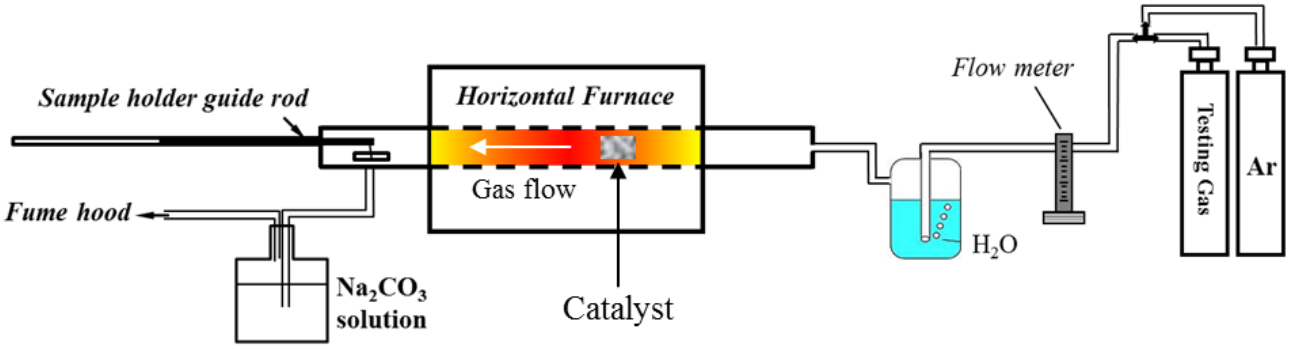

Figure 4-4 Schematic of testing system used in current study

4.4 CHARACTERIZATION TECHNIQUES

After a given exposure, the specimens were weighed and photographed. Metallographic cross-sections were prepared by cold mounting, sectioning and then polishing using standard techniques (polishing with SiC paper, and diamond and silica solutions). Final polishing of the cross-section of selected specimens were performed using a Fischione Instruments Model 1061

by broad beam Ar ion milling. This method was found to be the best solution for obtaining high quality cross-sections without damaging the brittle scale caused by conventional mechanical polishing. Selected specimens were characterized using the following techniques:

X-ray diffraction (XRD)

In order to identify the phases formed after the exposure, X-ray diffraction measurements of the samples were obtained using a Cu Kα characteristic radiation operated at 40 kV and 40 mA. Patterns were recorded over a 2θ range of 20 to 80° at a step size of 0.02. It should be noted that only the outer most layers can be analyzed using this technique.

Scanning electron microscopy (SEM)

Cross sections of the samples were examined using scanning electron microscopy (SEM). Energy-dispersive spectroscopy (EDS) was also used in order to obtain semi-quantitative composition analysis.

Electron backscatter diffraction (EBSD)

Microstructural characterization of selected samples has been carried out using SEM-FEI Apreo with high-vacuum field emission gun. Cross-section specimen preparation was done using the Fischione SEM mill (model 1060) to provide a damage-free surface for EBSD.

Electron probe microanalysis (EPMA)

Electron probe microanalysis was carried out on specimen cross-sections using a JEOL-JXA-8530F model, equipped with five wavelength dispersive spectrometers (WDS).

Transmission Electron Microscope (TEM)

Selected samples were characterized using transmission electron microscope. FEI Tecnai G2 TEM at University of Pittsburgh, FEI Tecnai F30 300kV TEM at Swagelok Center for Surface Analysis of Materials (SCSAM) at Case Western University and at Fischione instruments Inc. were used. TEM specimens were prepared using a focused ion beam (FIB) and further thinned using the Fischione Instruments Model 1040 NanoMill® TEM specimen preparation system in order to obtain ultrathin and defect free lamellae.

Etching and optical microscopy

Etching was performed using Murakami's reagent (1g $K_3Fe(CN)_6$, 1g KOH, 10 mL H_2O) to reveal chromium carbides for carburized samples. Optical microscopy was carried out on specimen cross-sections after etching.

5.0 RESULTS AND DISCUSSIONS

This Chapter presents a summary of the experimental results obtained for commercial and model alloys. The reaction behavior in several multi-oxidant environments is first presented, followed by insights on the effects of different species in the environment on corrosion mechanisms and reaction pathways. The next section focuses on the behavior of ternary model alloys and the final section is mainly focused on the effects of minor alloying elements on corrosion resistance in multi-oxidant environments.

5.1 COMMERCIAL ALLOY STUDY

5.1.1 Sulfidation-Oxidation

The weight-change measurements for six commercial alloys after 100 h exposure to gas 2 are summarized in Figure 5-1 and Figure 5-2. It should be noted that most of the commercial alloys used in this study are single-phase gamma alloys. The mass-change data can give an initial indication of whether or not sulfidation has occurred. It is evident that alloy HR-120 with 28% Cr exhibited the highest weight gain with an increase of almost 68 $mg.cm^{-2}$ after 100 h. Very high weight gains were also measured for HR-224 with 20% Cr, thus, the extent of corrosion is not necessarily reduced by increasing the chromium concentration. In contrast, alloys 214

(alumina former) and alloy 617 (chromia former) showed the lowest weight gains after 100 h. The initial weight gain for alloy 214 was high due to initial sulfide and oxide formation; however, once the continuous alumina layer is established no further attack was observed. These reaction products apparently spalled after 100 h exposure during cooling, which can be seen in the surface image of the sample after exposure in Figure 5-5. The negative weight gain recorded for alloy HR-160 (containing 2.75 wt. % Si) is also mainly due to scale spallation; but besides the spallation, no major metal attack was observed for this alloy.

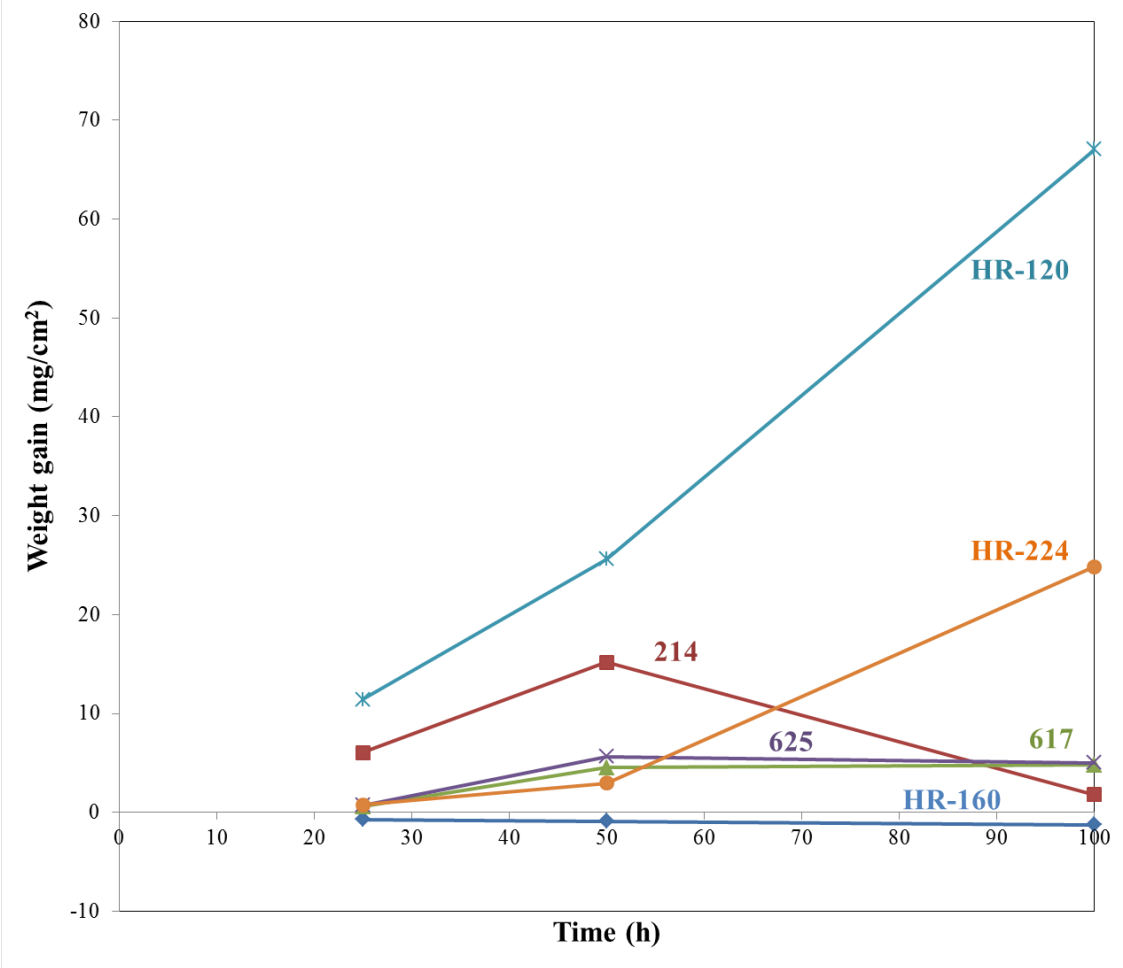

Figure 5-1 Weight change kinetics of the commercial alloys up to 100 h exposure to gas 2 at 871 °C

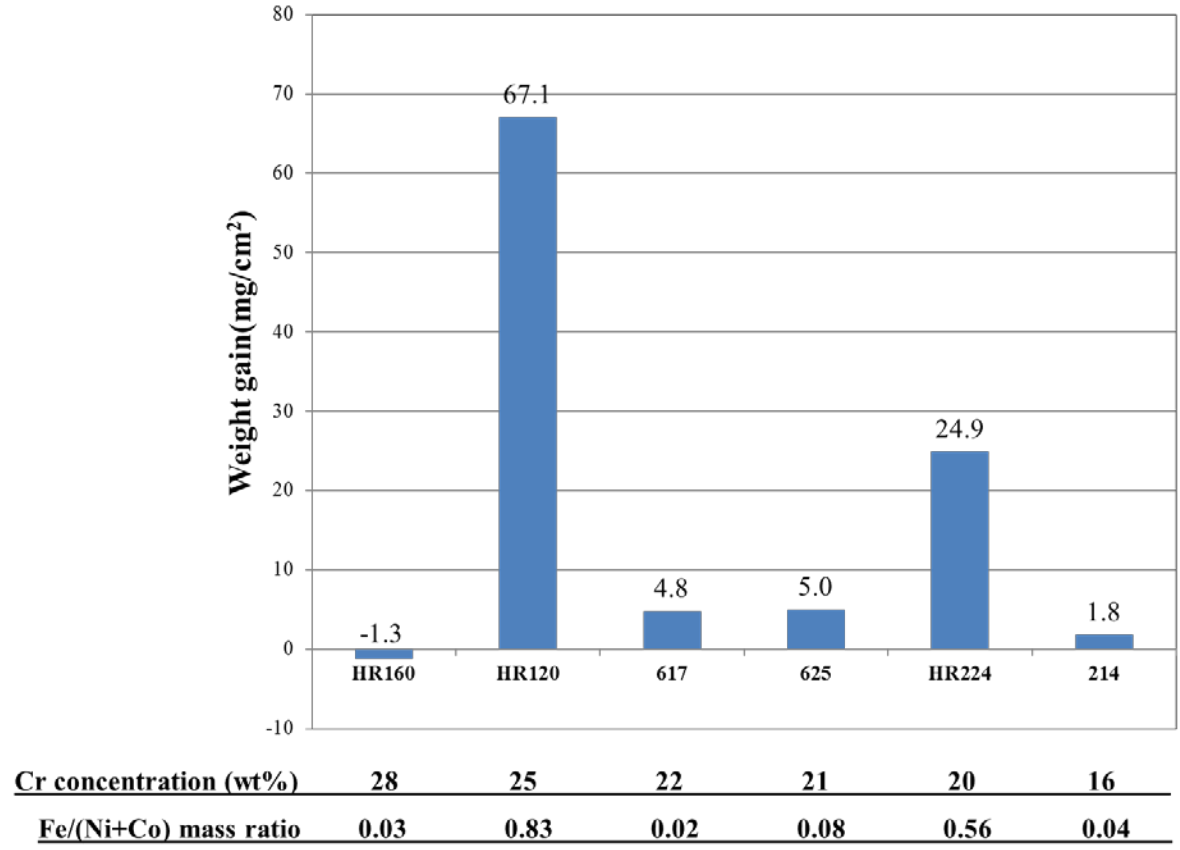

Cr concentration (wt%)	28	25	22	21	20	16
Fe/(Ni+Co) mass ratio	0.03	0.83	0.02	0.08	0.56	0.04

Figure 5-2 Weight change measurements of the commercial alloys after 100 h exposure to gas 2 at 871 °C

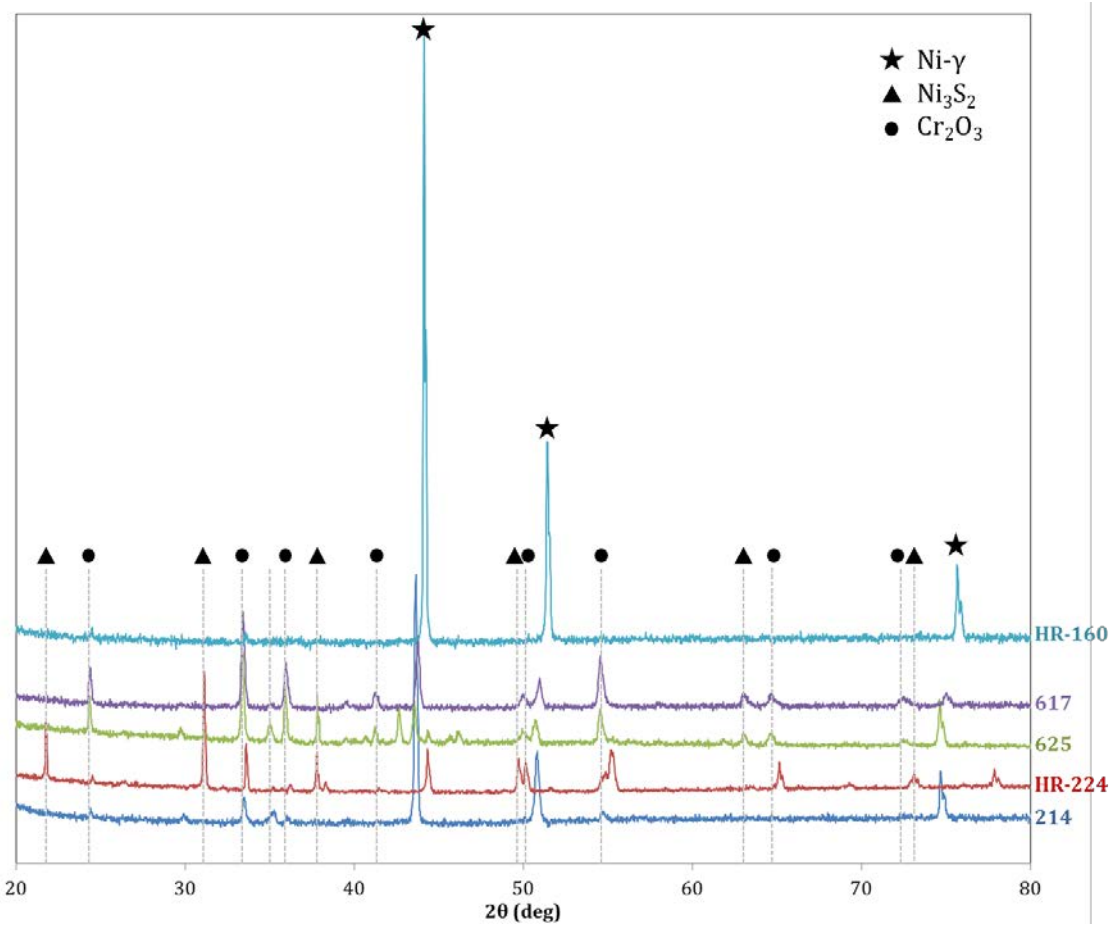

Figure 5-3 XRD spectra of the selected commercial alloys after 100 h exposure to gas 2 at 871 °C

X-ray diffraction analyses of the corroded sample surfaces (Figure 5-3) revealed the formation of chromia scale on almost all alloys. The main phases detected were Cr_2O_3, Ni_3S_2, and Ni-γ. SEM studies of the surface scales (Figure 5-4) showed major differences in morphology. Ni-rich sulfide nodules had grown and covered the surfaces of alloys HR-120 and HR-224. On the other hand, dense chromia scales were observed on alloys 617 and 625, which was in agreement with the XRD results. Surface images of alloy 214 revealed the formation of Cr- and Al-rich oxides, even though some spallation had occurred from this alloy. Alloy HR-160, on the other hand, shows extensive spallation and the alloy subsurface is revealed in the surface images.

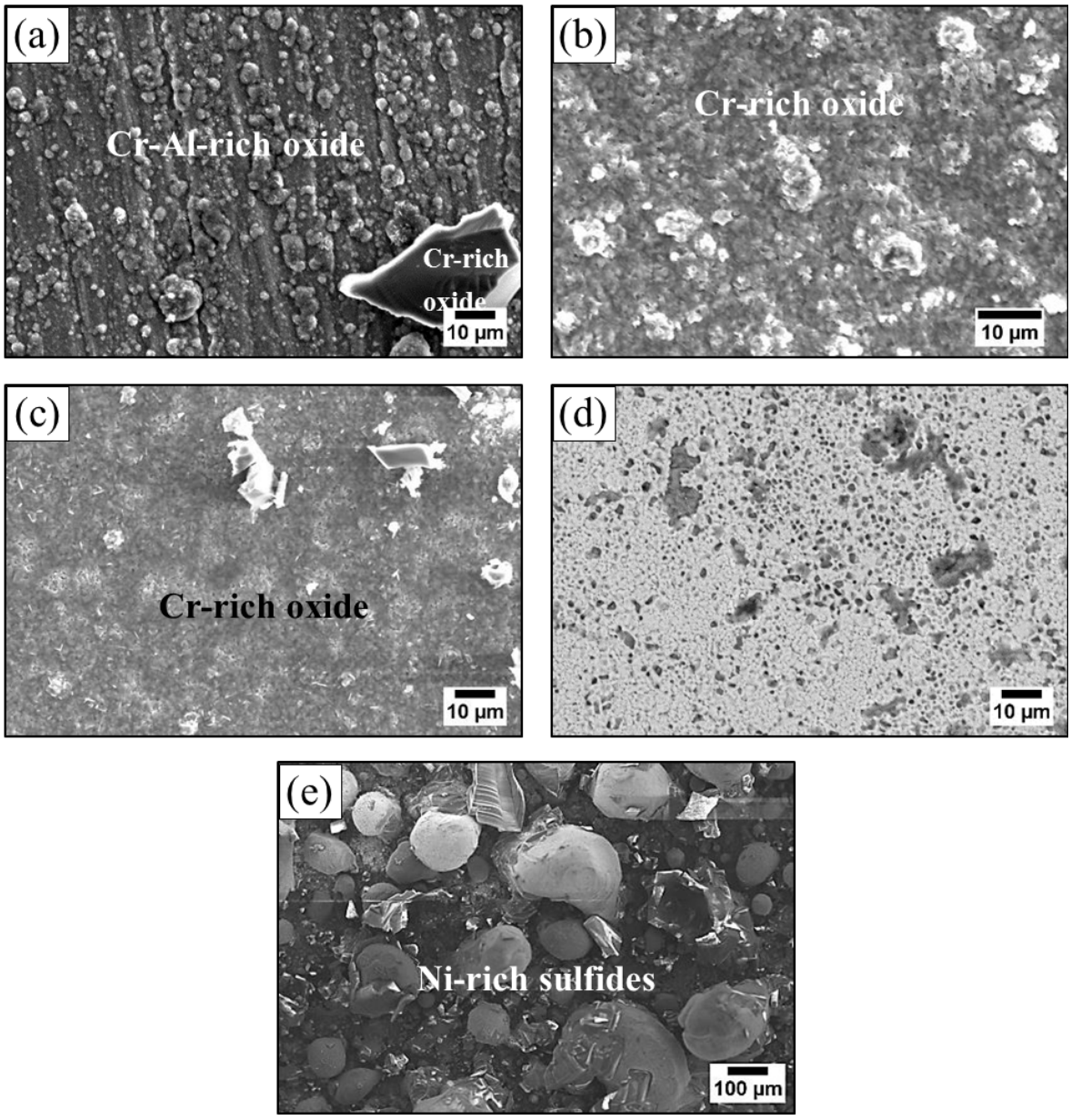

Figure 5-4 SEM surface images of: (a) 214, (b) 617, (c) 625, (d) HR-160, and (e) HR-224 after 100 h exposure to gas 2

According to SEM images of the polished cross-sections, significant amounts of sulfides and oxides are formed on the surface of HR-120 after 100 h exposure. The scale does not have a uniform thickness. Based on EDS analysis, this scale is composed of mixed Fe- and Ni-sulfides (light grey areas) in the form of nodules, metallic Ni and Fe (white areas) and chromium oxide

(dark grey areas). Nodules are also formed on the surface of alloy HR-224, which according to the EDS and XRD results are mainly composed of Ni_3S_2 and metallic Ni areas. At the testing temperature of 871 °C, liquid reaction products can form due to the low temperature of the Ni-Ni_3S_2 eutectic (645 °C), which involves the formation of Ni_3S_2 and metallic Ni during cooling.

Among the abovementioned alloys, 617, 214 and HR-160 showed the best corrosion resistance in gas 2. Figure 5-5 shows SEM cross-sectional images of these alloys after 100 h exposure to gas 2at 871 °C. Although spallation occurred from 214 and HR-160, no major metal attack was apparent. Alloy 214 has the highest levels of Ni and Al and lowest Cr concentration among the commercial alloys tested in this study. The good sulfidation resistance of this alloy is due to the formation of a thin external alumina scale, which can be seen in higher magnification micrograph of the cross-section in Figure 5-6. Formation of an external Al-rich oxide scale protects the substrate alloy from further sulfidation attack.

Alloy HR-160, developed originally by Lai in 1987 [73], is a Ni-base alloy with a combination of high Si, Cr and Co to optimize sulfidation resistance in combination with metallurgical stability, creep rupture properties and weldability. The good sulfidation resistance of this alloy is evident from Figure 5-5, which shows no major attack on the sample apart from the spallation that occurred. With high Co, Cr and Si concentrations in this alloy, formation of an outer Cr_2O_3 layer followed by an underlying SiO_2 layer, which is thermodynamically more stable than Cr_2O_3, is expected in addition to the beneficial effects of cobalt in sulfidation resistance. However, the scale spalls relatively easy during the cooling and it is difficult to preserve it on the sample for further characterization. Regarding the last point, high cobalt levels in Ni-base alloys reduce both the rate of sulfur diffusion in the matrix and the risk of Ni-Ni_3S_2 eutectic formation [7].

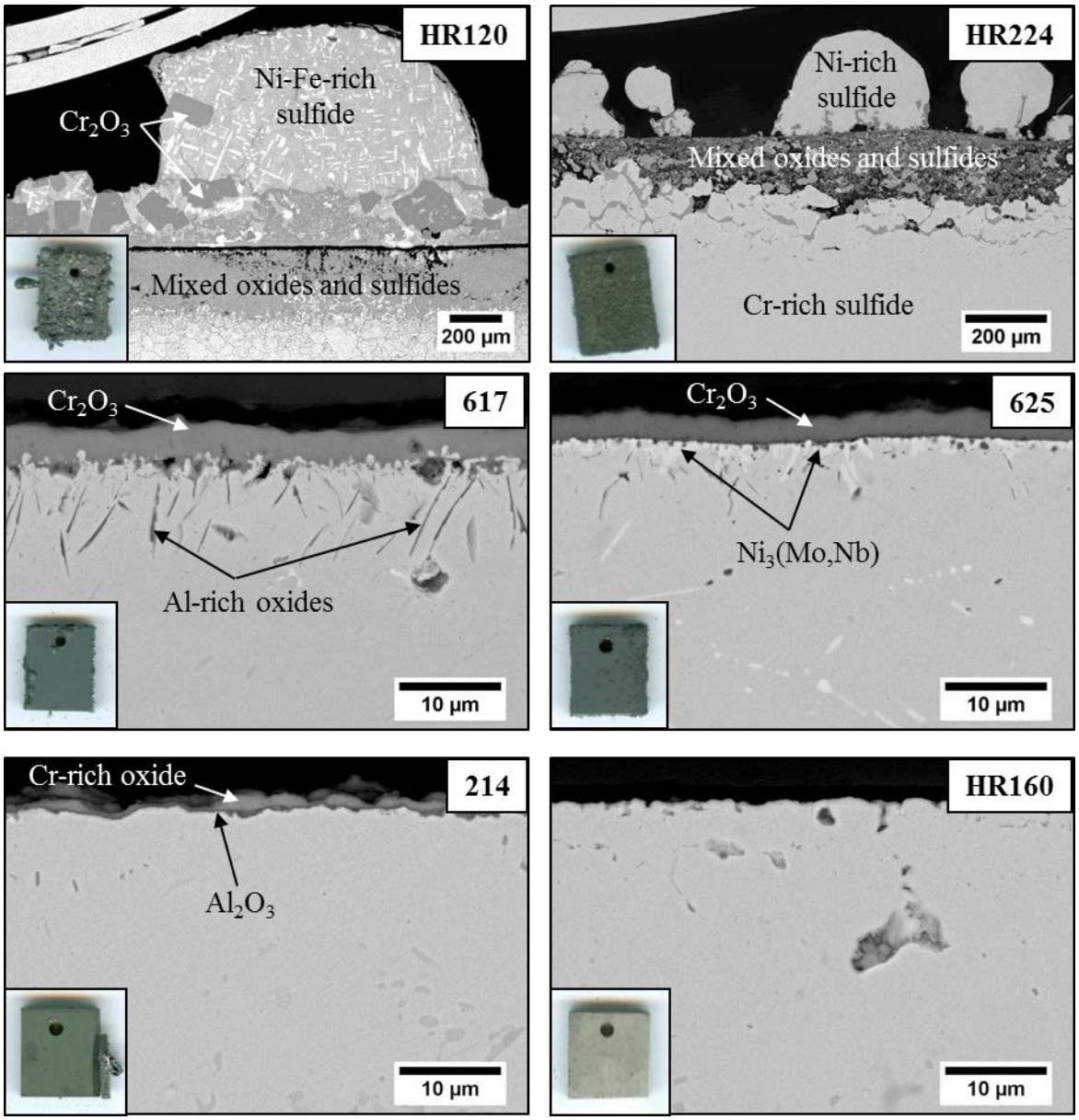

Figure 5-5 Cross-sectional scanning electron micrographs and EDS analyses of scale formed on commercial alloys after 100 h exposure at 871 °C

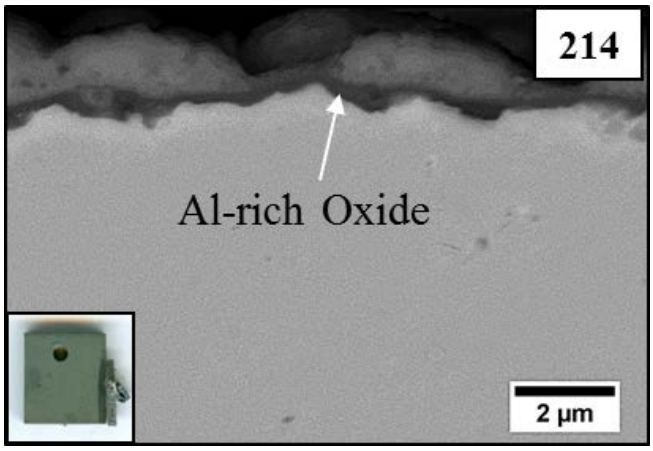

Figure 5-6 Scanning electron micrograph of cross-section of scale formed on alloy 214 after 100 hours of exposure

An adherent protective Cr-rich oxide scale formed on alloy 617 with an internal Al-rich oxide beneath. Alloy 625 also formed a continuous chromia scale layer and $Ni_3(Nb,Mo)$ precipitates in the subscale region. The adherence of the chromia scale on alloy 625 was not as good as that on alloy 617 and the scale was detached from the substrate at most parts after mounting. The 625 alloy has similar Mo concentration to alloy 617 (9% Mo) but much lower Co and Al concentrations. In both cases, formation of Ni- or Fe- or Co-rich sulfides was observed mainly on the edges of the samples, which indicates their vulnerability to sulfidation in the presence of any defects. Here, the focus will be on the behavior of the alloys mainly in the bulk (i.e., away from any edge effects).

Understanding the beneficial effect of molybdenum in increasing the alloy sulfidation resistance, in the environments containing low oxygen and high sulfur partial pressures, is important since Mo has been added to many high temperature alloys for solid-solution strengthening purposes. Alloys 617 and 625 are two alloys with high Mo concentrations and it is evident from Figure 5-5 that both of these alloys showed good sulfidation resistance and less localized breakdown and internal sulfidation attack even at the edges of the samples. Young et

al. [74] showed that the existence of MoS_2 in the internal sulfidation zone lowers the rate at which sulfur diffuses into the alloy. Due to the complicated nature of both alloys and environment here, it is very difficult to comment on the contribution of each of these elements on alloy's overall behavior. Thus, model alloys were designed to better study these effects. However, before getting into the results obtained from model alloys, the behavior of these alloys in other carburizing and mixed environments needed to be determined. Carburization resistance of these alloys will be discussed next.

5.1.2 Carburization

Carburization tests on commercial alloys were conducted for 1, 5, 10, 50, and 100 h exposures at 871 °C in gas 5 (Ar-5%H_2-2%C_3H_6). Figure 5-7 shows the weight-gain kinetics for all six commercial alloys used in this study. The two alumina former alloys 214 and HR-224 exhibited the lowest weight gains after 100 h exposure, while alloy HR-120 (Ni-Fe-base alloy with 25Cr) and alloy 625 (Ni-base alloy with 21Cr and 9Mo) showed the highest weight gains. The measured values for the alloys 625, HR-160, and HR-224 seem to be increasing at a faster rate between 50 and 100 h exposure times. It should be also noted that carbon deposit on the surface of some of the samples was observed, which can affect the measured weight gains.

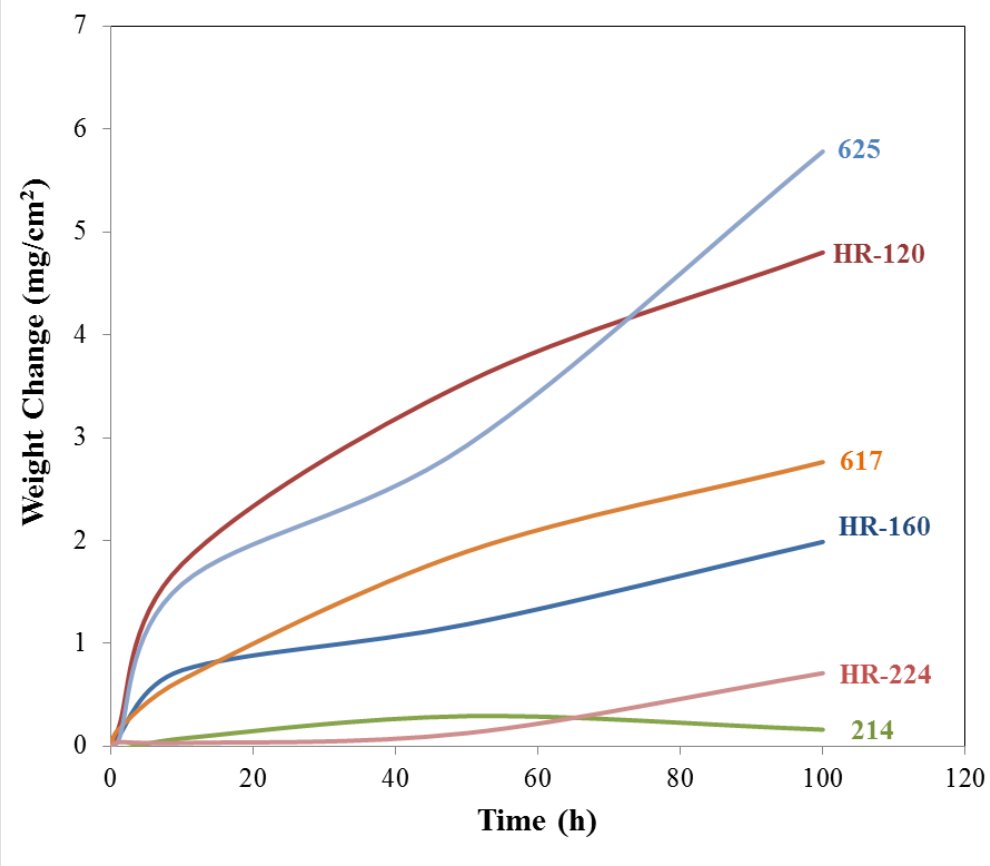

Figure 5-7 Weight change kinetics of the commercial alloys after exposure to gas 5 at 871°C

Figure 5-8 shows SEM cross-sectional images of all alloys after 100 h exposure. Formation of both intergranular and intragranular carbides can be observed in most of the alloys. However, only intergranular carbide was formed in alloy 214, even after 100 h exposure. This shows the high resistance of alloy 214 to highly reducing carburizing environments. Exposure for shorter times showed only the formation of intergranular carbides on alloy HR-224 up to 50 h exposure. However, formation of intragranular carbides can be observed clearly after 100 h exposure.

All carburized samples were etched with Murakami solution in order to reveal the carbides. Optical micrographs of the etched cross-sections of these samples are shown in Figure 5-9. Carbon penetration depth was considered as the average depth of intragranular (within

alloys grains) carbides, since in most cases intergranular or grain boundary carbides formed throughout the sample. The grain boundaries can act both as preferred nucleation sites for carbides and high diffusivity paths for carbon transport. The average carbon penetration depth values are presented in Figure 5-10. Alloy HR-120 with the highest Fe concentration and alloy 625 with low Cr and high Mo concentrations showed the highest penetration depths. The lowest carbon penetration depths were attributed to the two alumina-scale forming alloys 214 and HR-224. Increasing the Al concentration of the alloy is shown to be beneficial in decreasing the extent of carburization attack.

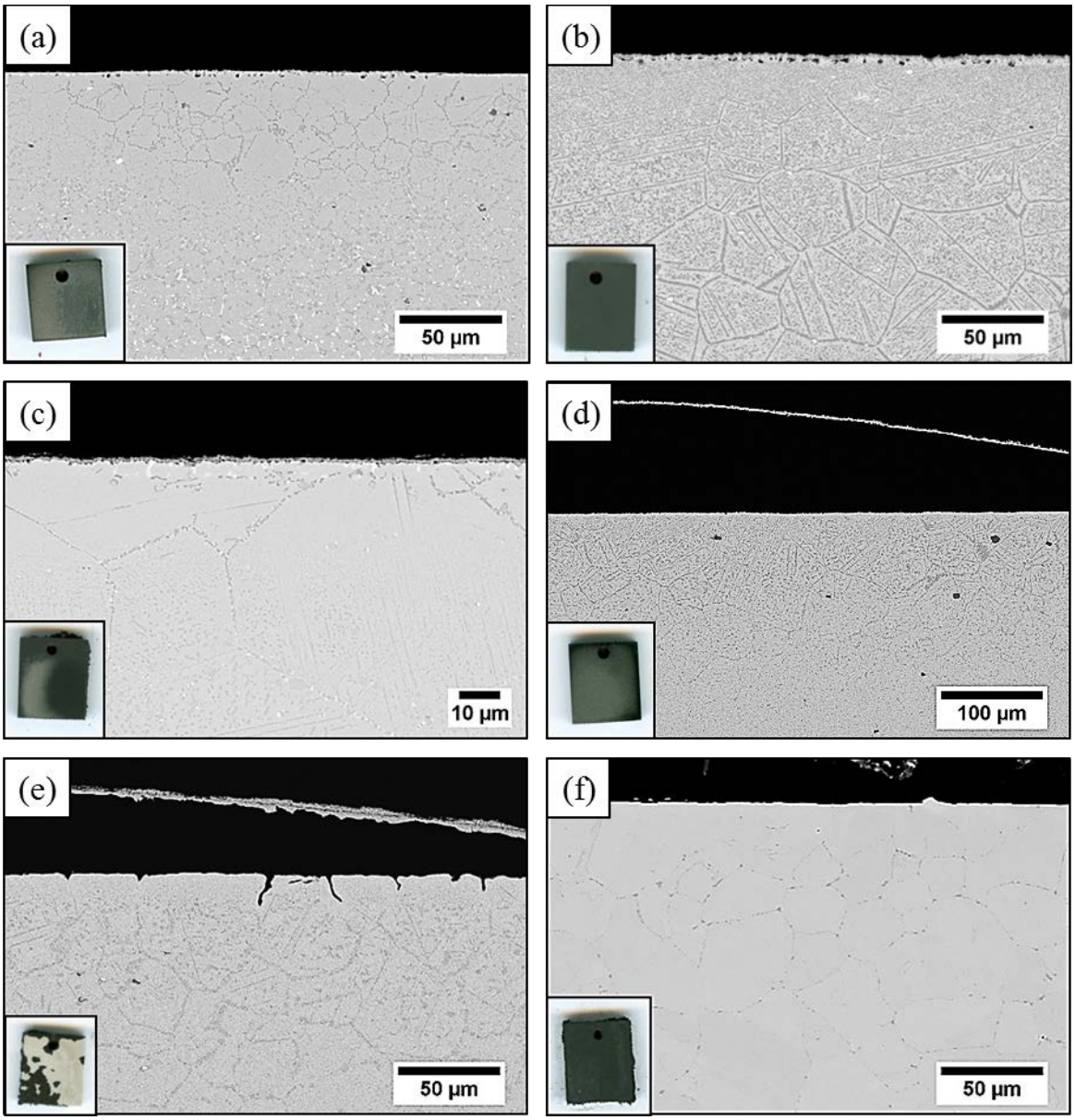

Figure 5-8 SEM cross-sectional micrographs of alloy a) 625, b) HR-120, c) 617, d) HR-160, e) HR-224, and f) 214 after 100 h exposure to gas 5 at 871°C

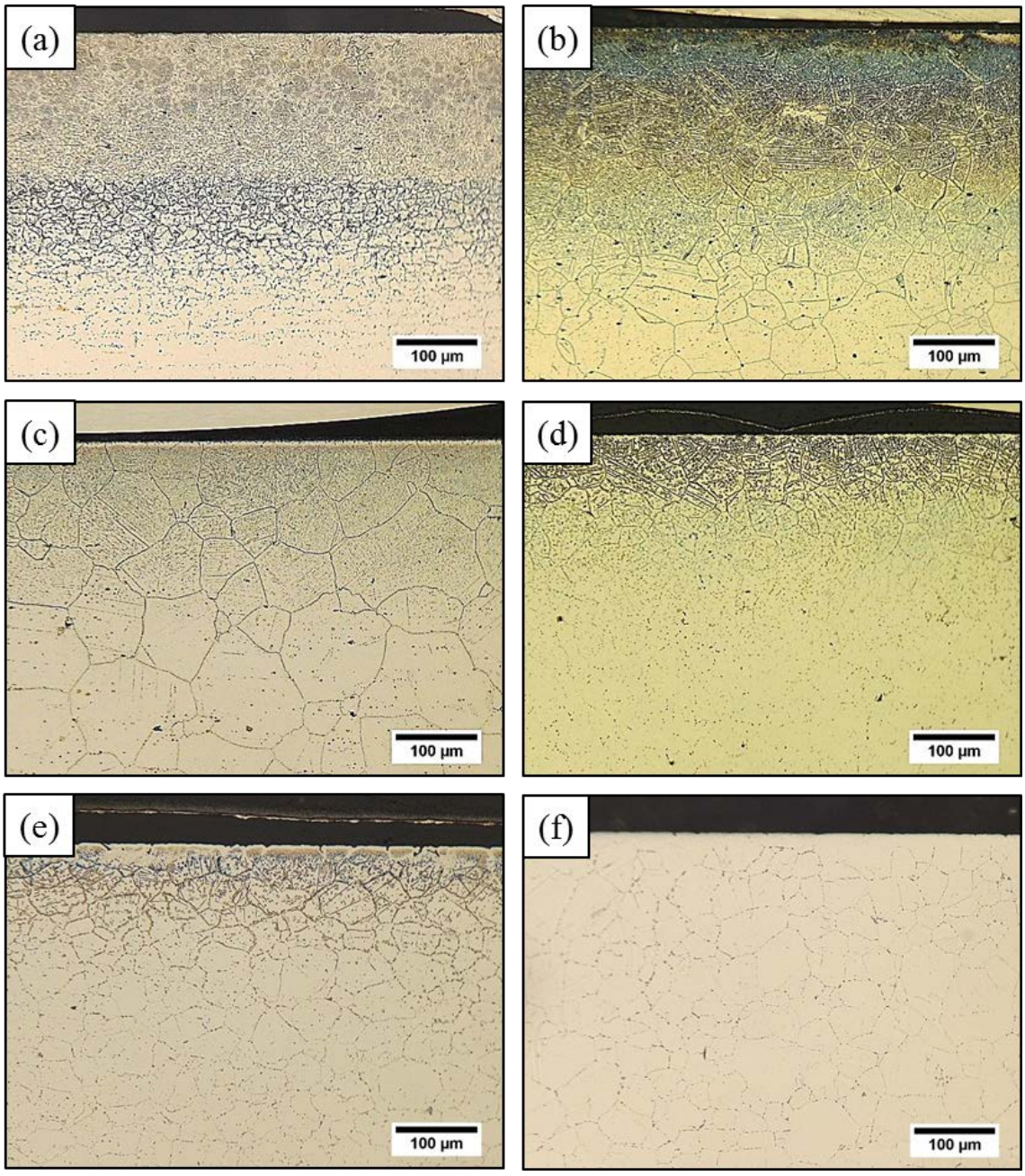

Figure 5-9 Optical cross-sectional micrographs of alloy a) 625, b) HR-120, c) 617, d) HR-160, e) HR-224, and f) 214 after 100 h exposure to gas 5 at 871°C (etched by Murakami solution)

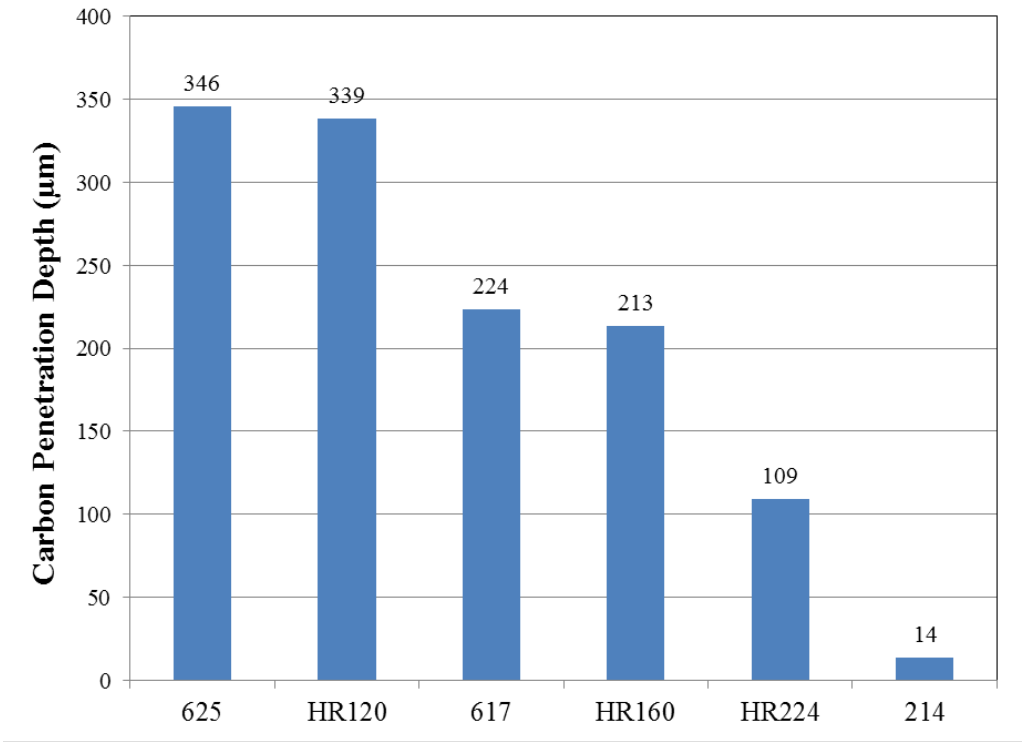

Figure 5-10 Carbon penetration depths in commercial alloys after 100 h exposure to gas 5 at 871°C

Figure 5-11 shows SEM cross-sectional images of the two alumina former alloys 214 and HR-224 and corresponding elemental maps of aluminum, chromium, and oxygen after 100 h exposure. A very thin and continuous alumina scale formed on the surface of alloy 214. Alloy HR-224, on the other hand, was able to form an external Al-rich oxide layer beneath a Cr-rich carbide layer; however, the scale is not as adherent as that on alloy 214. In order to study the behavior of these two alloys more carefully, cross-sections of these alloys after exposure for 10 and 50 h were also prepared and the results are shown in Figure 5-12 and Figure 5-13, respectively. It is seen that upon 50 h exposure to the carburizing gas, both alloy 214 and HR-224 formed a continuous alumina scale and no further carburization attack was observed. However, between 50 to 100 h exposure, the breakdown of the oxide scale clearly occurred on alloy HR-224 and internal carbides formed within alloys grains.

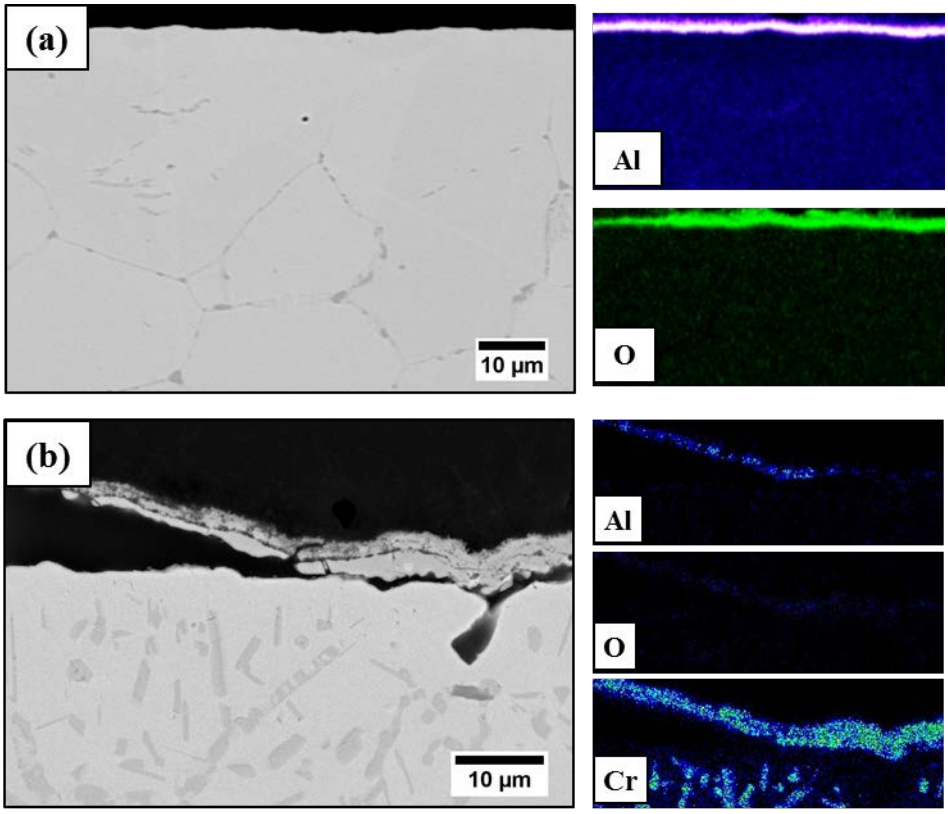

Figure 5-11 Scanning electron micrograph and elemental maps of alloy a) 214 and b) HR-224 after 100 h exposure at 871°C

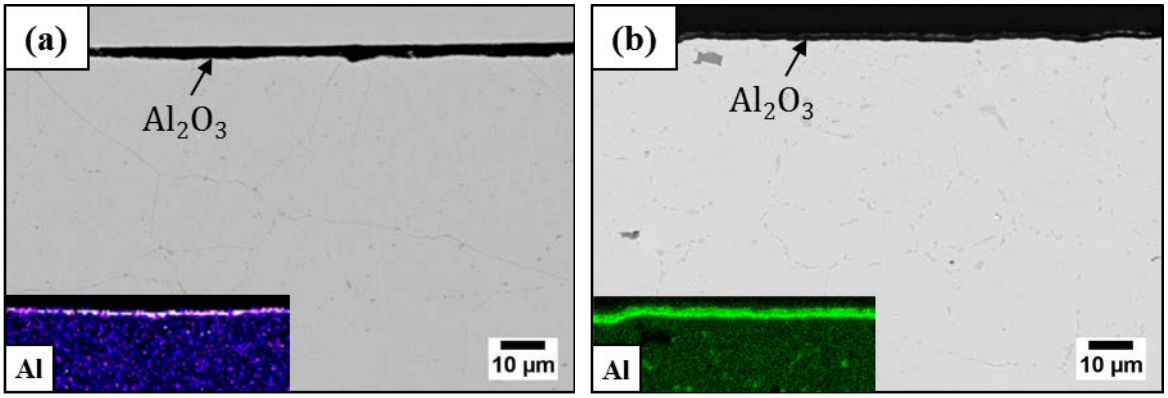

Figure 5-12 Scanning electron micrograph and elemental maps of alloy (a) 214 and (b) HR-224 after 10 h exposure at 871°C

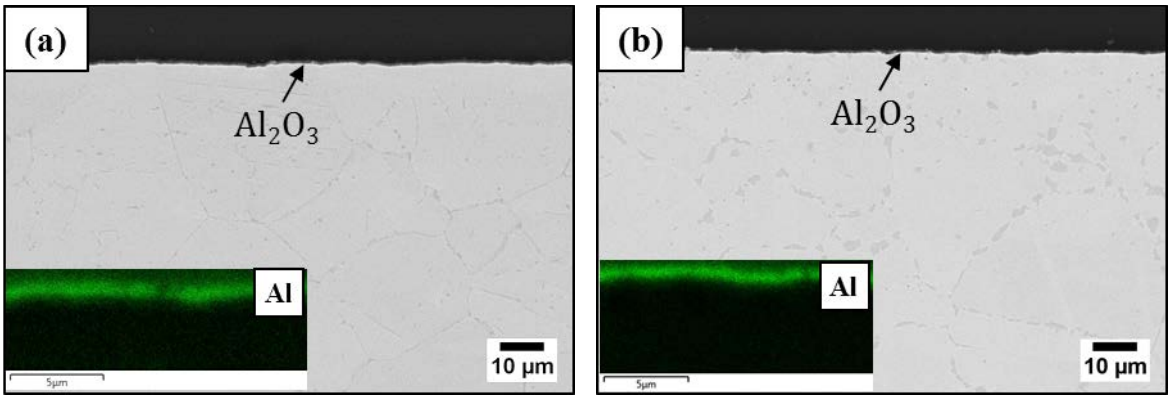

Figure 5-13 Scanning electron micrograph and elemental maps of alloy (a) 214 and (b) HR-224 after 50 h exposure at 871°C

Figure 5-14 shows the cross-sectional micrographs of alloy 617 after 10 and 100 h exposure to gas 5. Although alloy 617 is not an alumina former alloy (it has around 1.2% Al in its composition), it shows better resistance to carburization compared to the other chromia-former alloys. Formation of a non-uniform Al-oxide layer can be observed in addition to Cr-rich carbides on the alloys surface. This was followed by formation of Mo-rich precipitates beneath the scale and a thin Cr-depleted region. After 100 h exposure, the surface Cr-carbide layer and Cr depleted subscale region have grown.

In the case of alloy HR-160, formation of a duplex external scale of Cr-rich carbide above a Si-rich oxide layer was observed (Figure 5-15). However, the scale was not adherent and spallation occurred possibly during the cooling step. The carbon diffusion depth in this alloy is still less than those in alloys 617, HR-120, and 625. The better carburization resistance of this alloy can be attributed to both high Si and high Cr concentrations. As was discussed in Chapter 2.2.3, silicon additions to the alloy can increase the carburization resistance mainly by reducing solubility and diffusivity of the carbon in the substrate alloy. In 1982, Mitchell et al. [47] showed that addition of silicon decreased the solubility more than diffusivity. Moreover, the stability of silicon carbide (SiC) is much less than chromium carbides. Therefore, no SiC can be formed [42,

46, 47]. Alloy HR-160 contains high levels of chromium as well as silicon. According to the Wagner's theory [38] and Eq. (2-15), increasing the chromium content or other major carbide-former elements can decrease the carbon penetration depth. Combination of both high chromium and silicon content in alloy HR-160 provided good carburization resistance for this alloy.

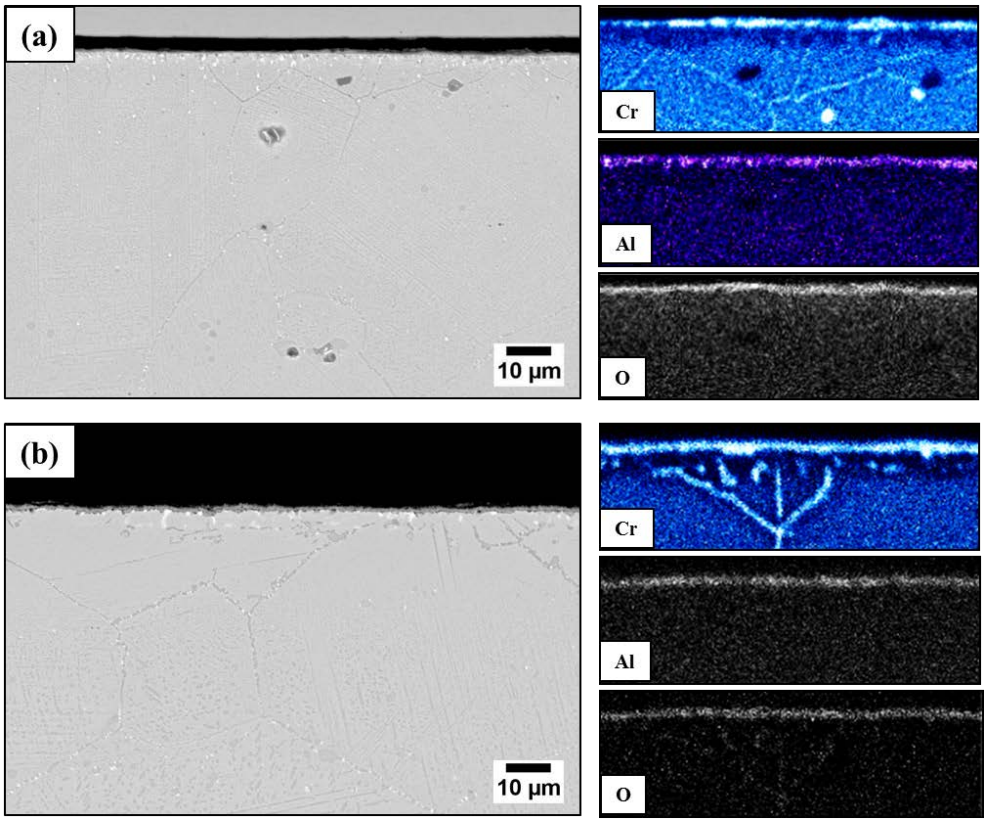

Figure 5-14 Cross-sectional SEM micrographs and elemental maps of Cr, Al, and O of alloy 617 after (a) 10 h and (b) 100 h exposure at 871°C

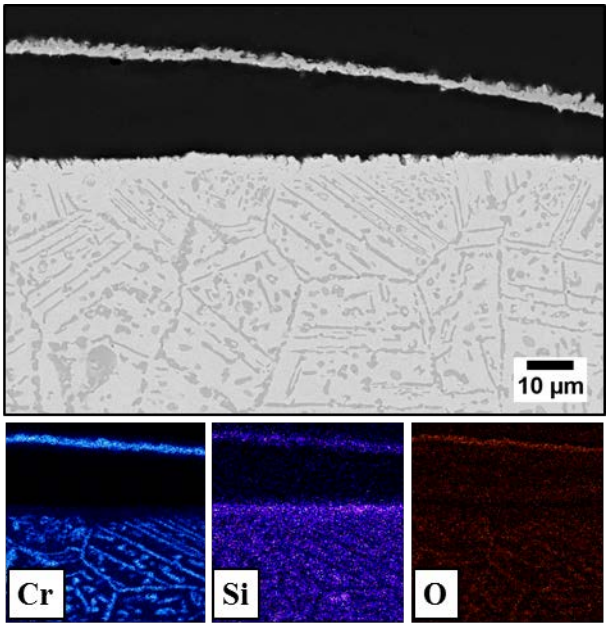

Figure 5-15 Cross-sectional SEM micrograph and elemental maps of Cr, Si, and O of alloy HR-160 after 100 h exposure at 871°C

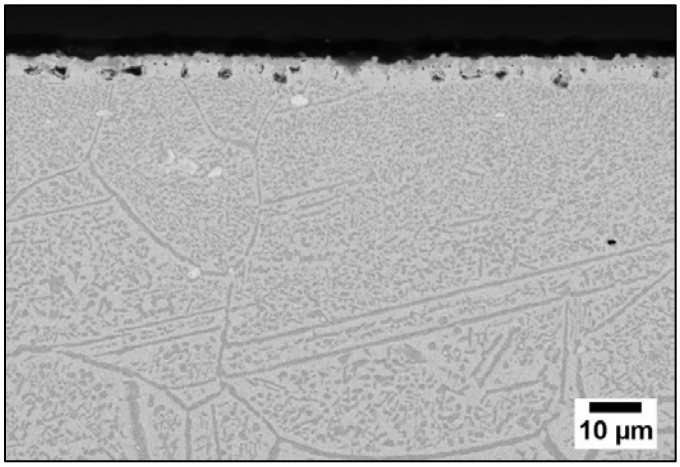

Figure 5-16 Scanning electron micrograph of alloy HR-120 after 100 h exposure to gas 5 at 871 °C

The detrimental effect of Fe on carburization resistance is evidenced in the results obtained from alloy HR-120. The SEM cross-sectional micrograph of alloy HR-120 after 100 h exposure is shown in Figure 5-16. This alloy was among the two alloys with highest carbon penetration depth. It has been previously shown [33] that the permeability of carbon decreases by

increasing the Ni/Fe ratio, which shows a minimum at Ni/Fe ~ 4. Thus, in alloy HR-120 with the lowest Ni/Fe ratio of 1.12, carbon penetration depth is expected to be the highest. An interesting observation from this sample was formation of a thin and non-continuous Cr-carbide scale compared to the other Ni-base alloys. XRD analysis verified the formation of $(Fe,Cr)_7C_3$.

5.1.3 Sulfidation-Carburization-Oxidation

The main purpose of this section is to study the corrosion behavior of these alloys in reducing environments containing both high sulfur and high carbon activities. The carbon activity of gas 3 was calculated to be about 1. The sulfur and oxygen potentials were intended to be kept constant between gas 2 and gas 3 for comparison; however, due to the multi-oxidant nature of this gas, there exist some variations. Specifically, the oxygen partial pressure of gas 3 was slightly lower than that of gas 2. Figure 5-17 shows surface images of all six alloys after only 25 h exposure to gas 3. Based on the surface appearance of these samples, severe degradation occurred on the two Fe-containing alloys HR-120 and HR-224 and also alloy 617, which previously showed the best resistance in gas 2. Extensive sulfide formation can be observed on these three alloys. Sulfide formation can also be observed to some extent on alloy 214. Alloys HR-160 and 625 showed much less reaction-product formation on the surface.

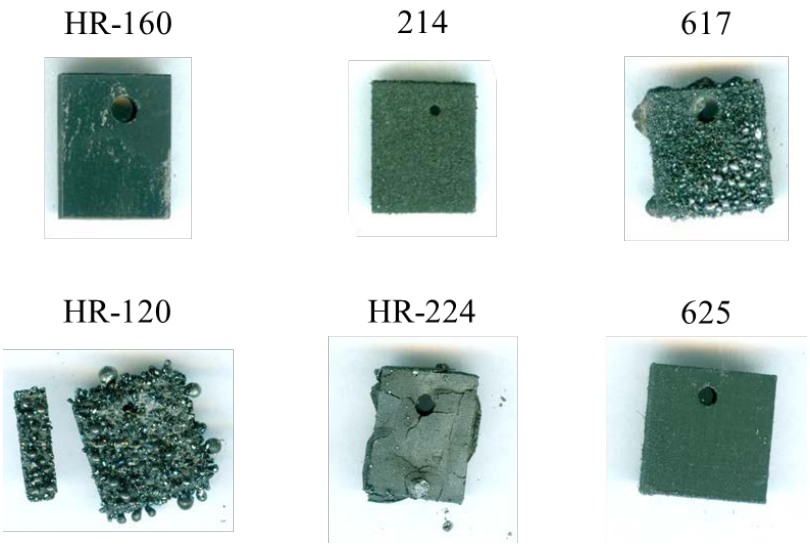

Figure 5-17 Photographs showing specimen surface appearance after reaction with gas 3 for 25 h at 871 °C

Cross-sectional micrographs of these alloys are shown in Figure 5-18. The attack on the two alumina-former alloys 214 and HR-224 was mainly internal with formation of internal Cr-rich sulfides. It has to be noted here that these two alloys have the lowest Cr concentration and can be very susceptible to rapid internal carburization attack if the alumina scale cannot be established. When the internal Cr-carbides form and no protective oxide scale was present, sulfur can easily diffuse into the substrate alloy and transform those carbides to sulfides.

Sulfide nodules together with a deep internal corrosion zone containing mixed oxides and sulfides can also be observed on alloys HR-120 and 617. Such extensive degradation was expected from HR-120 since this alloy had shown very poor resistance to both gas 2 (sulfidizing-oxidizing) and gas 5 (carburizing). This is also in agreement with results reported previously by Harper et al. [69] where they tested alloy HR-120 in a similar environment for 500 h at 900 °C. Nodules consisted of three main phases: Fe-Ni-sulfides with the lighter phase being metallic Ni and Fe, which likely formed during cooling, and also Cr_2O_3. Similar behavior was observed on alloy 617; however, inconsistency was observed with this alloy. Exposure of alloy 617 to gas 3

for 100 h showed a complete protective behavior by formation of a continuous chromia scale and an internal Al-rich oxide layer, as presented in Figure 5-19. These observations on alloy 617 confirms that gas 2 composition is very close to the kinetic boundary of oxide/sulfide and slight changes in the gas composition can completely alter the alloy's behavior. Alloy 625 also showed formation of a mixed Cr-oxide and Cr-sulfide scale and localized breakdown of this scale and formation of Ni-rich sulfides on top.

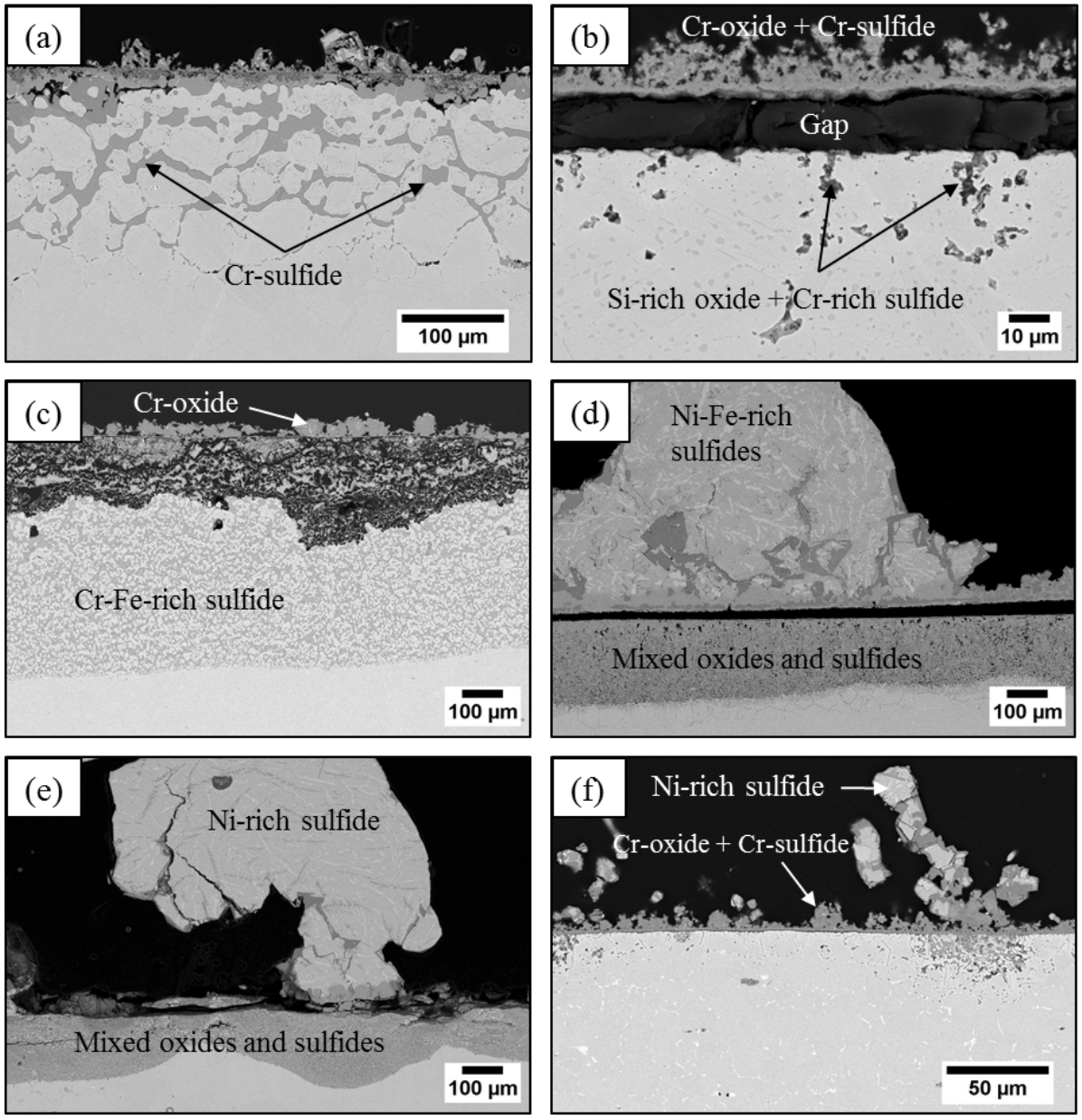

Figure 5-18 SEM cross-sectional micrographs of alloy a) 214, b) HR-160, c) HR-224, d) HR-120, e) 617, and f) 625 after 25 h exposure to gas 3 at 871°C

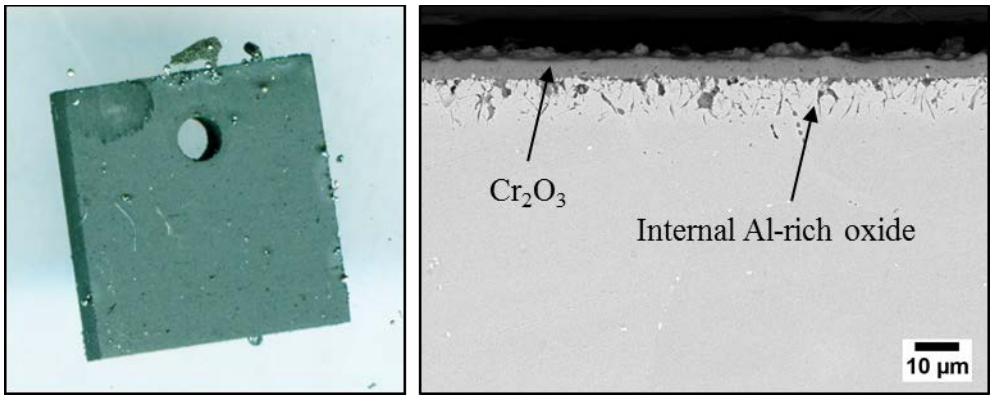

Figure 5-19 SEM cross-sectional micrographs of alloy 617 after 100 h exposure to gas 3 at 871°C

Based on previous observations of the corrosion behavior of these alloys in carburizing environment of gas 5, it was shown that increasing the iron content of the alloy will decrease the resistance to carburization and increasing the Ni+Co/Fe ratio in the alloy can significantly improve resistance. Figure 5-20 shows cross-sectional micrographs of the reaction fronts in HR-120 and HR-224, which both had lowest Ni+Co/Fe ratio. Formation of internal Cr-rich carbides at the reaction front can clearly be observed in both alloys. Thus, it can be inferred that carbon plays a significant role in degradation mechanism of these alloys. Formation of Cr-rich sulfides is appeared to follow the same pattern as the carbides. Similar internal attack and formation of internal Cr-sulfide was observed on alloy 214 after 25 h exposure. It is noteworthy that alloy 214 has a very low chromium concentration and can be very susceptible to carburization attack in the absence of a protective alumina scale.

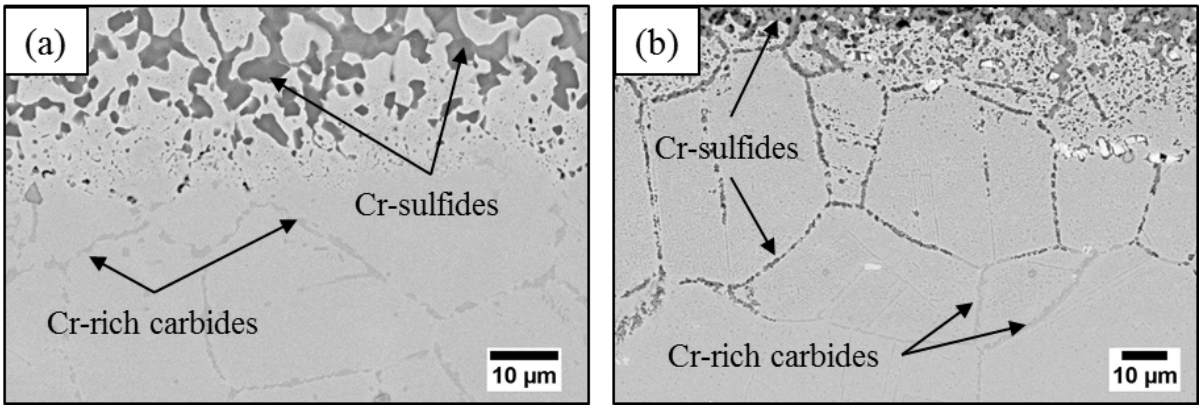

Figure 5-20 SEM micrographs of reaction front after exposure of alloys a) HR-224 and b) HR-120 to gas 3 for 25 h at 871°C. Formation of Cr-rich carbides at the reaction front can be observed.

HR-160 exhibited protective behavior. Although spallation of the scale occurred during cooling step of this alloy, no major attack could be observed for up to 25 h exposure. According to the cross-sectional micrograph of this alloy after 25 h exposure (Figure 5-18(b)), an external scale consisting of mainly chromium oxide with small amounts of sulfides above a Si-rich oxide layer was established on this alloy, with some indication of internal sulfides. However, no major sulfidation attack was observed.

5.1.4 Discussion

Since all of the commercial alloys tested in this study were heavily alloyed with a variety of elements, finding trends for their resistance to sulfidizing, carburizing, or mixed environments is difficult. In this section, some major observations and conclusions, which led to the design of different model alloy systems, will be discussed.

5.1.4.1 Sulfidation-Oxidation

Exposure of these alloys to the sulfidizing-oxidizing environment of gas 2, with low carbon activity, can aid us to gain insights on the effect of both major and minor alloying elements on sulfidation resistance. An understanding of the corrosion behavior of these alloys requires knowledge of the interactions between different species in the gas phase, the chemical composition of the alloy, and the temperature of the reaction. The observed results clearly showed that the gas 2 environment is very close to the kinetic boundary of sulfide/oxide at 871 °C and alloy chemistry can significantly affect scaling behavior of an alloy and the time to breakaway corrosion.

Severe degradation by formation of the base-metal sulfides was observed on the two alloys HR-120 and HR-224 with high Fe concentrations. Since the temperature of reaction in this study is above the low eutectic temperatures of most metal/metal-sulfides, liquid products can easily from in the absence of a protective oxide scale. Formation of a liquid product can lead to an extremely rapid degradation. Alloy HR-120 has a relatively high chromium concentration (25 wt. %) and is expected to be able to form a protective chromia layer. Alloy HR-224, on the other hand, has a high concentration of Al and about 20 wt. % Cr and is expected to form a protective alumina scale (similar to Figure 5-12 and Figure 5-13). However, both alloys have one thing in common and that is the high concentrations of Fe and the observed formation of (Fe,Ni) sulfide nodules. Since Fe-FeS eutectic temperature (988 °C) is higher than those of Ni-Ni_3S_2 (645 °C) and Co-Co_9S_8 (880 °C), it is usually expected that alloys containing higher Fe concentration show better resistance to sulfidation [10]. However, the poor corrosion resistance of alloy HR-120 in mixed-gas environments has also been reported by other researchers [69, 75]. A possible explanation for the more severe attack observed on alloys HR-120 and HR-224 might be the

presence of the carburizing species CO in the environment. As was observed in the carburization results in gas 5 (to be discussed in the next section in more detail), carbon has much higher permeability in Fe compared to Ni. Thus, since gas 2 still has a carbon activity of about 0.2, by increasing the Fe content of the alloy, carbon permeability and, consequently, carbide precipitation would increase. These carbides are rich in Cr, which will decrease the available Cr for the formation of the protective oxide, especially at initial stages of reaction. As a result, the remaining depleted substrate alloy will undergo a more severe sulfidation attack and rapid consumption of the alloy. It was previously discussed that carbon permeability shows a minimum at the ratio of Ni/Fe=4/1; however, the only oxides that can provide complete protection against carburization are alumina (Al_2O_3) and silica (SiO_2), which can be a contributing factor to the much better protection observed for alloys 214 and HR-160 in gas 2 environment as well. However, further study on the effect of carbon on the corrosion mechanism of similar alloy systems in gas 2 is needed.

Results on alloys HR-160, 214 and 617 clearly highlight the fact that there are more factors to consider than major alloying elements. It is inferred that the addition of minor alloying elements such as Al, Ti, Si and Mo play an important role in improving sulfidation resistance in these alloys, which were protected against sulfidation attack by formation of silica, alumina, and chromia scales, respectively. Although spallation occurred for the case of alloy HR-160 during cooling, no major metal attack was observed on the sample even after 100 h exposure. This is in agreement with the results reported by Lai [10, 73] for alloy HR-160 in mixed sulfidizing-oxidizing gases. The formation of an outer Cr_2O_3 layer followed by an underlying SiO_2 layer is expected for this alloy. In addition, a high concentration of Co contributes to the better sulfidation resistance. From the results observed after exposure of alloy 214 to gas 2, it is clear

that once a continuous alumina scale is established, no further sulfidation attack can occur. In a similar manner, alloy 617 is a chromia-forming alloy with about 1.2 wt. % Al and showed excellent resistance to sulfidation by formation of a Cr-rich oxide outer layer and Al-rich oxide on the inner layer.

Given that the requirement for these alloys to perform well in the harsh environments tested is the formation of slow growing oxides of Cr_2O_3, Al_2O_3, and SiO_2, it was clearly shown that addition of higher concentrations of Cr, Al, or Si solely, cannot account for a good resistance to sulfidation and consideration of both major and minor alloying element effects is necessary. Carburization resistance of these alloys will be discussed next.

5.1.4.2 Carburization

The parabolic kinetics of internal carburization can be explained through Wagner's theory as discussed in the previous chapter. Since carbon permeability is so high in these alloys, the inward diffusion of carbon to the reaction front dictates the carburization rate. Under such conditions the parabolic rate constant can be described as

$$k_P = \frac{\varepsilon D_C N_C^{(s)}}{N_M^{(0)}} \tag{5-1}$$

where D_C is the diffusion coefficient of carbon in the substrate alloy, N_C the surface concentration of the dissolved carbon in the alloy, N_M is the original alloy concentration of the carbide-former element, ε is a diffusional blocking parameter known as "labyrinth factor", and ν is the stoichiometric ratio for the carbide MC_ν. The experimentally determined parabolic rate constants for all six commercial alloys are presented in Table 5-1.

Table 5-1 Experimentally determined parabolic rate constants for all six commercial alloys

Alloy	k_P ($g^2/cm^4.s$)
214	2.7×10^{-13}
HR-224	7.5×10^{-13}
HR-160	9.4×10^{-12}
617	2.1×10^{-11}
HR-120	6.7×10^{-11}
625	7.0×10^{-11}

Carburization kinetics depend on carbon solubility and diffusivity ($N_C D_C$). Carbon solubility is a function of chemical composition. As was mentioned before (Chapter 2.2.3), Ni reduces both diffusivity [44] and solubility [76] of carbon in Fe-Ni-Cr alloys with a maximum carburization resistance achieved when the Ni:Fe mass ratio is 4:1 [43]. Assuming that Co has a similar effect as Ni, the high (Ni+Co) content in alloy HR-160 can partially explain the slower kinetics in this alloy. It has also been found that when Cr and Fe are the main carbide-forming elements in the alloy, there exists a correlation between carburization resistance and Ni:(Cr+Fe) ratio or (Ni+Co):(Cr+Fe) ratio [45]. Thus, it would be expected that alloy 214, 617 and 625 with highest (Ni+Co):(Cr+Fe) ratios show the lowest carburization attack. However, a wide range of behavior was observed among these alloys (Figure 5-21). This suggests that in the presence of other elements such as Al, Ti, Mo, or Si the above correlation may not be entirely valid. The significant concentrations of such elements (Al in 214 and HR-224 and Si in HR-160) can affect carburization resistance by forming protective oxides such as Al_2O_3 and SiO_2, which are stable at the oxygen impurity levels in the environments.

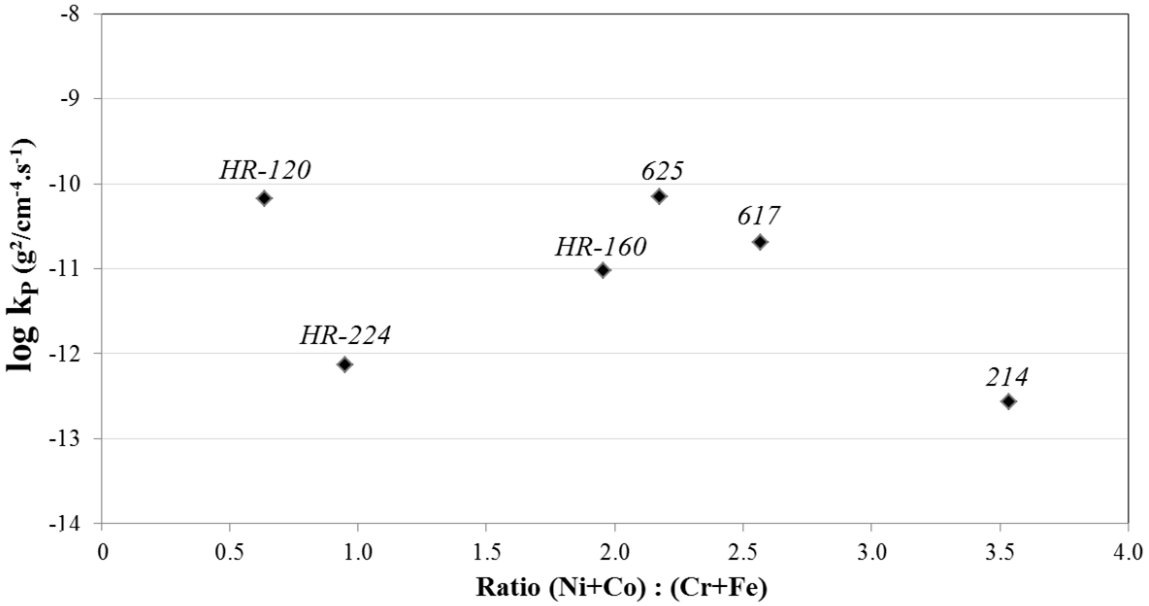

Figure 5-21 Carburization rate constants as a function of (Ni+Co):(Cr+Fe) ratio for several commercial alloys tested at 871 °C in the gas 5

Despite the complexity of these alloys, their performance can be understood to some extent using Wagner's theory for internal oxidation (Eq. 2-15), which can also be used to described the internal carburization [38]. Figure 5-22 illustrates the dependence of carburization depth of commercial alloys on their chromium contents. It is seen that the carbon penetration depth decreases by increasing the chromium content. In accordance with Wagner's limiting Eq. 2-15, carbon penetration depth is expected to be inversely proportional to the Cr concentration. As can be seen from the results, with increasing the Cr concentration the carbon penetration depth decreases for most chromia-former alloys. However, in the case of alumina-former alloys, the carbon penetration depth decreases rapidly with increasing Al concentration. Taking a closer look at the microstructures of alloys 617, HR-224, and 214 after 100 h exposure to gas 5, it was clearly observed that formation of a continuous alumina scale, as in the case of alloy 214, can completely prevent carbon penetration in the substrate alloy. These findings are in agreement

with previous studies by Lai [77] and Kane et al. [78] showing that alumina-scale forming alloys such as 214 and MA956 performed significantly better than the other alloys. However, if this oxide scale cracks or spalls (alloy HR-224) or if the alloy is unable to form a continuous layer of alumina, carbon can penetrate into the alloy and internal carbides will form. Since Cr-carbide is more stable thermodynamically than Cr-oxide under these highly reducing conditions, any chromium oxide formed at the initial stages (i.e., during heating) will be transformed to Cr-carbide, in which carbon has a relatively high mobility [79] (will be discussed in more detail on model alloys in Chapter 5.4.2).

Alumina was shown to be the most protective barrier against carburization attack in strongly reducing carburizing atmospheres (gas 5). It should also be noted that, in the environments with lower carbon and higher oxygen activities, where chromia is stable to form an external layer, internal carburization often still occurs. In recent studies by Young et al. [63, 80], the formation of internal carbides were observed on Fe-Cr alloys after exposure to Ar-20CO_2 at 650 °C. A two-stage test performed in Ar-O_2 followed by Ar-CO_2 gases clearly demonstrated that carbon species could transport through the pre-existing Cr_2O_3 layer. Atom probe tomography showed the enrichment of carbon at scale/alloy interface and at some oxide grain boundaries. Considering that carbon has a very low solubility in the oxide [60], it was suggested that grain-boundary transport of carbon is the main mechanism for carbon permeation through the scale. However, no carbon transport through alumina scale, which has similar crystal structure as chromia, has yet to have been reported to our knowledge.

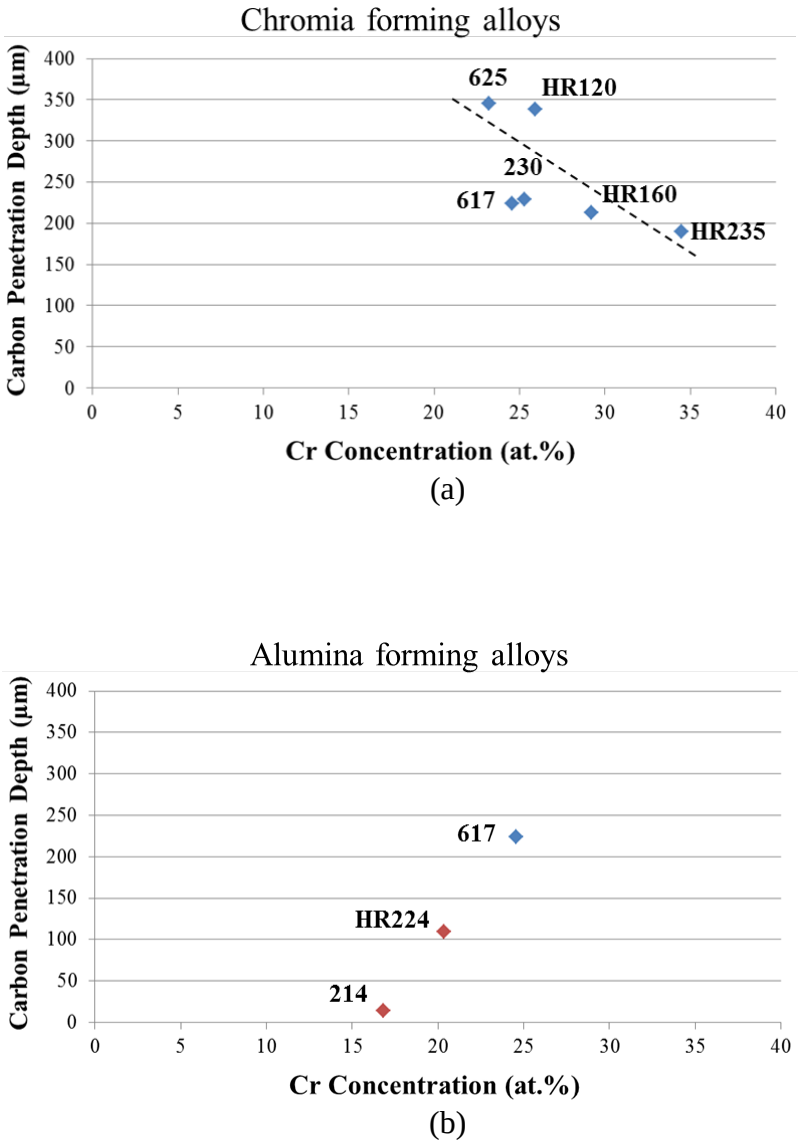

Figure 5-22 The dependence of carburization depth of a) chromia forming and b) alumina forming alloys after 100 h exposure at 871 °C on their chromium contents

The distinctive behavior of alloy 214 may, at least in part, be attributed to the beneficial effects of Y, which is present in a small amount in this alloy. The current results are in agreement with a previous study by Tawancy et al. [45]. According to their TEM observations, the oxide is mainly α-Al_2O_3 with small concentrations of Cr, Y and Ni. The beneficial effect of Y on

improving the adherence of alumina scales is now established [81, 82, 83]. Several different mechanisms have been proposed such as: enhanced scale plasticity, graded seal mechanism, growth process modification, chemical bonding, vacancy sink model, formation of oxide pegs at alloy/scale interface, and tying up sulfur in the alloy and preventing its segregation at alloy/oxide interface. Relatively recent work by Smialek [83] conclusively identified the latter as the main mechanism. It has been clearly shown that sulfur is the major source of spallation in alumina scales and the interaction between reactive elements and sulfur improves the adhesion of scale. The beneficial effect of Y may be seen by comparison of the results between alloy 214 and HR-224. In both cases carbon penetration has been prevented at the initial stages (up to 10 h) due to the formation of a continuous layer of alumina at the surface. However, in alloy HR-224 after 100 h exposure due to the failure of the oxide layer, carbon was able to penetrate into the substrate alloy and form intragranular carbides. Although the effect of Y on scale adhesion has been discussed mainly for the systems under cyclic conditions, it might also affect the adhesion and overall quality of the scale during the isothermal exposures. In almost every study of alumina-scale forming alloys, the formation of voids or cavities at the scale/alloy interface has been mentioned. It has also been reported that segregation of RE elements affects surface energy and, thus, can inhibit the formation interfacial voids by reducing the driving force for these voids to grow and thereby improving the scale adhesion [84].

For the cases where a surface scale forms, the value of N_C in Eq. 5-1 can be perturbed. It should be noted that the carburizing atmosphere is the same for all exposure conditions; however, when the scale forms, it can separate the alloy from the gas. The current results clearly show that the alumina scales in two alloys 214 and HR-224 or silica scale in alloy HR-160 has essentially no permeability for carbon. Carbide scales, on the other hand, grow by outward

diffusion of chromium and when they form a continuous layer on the alloy surface, the carbon activity beneath is established by the carbide-dissociation equilibrium. Since in most cases this external carbide layer was characterized as Cr_3C_2, the carbon activity at alloy/scale interface can be calculated through

$$Cr_3C_2 = 3\underline{Cr} + \underline{C} \tag{5-2}$$

The underlined Cr and C in this reaction represent these constituents in the solid solution state and, thus, they are not at unit activity. The equilibrium for this reaction can be defined in terms of the activities of Cr and C in the alloy and the equilibrium constant K, as:

$$K = \frac{a_{Cr}^3 . a_C}{a_{Cr_3C_2}} \tag{5-3}$$

The activity of carbon dissolved in the metal matrix in equilibrium with the carbide can then be obtained as:

$$\therefore\ a_C = \frac{K.a_{Cr_3C_2}}{a_{Cr}^3} \approx \frac{K}{[Cr]^3} \tag{5-4}$$

$$\therefore\ a_C \downarrow \quad as \quad X_{Cr} \uparrow \tag{5-5}$$

Assuming that the metal matrix to be a regular solution, the a_{Cr} can be written as γX_{Cr}, where γ is the activity coefficient. The activity of carbon at the alloy/scale interface is, therefore, dictated by Eq. 5-4, which is lower than the carbon activity in the environment and therefore the depth of the carbide precipitation zone would be expected to be shallower. It is also shown that the activity of carbon is inversely related to Cr concentration in the alloy and, thus, the carbon activity will decrease as the Cr concentration of the alloy increase, which, in turn, should decrease the carburization depth.

Formation of internal carbide precipitates below the external carbide scale clearly shows that carbon can easily diffuse through the carbide scale. It has been reported [79] that the atomic

mobility of C in Cr_3C_2 is high mainly due to its small binding energy, as reflected in its relatively low enthalpy of formation [45, 79]. In the case of alloys such as 617, Al_2O_3 forms during the initial stages. However, since the concentration is not enough to support the formation of a continuous alumina scale, carbon can still diffuse in and form internal carbides. This initially formed Al_2O_3 will later be overgrown by Cr-carbide layer due to the outward diffusion of chromium, especially in Ni-based alloys. This mechanism is shown schematically in Figure 5-23.

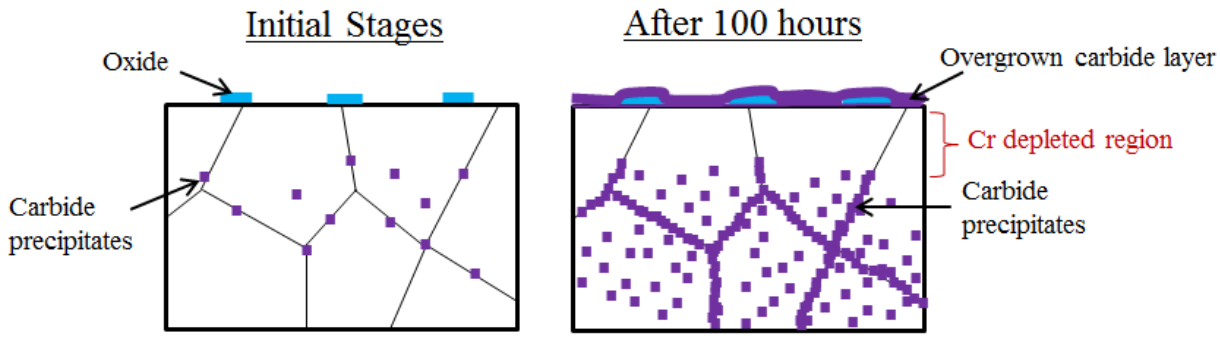

Figure 5-23 Schematic diagram illustrating the progress of carburization as a function of time in the presence of a less protective surface carbide scale

In 1986, Kinniard et al. [85] showed that among several austenitic heat-resistant steels, high nickel alloys are able to form Cr_3C_2 as a continuous layer in the external scale. In low nickel materials, on the other hand, external scales of chromium-rich M_7C_3 might form, which is in agreement with the results observed in this study. However, very little information is available on the mechanism of the formation of such scales, since carbides form mainly internally due to high inward flux of carbon in these alloys. Formation of external carbide scales under carburizing conditions will be studied in more detail later in this thesis study using the designed model alloys (Chapter 5.4.2).

The effect of refractory-element additions on carburization resistance was unclear even though refractory elements had an effect on carbide morphology. The two alloys 625 and 617 that contained high levels of refractory elements had a wide range of behaviors, where alloy 617 showed good and alloy 625 showed very poor carburization resistance. Refractory additions such as Mo are expected to improve carburization resistance as they can increase N_M in Eq. 5-1 by forming additional carbides like Mo_6C. The variation in behavior is inferred to be by the addition of other alloying elements like Al in 617 that could have a stronger effect on carburization resistance than refractory content.

5.1.4.3 Sulfidation-Carburization-Oxidation

Figure 5-24 shows the effect of chemical composition on the weight gain for all six commercial alloys used in this study. It was shown previously that alloys with higher Fe content show much higher weight gains after exposure to the gas 2 environment. Almost similar behavior can be observed here in gas 3, apart from alloy 617, which showed a borderline behavior of both protective and non-protective. In general, much higher weight gains were observed after 25 h exposure to gas 3 compared to 100 h in gas 2, which shows the much faster corrosion kinetics in this environment.

Formation of Cr-rich sulfides was observed in the outer scale of almost all alloys after 25 h exposure. Based on the location of gas 3 on Cr-O-S stability diagram (Figure 4-3), the co-formation of Cr-oxide and Cr-sulfide is expected on these alloys. However, these diagrams are generally limited to three component systems. Due to the multi-component nature of the gases and complex alloy compositions in current study, the kinetic boundary can shift and also a third dimension for carbon activity needs to be considered. It is known that the chemistry of the alloy

can play a major role on the location of the kinetic boundary and stabilities of the oxides, sulfides and carbides, which can be formed after exposure to mixed gas environments. This can clearly be observed in the wide range of results obtained after 25 h exposure of different commercial alloys to gas 3 at 871 °C. Higher stability of Cr-oxide is expected in alloy HR-160 with highest Cr- and Co-content and in alloy 617 with addition of about 1.2 wt. % Al.

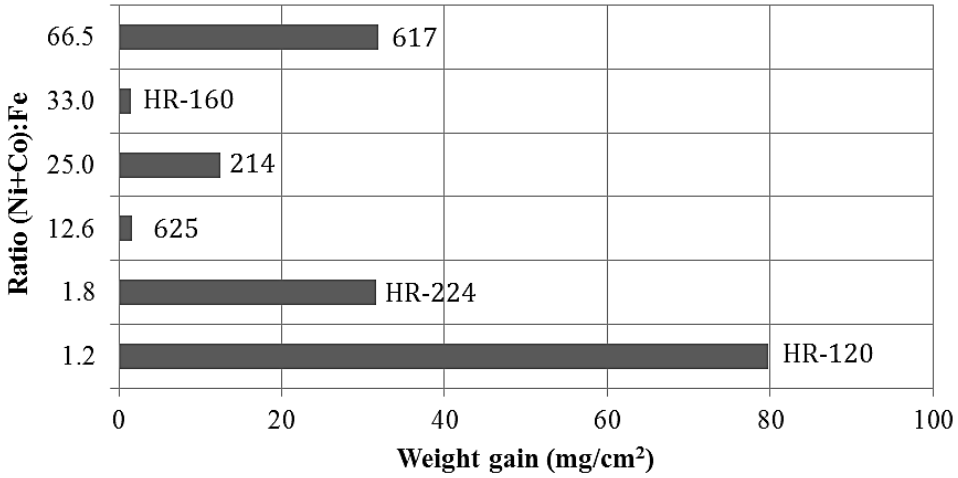

Figure 5-24 Effect of (Ni+Co):Fe ratio on the weight gain for six different commercial alloys after exposure to gas 3 for 25 h at 871 °C

As shown by the cross-sectional micrographs (Figure 5-18), in most alloys formation of Cr-sulfide was observed even at small amounts. In addition, all of the alloys except HR-160 exhibited some degree of internal sulfidation. It is important to note that gas 3 has slightly lower oxygen potential compared to gas 2 and also higher carbon activity. So, it is possible that the majority of internal attack is actually due to the internal carburization and presence of a less protective oxide scale due to the co-formation of sulfides and oxides.

Three different corrosion-product microstructures were observed on the alloys studied. The first group is represented by localized breakdown of a Cr_2O_3 scale and subsequent formation

of Ni-rich sulfides on top such as alloy 617 (100 h exposure) and 625 (25 h exposure). The second group, including alloy HR-120 and 617 after 25 h exposure, showed the formation of Ni-Fe or Ni-Co-rich sulfide nodules on top, followed by a Cr-oxide and Cr-sulfide mixed region and a porous substrate containing a mixture of oxides and sulfides. A reaction model for formation of such structure was previously proposed by Tiearney et al. [86]. In their model they explained that at initial stages Cr_2O_3 and sulfides of the base metal (Ni, Co or Fe) compete for the surface sites. Since the sulfides of the base metal grow faster than Cr-oxide, they overgrow the oxide as the reaction proceeds and they can quickly cover the whole surface if they are molten at the temperature of the reaction. Then the chromium diffusing up from the matrix will react with the base metal sulfide at the scale-metal interface and forms chromium sulfide, which also grows by outward cation diffusion. Outward diffusion of metals leads to formation of voids and porosity in the substrate alloy. As a result, sulfur diffuses in and reacts with the remaining chromium in the matrix to form internal chromium-rich sulfides in a Cr-depleted matrix.

However, the effect of carbon is absent in this model by Tiearney et al. [86]. Based on our observation from the third group of alloys (214 and HR-224) and the extensive internal degradation observed on these alloys, carbon plays a major role in corrosion behavior in such atmospheres. The chromium content of alloys 214 and HR-224 among the tested commercial alloys are the lowest. Therefore, in the absence of a protective alumina layer, these alloys are most susceptible to extreme carburization attack. In addition, closer investigation of the reaction front in HR-224 and HR-120 clearly showed the formation of internal Cr-rich carbides. Rapid transformation of these internal carbides to sulfide by the sulfur diffusing into the alloys and releasing the carbon, which diffuses further into the alloy to react with chromium, was shown previously by Young et al. [55, 54]. However, the question remains if carbon is the main reason

for changing the mode of degradation from mainly external in group 2 to mainly internal in group 3. Also, it is still not clear if increasing the carbon content in gas 3 compared to gas 2 can shift the oxide/sulfide kinetic boundary to lower oxygen partial pressures.

Detailed and systematic study of the effect of different gas species and chemical composition on degradation mechanisms using commercial alloys can be an extremely difficult task. Since all commercial alloys tested in this study were heavily alloyed with a wide variety of elements, finding trends for their resistance to sulfidizing, carburizing, or even more complex mixed environments is difficult. As a result, the main focus of the next chapter will be on the effect of different species in the environment on corrosion behavior of the simplest case, pure chromium, to better understand the interactions among these species and their effects on modes of degradation. In the following chapters, using the preliminary results of commercial alloys, model alloys will be designed to study the effect of both major and minor alloying elements.

5.2 ENVIRONMENTAL EFFECT

5.2.1 Results

The behavior of pure chromium in several environments containing different oxygen, sulfur and carbon activities was studied at 871°C. Measured weight changes of pure Cr exposed for 25 h to the four environments at 871 °C are compared in Figure 5-25. It is seen that the highest weight gain occurred for the sample exposed to gas 3, which had both high sulfur and carbon activities. The lowest weight gain, on the other hand, occurred to the sample exposed to gas 4, which had 10% water vapor. SEM and EDX analyses of the corroded cross-sections (Figure 5-26) showed

the formation of a multi-layer structure on the sample exposed to gas 1. The scale in this case consisted of an outer layer of Cr-sulfide (56.9S-43.1Cr), followed by a thin intermediate mixed region of Cr-oxide and Cr-sulfide (38.2O-4.8S-57Cr overall) and a thick inner zone rich in both Cr-oxide and Cr-sulfide. (All compositions are given in at.% unless stated otherwise.) In gas 2 on the other hand, a relatively thick and porous Cr2O3 layer containing dispersed Cr-sulfide particles formed. EDX analysis of the scale showed an average of 7at.% sulfur in the scale. In gas 3, simultaneous formation of oxide and sulfide occurred followed by a mixed inner zone. In the case of gas 4 exposure, a continuous chromia scale formed together with void formation at the metal/scale interface. No sulfidation or carburization attack was observed.

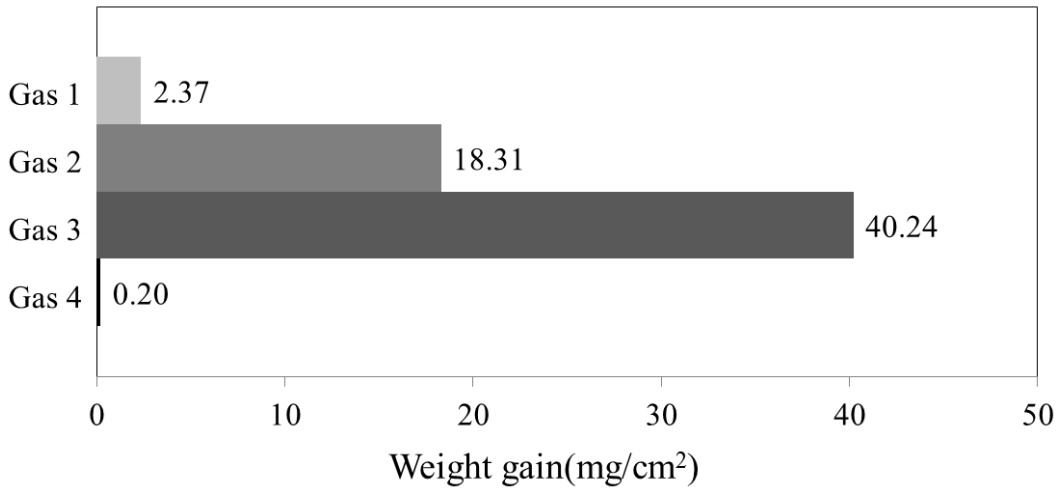

Figure 5-25 Weight change measurements after 25 h exposure to different environments at 871°C

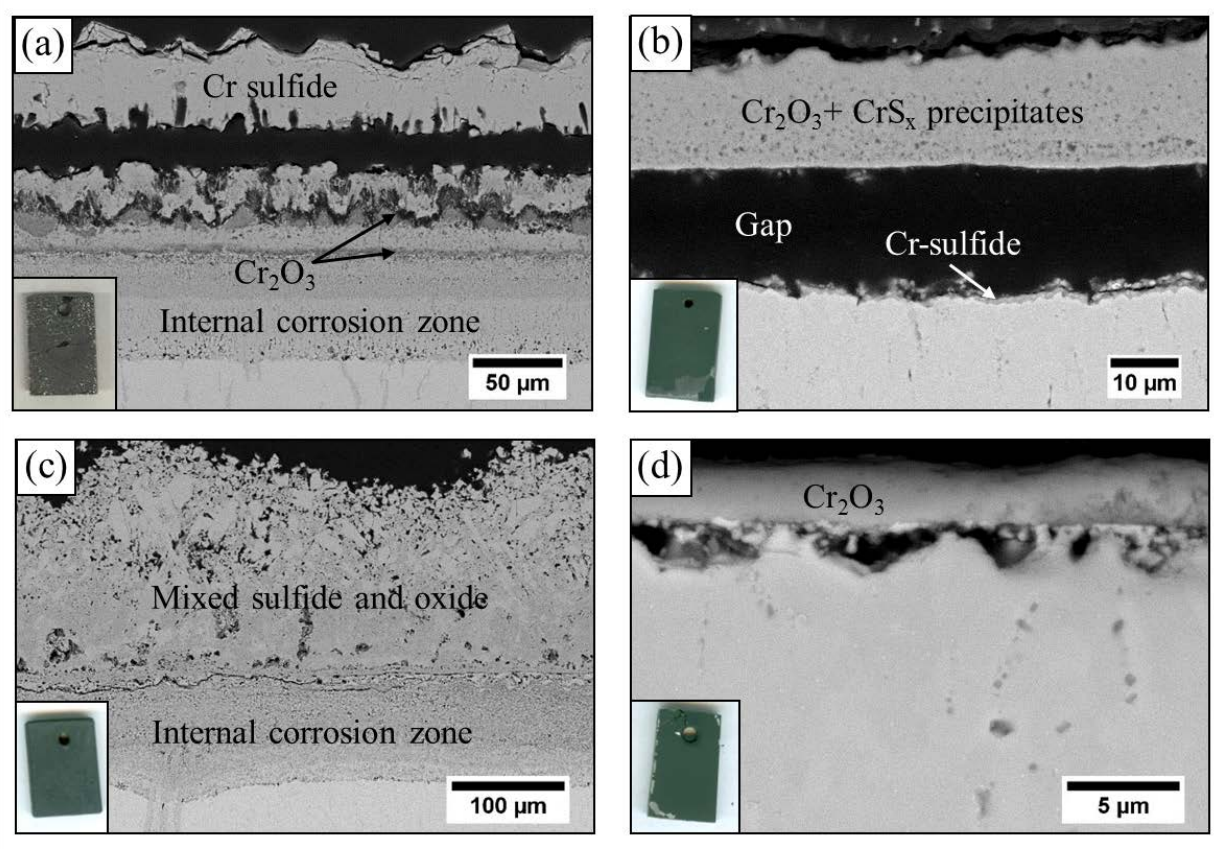

Figure 5-26 SEM cross-section images of pure Cr after exposure (a) gas 1, (a) gas 2, (a) gas 3, and (a) gas 4 for 25 h

Exposure to gas 1 resulted in the formation of a chromium sulfide scale even though the oxygen partial pressure was higher than that in both gas 3 and gas 4. Based on the cross-sectional images it is inferred that gas 3 is very close to the so-called "kinetic boundary" [87, 88], where simultaneous oxide and sulfide formation can occur. Gas 4, on the other hand, is completely in the oxide stability regime even though it has an oxygen partial pressure lower than that in both gas 1 and gas 2. As will be presented, O_2 is not the main oxidant under these gas conditions. Rather, mass-transfer calculations confirmed that either H_2O or CO_2 is the main reactant.

The effect of atmosphere composition is most interesting in the cases of gases 2 and 3. For the pure chromium exposed to gas 2 for 25 h, the chromia scale that formed was remarkably

thick. In addition, by increasing the carbon activity from 0.2 in gas 2 to 1 in gas 3, more extensive degradation was observed in which the mode of attack changed from oxidation to mixed sulfidation-oxidation-carburization. Thus, key questions to address are with regard to the criteria to form a thick chromia scale under conditions of gas 2 and a complex structure resulting from mixed attack under gas 3.

Figure 5-27 shows an SEM cross-sectional image of pure chromium after exposure to gas 2 for 25 h and the associated EDS maps of oxygen (blue) and sulfur (green), which are superimposed. It is seen that sulfur is detected throughout the scale. Chromium-sulfide precipitates were also found to be present at the metal surface.

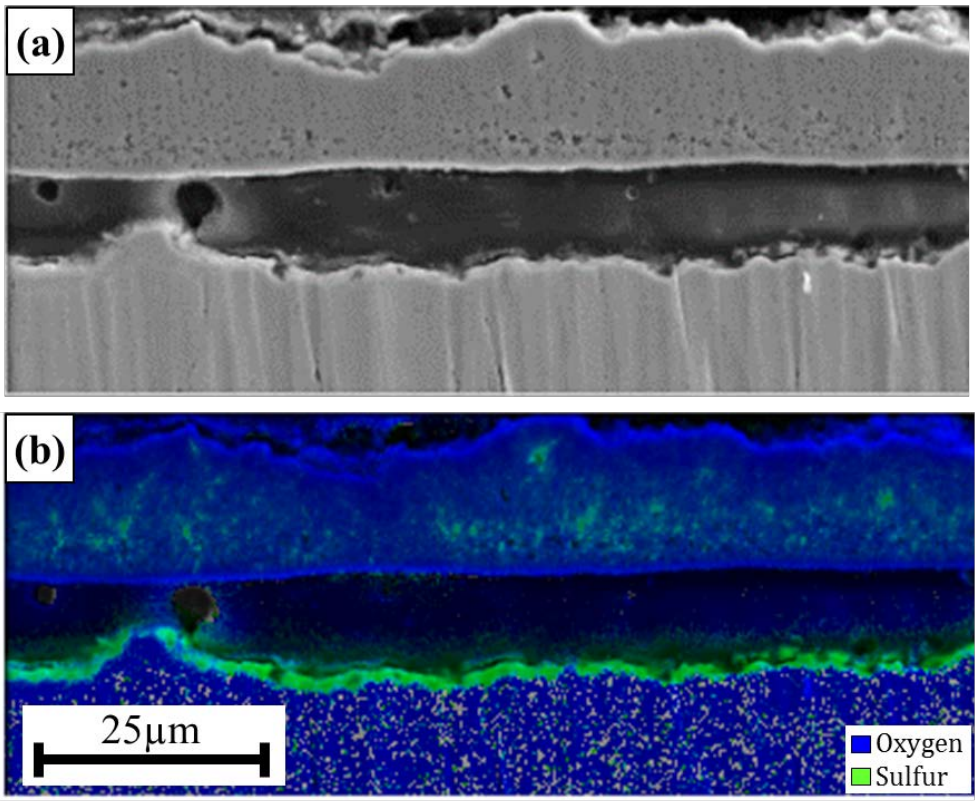

Figure 5-27 (a) SEM cross-sectional image of pure Cr after exposure to gas 2 for 25 h and (b) overlapped EDS maps of sulfur and oxygen. The middle region is epoxy resin stemming from detachment of the scale from the metal substrate

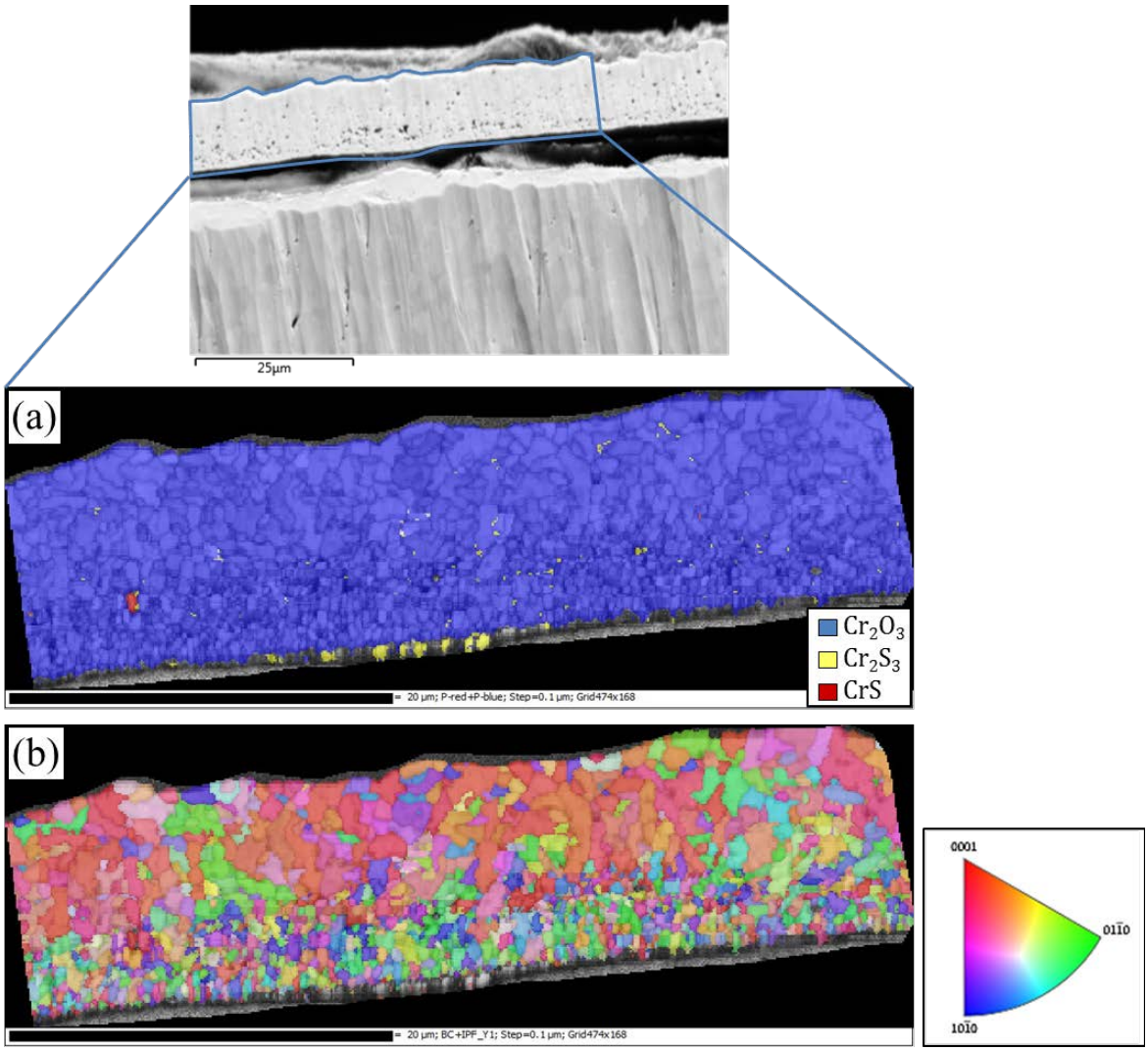

Figure 5-28 Electron backscatter diffraction (EBSD) data acquired from the scale formed on pure Cr after exposure to gas 2 for 25 h at 871°C: (a) phase distribution map and (b) inverse pole figure orientation map

Figure 5-28 presents a phase-distribution map and corresponding microstructure of the scale formed on pure chromium after 25 h exposure to gas 2. The grain structure is mainly equiaxed throughout the scale. However, the grain size varies from the metal/scale interface to the scale/gas interface. According to the orientation map in Figure 5-28(b), the scale is duplex in structure, with an inner layer comprised of smaller grains with random orientations and an external layer of ⟨0001⟩-textured larger grains. According to the phase distribution map, the

scale is mainly chromia. However, small Cr_2S_3 particles concentrated along the boundary between the duplex layers was observed. This boundary is believed to be the location of the original alloy surface, with the sulfide precipitates formed during the initial stages of exposure and then later overgrown by chromia.

To obtain further insight on the growth mechanism of the scale formed in gas 2, additional experiments with varying exposure times were carried out in this environment. Figure 5-29 shows the mass change after 5, 10, and 25 h exposure at 871°C. It is seen that the scaling kinetics increased rapidly between 5 and 10 h exposure. SEM images of the polished cross-sections of these samples are presented in Figure 5-30. A continuous chromia scale formed after 5 h exposure, together with voids at the metal/scale interface. No sulfide could be detected in the scale or at the metal/scale interface at this stage. The amounts of the initially formed sulfides may be too low to be detected by EDS. The formation of interfacial voids is a manifestation of the Kirkendall effect [89] owing to the oxidation of Cr and its outward transport through the scale to react at the scale/gas interface. The relatively thick scale observed after 10 h exposure had a similar structure to that formed after 25 h exposure. The presence of dispersed sulfide particles inside the chromia scale and a sulfide layer at the metal/scale interface were clearly observed (Figure 5-30(b)).

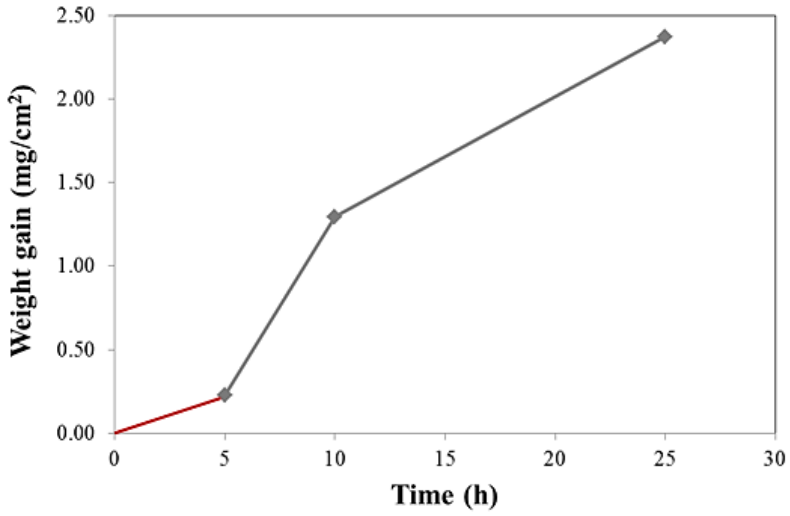

Figure 5-29 Measured weight-changes for pure chromium exposed to gas 2 at 871°C for 5, 10, and 25 h

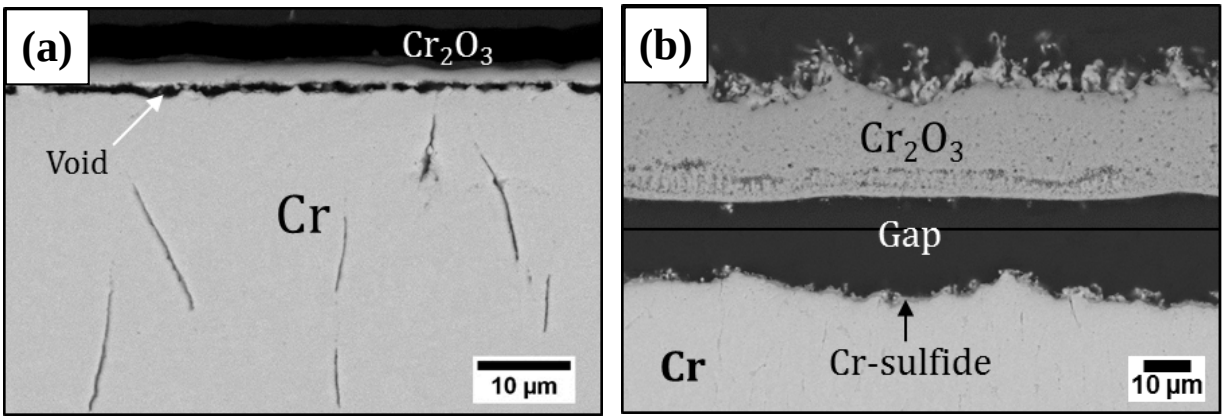

Figure 5-30 SEM cross-sectional image of pure Cr after exposure to gas 2 for (a) 5 h and (b) 10 h (the scale after 10 h exposure was detached from the metal substrate; as a result, the position of the scale shown here does not match exactly with the substrate)

For a more detailed analysis of the sample exposed to gas 2 for 25 h (Figure 5-31), two FIB lamellae were prepared for TEM characterization. Figure 5-31 presents resulting cross-sectional STEM images of the scale. The scale has an average grain size of about 440 nm; however, the grain-size distribution varies across the thickness, with larger grains about 640 nm in breadth close to the scale/gas interface and smaller grains about 240 nm in breadth at the

bottom of the scale closer to the metal/scale interface. The void content increases closer to the metal/scale interface, such that the scale close to the scale/gas interface is apparently dense.

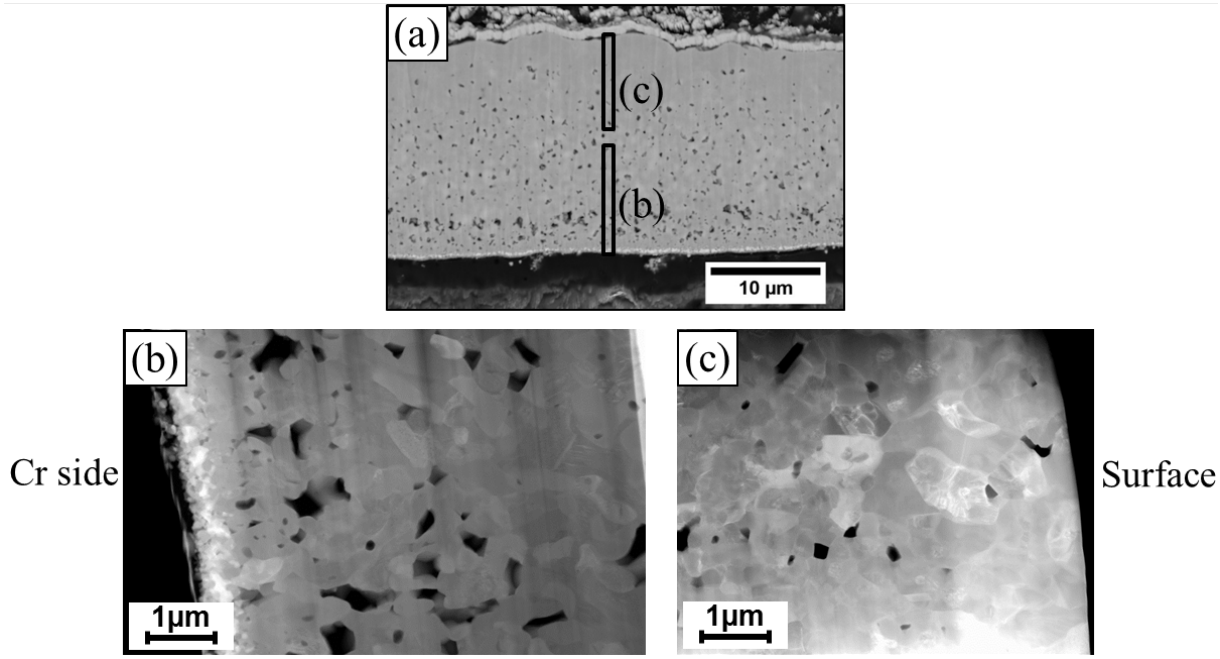

Figure 5-31 (a) SEM cross-sectional image of the scale formed on pure Cr after exposure to gas 2 for 25 h at 871 °C with the selected areas for FIB preparation indicated, (b) cross-sectional STEM image of the scale close to Cr/scale interface and (c) cross-sectional STEM image of the scale close to the scale/gas interface

To better understand the effect of environment on chromia-scale growth, a pure chromium sample was exposed to dry air in a thermogravimetric analysis (TGA) system for 25 h at 871°C. The weight-gain kinetics were found to be in accordance with the parabolic rate law (Figure 5-32), with the oxdiation rate constant calculated to be 4.1×10^{-12} $g^2cm^{-4}s^{-1}$. This value is in agreement with previously reported data [90, 91] which, from interpolation, give a k_p of about 4×10^{-12} $g^2cm^{-4}s^{-1}$ at 871°C in oxygen.

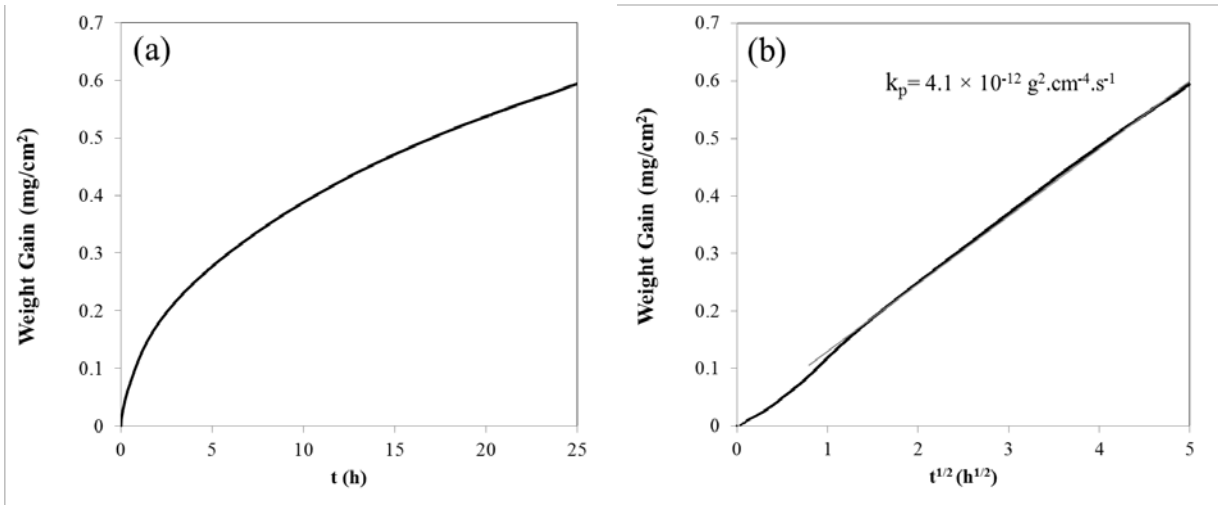

Figure 5-32 Measured weight-change kinetics for pure chromium isothermally exposed to untreated air at 871°C

As indicated in Figure 5-33, the chromia scale that formed after 25 h of exposure detatched from the substrate on cooling to room temperature. The scale was also highly convoluted, suggesting the presence of large internal stresses. According to the EBSD orientation map, the scale consists mainly of large columnar grains with random orientaions and an average grain width of about 940 nm. Figure 5-34 shows corresponding cross-sectional STEM images of the scale formed in air. The average scale thickness is around 3.5 µm. The observed columnar grains have an average length of 2.5 µm and width of about 0.9 µm. A much finer grain structure was observed at the bottom of the scale near to the metal/scale interface, which is believed to be the initially formed oxide grains. It is noteworthy that the scale thickness increased from 3.5 µm in air to 17.4 µm in gas 2 for the same exposure time of 25 h.

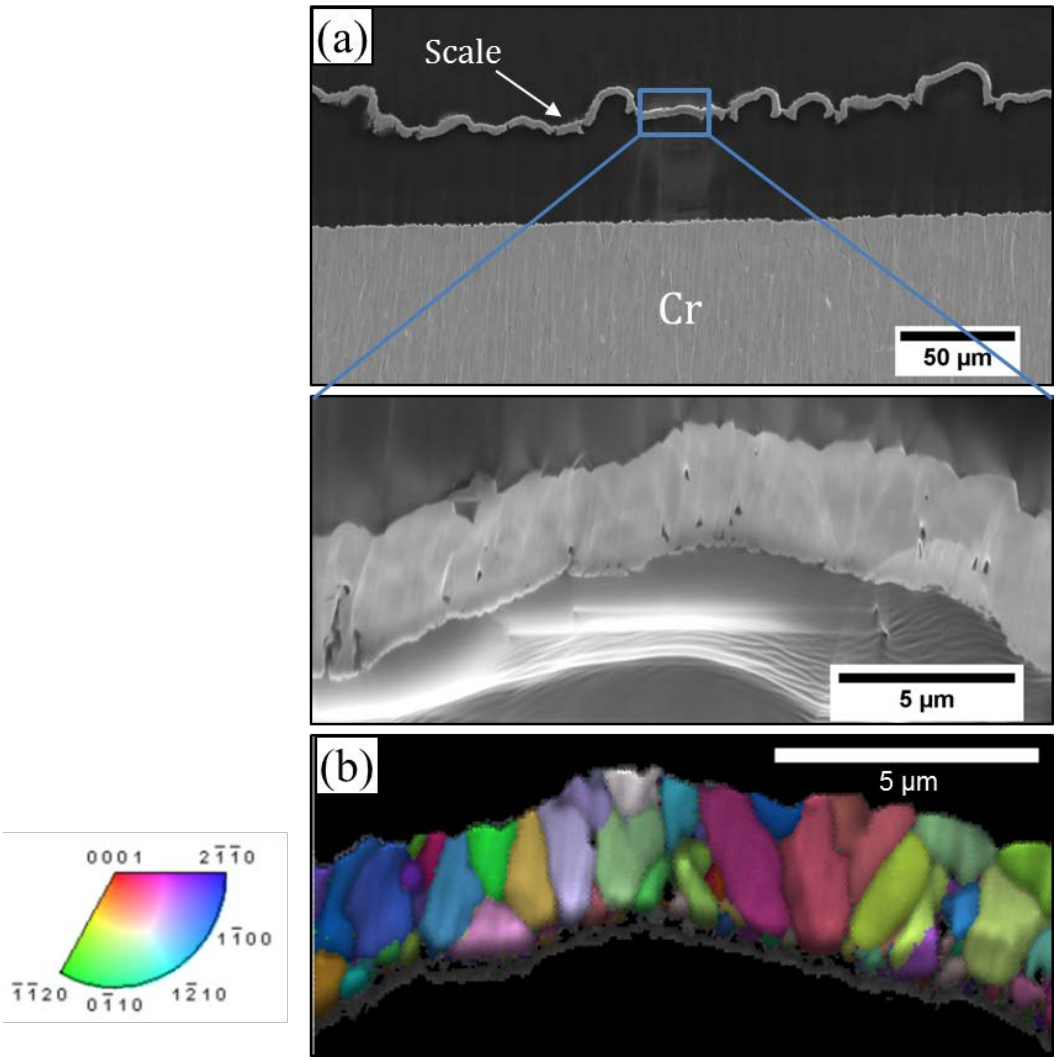

Figure 5-33 (a) Cross-sectional SEM image and (b) EBSD inverse pole figure orientation map of pure chromium exposed to dry air for 25 h at 871°C

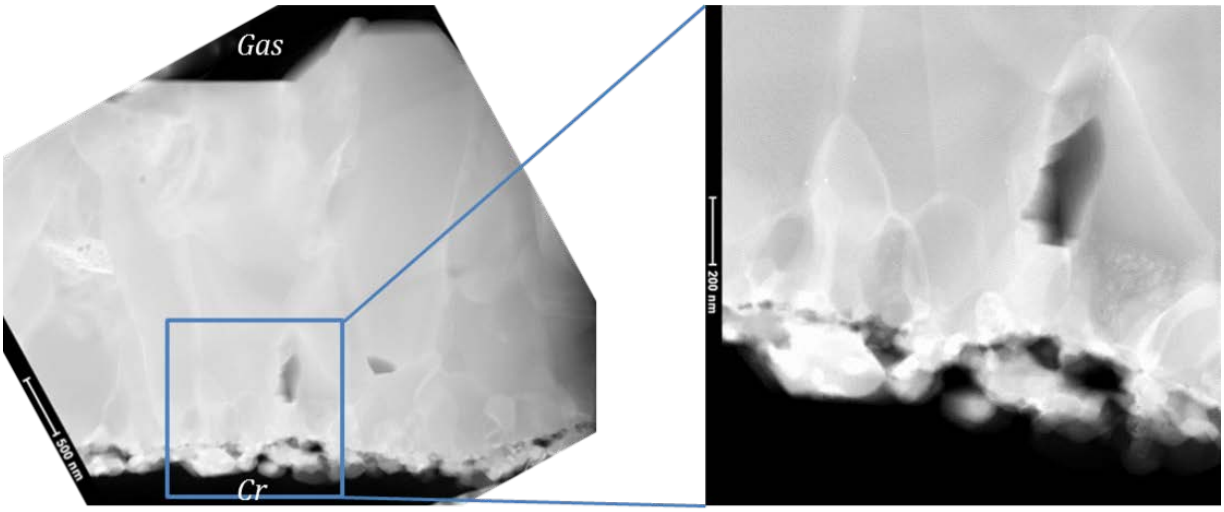

Figure 5-34 Cross-sectional STEM image of the scale formed on pure chromium after exposure for 25 h in dry air at 871°C

Significantly greater weight gains was observed for the pure chromium sample exposed to gas 3 compared to other environments. Figure 5-35(a) shows a cross-sectional image of the pure chromium sample exposed to gas 3 for 25h. The co-formation of chromium oxide and chromium sulfide can clearly be seen from the EDS maps of oxygen and sulfur. The EBSD band contrast and phase distribution maps, Figure 5-35(b) and (c), identified the scale constituents to be Cr_2O_3 and Cr_2S_3. The external scale consists of a mixture of sulfide and oxide with an extremely fine grain size at the bottom and larger columnar grains of Cr_2S_3 at the top. The inner attack region (Figure 5-36), however, shows three major zones, as indicated by differences in contrast. EDS measurements in each of these zones gave compositions of 51Cr-28S-21O in zone 1, 45Cr-19S-25O-11C in zone 2, and 69Cr-1S-18O-12C in zone 3. The relative differences in carbon content in these zones is more indicative of a trend than anything specific owing to the semiquantitative nature of the EDS measurement method, particularly of a light element like carbon. Even so, it is inferred that the carbon content progessively increases from almost nothing in zone 1 to a measureably significant level (~12 at. %) in the innermost zone 3. Sulfur, on the

other hand, decreases from 28 at. % in zone 1 to about 1 at. % in zone 3, suggesting that the main constituents in the inner corrosion zone are (Figure 5-36): sulfide and oxide in zone 1; sulfide, oxide, and carbide in zone 2; and mainly oxide and carbide in zone 3.

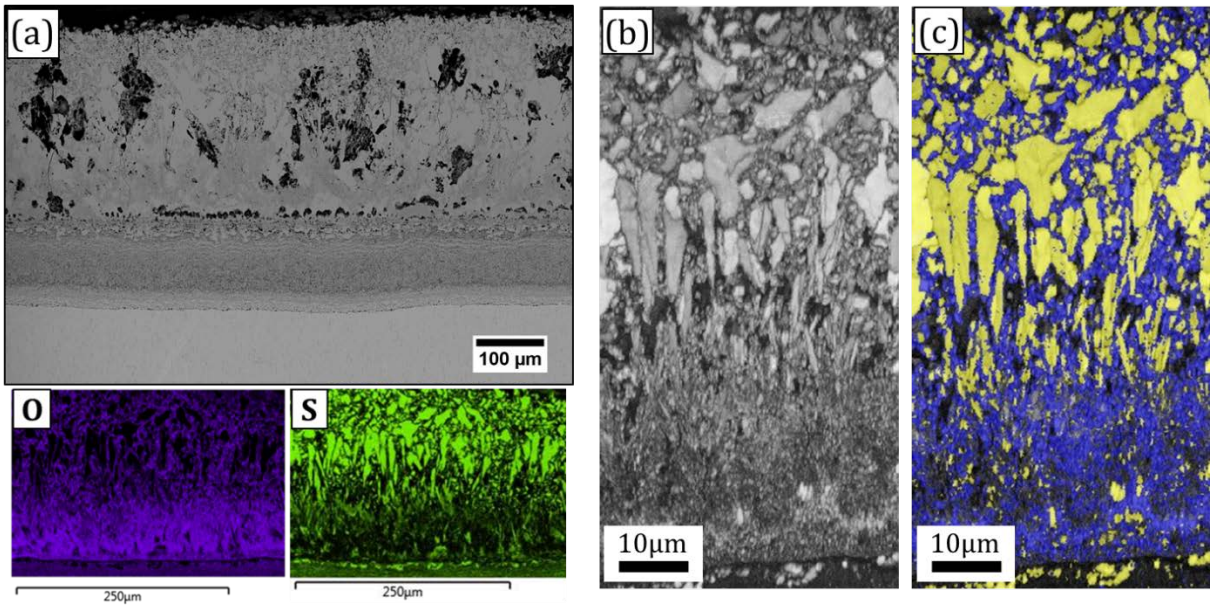

Figure 5-35 (a) SEM cross-sectional image and EDS maps of sulfur and oxygen, (b) EBSD band contrast map, and (c) phase distribution map of pure Cr after exposure to gas 3 for 25 h

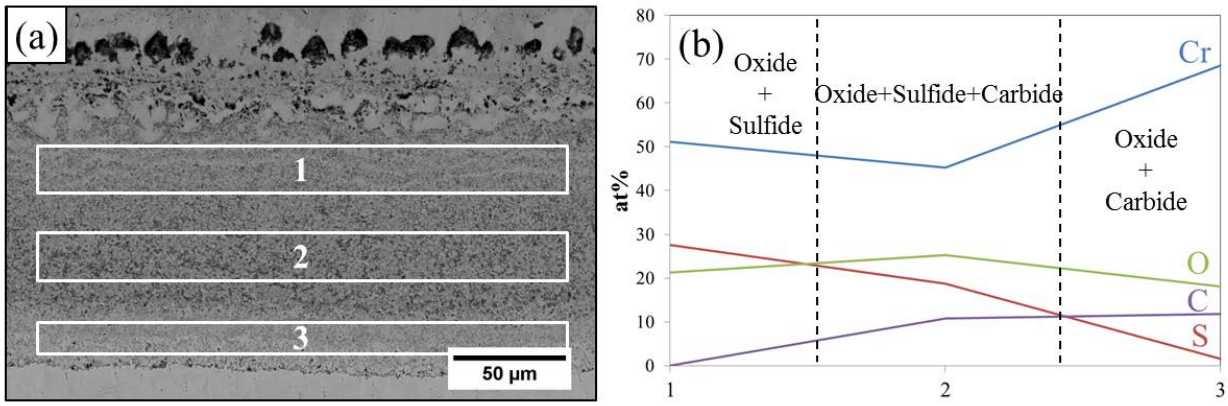

Figure 5-36 (a) SEM cross-section image and (b) EDS measurements of the inner corrosion zone of pure Cr after exposure to gas 3 for 25 h

5.2.2 Discussion

5.2.2.1 Gas flux calculations

Before proposing any possible corrosion mechanisms under the atmospheres tested, it is informative to ascertain the main oxidant(s). The maximum flux of a given gaseous species i to the alloy surface can be approximated by the expression [92, 93]

$$J_i = \frac{k_{m(i)} P_i}{RT} \tag{5-6}$$

where J is the flux and km is the mass transfer coefficient, which can be estimated from mass-transfer theory via

$$k_m = Sh \frac{D_{i(N_2)}}{L} \tag{5-7}$$

Here L is the sample length, $D_{i(N_2)}$ the diffusion coefficient of species *i* in nitrogen, and *Sh* is the Sherwood number. The diffusion coefficient can be calculated from the kinetic theory of gases as formulated in the Chapman–Enskog equation. The Sherwood number is estimated from the gas density and viscosity. Using calculated k_m values and the equilibrium partial pressures for a given gas mixture, the mass fluxes of O_2, CO_2, H_2O, and H_2S were calculated via Eq. (5-6) and the results are summarized in Table 5-2.

Table 5-2. O_2, CO_2, H_2O, and H_2S mass fluxes

	Gas 1		Gas 2		Gas 3		Gas 4	
	P_i (atm)	J_i (g/cm^2.s)	P_i (atm)	J_i (g/cm^2.s)	P_i (atm)	J_i (g/cm^2.s)	P_i (atm)	J_i (g/cm^2.s)
O_2	7.9×10^{-22}	5.6×10^{-26}	2.1×10^{-20}	1.5×10^{-24}	1.3×10^{-22}	9.3×10^{-27}	4.1×10^{-22}	2.9×10^{-26}
CO_2	9.4×10^{-4}	7.8×10^{-8}	4.7×10^{-3}	3.9×10^{-7}	1.6×10^{-4}	1.3×10^{-8}	5.0×10^{-4}	4.1×10^{-8}
H_2O	2.3×10^{-4}	1.0×10^{-8}	1.3×10^{-3}	5.8×10^{-8}	2.5×10^{-3}	1.1×10^{-7}	4.2×10^{-3}	1.9×10^{-7}
H_2S	1.2×10^{-3}	8.2×10^{-8}	1.2×10^{-3}	8.2×10^{-8}	4.6×10^{-3}	3.1×10^{-7}	4.1×10^{-3}	2.8×10^{-7}

An actual instantaneous oxygen flux for chromia-scale growth can be calculated from the scale thickness formed on Cr after 25 h in gas 4 by assuming

$$x^2 = 2k_P t \tag{5-8}$$

where x is the scale thickness (cm), t is time (s), and k_P is the parabolic scaling constant in cm^2/s. The oxygen flux necessary to form such a scale is therefore generally given by

$$J_O = \frac{1}{2}\sqrt{\frac{k_P}{t}} \tag{5-9}$$

which is about 5.1×10^{-10} g/cm^2.s after 25h of reaction and much higher than the calculated oxygen flux for all four environments (Table 5-2). Thus, O_2 cannot be the principal oxidant in all gases studied. Knowing that the decomposition of CO_2 is relatively slow [13], H_2O is inferred to be the main oxidant in each environment tested. In accordance with this, the sample exposed to gas 4 had the highest flux of H_2O and formed a continuous and exclusive chromia scale, while the sample exposed to gas 1, which had the lowest H_2O flux, was apparently on the sulfidation side of the Cr-sulfide/Cr-oxide kinetic boundary, such that sulfidation was the predominant mode of attack.

5.2.2.2 Microstructural development in gas 2

Observations of the chromium samples reacted in different environments illustrate the complex effect of different gas species on the reaction mechanisms. Under conditions of the gas 2 environment with an oxygen partial pressure of about 2.1×10^{-20} atm, a thick duplex chromia scale had formed followed by sulfide formation at the Cr_2O_3/Cr interface. Chromia-scale growth in H_2O-containing environments with low partial pressures of oxygen has been studied by others [94, 95, 96, 97]. Hänsel et al. [97] studied the oxidation of Ni-25Cr at 1000˚C in a low P_{O2} test gas of Ar-2%H_2-2%H_2O and inferred that oxygen from the water vapor is the principal oxidant for chromia-scale growth. According to these authors, the oxide growth is dictated mainly by the outward diffusion of Cr, which led to Kirkendall void formation at the alloy/scale interface. These voids may subsequently fill with oxide via an H_2-H_2O dissociation process [98, 99]. By contrast, Zurek et al. [94] showed using isotope profiling that Cr_2O_3-scale formation in H_2O-containing environments mainly proceeds by the predominance of inward oxygen grain-boundary diffusion which, in combination with the H_2-H_2O dissociation process, causes better adherence and prevents the establishment of voids at the alloy/scale interface. It is clear from those two recent studies that the growth mechanism of chromia scales in H_2O-containing environments is unresolved.

In the present investigation, a time study was done using pure chromium in gas 2 in order to more carefully elucidate the growth mechanism. Based on the current results and literature data, the deduced scaling mechanism is summarized schematically in Figure 5-37. During the initial stages of the reaction, oxide and sulfide can form simultaneously due to the high H_2O and H_2S fluxes in the gas; however, since Cr_2O_3 is thermodynamically more stable in gas 2 conditions, it can overgrow the initially formed sulfides to establish gas/scale equilibrium.

During the scale growth process, voids start to form at the metal/scale interface. The void formation at the Cr/Cr_2O_3 interface clearly resulted from chromium consumption and can, therefore, be interpreted as a sign of outward scale growth during the initial stages of reaction. The interfacial voids were apparently able to persist for a certain period. This is not in agreement with other studies [94, 98, 99, 100], which clearly revealed that in water vapor-containing environments the tendency for formation of the interfacial voids and porosity can be eliminated or at least reduced by the rapid gas-phase transport of oxygen within the pore space. A plausible explanation could be linked to the adsorption of sulfur at the internal surfaces of these voids, which poisons the oxidation reaction and hence precludes void space filling. Due to the large number of the interfacial voids, scale contact with the substrate is greatly reduced, which restricts Cr supply and consequently causes a relatively low effective growth rate of the scale. However, water vapor can eventually diffuse through the chromia scale and facilitate oxide formation within the void space at the metal/oxide interface. By filling these void spaces, continuity between the scale and substrate metal is achieved and there is a consequent increase in the scaling kinetics (Figure 5-29). Such a mechanism can result in the formation of a duplex layer, where the outer scale growth is dictated by cation diffusion and the inner zone, on the other hand, is the result of the oxide growth within the metal consumption zone.

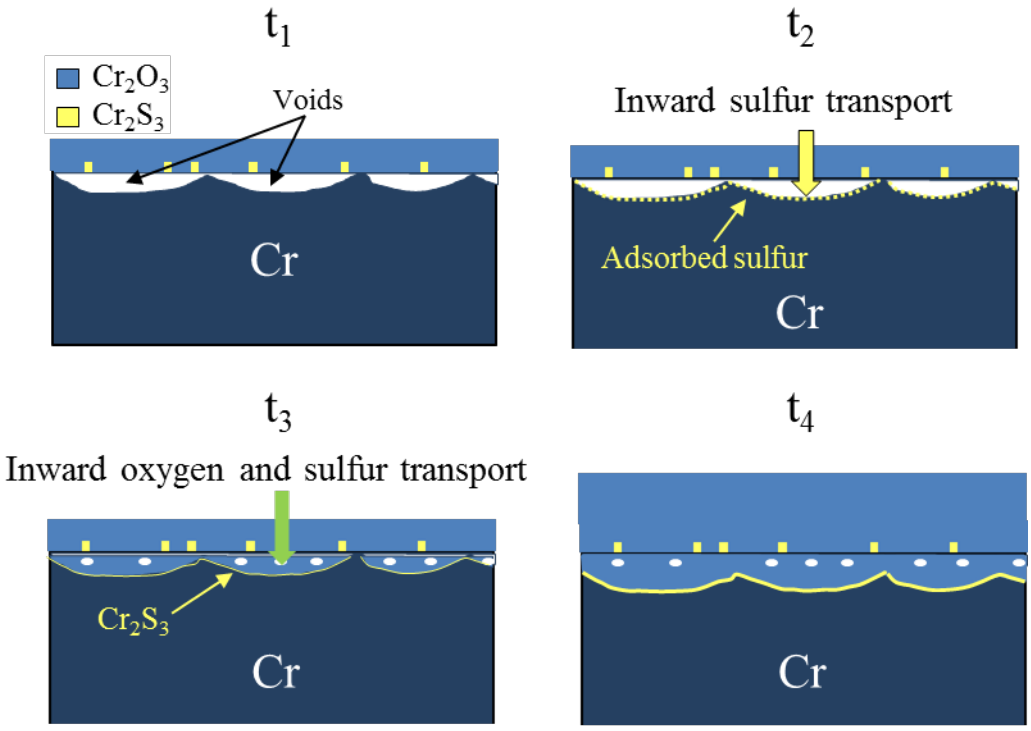

Figure 5-37 Schematic of the oxide scaling process on pure Cr in gas 2 at 871 °C

In the cases where the chromia scale grows mainly by outward chromium diffusion (especially in the absence of H_2O and at high P_{O_2} levels), formation of a large columnar grain structure is reported [94, 95, 96, 97]. Under such conditions, the oxide grains at the free surface can easily grow in size without any constraints. Similar behavior was observed in this study with the sample exposed to the dry-air atmosphere. However, comparison of the results between dry and wet atmospheres suggests that water vapor in the environment interacts with oxide grain-boundaries. According to Young [95], under wet oxidizing conditions the H_2O molecules can be adsorbed on the oxide grain boundaries and hinder their movement and grain growth. What results is a fine-grained equiaxed structure. It was also reported by Galerie et al. [101] that in the presence of water vapor and at lower P_{O_2} levels, the growth mechanism changes to mainly inward growth, possibly due to the transport of hydroxyl ions along the grain boundaries. By

contrast, in the current study, the grain structure observed in the outer scale (believed to grow mainly by outward diffusion of cations) after exposure to gas 2 was more equiaxed and the grain size was much smaller than in dry air. Indeed, adsorption of H_2O molecules may be one possibility causing the change in grain size and structure. However, the sulfur- and carbon-containing species in the environments used in this study may also be a factor by adsorbing on grain-boundaries and, thus, affecting their movement and growth. Specifically, under such conditions nucleation is favored over growth and a fine equiaxed-grained scale structure results. Competetive adsorption of different species on internal surfaces of the scale, such as grain boundaries, has been reported previously [102, 103, 104, 105]. Young and Watson [55] and Zheng and Young [54] also showed that the presence of sulfur and water vapor in the atmosphere affects the transport properties of other species, such as carbon and nitrogen, through the scale. The results observed by other researchers and those observed in this study together strongly indicate the ability of sulfur-containing species and water vapor in the gas to interact with internal surfaces of a chromia scale, to the extent that transport properties are changed and the scaling mechanism is affected. The grain-boundary diffusion contribution to the scaling kinetics will be discussed next.

5.2.2.3 Grain size effect

Although an exclusive chromia scale had formed under both gas 2 and dry air conditions, it was observed that scaling was much faster in the former. According to the TEM cross-sectional images of these two specimens, the oxide scale formed in the dry air showed large grains with a columnar morphology. In contrast, the oxide formed in the gas 2 was polycrystalline with a very small grain size. These results suggest that the faster scale growth in gas 2 proceeds to a large extent via relatively rapid grain-boundary diffusion. Considering that the oxide grew according

to parabolic kinetics in both gas 2 and dry air, the scale thickness at a given time is given by the rate law in Eq. (5-8)

According to the Wagner's theory [38], the oxidation kinetics are controlled by the transport properties of the oxide scale. As summarized by Atkinson [14] the following expression for the parabolic rate constant is related to the tracer self-diffusion coefficients D^* in the oxide (Mo_α),

$$k_P = \int_I^{II} \left(\alpha \frac{D_M^*}{f_M} + \frac{D_O^*}{f_O}\right) d\left(ln a_{O_2}\right) \tag{5-10}$$

where f is the correlation coefficient for diffusion, a_{O_2} is the molecular oxygen activity (approximately equal to the partial pressure of oxygen) and the limits of integration are the metal/scale (I) and scale/gas (II) interfaces.

In the case of Cr_2O_3-scale formation, the existing data show that the oxide itself has very good protective properties and the reported lattice diffusion coefficients are extremely low [14]. In fact, the reported diffusion coefficients are far too low to explain the oxidation rates observed for chromium under the different environments used in this study. According to the literature [14, 106, 107, 108], grain-boundary diffusion coefficients are orders of magnitude faster than the coefficients for lattice diffusion. The contribution of grain-boundary diffusion can be represented in an effective diffusion coefficient D_{eff}^* given by [109]

$$D_{eff}^* \simeq D_{Lattice} + 2\frac{(D_g\delta)^*}{g} \tag{5-11}$$

where $D_{Lattice}$ is the lattice and D_g is the grain boundary diffusion coefficient, δ is the grain boundary thickness, and g is the grain size of the oxide scale. Using Eq. 5-11 and taking $D_g >> D_{Lattice}$, the ratio of effective diffusion coefficients in gas 2 and dry air can be written as

$$\frac{D_{eff\ (gas\ 2)}^*}{D_{eff\ (dry\ air)}^*} = \frac{g_{dry\ air}}{g_{gas\ 2}} \tag{5-12}$$

for the oxide scales having grain sizes of 440 nm (gas 2) and 940 nm (dry air), this ratio is calculated to be around 2.1. However, substituting D_{eff}^{*} in Eq. 5-10 gives

$$k_P = \int_{I}^{II} D_{eff}^{*}\, d\left(ln a_{O_2}\right) \tag{5-13}$$

and knowing the scale thickness, reaction time, and partial pressures of oxygen at both interfaces, the ratio of effective diffusion coefficients in gas 2 to dry air is calculated to be 110, which is far higher than the calculated 2.1 based on the grain-size measurements. Thus, grain-boundary diffusion cannot solely account for the observed oxidation rates in gas 2. This shows that the scale formed under the conditions of gas 2 contains even faster transport pathways perhaps due to the presence of other species (sulfur or carbon containing species) in the gas affecting D_g in some way that is currently not understood in chromia scale systems.

A previous study by Heuer et al. [110] on alumina scales showed that both grain-boundary diffusion coefficients of Al (D_g^{Al}) and oxygen (D_g^{O}) are orders of magnitude larger than lattice diffusion (10^5 for Al and 10^8 for oxygen). Moreover, it was also shown that not all grain boundaries are equal when it comes to enhanced diffusion. The diffusion properties of the scale can vary according to the differences in diffusion coefficients along random high-angle grain boundaries. That study along with others [111, 112] clearly showed that oxygen diffusivities in alumina scales can vary by a factor of 10^3, depending on the grain boundary character and atomic structures. In this study, the measured grain-boundary diffusion coefficient in the chromia scale formed in gas 2 is higher than that formed in dry air atmosphere by a factor of 10^2, which is within the 10^3 range reported for diffusivities in alumina scale. Thus, it is possible that the significantly enhanced diffusion in the chromia scale formed in gas 2 could also be due to the higher diffusion coefficient of the grain boundaries aligned in the growth direction of the scale. The predominance of one orientation in the outer scale of the sample exposed to gas 2 compared

to that exposed to dry air might also be due to the sulfur presence at the internal surfaces such as grain boundaries, favoring a specific rapid transport orientation. Further investigation of these hypotheses for Cr_2O_3 scales is clearly needed.

5.2.2.4 Microstructural development in gas 3

The scale formed during exposure to gas mixture 3 contained both oxide and sulfide. The total weight gain per unit area was more than two times greater than that for gas mixture 2 (see Figure 5-25). Continuous sulfide paths through the entire scale thickness were observed, with larger sulfide grains close to the scale/gas interface. It should be noted that although the calculated equilibrium partial pressure of sulfur (P_{S_2}) is lower in gas 3 compared to gas 2, the flux of H_2S to the surface of the sample is more than three times higher, which can increase the relative amounts of sulfide formation at the initial stages compared to oxide. LaBranche and Yurek [8] previously studied the effect of P_{H_2O}/P_{H_2S} ratio on oxidation resistance of pure chromium in H_2-H_2O-H_2S gas mixtures at 900 °C. They showed that a critical value of the P_{H_2O}/P_{H_2S} ratio in the environment is necessary to promote formation of a protective Cr_2O_3 scale over the metastable sulfide. Based on their observations, this critical value of the P_{H_2O}/P_{H_2S} ratio was determined to be between 3 and 10 in the case of pure chromium at 900 °C. In this study, exposure of chromium to the gas mixture 3 with a lower P_{H_2O}/P_{H_2S} =0.5 resulted in a more aggressive attack than what was observed for gas mixture 2 with P_{H_2O}/P_{H_2S} =1.1. Even though Cr_2O_3 is still the thermodynamically more stable phase in gas mixture 3, the observed co-formation of oxide and sulfide in the outer scale indicates that the kinetic boundary of Cr-oxide/Cr-sulfide in Cr-O-S phase stability diagram is slightly shifted to the right, where gas 3 is now located on this boundary. As a result, the initially formed metastable sulfides can continue to grow due to the

kinetic factors, which will result in a fast-growing scale comprised of Cr-oxide and Cr-sulfide. The fast growth rate of the scale under such conditions is a consequence of both continuous diffusion pathway through the sulfide phase and the phase boundaries of oxide/sulfide, which can act as fast diffusion pathways.

It should also be noted that the presence of other species, most importantly carbon, can affect the oxide/sulfide transition and the corrosion mechanism. Gas 3 in this study had a higher carbon activity than that in gas 2 and a relatively deep porous inner corrosion zone was observed after 25 h exposure to gas 3. EDS measurements across the inner attack zone confirmed the formation of the Cr-carbide at the reaction front (Figure 5-36). Formation of the inner corrosion zones depends on the ability of different oxidants in the gas to penetrate the scale. It has been shown [54, 55, 63] that carbon penetrates the Cr_2O_3 scale mainly by molecular transport through internal surfaces and physical imperfections. The mixed interwoven oxide-sulfide structure of the external scale with phase boundaries aligned in the diffusion direction apparently increases the carbon permeability toward the scale/metal interface compared to only oxide grain boundaries in the sample exposed to gas 2. The increased carbon permeability led to an increase in carbon activity at the scale/metal interface, where oxygen activity is lowest. As a result, the carbide was stable to form. Finally, the sulfide also dissociated at the heavily voided metal/scale interface (formed mainly due to the rapid outward growth of the mixed scale) and released sulfur, which could also form Cr-sulfides. In accordance with the analysis presented by Meijering [113], the sequence of phases formed in the mixed inner attack zone occurred in the order of their thermodynamic stability, with the most stable phase (oxide) at the surface and the least stable (carbide) at a greater depth in the alloy. Furthermore, the higher carbon activity in gas 3 might play a more important role in changing the reaction pathways for gas 2 to gas 3 by affecting the

corrosion mechanism at initial stages of reaction. However, a clearer understanding of the effect of carbon requires further investigation.

5.3 MODEL Ni-Co-Cr ALLOYS

The first set of model alloys used in this study are two ternary Ni-Co-Cr alloys with chemical compositions of 38Ni-40Co-22Cr and 32Ni-40Co-28Cr (compositions in at.%). Based on the previous study done by Wu [70], it was shown that in Ni-Co-base alloys when the Ni:Co major-element ratio is near unity, the alloy has optimum sulfidation resistance by lowering the risk of Ni_3S_2 formation (at 750 °C). In the current study, the abovementioned ternary model alloys, both with a Ni:Co ratio close to 1 and different levels of Cr were tested at a higher temperature of 871 °C. The corrosion behavior of these alloys was studied in all five environments with different oxygen, sulfur, and carbon potentials. The results after exposure to these environments are discussed in this chapter.

Figure 5-38 summarizes the weight-gain results of the 38Ni-40Co-22Cr and 32Ni-40Co-28Cr alloys after 25 h exposure to all five environments. The lowest weight gains occurred to the samples exposed to gas 4 containing 10% water vapor. Under this condition, a protective chromia scale formed on both alloys and no further attack was observed. The highest weight gains, on the other hand, were observed for the samples exposed to gas 3 containing 3% water vapor and high sulfur and carbon activities. The complex morphological developments after exposure to these environments are discussed next.

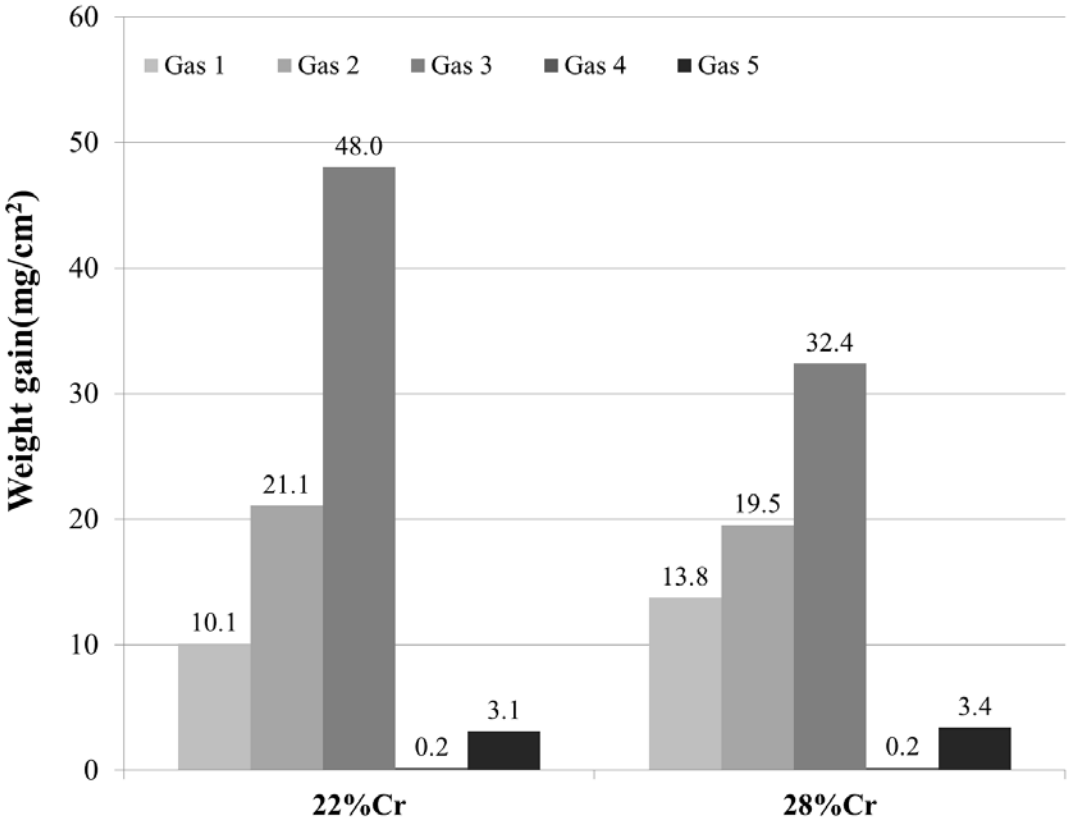

Figure 5-38 Weight change measurements of 38Ni-40Co-22Cr and 32Ni-40Co-28Cr after 25 h exposure at 871 °C

5.3.1 Sulfidation-Oxidation

Cross-sectional micrographs of both alloys after 25 h exposure to gas 1 (Figure 5-39) exhibit mainly Cr-sulfide in the outer scale with metallic Ni and Co regions at the grain boundaries. The sulfide scales on both alloys contain small amounts of Ni and Co (3-5 at. % combined). The grain boundary regions in both scales contain bright phases, which were identified as metallic nickel and cobalt. These metallic regions may have formed upon cooling due to the rejection of Ni and Co from the sulfide (i.e., solubility decreases with decreasingtemperature). The subscale region contained a substantial amount of porosity and internal chromium sulfides (58.6S-36.7Cr-2.8Co-2Ni (at. %) near the interface and 42.2S-32Cr-13.4Co-12.5Ni (at. %) at the bottom of the

internal attack area). The above results show that the composition of gas 1 is located on the left side of the Cr-sulfide/Cr-oxide kinetic boundary in Cr-O-S stability diagram (Figure 4-3) and, hence, in the sulfide stable region, where no protective oxide scale can be formed and the mode of attack is mainly sulfidation.

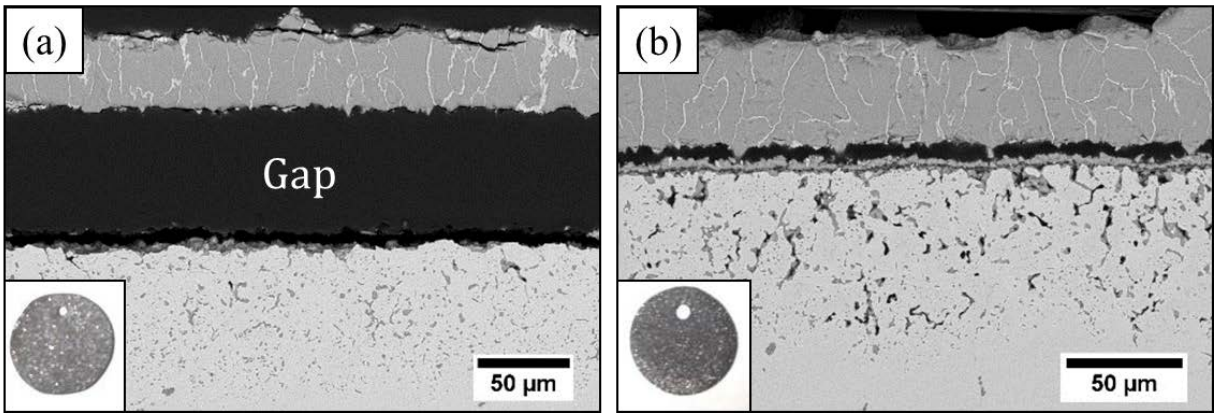

Figure 5-39 SEM cross-sectional micrographs of ternary model alloys (a) 38Ni-40Co-22Cr, and (b) 32Ni-40Co-28Cr after 25 h exposure to gas 1

Addition of 0.6% water vapor to the gas 1 (gas 2) completely changed the behavior of these alloys. Figure 5-40 shows SEM cross-sectional images of the abovementioned model alloys after 25 h exposure to gas 2. According to the EDS measurements, a Cr_2O_3 layer was formed initially on both model alloys. However, this scale was not protective enough and localized breakdown of the scale and formation of Ni_3S_2 and Co_9S_8 nodules can be observed. Cr-sulfide also formed at the scale/metal interface. The scale was again followed by a porous subscale, which also contains internal chromium sulfides. Taking a closer look at the surface images of these two samples, it is seen that a relatively large protective region of Cr-oxide still remains after 25 h exposure of the alloy with higher Cr additions of 28%. This shows the slightly better protection provided at higher levels of chromium addition.

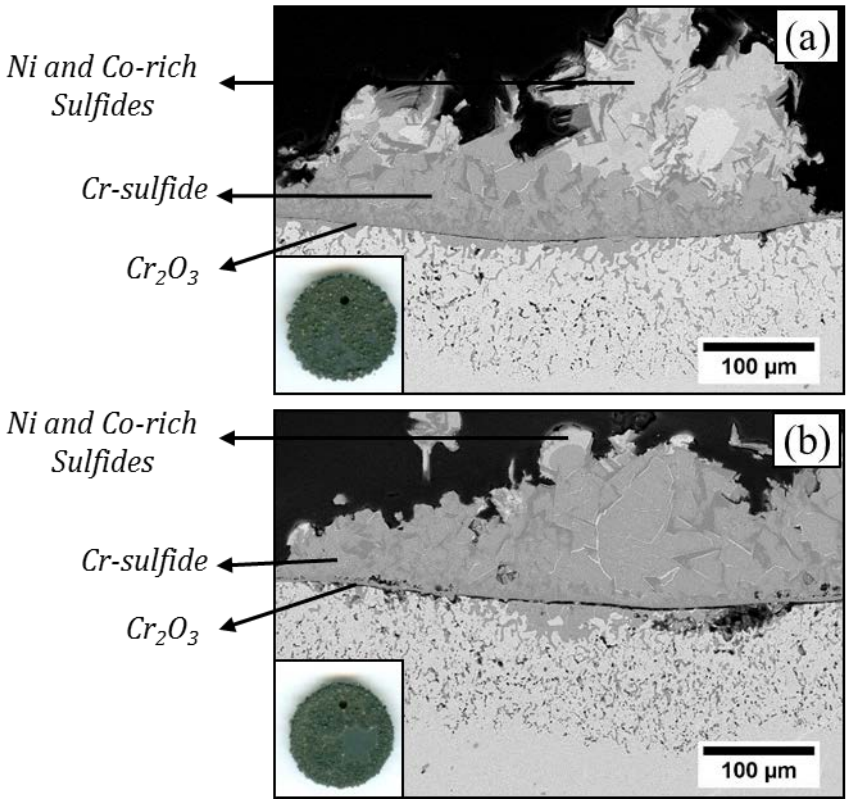

Figure 5-40 SEM cross-sectional micrographs and surface images of (a) 38Ni-40Co-28Cr, and (b) 32Ni-40Co-28Cr after 25 h exposure to gas 2

It should also be noted that although the two environments of gas 1 and 2 contain all corrosive species of oxygen, sulfur, and carbon, the carbon activity (a_C=0.2) is considerably lower than gases 3 and 4 (a_C=1, which will be studied later in this chapter). No carbide formation was observed after exposure to gas 1 or 2, although, it is possible that the amount of the carbides formed is too low to be detected with EDS. Before moving on to the more aggressive environments of gas 3 and 4, it is worthwhile to study the effect of carbon on the corrosion behavior of these alloys. The behavior of these model alloys in a carburizing environment will be studied next.

5.3.2 Carburization

In order to better understand the effect of carbon, reaction in a single oxidant (carburizing) environment was considered. The experiments were done in an Ar-H_2-C_3H_6 (gas 5) atmosphere with a carbon activity close to unity. The precipitation of Cr_3C_2 (confirmed by XRD) near the surface and the formation of internal Cr_7C_3 after carburizing of both ternary model alloys are in agreement with the results of a previous study [114], which also identified Cr_3C_2 and Cr_7C_3 in Ni-25Cr in an Ar-CH_4 environment at 850°C after 1000 h of exposure.

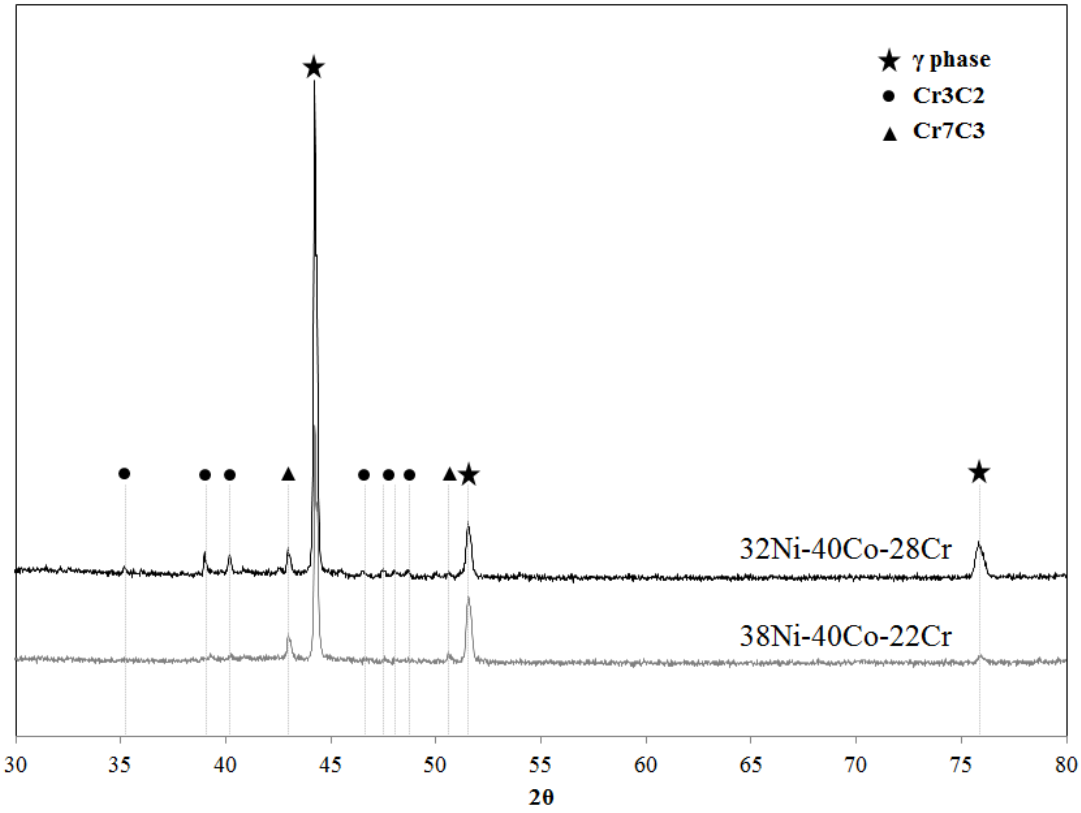

Figure 5-41 XRD spectra of the carburized surfaces of the tested model alloys

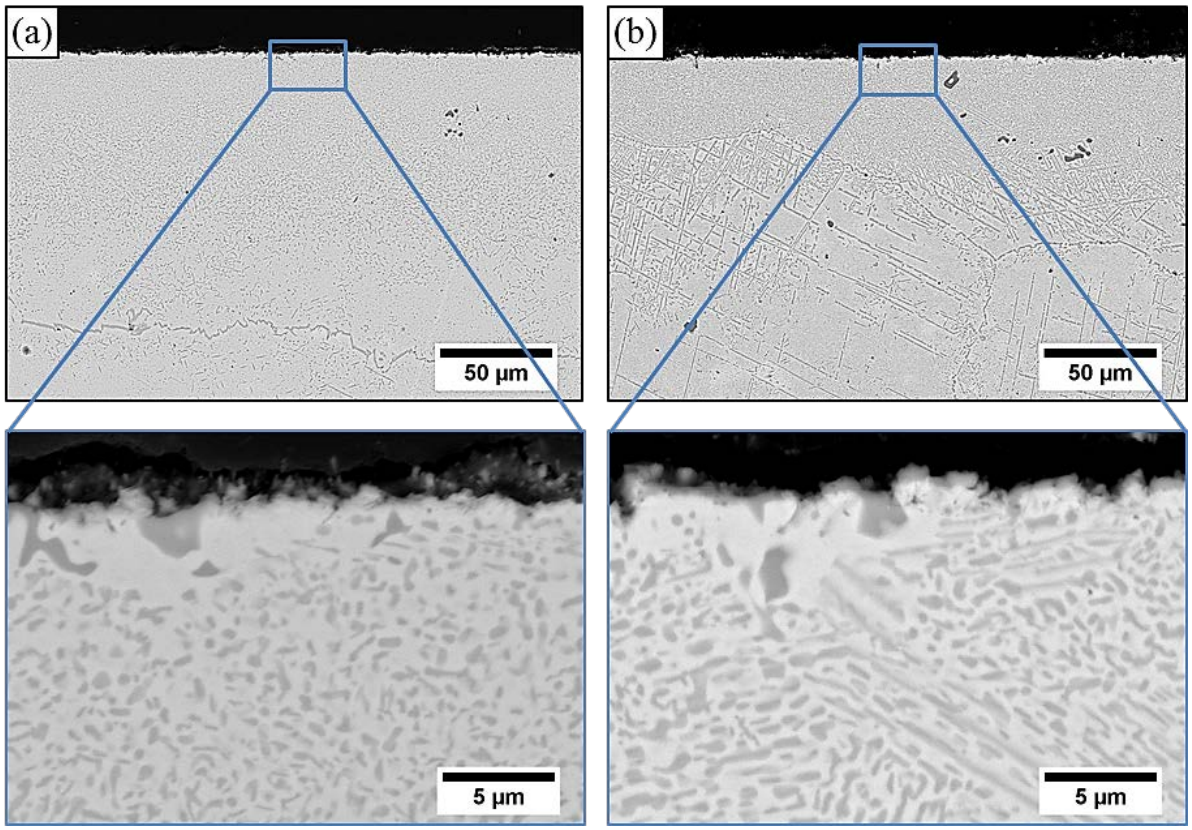

Figure 5-42 SEM cross-sectional micrographs of (a) 38Ni-40Co-22Cr, and (b) 32Ni-40Co-28Cr after exposure to gas 5 for 25 h

Figure 5-42 shows the cross-sectional images of these alloys after exposure to gas 5 for 25 h. Formation of internal Cr-rich carbides can clearly be seen. When alloys are exposed to very reducing carburizing gases similar to gas 5, no protective oxide scale can be formed. Therefore, carbon can easily diffuse into the substrate alloy and tie-up the chromium in the alloy by formation of internal Cr-carbides. The remaining substrate alloy around these carbides has very little chromium content.

As was discussed in chapter 2 of this thesis, carburization (in most cases) follows the parabolic behavior. Using the average carbon penetration depth in these alloys and Eq. 2-16, parabolic rate constants can be calculated. It has also been known that the rate at which the carbide precipitation zone deepens is given by Eq. 5-1. Accordingly, the k_P and carbon

permeability in both alloys were calculated and are reported in Table 5-3. Comparison of the calculated permeability with values found in the literature for Ni-20Cr [13] shows that they are approximately in agreement with each other. Thus, it can be concluded that the internal carburization of these Ni-Co-Cr alloys are controlled by lattice diffusion of carbon through the depleted metal matrix.

Table 5-3 Comparison of experimentally determined carbon permeabilities $N_C^{(s)}D_C$ ($cm^2.s^{-1}$) for alloys 1 and 2 in comparison with the calculated values from the literature [13]

Alloy	800°C	871°C		900°C
	$N_C^{(s)}D_C$ ($cm^2.s^{-1}$)	k_P ($cm^2.s^{-1}$)	$N_C^{(s)}D_C$ ($cm^2.s^{-1}$)	$N_C^{(s)}D_C$ ($cm^2.s^{-1}$)
38Ni-40Co-22Cr	-	3.5×10^{-10}	5.5×10^{-10}	-
32Ni-40Co-28Cr	-	3.2×10^{-10}	6.3×10^{-10}	-
Ni-20Cr [13]	0.8×10^{-10}	-	-	8×10^{-10}

5.3.3 Sulfidation-Carburization-Oxidation

As was discussed in previous chapter, gas composition 1 and 2 are similar to the atmosphere that exists in a low NO_x burner, which has both sulfur and carbon; however, carbon activity is either too low to form the carbides or the amount of carbide formed internally is far too low to be detected. Other environments such as those for coke production or coal gasification contain a higher amount of carbon. The next environment (gas 3) represents the simulated coke production oven atmosphere, which has high activity of both sulfur and carbon and was previously used by Harper et al. [69].

Figure 5-43 shows cross-sectional images of ternary model alloys after 25 h exposure to gas 3. Extensive degradation was observed on both alloys. However, the internal attack on the alloy with 22%Cr was much more severe. Islands of Cr-sulfide at the surface followed by dispersed chromia particles at the alloy/scale interface and internal attack zone consisting of Cr-sulfide, Ni- and Co-rich sulfides and metallic Ni and Co areas can be observed on alloy 38Ni-40Co-22Cr. It is recalled again that the main difference between gas 2 and 3 is increasing the carbon activity from 0.2 in gas 2 to about 1 in gas 3. However, due to the nature of the multi-oxidant environments, it is difficult to keep the oxygen potential constant while increasing the carbon activity and, thus, the oxygen potential in gas 3 is also slightly lower than in gas 2.

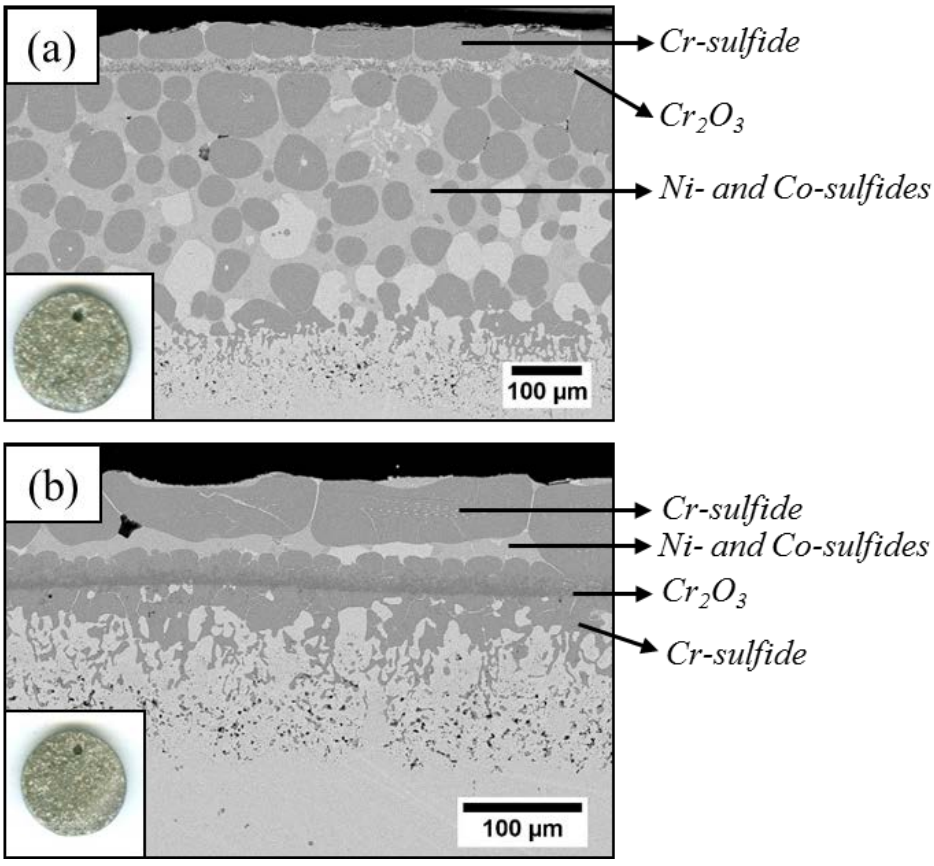

Figure 5-43 SEM cross-sectional micrographs of alloy (a) 38Ni-40Co-22Cr, and (b) 32Ni-40Co-28Cr after 25 h exposure to gas 3

In order to further investigate the mechanism of formation of such complex structure in gas 3, a time study was also done with alloy 38Ni-40Co-22Cr. Figure 5-44 shows the weight gains of the samples after different exposure times. The corresponding surface SEM images of these samples after each exposure time is also shown in Figure 5-45. After 1 h exposure the surface mainly consists of Cr-oxide, Cr-sulfide and some Ni- and Co-rich sulfide nodules. These sulfide nodules tend to grow with time and cover the surface up to about 17 h. After 25 h, however, the surface microstructure is different and mainly consists of islands of Cr-sulfide with Ni- and Co-rich sulfides in between, on the boundaries.

Figure 5-46 shows cross-sectional micrographs of alloy 38Ni-40Co-22Cr after different exposure times. It can be seen that for up to 10 h of exposure, the microstructure of the corroded sample is similar to that observed under gas 2 conditions. Formation of a mixed Cr-oxide and Cr-sulfide layer was observed after 1 h. Localized breakdown of this scale and formation of nodules of Ni- and Co-rich sulfides was also observed. These nodules grew with time and similar structures were observed up to 10 h. However, after 17 h exposure, the sample went through severe localized internal attack, developing a similar structure to the sample after 25 h exposure.

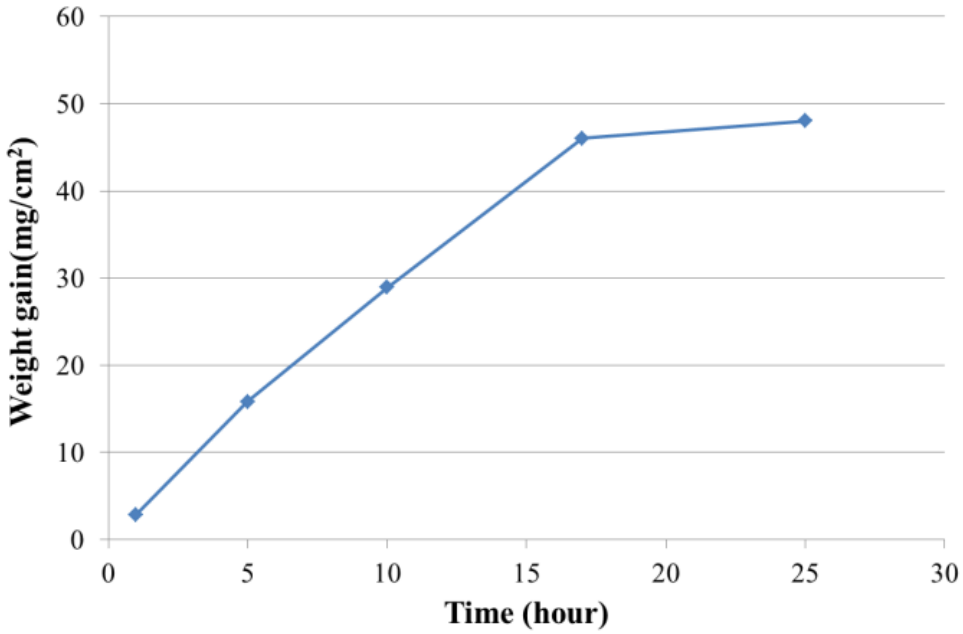

Figure 5-44 Weight change per unit area as a function of time for alloy 38Ni-40Co-22Cr in gas 3 at 871°C

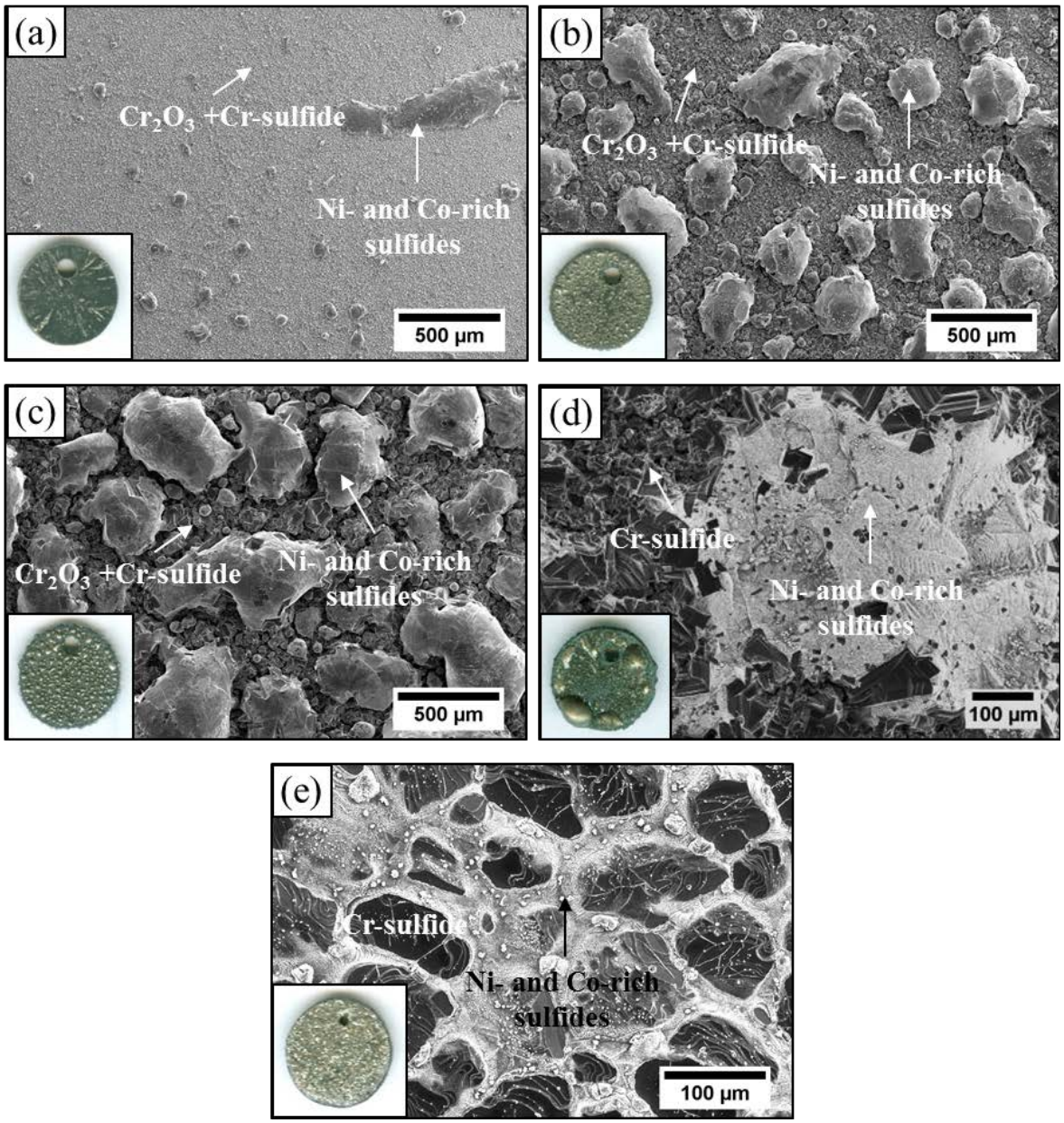

Figure 5-45 SEM surface images of alloy 38Ni-40Co-22Cr after exposure to gas 3 for (a) 1 h, (b) 5 h, (c) 10 h, (d) 17 h and (e) 25 h

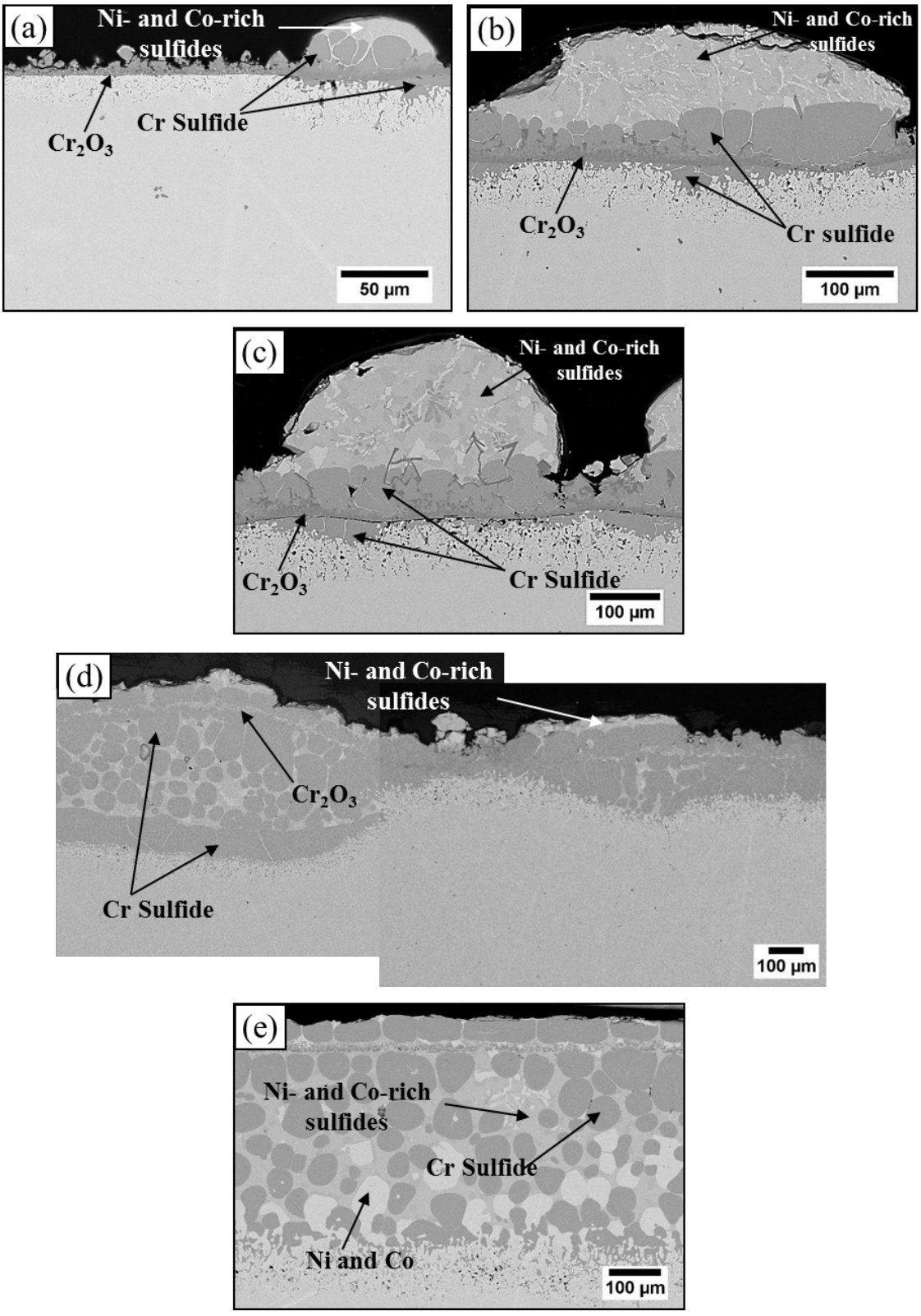

Figure 5-46 SEM cross-sectional micrographs of alloy 38Ni-40Co-22Cr after exposure to gas 3 for (a) 1 h, (b) 5 h, (c) 10 h, (d) 17 h, and (e) 25 h.

Comparison of the results after exposure to the gas 3 environment with previous results observed after exposure to gas 2, showed a major difference in corrosion mechanisms. As it was mentioned before, the gas 3 environment has a higher carbon activity and slightly lower oxygen activity compared to gas 2. Therefore, in order to clarify the role of carbon in changing the reaction mechanism when changing from gas 2 to gas 3, a two-step test was performed. In this new experiment, alloy 38Ni-40Co-22Cr was first exposed to the carburizing gas 5 for 5 h followed by 20 h exposure to gas 2 with high sulfur but lower carbon activity. Figure 5-47 shows the microstructure of the corrosion products after the total 25 h reaction time. A similar structure to the one after exposure to gas 3 was observed, with the formation of islands of Cr-sulfide surrounded by Ni- and Co-rich sulfides. Cr-rich carbide precipitates can also be seen at the reaction front. A higher magnification image of the reaction front clearly shows the transformation of these carbides, which is believed to be formed during the 5 h exposure to gas 5, to Cr-sulfide. These sulfide particles tend to coarsen with time and further transform to the large sulfide islands, which can be observed at the top.

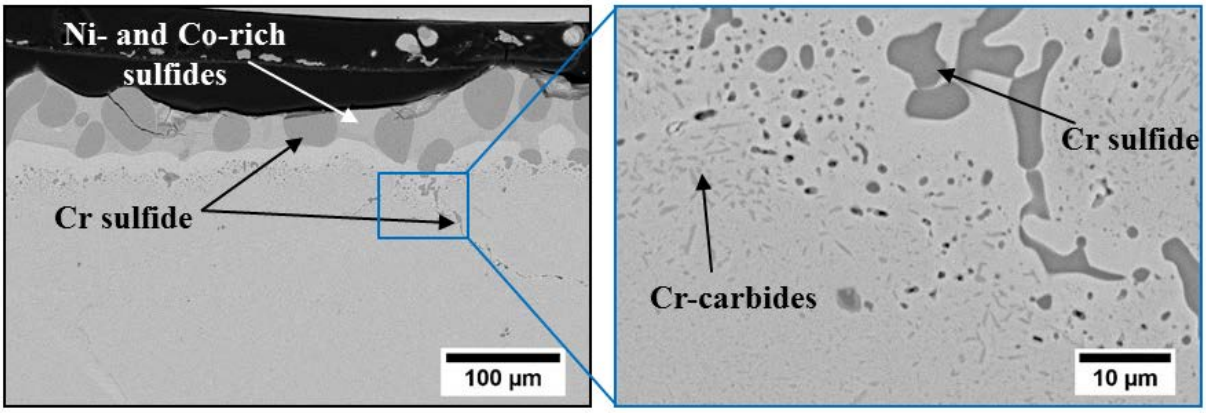

Figure 5-47 SEM cross-sectional micrographs of alloy 38Ni-40Co-22Cr after exposure first to carburizing gas (gas 5) for 5 h, followed by exposure to sulfidizing-oxidizing gas (gas2) for 20 h at 871°C

The results observed after exposure of these alloys to gas 4 (Figure 5-48) containing 10% water vapor showed the formation of protective chromia scale on both alloys and no sulfidation or carburization attack was observed (similar to the results of pure chromium in the same gas). It can, therefore, be concluded that under conditions of gas 4 the flux of H_2O to the surface of the sample is much higher than H_2S and the mode of attack is mainly oxidation. Thus, in the next set of experiments gas 4 will not be considered.

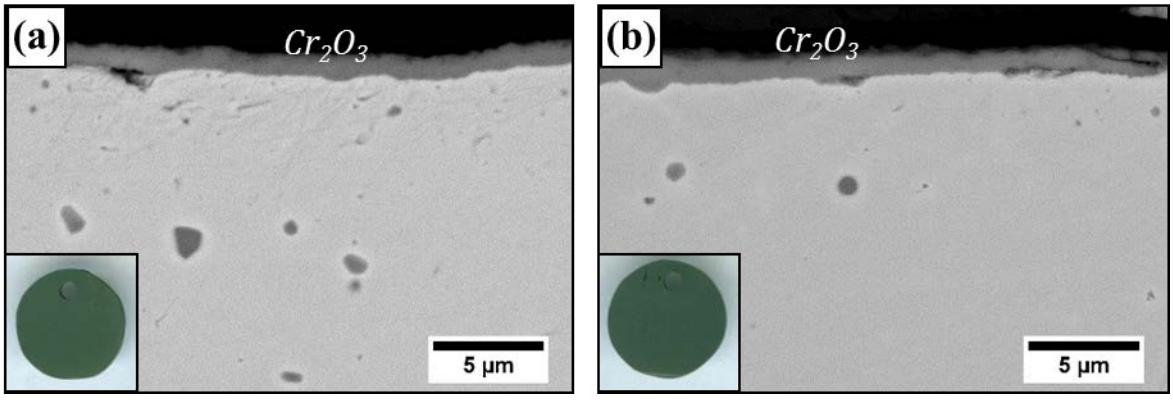

Figure 5-48 SEM cross-sectional micrographs of alloy (a) 38Ni-40Co-22Cr and (b) 32Ni-40Co-28Cr after 25 h exposure to gas 4

5.3.4 Discussion

The results obtained after exposure of pure Cr to gas 2 mixture previously showed that the composition of this gas is close to the oxide/sulfide kinetic boundary in the Cr-O-S phase stability diagram, but still in the oxide stable region. The observed behavior of ternary model alloys in the same environment also shows that a chromia scale initially developed on both alloys. However, the results after 25 h clearly show the localized breakdown of the oxide scale and outburst of sulfides, similar to the results previously reported by Giggins et al. [57]. Figure 2-19 shows the reaction path they proposed for a similar system of Ni-30Cr in H_2S-H_2O-H_2 gas mixture. It was shown that during the initial stages of corrosion, Cr_2O_3 formed at the surface. As the Cr_2O_3 layer grows, sulfur can apparently penetrate through this scale toward the scale/alloy interface, likely by a short-circuit mechanism as discussed in Chapter 2.3.1 (grain boundaries or defects such as cracks or pores in the oxide scale). As a result, Cr-sulfides can eventually start to form beneath the Cr_2O_3 scale. Formation of rapidly growing sulfides beneath the oxide scale can gradually breakdown the oxide scale and cause the rapid outward growth of sulfides. Since transport through the sulfide phase is faster and, more importantly, due to the formation of the oxide/sulfide boundaries, base-metal elements can now transport to the scale/gas interface at a faster rate. Similar mechanisms have been proposed by others [115, 116], in which rapid sulfidation initiates on a sample when continuous sulfide channels across the oxide scale forms. The localized scale breakdown eventually leads to the formation of Ni- and Co-sulfides. Due to the low eutectic temperatures of Ni and Co and their sulfides, the reaction products tend to be liquid and in the shape of nodules. Cr-sulfide at the bottom of these nodules will continue to grow rapidly due to Cr enrichment owing to the rapid and selective Ni and Co sulfidation and form large islands of Cr-sulfide above the initially formed Cr_2O_3. Based on the weight gains of

these samples and surface images after 25 h (Figure 5-40), it can be seen that the alloy with higher chromium content experienced less localized attack compared to the one with lower chromium, which shows that better protection can be provided at higher levels of chromium addition.

The two model alloys showed completely different behavior in gas 3 with the higher carbon activity. The results clearly show that carbon is playing an important role in changing the reaction pathways in gases 2 and 3. Therefore, it is necessary to answer two main questions that will arise from these observations: First, what is exactly the role of carbon on alloy degradation in gas 3 compare to gas 2? Second, what is the mechanism of formation of the observed globular structure on alloy 38Ni-40Co-22Cr? New experiments were designed in order to better understand the effect of carbon and corrosion mechanism of these alloys in gas 3.

In the new set of experiments, alloy 38Ni-40Co-22Cr was first exposed to the carburizing gas 5 for 5 h followed by 20 h exposure to gas 2 with high sulfur but lower carbon activities and the results were presented in Figure 5-47. It was shown that the microstructure of the corroded alloy after the two-step test was similar to the structure of the sample exposed to gas 3 for 25 h. Formation of Cr-sulfide islands surrounded by Ni- and Co-rich sulfides was observed. Cr-rich carbide precipitates can also be seen at the reaction front. Carburization behavior of these alloys in pure carburizing gas was previously discussed. As was shown (Figure 5-42), when carbon is present in the environment, it can react with Cr in the alloy and form internal carbides. As a result, in environments similar to gas 3, where carbon activity is high, carbon can immediately react with Cr in the alloy and tie-up chromium in the form of carbides at initial stages of the reaction and, thus, decrease the Cr available in the alloy matrix for formation of a chromia scale. It should also be noted that the gas 3 environment also has a high sulfur potential and, more

importantly, low P_{H2O}/P_{H2S} ratio (compared to gas 2). Therefore, the amount of initially-formed sulfides is also higher than in the gas 2. As a result, it would be much more difficult to form a protective chromia scale in gas 3 compared to gas 2. In the absence of a protective chromia scale, sulfur can easily react with the depleted substrate alloy and form sulfides. As the sulfur activity within the alloy increases, the previously-formed carbides will also transform to sulfides. As a result, carbon is released into the alloy, which can again react with chromium to form chromium carbides. This will cause further chromium depletion in advance of the sulfide layer. The transformation between carbides and sulfides can happen relatively fast, causing the formation of the internal chromium sulfides and leaving the depleted substrate alloy, rich in nickel and cobalt (both susceptible to forming sulfides), in direct contact with the highly sulfidizing environment. Consequently, sulfides of Ni and Co start to form. Due to the low eutectic temperatures of these sulfides and their metals, at the test temperature of 871°C these corrosion products are liquid. The liquid sulfides surround the previously formed Cr-sulfide particles. At the same time, the mixture undergoes a coarsening process driven by the curvature of the particles. In accordance with particle coarsening behavior [117], larger particles of Cr-sulfide with a low interfacial curvature grow at the expense of smaller particles with a high curvature. Thus, the average sulfide particle size increases with time.

Knowing the effect of carbon in changing the reaction pathway in environments similar to gas 3, we are now in a position to address the formation mechanism of the observed structure after 25 h exposure to this gas. Figure 5-49 shows the schematic of the proposed mechanism. At the initial stages of the reaction, carbon can tie-up the chromium at the surface in the form of carbides (as discussed before). This will cause lowering the Cr available in the alloy matrix for formation of a protective oxide. As a result, a mixed Cr-oxide and sulfide layer forms on the

alloy surface. As this layer grows, sulfur can diffuse from the environment to the alloy/scale interface, where the Cr activity is higher and form internal Cr-rich sulfides (also transforming the previously formed carbides into the sulfides). On the other hand, sulfides of Cr can grow outward faster than the oxide and so the former begin to form on top of the oxide layer. The many oxide/sulfide boundaries that develop in the scale coupled with any defects in the scale, ultimately facilitates sulfidation of the base metal elements of Ni and Co. The fast-growing sulfides of Ni- and Co evolve to be present at the product surface. Since they are liquid at the temperature of reaction (low-melting point eutectics) and due to a low degree of wetting (at least initially), they tend to form nodules at the surface. At the bottom of these nodules, Cr-sulfide phases begin to grow rapidly by reduction of the base metal sulfide and form large islands of Cr-sulfide. These nodules continue to grow and finally they merge. As a result, the surface of the sample becomes entirely covered by liquid Ni- and Co-rich sulfides.

Looking at the cross-sectional observations (Figure 5-46), it is seen that the liquid sulfide nodules are initially separated and do not wet the surface of the scale (mixed Cr-oxide and Cr-sulfide). However, as mentioned before, these nodules and Cr-sulfide at the bottom of them tend to grow by time and after certain amount of time, they merge. At this point, it can clearly be seen that the liquid sulfide completely wet the surface of the Cr-sulfide layer, tending toward a continuous layer. Thus, there should exist a certain amount of Cr-sulfide at the scale that changes the behavior of the liquid Ni+Co sulfide from non-wetting to complete wetting of the surface. The ability to wet is controlled by the conditions of minimum interfacial energy between solid-solid and solid-liquid interfaces. If the "wetting angle," between the liquid sulfide and the solid Cr-sulfide at the bottom is less than a certain value, the solid Cr-sulfide will be "wetted" by the liquid sulfide, that is, the liquid sulfide phase will form an interconnected network within the

solid Cr-sulfide layer. It should be noted that most of the transition metal sulfides (Ni, Co, Fe, and Cr) usually adopt the NiAs structure [13] (hexagonal close packed with Ni at octahedral sites and As at trigonal sites). All different types of Cr-sulfides (CrS, Cr_3S_4, and Cr_2S_3 at high temperatures) can also be considered as defective NiAs structures [13, 118]. Cr_2O_3, by contrast, has a corundum structure (hexagonal close packed with Cr atoms at octahedral sites and O at tetrahedral sites). In addition, difference in the anion size causes the metal-sulfur bonds to be longer than metal-oxygen bonds and, thus, smaller lattice energy for sulfides is expected [13]. Considering all the abovementioned differences between Cr-sulfide and Cr-oxide, a considerable difference in their surface energies is also expected. The exact values for the surface energies of Cr-oxide and Cr-sulfide are not available to the best of our knowledge; however, the observed results clearly demonstrate that the liquid sulfide can easily wet the Cr-sulfide layer beneath and form the interconnected network within the Cr-sulfide layer that is observed in the current results. Considering the crystal structure of these sulfides, the values of the calculated densities (CrS=5.37 $g.cm^{-3}$ and Ni_3S_2=5.82 $g.cm^{-3}$) suggest that Cr-sulfide tends to have slightly lower density than Ni-sulfide. Consequently, the islands of Cr-sulfide start to float in the liquid sulfide and separate from the alloy/scale interface, as indicated in Figure 5-49 (25 h). When this happens, the remaining Cr-oxide particles at the alloy/scale interface cannot protect the substrate alloy from the liquid sulfide attack and rapid internal sulfidation attack can occur on the substrate alloy.

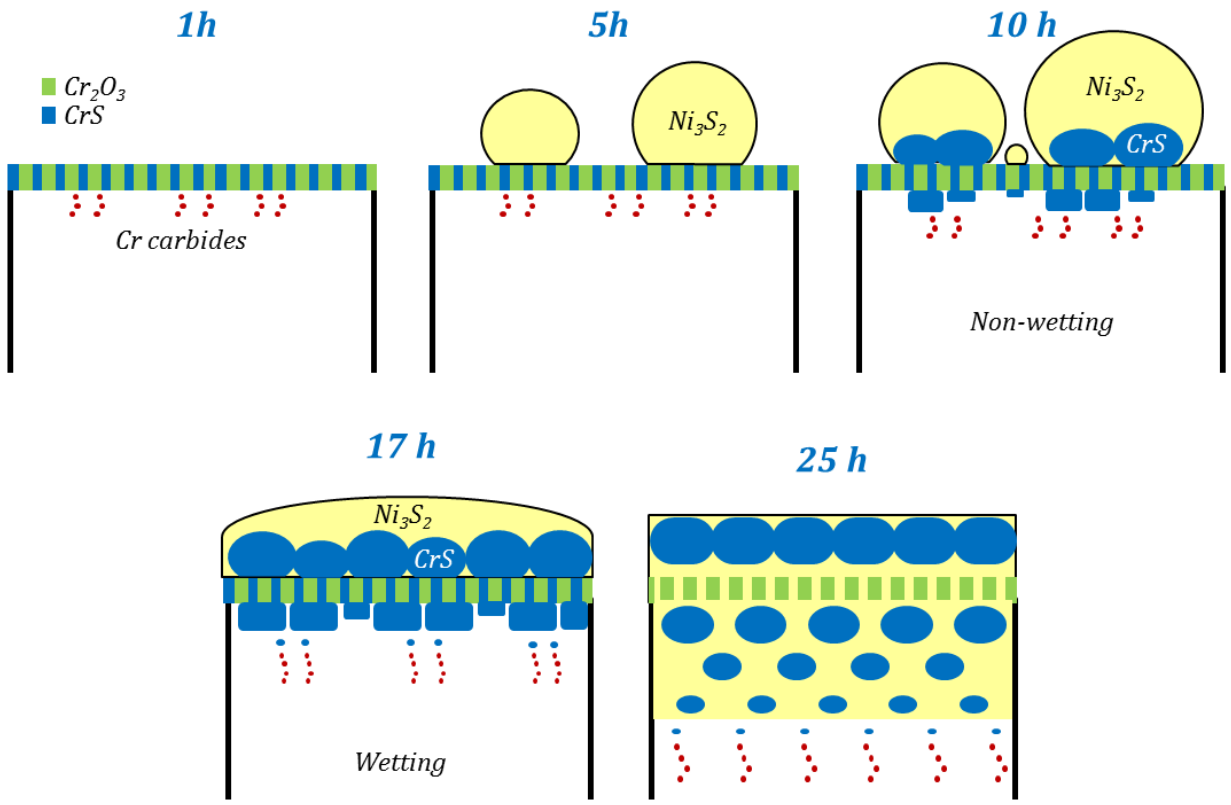

Figure 5-49 Schematic of proposed mechanism for corrosion of Ni-Co-Cr alloys under reducing conditions of gas 3 with high sulfur and carbon activities

Taking a closer look at the results for both alloys in the gas 3 environment, it can be seen that the internal attack observed on the alloy with 28%Cr is much less than the alloy with 22%Cr and it mainly consists of Cr-sulfide and no Ni- or Co-rich sulfides were observed. High magnification images of alloy/scale interface in both alloys show that the initial oxide formed at this boundary is more continuous on the alloy with higher Cr content and after 25 h of reaction sulfides of chromium still exist in contact with the oxide at the interface. Thus, the substrate alloy is protected from liquid sulfide attack by this mixed layer. These results clearly show the beneficial effect of higher chromium additions in ternary Ni-Co-Cr model alloys. However, the degradation is still severe on both alloys. As a result, minor alloying elements were added to

these alloys in order to further stabilize the formation of a protective oxide scale. The effect of these minor alloying element additions will be discussed next.

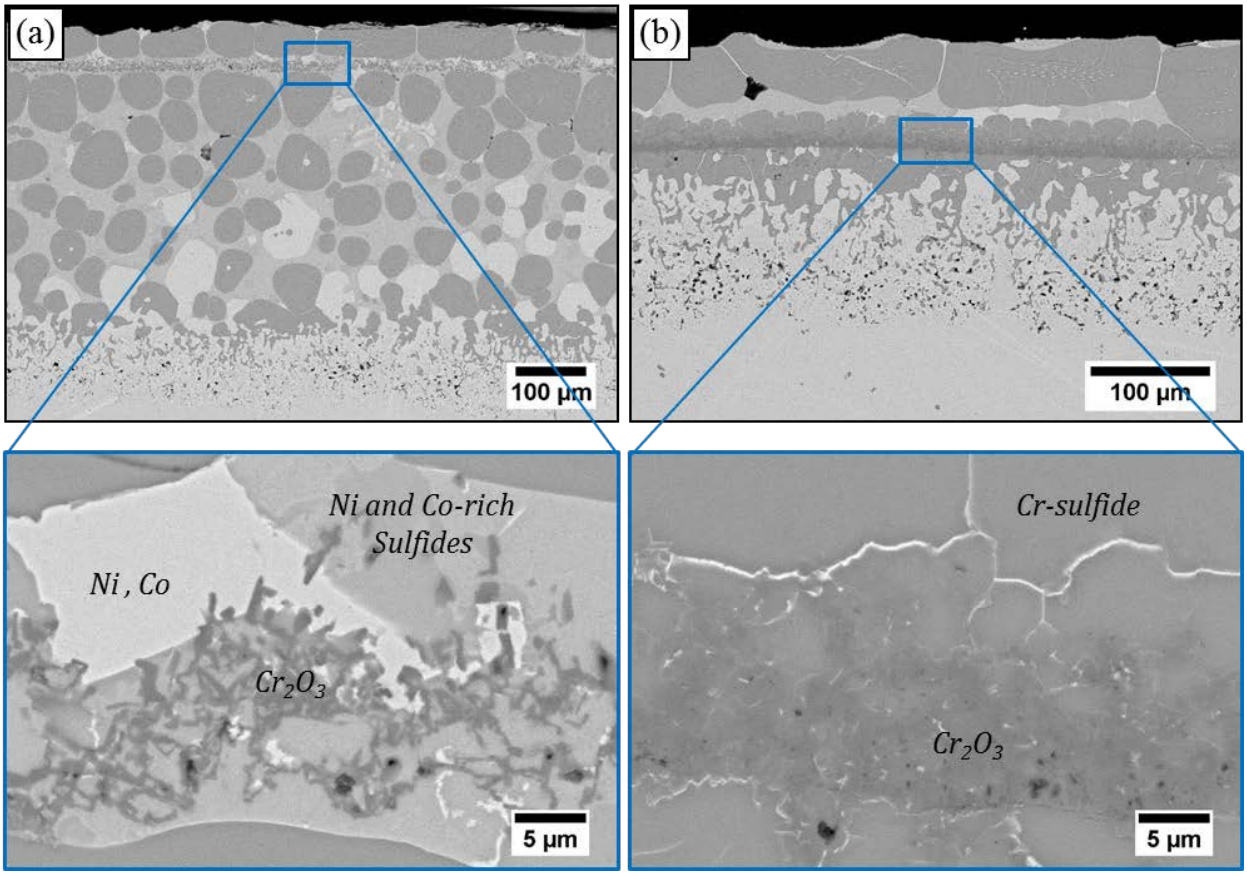

Figure 5-50 SEM cross-sectional micrographs of the alloy/scale interface of alloy (a) 38Ni-40Co-22Cr and (b) 32Ni-40Co-28Cr after 25 h exposure to gas 3

5.4 MINOR ALLOYING ELEMENT EFFECT

Discussed findings on both commercial (Chapter 5.1) and ternary model alloys (Chapter 5.3) showed that the alloy chemistry plays an important role on corrosion behavior. It was observed that alloys with higher Ni and Co contents, such as HR160 and 617, show better resistance in

both sulfidizing and carburizing atmospheres. It was also shown that in ternary model alloys, increasing the Cr content is a beneficial way to increase the resistance to sulfidation. However, alloys such as 214, 617 and 625 clearly showed that it is possible to have a better sulfidation resistance with lower Cr content via the addition of minor alloying elements that can help the chromia-scale growth. On the other hand, it was shown that alloys with higher Al or Si contents have better carburization resistance. Based on these findings, eight model alloys were designed in order to systematically study the effect of both major (Ni, Co, and Cr) and minor (Al, Ti, Mo, and Si) alloying elements. In the current chapter, the behavior of these model alloys in the different environments of gas 2, 3 and 5 will be presented and discussed.

5.4.1 Sulfidation-oxidation

5.4.1.1 Model alloys with minor alloying elements of Al, Ti, and Mo

Weight-gain measurements for up to 100 h exposure to gas 2 for the first set of model alloys (alloys 1, 2 and 3), containing similar Al, Ti, and Mo contents, are shown in Figure 5-51. The effect of Ni:Co ratio and Cr content of the alloy on corrosion behavior in the presence of the abovementioned minor alloying elements is the focus of this chapter. The beneficial effect of these elements on sulfidation behavior of Ni-Co-base alloys at lower temperatures of 750 °C was previously shown by Wu et al. [70]. However, the extent of attack was observed to be much higher at 871 °C. Among these alloys, alloy 3 showed the lowest weight gain. The main difference between alloy 3 and the other two alloys is the lower Ni:Co ratio and Cr concentration in alloy 3. By lowering the Ni:Co ratio from 2.9 in alloy 1 to 0.95 in alloy 3, weight gain decreased from 28 to 22 mg/cm^2. It can also be seen that after 25 h exposure, mass gain data for alloy 2 increases rapidly between 25 h and 50 h exposures, which can be a sign of breakaway

corrosion and the formation of fast-growing sulfides. Although the Cr content in alloy 2 is 28% and higher than both alloys 1 and 3, it is clear that the incubation period for alloy 2 is shorter under these conditions.

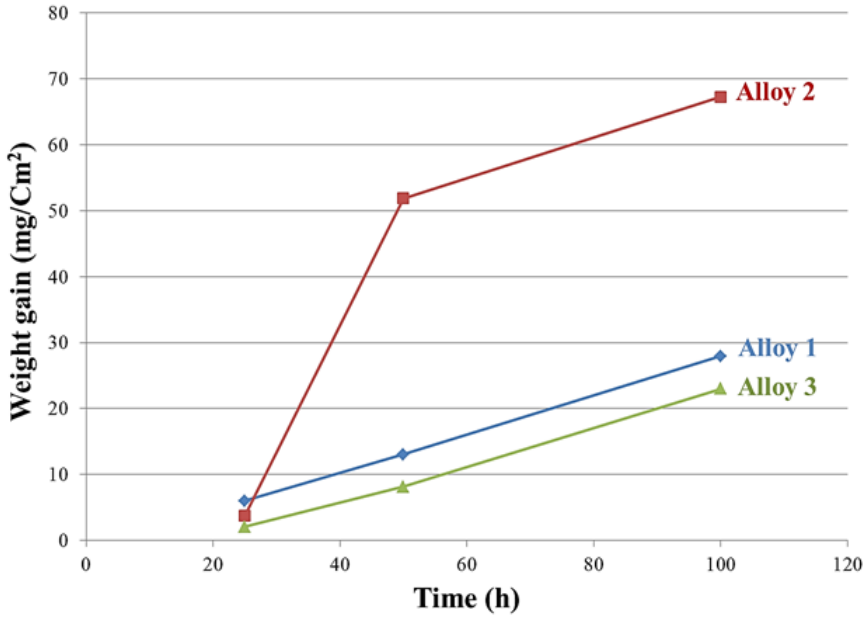

Figure 5-51 Weight change measurements of model alloys 1, 2, and 3 after 100 h exposure to gas 2 at 871°C

X-ray diffraction analyses of the scales formed after 50 h exposure to gas 2 (Figure 5-52) revealed the formation of chromia as the major phase present on all three alloys. The other phases detected were Ni_3S_2, Co_9S_8. These sulfides were predominant phases on alloy 2 with high Cr content (28%) after 100 h exposure and exist in the form nodules on the surface, which can be seen in Figure 5-53. Ni- and Co-rich sulfide nodules had grown and covered the surface of alloy 2 at most parts. They also appeared around the edges and on the casting defects in alloys 1 and 3. Dense chromia scales were observed in the bulk of alloys 1 and 3, which are in agreement with the XRD results.

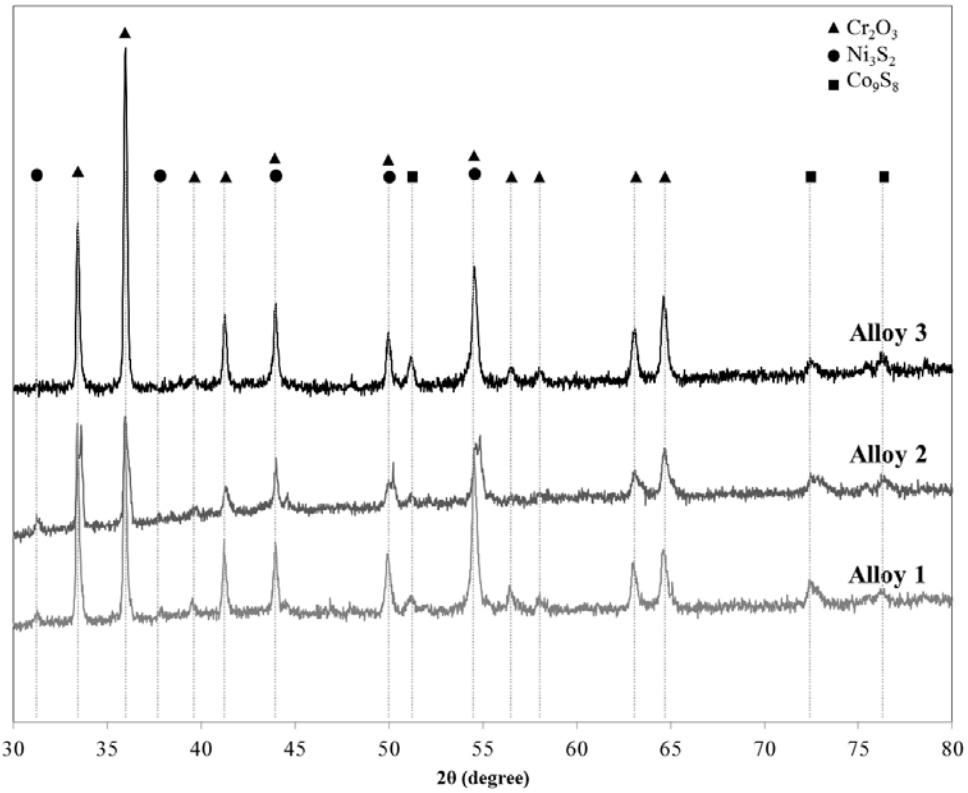

Figure 5-52 XRD spectra of the Model alloys 1, 2, and 3 after 50 h exposure in gas 2 at 871 °C

Cross-sectional micrographs of these three model alloys after 100 h exposure to gas 2 are presented in Figure 5-53. Excluding the sulfides formed around the edges of the samples and on the casting defects at the center, alloys 1 and 3 both showed intrinsically protective behavior. Any edge effects will not be considered in this study since many factors can affect the behavior of the alloy at the edge. Formation of an adherent and continuous chromium-rich oxide at the surface followed by internal alumina subscale provided good resistance to sulfidation for these alloys at the reaction temperature of 871 °C.

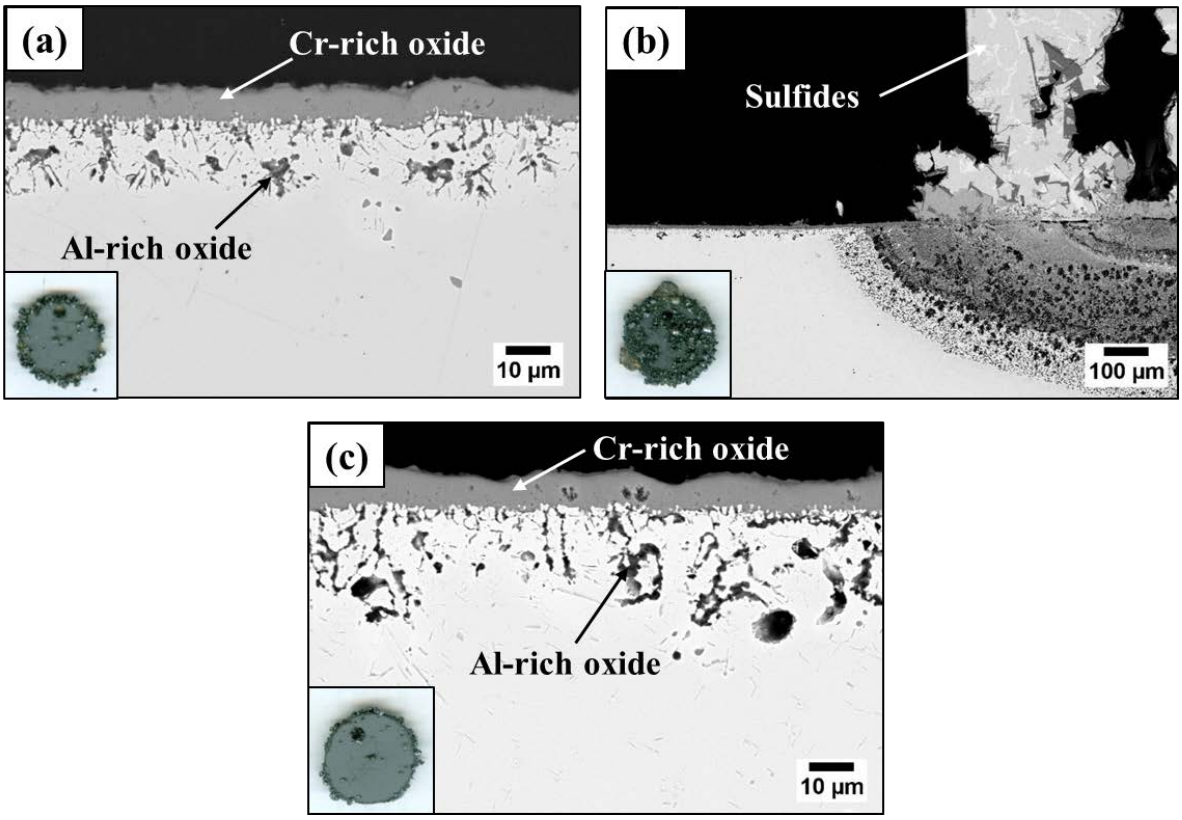

Figure 5-53 Scanning electron micrograph of cross-sections and EDS analysis of scale formed on (a) alloy1, (b) 2, and (c) 3 after 100 h exposure to gas 2 at 871 °C

Further detailed analysis of the scale formed on alloy 3 was done using scanning transmission electron microscopy (STEM) (Figure 5-54 and Figure 5-55). EDS analysis showed that the outermost surface contained crystals of TiO_2. The thicker chromium-rich oxide layer was characterized as chromia followed by internal Al_2O_3 at alloy/scale interface. The cross-sectional micrographs also demonstrate that after 100 h, the metal/scale interface is not planar and some protuberances of substrate alloy into the oxide scale can be observed. These protuberances generally consist of metallic regions rich in Ni and Co which may have been developed due to the undercutting by oxide formation or actual protuberances formed by outward alloy creep as a result of the internal oxide formation [119].

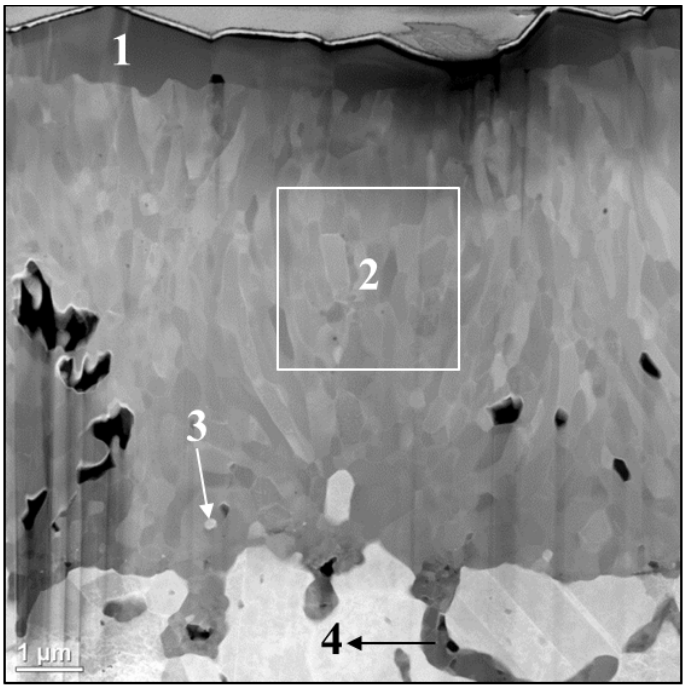

	O	Al	S	Ti	Cr	Co	Ni	Mo
1	66.2	-	-	31.4	2.3	-	0.1	-
2	65.7	-	-	0.8	33.3	0.1	-	-
3	9.2	0.2	49.1	0.3	39.4	0.5	0.4	0.9
4	57.1	42.5	-	-	0.2	-	0.1	-

Figure 5-54 STEM micrograph of the cross-section of alloy 3 after 100 h exposure to gas 2 at 871 °C

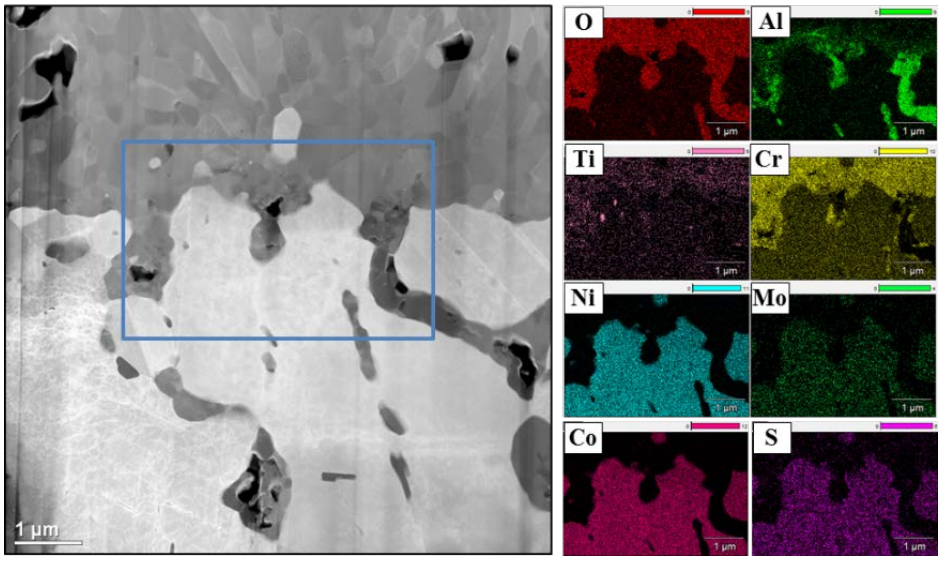

Figure 5-55 STEM micrograph and EDS maps of the cross-section of alloy 3 after 100 h exposure to gas 2 at 871 °C

No sulfide could be detected at the scale/gas interface or in the scale formed after 100 h exposure. Thus, it is possible that sulfides formed under these conditions are isolated at the metal-scale interface. It should be noted that since the sulfur K lines and molybdenum L lines in the EDS spectra both exist at about 2.3 keV, it is difficult to distinguish between them. Therefore, cross-sections on the scales of all three alloys in the protective region were examined using an electron probe micro-analyzer (EPMA) equipped with WDS (Figure 5-56).

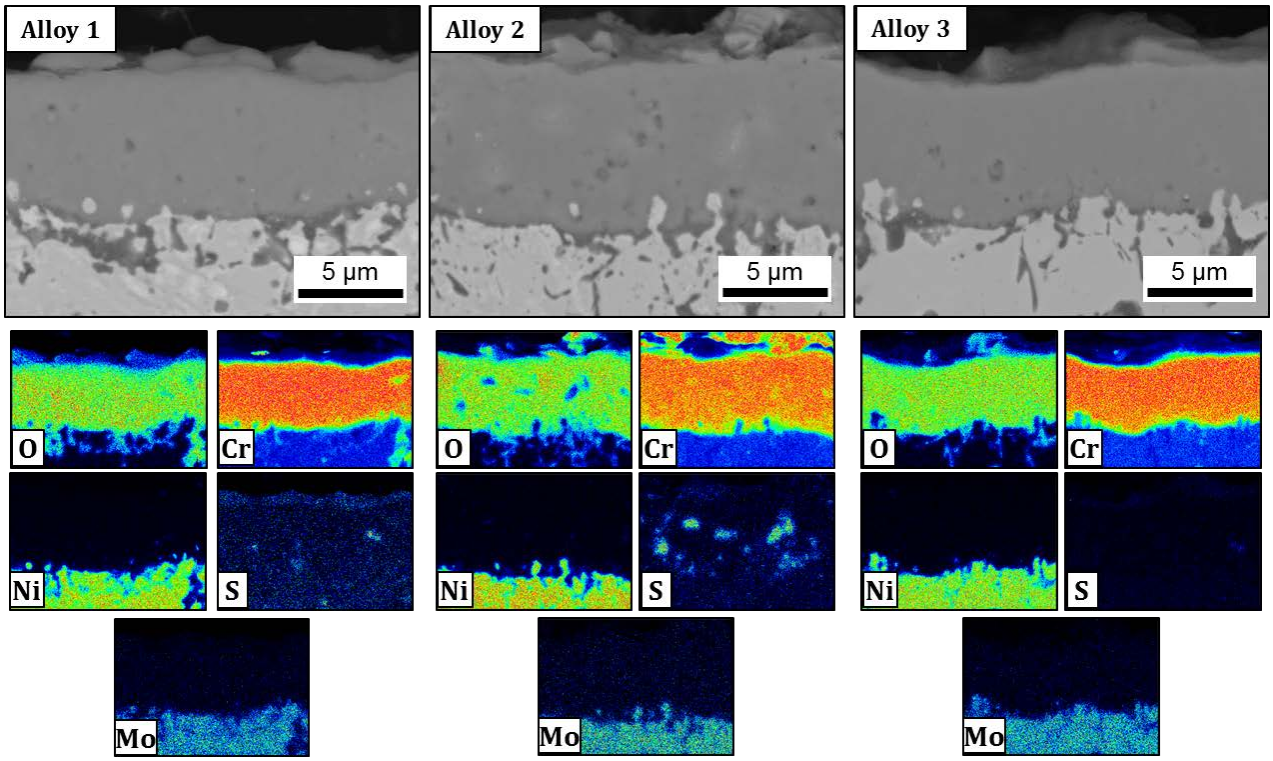

Figure 5-56 EPMA cross-sectional micrographs and WDS elemental maps of alloys 1, 2 and 3 after 100 h exposure to gas 2 at 871 °C

According to the WDS maps of the scales on all three samples at the remaining protective regions after 100 h, Cr-sulfides were present as discrete particles inside the chromia scale formed on alloy 2 with 28% chromium. On the other hand, based on the weight changes observed on

these three samples, alloy 2 was shown to have the lowest incubation period. Thus, increasing the Cr content might be the reason for decreasing the incubation period of the alloy. In order to clarify this hypothesis, GDOES depth profiles of the above mentioned samples after exposure for only 5 min to gas 2 were acquired. These results are presented in Figure 5-57, where it shows that the sulfur content at the surface of alloy 2 with higher Cr content is 3 times higher than for alloys 1 and 3. The main questions here are first: is alloy 3 having better resistance due to the lower Ni:Co ratio or lower Cr content?; and second: why would adding more Cr decrease the time to breakaway corrosion in alloy 2?

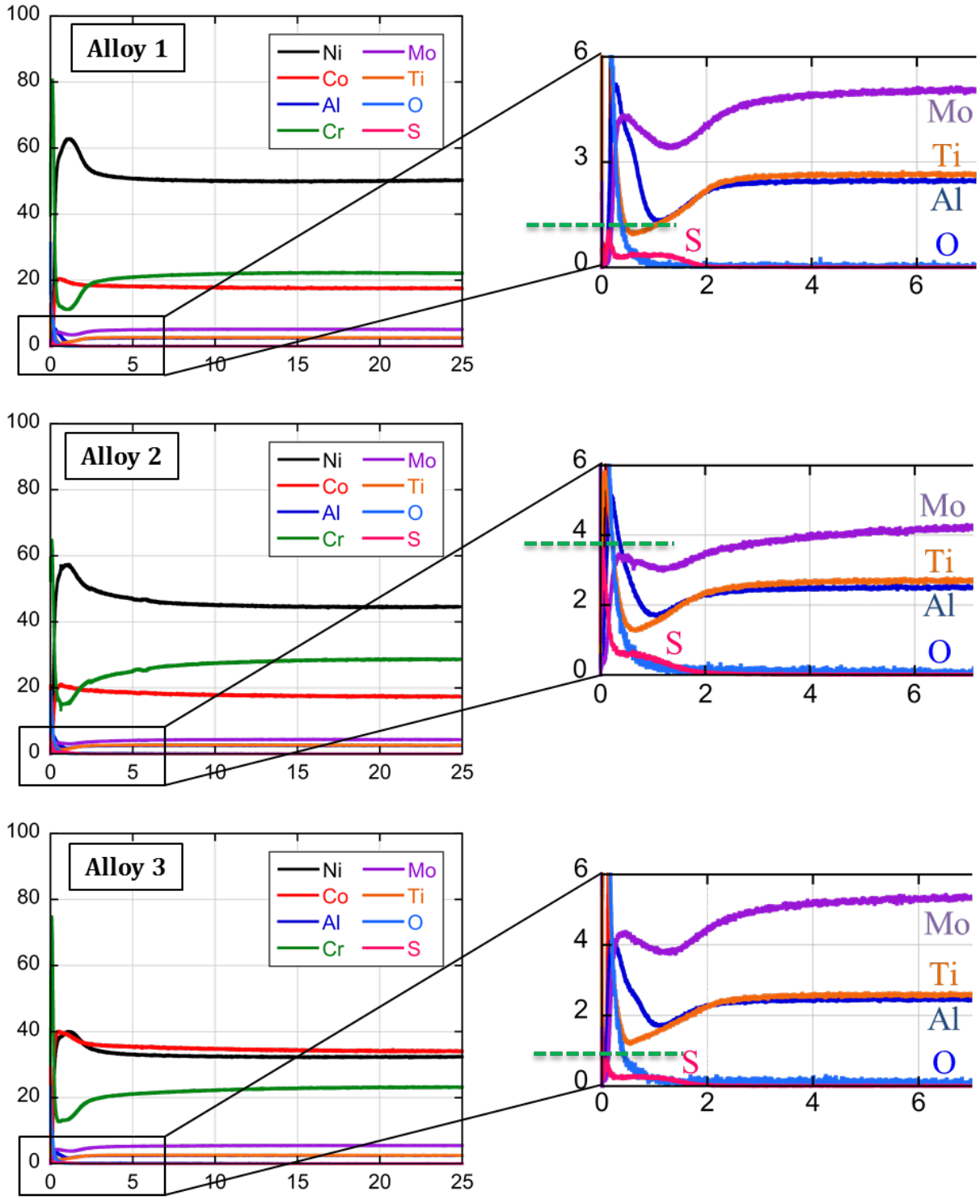

Figure 5-57 GDOES depth profiles of alloys 1, 2, and 3 after 5 min exposure to gas 2 at 871 °C. The dashed lines in the magnified diagrams on the right represent the maximum sulfur content present on the surface of the samples after exposure

5.4.1.2 Model alloys modified with Si and higher Al contents

In order to study the abovementioned questions a new set of model alloys were designed, where the Ni:Co ratio were kept constant (0.95) similar to alloy 3. The compositions are summarized in Table 4-2. The weight-gain results obtained from these samples are shown in Figure 5-58 in comparison with alloys 1, 2, and 3. The effect of higher Cr concentration was studied with alloy 5 (similar composition to alloy 3 with increasing the Cr content up to 28%). The weight gain after 100 h exposure decreased from 67.2 mg/cm^2 in alloy 2 to 45.9 mg/cm^2 in alloy 5 (both with 28 wt. %Cr). However, it is still much higher than other alloys with 22% Cr. Based on the results obtained from commercial alloy HR160 (2.75 wt. % Si), the effect of Si additions was studied with model alloys 4 and 7 (with addition of 3 wt. % Si), where they both showed very low weight gains of 0.5 and 0.3 mg/cm^2, respectively. The effect of Al was also examined at higher levels of 5 wt. % with alloys 6, 7, and 8 based on the perfect results achieved from commercial alloy 214 (4.5 wt. % Al). The weight gains were still much lower than alloys 1, 2, 3, and 5, however, some sulfide nodules were observed on alloy 6 with 22% Cr and around the edges of alloy 8 with 28%Cr.

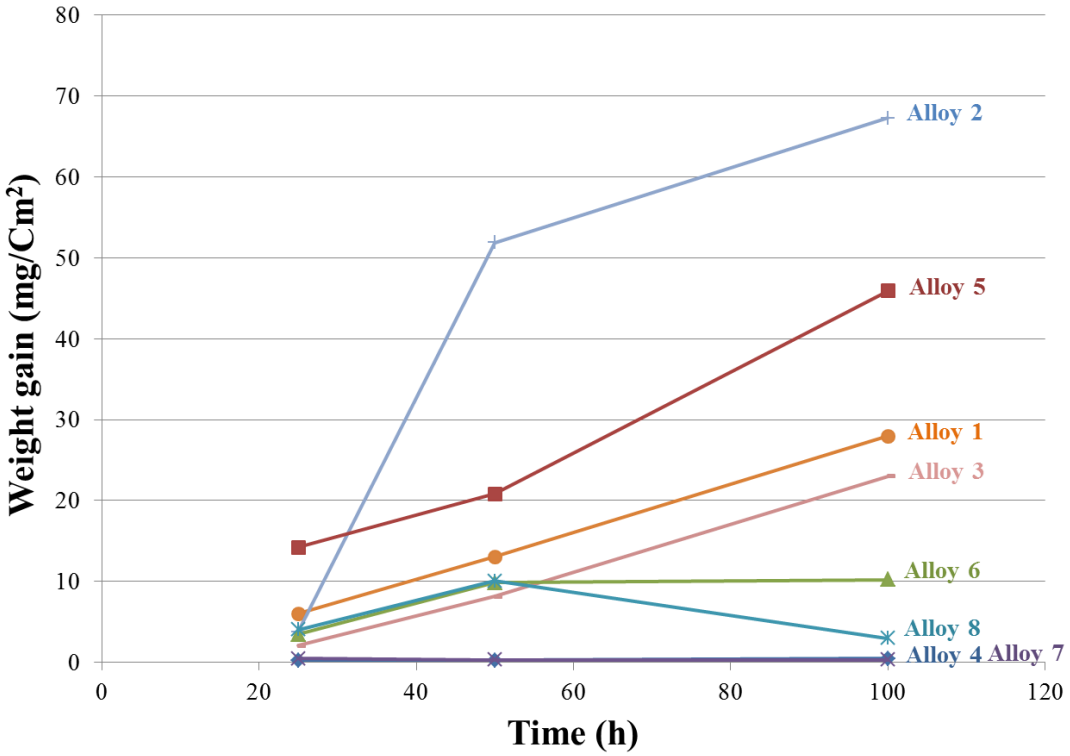

Figure 5-58 Weight change measurements of model alloys after 100 h exposure to gas 2 at 871°C

Surface SEM images of these alloys can be seen in Figure 5-59. Formation of Cr- and Cr+Ti-rich oxides were revealed on all alloys in addition to Ni- and Co-rich sulfide nodules mainly on alloys 5 and 6. According to the surface images, formation of Ni- and Co-rich sulfides can also be observed around the edges of the alloy 8, which is the alloy with both high Cr (28%) and Al (5%).

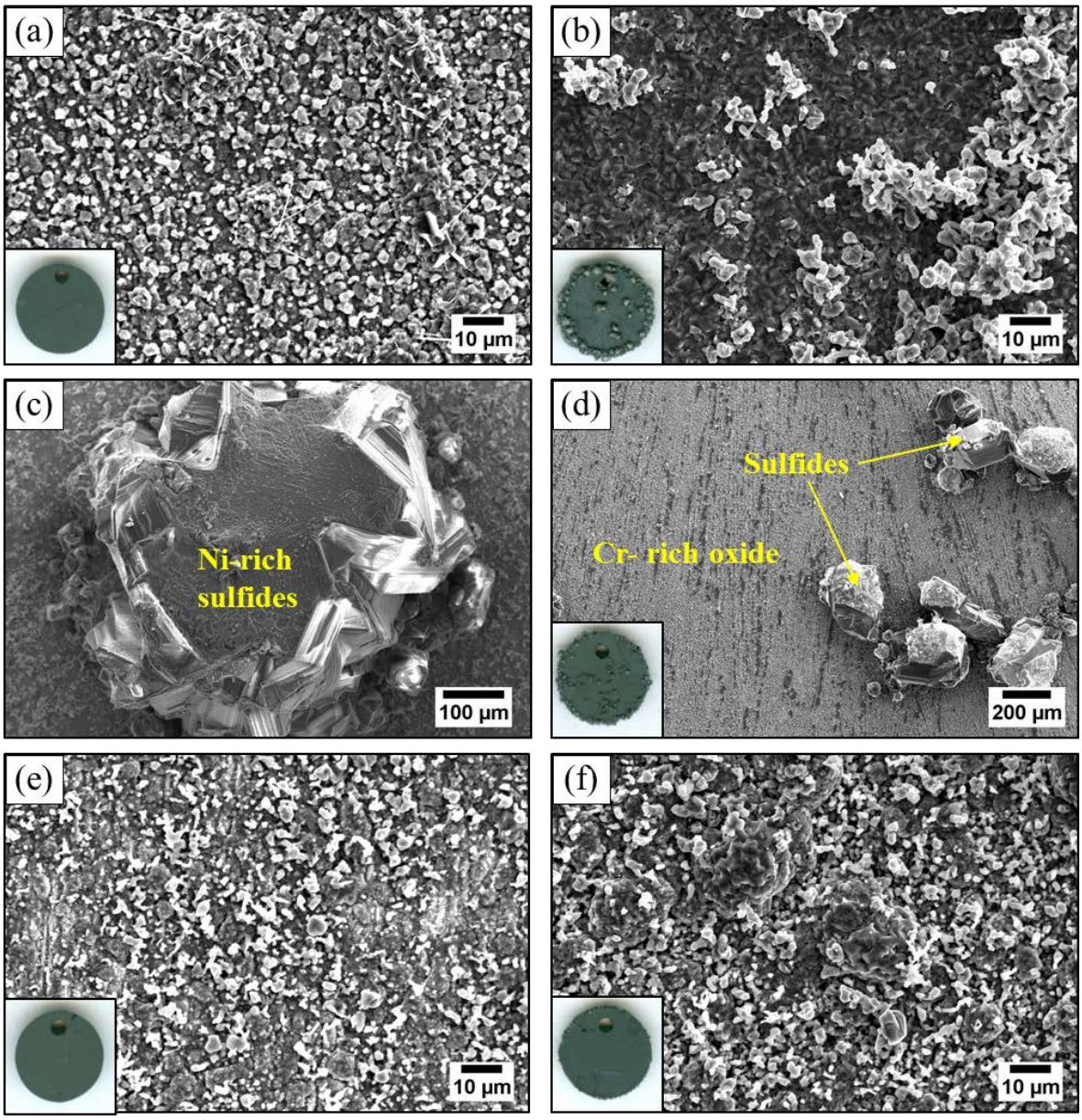

Figure 5-59 SEM surface images after 100 h exposure to gas 2 for alloy (a) 4, (b) 5, (c) 5, (d) 6, (e) 7 and (f) 8

Figure 5-60 shows the EPMA cross-sectional images of the two silicon-containing alloys 4 and 7, which showed the lowest weight gains after 100 h. Formation of a protective alumina layer with a Si-rich sub-layer phase provided exceptional sulfidation resistance in these alloys with no oxide scale breakdown at any part of the samples.

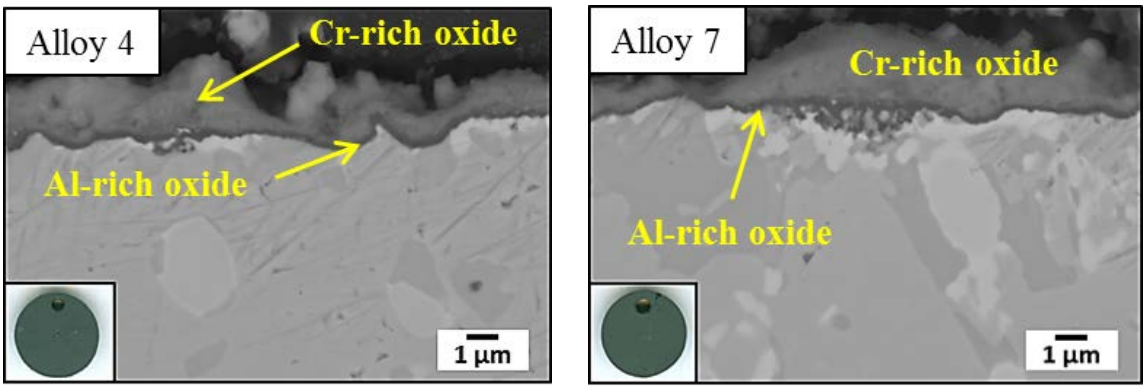

Figure 5-60 EPMA cross-sectional micrographs and EDS analysis of scale formed on alloy 4 and 7 after 100 h exposure to gas 2 at 871 °C

In order to study the effect of Si in more detail, alloys 3 and 4, in which addition of Si in alloy 4 is the only difference, were exposed to air up to 100 h using TGA. The weight change behavior of these two alloys and SEM surface images after exposure can be observed in Figure 5-61 and Figure 5-62, respectively. It was found that these alloys follow parabolic behavior and the parabolic rate constant of alloy 3 is about two orders of magnitude higher than that of alloy 4. According to the SEM surface images and EDS analysis of the scale, the formation of Cr+Ti-rich oxide on alloy 3 and Cr+Al-rich oxide on alloy 4 was observed. Further cross-sectional analyses of these alloys (Figure 5-63) showed that alloy 3 has a similar structure as was observed after exposure to gas 2 with formation of chromia layer on top followed by internal Al-oxides. However, not much could have been observed on alloy 4 using SEM and EDS. Thus, further detailed TEM characterization was done on this sample. A STEM cross-sectional micrograph and EDS measured composition of different phases formed are presented in Figure 5-64. Formation of an outermost Cr+Al-rich scale followed by a continuous and adherent alumina layer beneath was observed. An important observation was the formation of a Si+Ti+Ni-rich sub-layer (beneath the alumina layer. According to the EDS measurements of this phase and according to the Ni-Ti-Si ternary phase diagram (Figure 5-66), the composition of this phase

falls solely into the G-phase region. This phase, with a cubic unit cell was found to have a quite large composition range. According to STEM-EDS measured concentration profile for all the major elements (Figure 5-65), an increase in concentrations of Si and Ti from the bulk alloy toward the G-phase can be observed. Formation of another layer beneath the G-phase was also detected. This phase has an average composition of $(Co, Ni)_{46}(Cr, Al, Mo)_{38}(Si, Ti)_{16}$, which can be simplified to $(Co, Ni)_{2.9}(Cr, Mo)_{2.3}(Si, Ti)$.

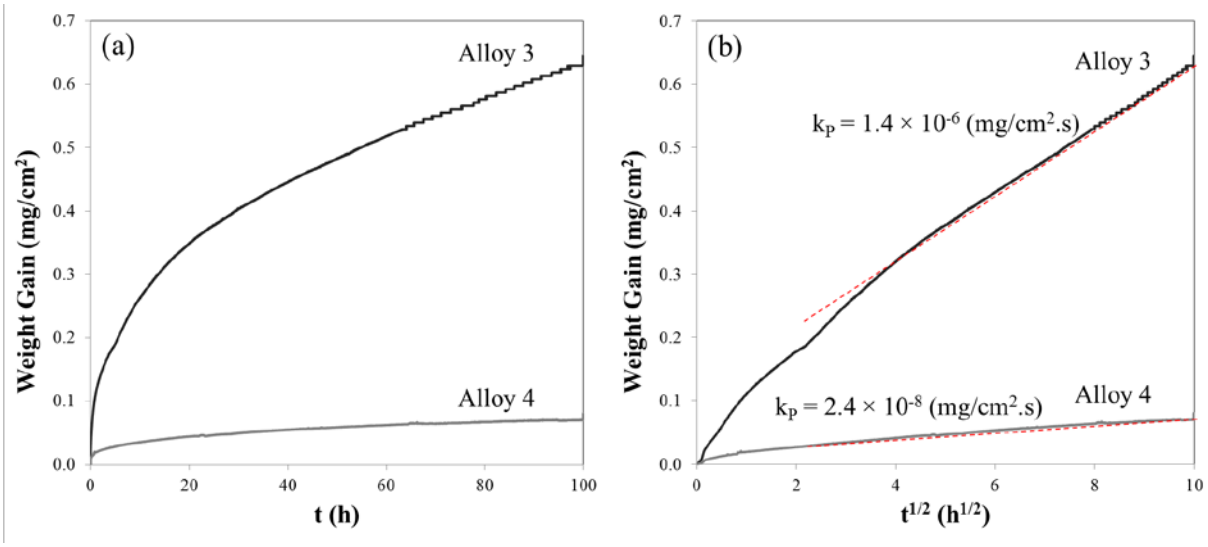

Figure 5-61 (a) Weight change data and (b) experimentally measured parabolic rate constant for alloys 3 and 4 after 100 h isothermal exposures to dry air at 871 °C

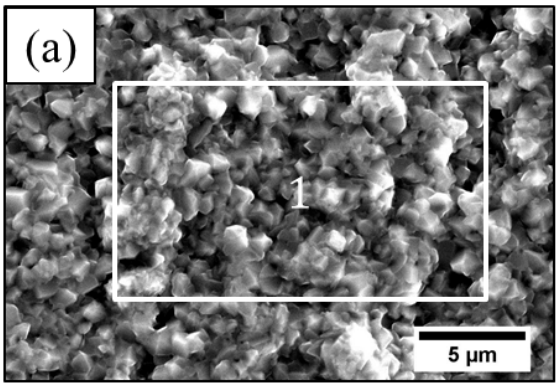

	O	Ti	Cr	Co	Ni
1	67.6	3.7	28.1	0.4	0.2

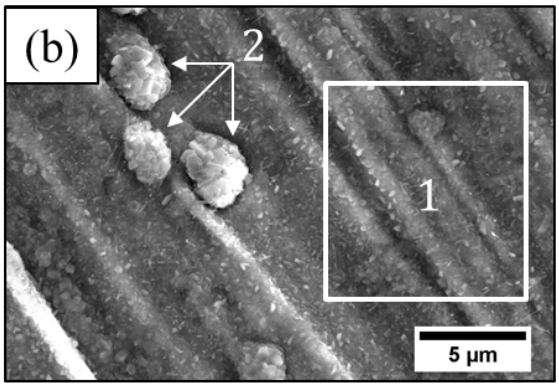

	O	Al	Si	Ti	Cr	Co	Ni	Mo
1	47.0	14.6	3.5	2.9	10.2	11.1	9.8	0.7
2	67.5	10.8	2.1	5.5	6.9	3.9	2.9	0.4

Figure 5-62 SEM surface images and EDS composition measurements of (a) alloy 3 and (b) alloy 4 after 100 h exposure to dry air at 871 °C

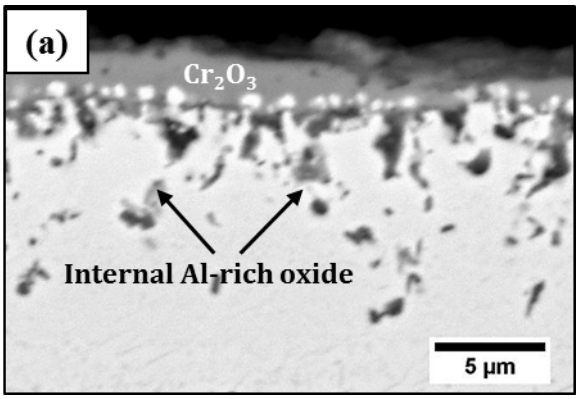

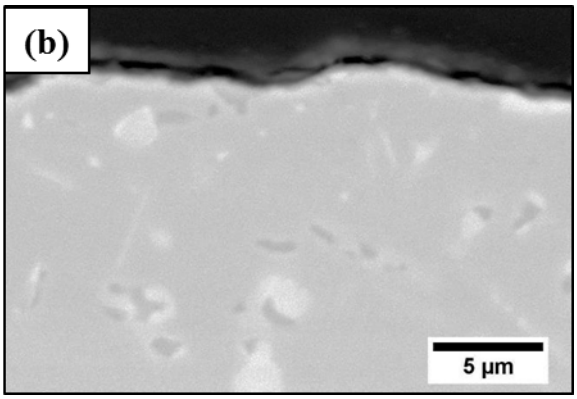

Figure 5-63 SEM cross-sectional micrographs of (a) alloy 3 and (b) alloy 4 after 100 h exposure to dry air at 871 °C

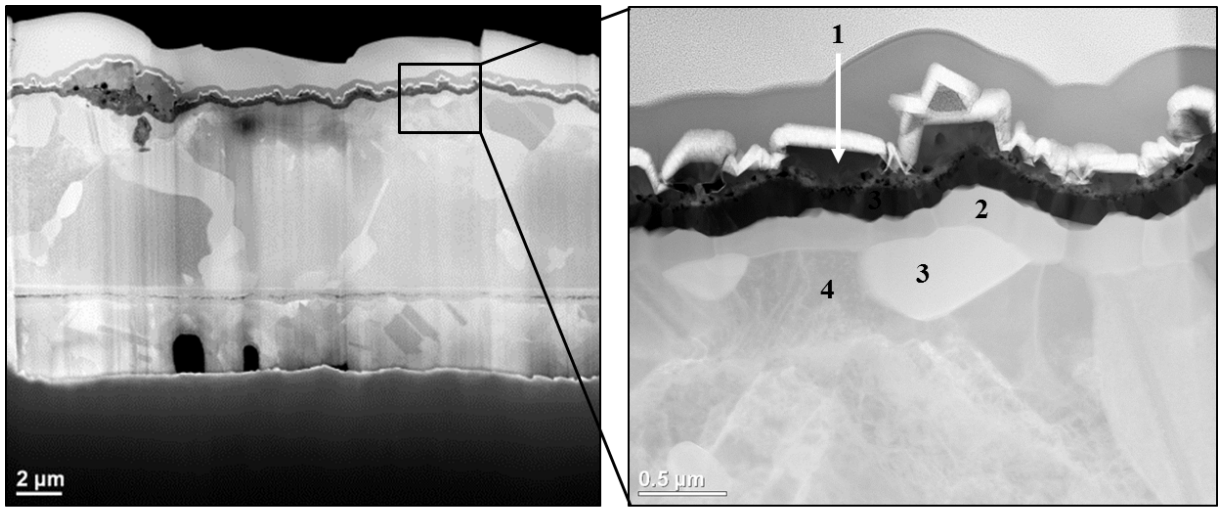

	O	Al	Si	Ti	Cr	Co	Ni	Mo
1	50.2	39.6	-	0.4	9.3	0.2	0.3	-
2	2.2	0.5	24.3	18.4	1.1	18.3	34.8	0.4
3	-	0.4	10.6	2.8	29.6	31.4	18.2	7.1
4	-	2.0	3.4	1.2	28.3	35.6	28.3	1.1

Figure 5-64 STEM cross-sectional micrographs and EDS point analysis of the scale formed on alloy 4 after 100 h exposure to dry air

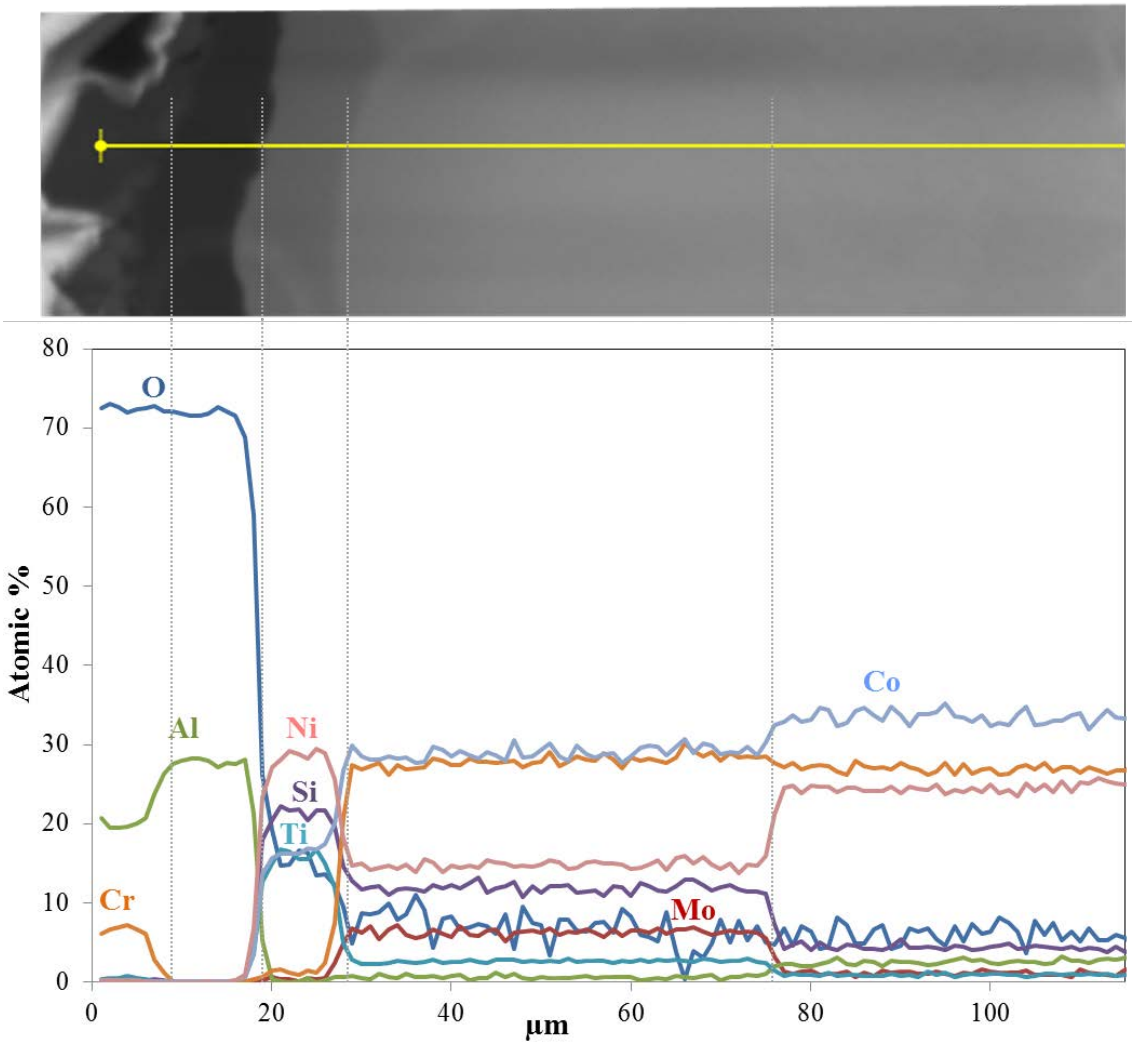

Figure 5-65 Cross-sectional STEM image of alloy 4 after 100 h exposure to dry air and EDS concentration profiles

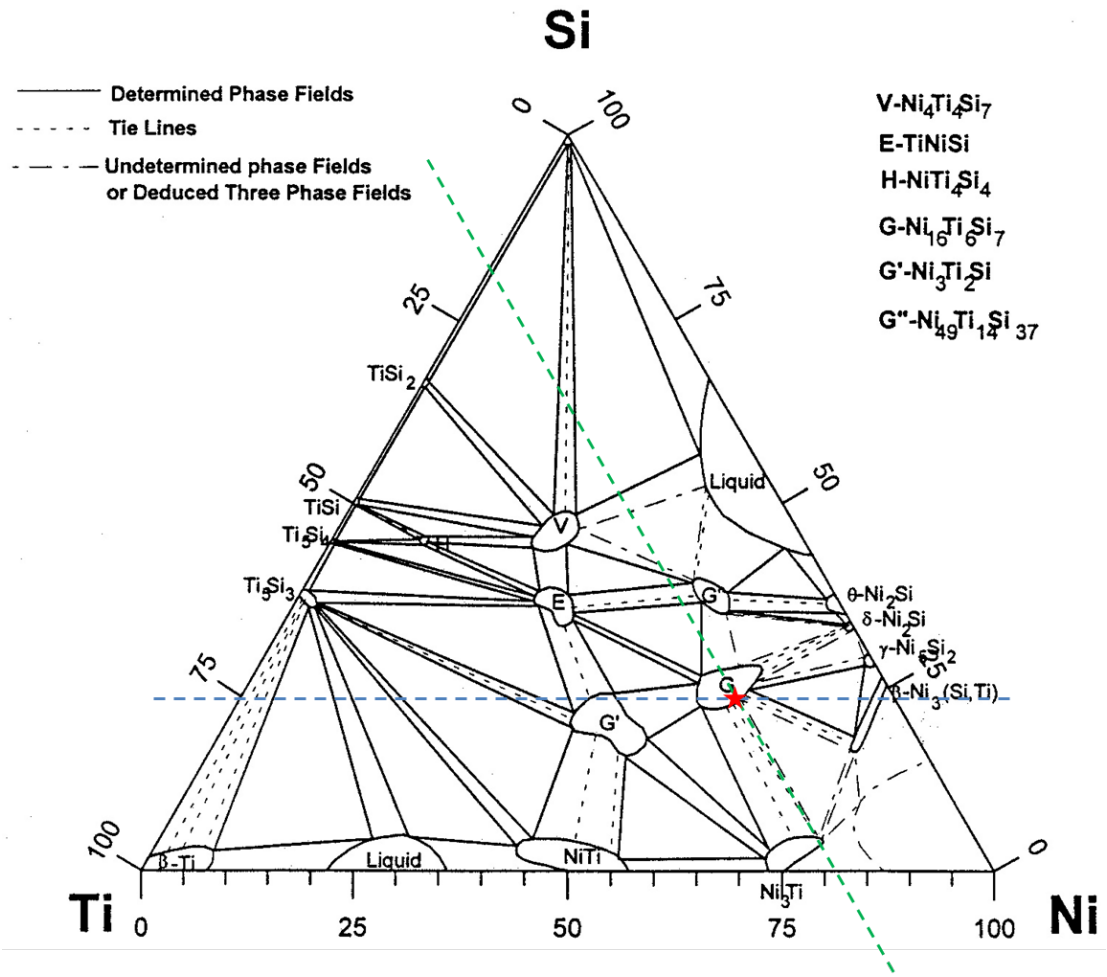

Figure 5-66 Ti-Ni-Si isothermal section at 1100 °C. The star mark on the diagram shows the EDS measured composition of the sub-scale phase after exposure of alloy 4 to dry air atmosphere for 100 h at 871 °C [120]

Figure 5-67 shows an SEM cross-section of alloy 5, which has the Ni:Co ratio close to 1 (as in the case alloy 3) but with a higher Cr content of 28%. It is clear that this alloy showed the least sulfidation resistance among the modified model alloys. The weight gain was lower than alloy 2 but still much higher than alloy 3. From the cross-sectional images, localized breakdown of the chromia scale and formation of Ni- and Co-rich sulfide nodules can easily be observed in the bulk of the alloy. The rapid outward growth of these nodules was followed by extensive internal attack (mixture of oxides and sulfides). Taking a closer look at the chromia scale in the remaining protective regions using EPMA (Figure 5-68), shows the formation of discrete sulfide

particles inside the oxide scale, similar to previous observations on alloy 2. Comparison of alloy 5 with alloy 3 with less chromium content confirms that increasing the chromium content in these alloys is not necessarily beneficial in providing a better sulfidation resistance and can cause a shorter incubation period.

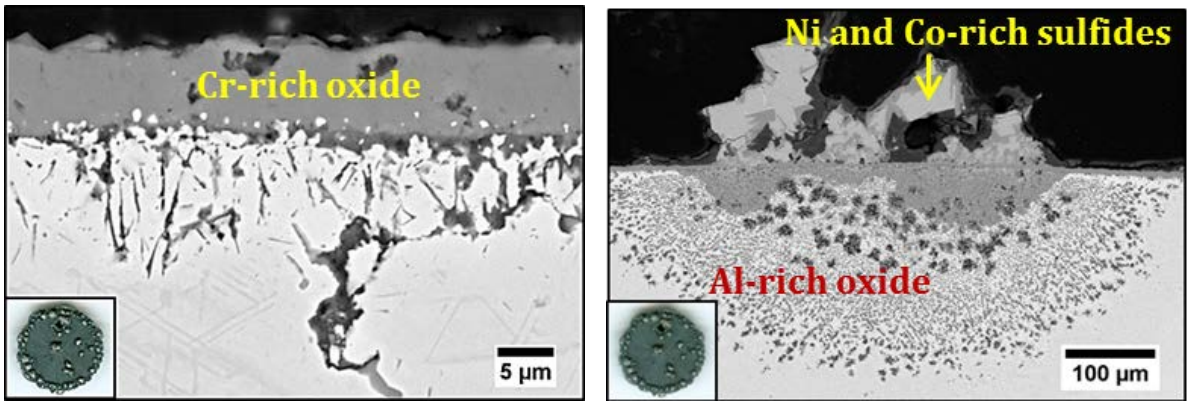

Figure 5-67 SEM cross-sectional micrographs and EDS analysis of the scale formed on alloy 5 after 100 h exposure to gas 2 at 871 °C

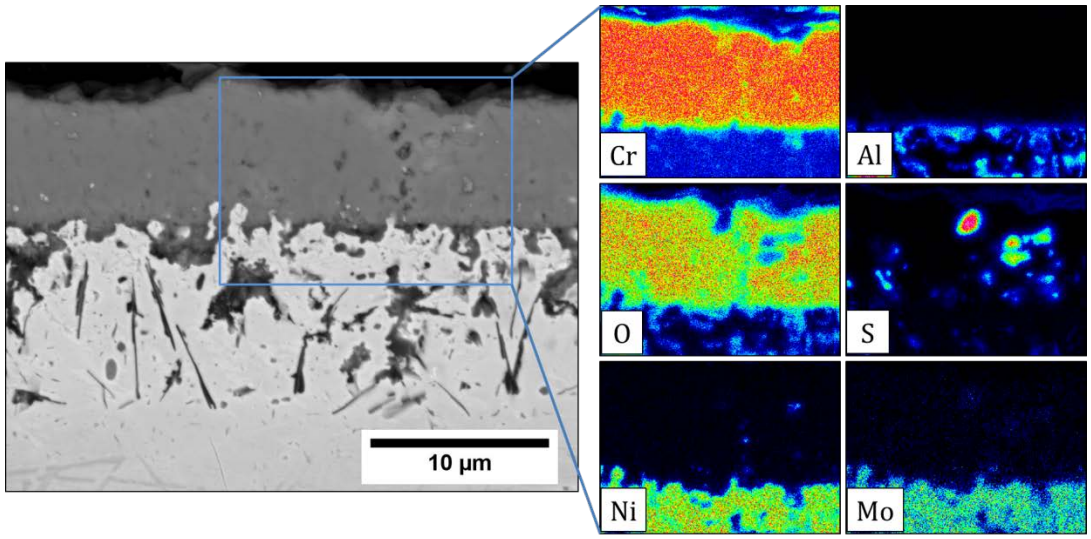

Figure 5-68 SEM cross-sectional micrograph and WDS elemental maps of the scale formed on alloy 5 after 100 h exposure to gas 2 at 871 °C

It was shown previously that the alumina forming commercial alloy 214 is one of the most resistant alloys under mixed gas conditions at elevated temperatures. Based on these observations, the effect of higher aluminum additions was studied in alloy 6, 7, and 8, which also contain 3 wt. % silicon (alloy 7) and a higher chromium content of 28 wt. % (alloy 8). However, due to high contents of the above mentioned minor alloying elements, extensive formation of different brittle phases was observed; especially in alloy 7 where high concentrations of Al and Si exist together. A cross-sectional image of alloy 7 with silicon additions is shown in Figure 5-60. The behavior of this alloy was similar to alloy 4 and no major difference was observed. Alloy 6, on the other hand, with 22% chromium and 5% aluminum showed the formation of an outer layer of Cr-rich oxide followed by formation of a continuous inner layer of alumina (Figure 5-69). However, localized breakdown of this scale was still observed after 100 h exposure. It should be noted that the substrate alloy was composed of 3 phases: γ phase and two unspecified Cr-Mo-rich (darker) and Al-rich (brighter) phases. Higher concentrations of these phases can be observed in alloy 8 with high Al and Cr contents. Cross-sectional image of alloy 8 after exposure to gas 2 (Figure 5-70), shows the formation of external Cr-rich oxide scale followed by some internal Al-rich oxide beneath. The extent of internal oxide formation is less than alloys 1, 2 and 3. Taking a closer look at the cross-sectional micrograph of alloy 8, it is seen that the internal oxidation of Al follows a similar pattern to the Al-rich phase in the substrate alloy. Formation of a small amount of sulfides can be observed around the edges of this alloy, which shows the lower resistance of this alloy compared to the Si-containing alloys.

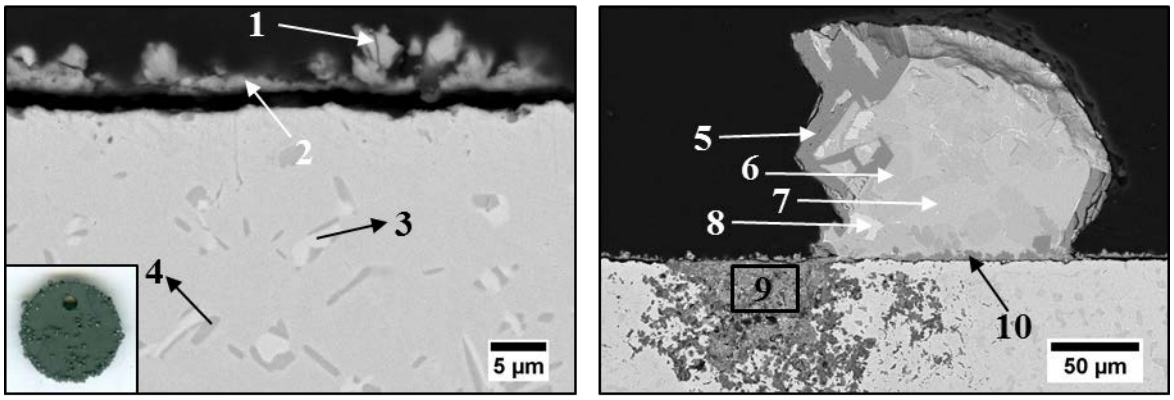

	Ni	Co	Cr	Al	Ti	Mo	O	S
1	7.3	15.9	19.4	-	-	-	14.5	42.9
2	-	-	26.8	-	4.5	-	66.1	2.7
3	11.8	32.4	47.7	-	-	8.1	-	-
4	38.4	16.8	10.0	32.5	2.3	-	-	-
5	-	-	40.3	-	-	-	59.73	-
6	13.3	36.0	-	-	-	-	-	50.7
7	39.8	15.4	-	-	-	-	-	44.7
8	58.7	41.3	-	-	-	-	-	-
9	-	-	20.5	9.5	2.9	-	55.1	12.0
10	-	-	35.6	-	2.0	-	62.4	-

Figure 5-69 Scanning electron micrographs and EDS analyses of the cross-section of the alloy 6 after 100 h exposure at two location of protective and non-protective

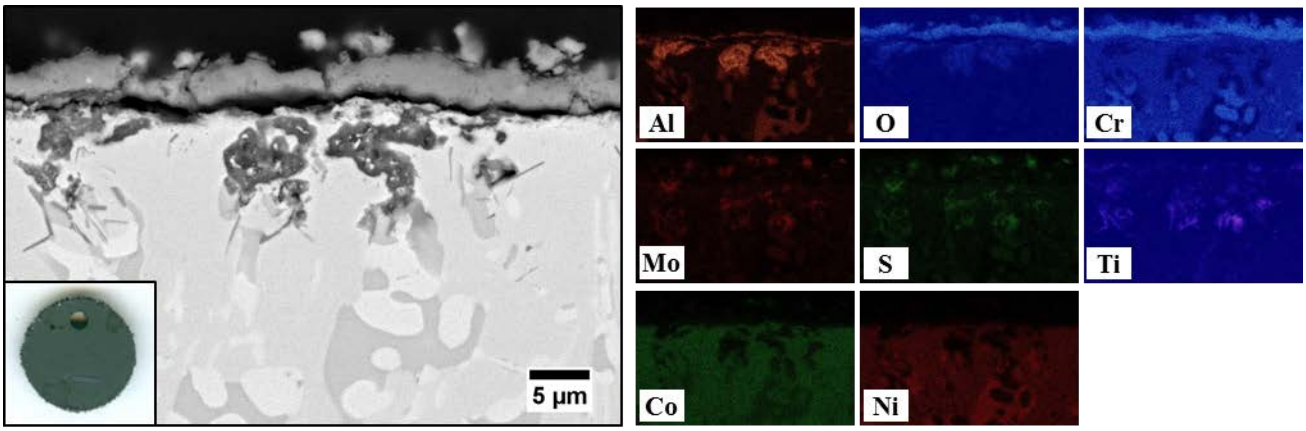

Figure 5-70 Scanning electron micrograph and EDS elemental maps of cross-section of the alloy 8 after 100 h exposure

5.4.1.3 Discussion

After exposure of model alloys 1, 2, and 3 to gas 2, an adherent and continuous Cr_2O_3 scale is established on all these alloys. Once this continuous Cr_2O_3 layer has developed, the oxygen potential at the scale/alloy interface will drop to a level that can be determined by the scale/alloy equilibrium. The resulting oxygen potential is sufficient to oxidize other stable-oxide-forming elements such as aluminum, since Al_2O_3 is more stable than Cr_2O_3. Precipitates of Al_2O_3 form easily beneath the Cr_2O_3 layer, even at a relatively low activity of aluminum in the alloy. The formation of internal or external Al-rich oxide beneath the chromia layer depends on many factors, most importantly the oxygen and aluminum activities at the Cr_2O_3/alloy interface and the rate of aluminum diffusion to the surface from the substrate alloy [121]. At an exposure temperature of 871°C and with an aluminum concentration of 2.5 wt. %, it is kinetically unfavorable for a continuous alumina sub-layer to develop. As a result, internal Al-rich oxide forms. Formation of the internal oxide cannot provide a barrier for oxygen or other oxidants such as sulfur and, therefore, oxide precipitates continue to grow internally as the oxygen diffuses inward.

The internal alumina formed on the above-mentioned alloys usually takes the form of continuous platelets from the surface rather than discrete particles. The reason for such a behavior was previously discussed by Stott and Wei [122]. They postulated that development of this continuous mode rather than discrete particles is a consequence of the growth of existing oxide particles being favored over nucleation of new particles. When the oxygen flux is relatively low compared to Al flux, continued growth of the existing oxide particles is favored. By formation of the oxide platelets, enhanced oxygen transport along the oxide/metal interfaces will support their continued growth into the alloy substrate. There has been some discussions that

the deformation caused by formation of aluminum oxide precipitates with an increase in volume can lead to the faster transport of solvent metal to the surface as a result of the generated high stresses at the internal oxide/alloy interface, possibly by a diffusion-controlled creep process [123, 124].

Addition of the minor amounts of Ti (2.5 wt. %) in these alloys also appears to play an important role in imparting sulfidation resistance. The beneficial effect of Ti is to stabilize and maintain an extended period of oxide-scale formation under the reducing conditions tested in this study. The beneficial effect of Ti on the location of the kinetic boundary was previously reported by Wang et al. [125]. According to that study, Ti additions can improve the scaling resistance of Fe-25Cr alloys against sulfidation in H_2-H_2O-H_2S environment at high temperatures by shifting the kinetic boundary between Cr-oxide/Cr-sulfide to lower partial pressures of oxygen.

However, localized breakdown of the oxide scale was found for all three Ti-containing model alloys. During the initial stages of exposure, both oxide and sulfide can nucleate on the surface, as was shown in GDOES depth profiles in Figure 5-57. Continuation of their growth at the temperature of the reaction depends on both kinetic and thermodynamic factors. The presence of the sulfide on the specimen at oxygen and sulfur activities in which Cr_2O_3 is stable is clearly attributed to kinetic factors. This sulfide is immediately overgrown by the oxide and will be protective until the breakaway corrosion happens and the fast growing sulfides overgrow the Cr_2O_3 scale. Detailed discussions on possible paths of sulfur penetration through the chromia scale have been presented previously [126, 127]. According to those studies, formation of microcracks within the chromia scale is generally considered to be the main short-circuit mechanism. However, it seems that the breakaway corrosion first happens either around the edges of the samples or on the defects such as casting defect in the middle. It has been shown

previously [128] that sulfides tend to grow preferentially at structural features such as variations from grain to grain, scratches, and the edges. It may be that the cracking of the scale happens more readily at such locations. Rapid growth of sulfide in the resulting fissure happens when the existing sulfide is interconnected with the underlying alloy to ensure a plentiful supply of Cr and base-metal cations.

Previous studies have shown that Co-base alloys are more resistant to sulfidation compared to Ni- and Fe-Ni-base alloys with similar chromium contents [129, 70]. In the current study, it was also shown that increasing the Co content is definitely beneficial in increasing the sulfidation resistance in alloy 3 with Ni:Co=1 compared to alloy 1 and 2 with Ni:Co ratios of 2.9 and 2.6, respectively. When the Ni:Co ratio is close to 1, the availability of both of these elements for sulfide formation is the lowest and thus, an optimum sulfidation resistance can be achieved.

It is also common to consider Cr as one of the main variables for conferring sulfidation resistance as well as Co, as it was also shown in the results from ternary model alloys. However, alloy 2 showed a shorter incubation period compared to alloy 1 with a lower Cr content of 22% and the same Ni:Co ratio. The main question here is why higher Cr content in this alloy is somehow destructive with respect to sulfidation resistance? It was previously discussed in chapter 2 that when metals and alloys are exposed to gaseous atmospheres containing oxygen and sulfur the following reactions need to be considered,

$$H_2 + \frac{1}{2}O_2 = H_2O \tag{5-14}$$

$$H_2 + \frac{1}{2}S_2 = H_2S \tag{5-15}$$

$$xM + \frac{1}{2}O_2 = M_xO \tag{5-16}$$

$$yM + \frac{1}{2}S_2 = M_yS \quad (5\text{-}17)$$

At the initial stages of the reaction, when equilibrium has not yet been established and activity of the metal is high at the alloy surface, both oxide and sulfide can form. Thus, the metastable sulfide forms for kinetic reasons and will eventually further react with oxygen containing species in the gas through the following reaction in order to transform to oxide.

$$2xM_yS + yO_2 = 2yM_xO + xS_2 \quad (5\text{-}18)$$

Reaction (5-18) can introduce sulfur into the scale at an activity higher than that existing in the gas phase. Under this condition, if the metal and sulfur activities at some position within the scale are sufficiently high for sulfide stability, the reaction can occur and sulfide can form. This is in agreement with our observation on pure Cr exposed to gas 2 in previous chapter. Formation of discrete sulfide particles were observed in the relatively thick chromia scale formed after 25 h exposure in gas 2. Assuming that the thermodynamic equilibrium is established throughout the scale, the activity gradient of chromium decreases in progressing from the alloy/scale to scale/gas interface, while the activity gradient of sulfur increases. The activity of the metal at the scale/gas interface is fixed and can be calculated through reaction (5-16). However, activity of chromium at the alloy/scale interface depends on its concentration in the alloy. Thus, the activity of Cr at a certain distance from the alloy/scale interface inside the chromia layer has to increase by increasing the chromium content of the alloy. Comparison of the results of the alloys containing 22% and 28% chromium and also the pure chromium clearly shows that under the same conditions (gas 2), the amount of discrete Cr-sulfide particles inside the chromia scale increases as the chromium content of the alloy increases. The observed results from the GDOES depth profiles of the samples exposed to gas 2 for a very short period of time

(5 minutes) also confirmed that increasing the Cr activity of the alloy results in an increase in the amount of the metastable sulfides formed at initial stages.

Formation of the sulfide particles inside the chromia scale can make the alloy prone to breakaway corrosion, as was shown in the shorter incubation period of alloy 2 with 28% chromium. The localized breakdown of the oxide scale can clearly be seen in the cross-sectional micrograph of alloy 2 after 100 h. The mechanism by which sulfur penetrates through the chromia scale is generally believed to be the molecular transport of the sulfur or sulfur-containing species through grain-boundaries of oxide scale or physical defects such as cracks or pores in the oxide scale [6, 54, 130]. Once sulfur reaches the alloy/oxide interface, rapidly growing sulfides begin to form. This leads to the gradual destruction of the chromia scale. Once the continuous paths of sulfide connecting the substrate alloy to the gas environment develop, it provides a continuous supply of base metal to the rapidly outward growing sulfide, which leads to the rapid degradation and consumption of the material. The presence of any defects, such as cracks or pores or even dispersed sulfide particles, in the oxide scale can increase the inward transport of sulfur and, thus, shorten the incubation period of the protective behavior of the alloy.

Based on the findings from the initial set of model alloys, a second series of tests were done in a similar environment on a new set of model alloys in order to systematically study the effects of Si, Cr and higher levels of Al additions to the alloys. As the beneficial effect of Ni:Co=1 was previously shown, the second set of model alloys maintained a Ni:Co ratio of 1. It needs to be noted that the structures of these alloys are different compared to alloys 1, 2 and 3. As a result of higher concentrations of minor alloying elements, these alloys consist of multiple phases. It is apparent from the results that in both alloys 4 and 7 improvements in sulfidation resistance can be achieved through Si additions at levels within the limits of what can be found

in commercially available alloys. Weight gain measurements and cross-sectional analysis using EPMA clearly show the significant improvements in sulfidation resistance of these alloys compared to alloy 3 with no Si additions. However, the inner parts of the scales in both of these alloys are complex in nature. Continuous alumina scales were observed on the surfaces with a thin Cr-rich oxide on top. In addition, a Si-enriched sub-layer was observed beneath the alumina layer. Further detailed analysis of the oxidized sample (alloy 4) with TEM clearly shows the formation of a protective alumina layer followed by what interpreted based on EDS analysis to be G-phase ($Ni_{16}Ti_6Si_7$). It is believed that the formation of this phase is linked to or can be accelerated by the formation of the alumina layer on top. Due to the Al depletion by selective oxidation and Si enrichment in the subscale region, the latter can react with the Ti from the substrate alloy and precipitate out as G-$Ni_{16}Ti_6Si_7$ in the Ni-rich matrix. A previous study by Leyens et al. [131] also reported the formation of this G-phase due to the selective oxidation of Al in a Ni-Cr-Al-Ti-Si bond-coating alloy. However, a simple calculation of the composition change of the substrate alloy after removal of Al and Cr due to selective oxidation to form the transient Al-Cr-rich oxide and the continuous alumina scale clearly shows that additional mass transport (i.e., Si and Ti enrichment) is needed for the G-phase formation.

Measured EDS profile through the scale, the G-phase and the sub-scale depleted region of the alloy was presented in Figure 5-65. Table 5-4 shows the comparison of the EDS results obtained for the G-phase with the composition of the alloy substrate and calculated composition of the alloy after complete removal of the Al and Cr. If it is assumed that the G-phase is formed due to the selective oxidation of Al and Cr, the concentrations of Si and Ti in the sub-scale region after depletion of Al and Cr should be close to their concentrations in the G-phase. Even if it is considered that the total chromium and aluminum contents in the bulk alloy would be

completely removed by oxide formation, the Si and Ti concentrations in the resulting depleted substrate alloy would rise to 8.1 at.% and 4 at.%, respectively (the concentration of the other elements in the depleted zone should increase in order for the sum of all elements to remain 100%). These concentrations are still much lower than the measured Si and Ti concentrations in the G-phase (24.3 Si- 18.4 Ti at.%). Therefore, it is apparent that the main requirement for formation of the G-phase near the alloy/scale interface should be the diffusion of Si and Ti from the bulk alloy toward alloy/scale interface. This means that both Si and Ti need to diffuse from a region with lower concentration (bulk alloy) to a region with high concentration (sub-scale region) against their concentration gradients, which is usually referred to as “uphill diffusion” [132]. In other words, the chemical potentials or the activities of Si and Ti should be higher in the bulk alloy compared to the depleted region. The establishment of such driving force must be related to the sub-scale depletion of Al and Cr since these elements are the main constituents of the surface scale.

Table 5-4 EDS measured composition of the G-phase and nominal composition and calculated remaining composition of the alloy 4 after depletion of Al and Cr in the sub-scale region

at.%	O	Al	Si	Ti	Cr	Co	Ni	Mo
Alloy substrate		5.1	5.8	2.9	23.1	30.9	29.4	2.8
G-phase	2.2	0.5	24.3	18.4	1.1	18.3	34.8	0.4
Al + Cr depleted substrate			8.1	4.0		43.0	40.9	3.9

In order to confirm, whether the formation of the G-phase is due to the oxidation induced sub-scale depletion of the Cr and Al, Pandat software and the thermodynamic database developed by CompuTherm LLC were used to calculate the activities of Si and Ti in the alloy

before and after the depletion of Al and Cr. At 871 °C it was found that the activity of Si and Ti in the alloy will decrease from 9.14×10^{-6} to 2.51×10^{-6} for Si and from 5.23×10^{-4} to 4.25×10^{-5} for Ti, as Al and Cr in the alloy will be removed. This clearly shows that the uphill diffusion is expected for both Si and Ti to the alloy/scale interface. The STEM-EDS concentration profiles for Si and Ti (presented in Figure 5-65) shows the establishment of these gradients from the bulk alloy to alloy/G-phase interface. Similar behavior has been reported by other researchers [133, 134, 135] on the oxidation of alloy 625. A thin layer of δ-Ni_3Nb phase formed at the alloy/oxide interface in those studies. Further, modeling phase equilibria and diffusion processes using Thermo-Calc and DICTRA showed that the formation of this phase is mainly governed by the influence of alloy matrix chromium concentration on the thermodynamic activities and chemical potentials of the other alloying elements, mainly niobium, which causes the uphill diffusion of Nb and formation of a layer of δ-Ni_3Nb at alloy/scale interface.

Formation of another phase with average composition of $(Co, Ni)_{2.9}(Cr, Mo)_{2.3}(Si, Ti)$ was observed beneath the G-phase. Similar phase with a similar composition has been reported by other researchers [136] in Co-Cr-Mo-Si quaternary system at 800 °C.

The effect of Cr content on sulfidation resistance was examined using model alloy 5, which has the same Ni:Co ratio of 1 but with higher Cr content (28 wt. %) compared to alloy 3 (22 wt. %). Based on the observations on this alloy after 100 h exposure to gas 2, alloy 5 behaved very similar to alloy 2 by formation of discrete Cr-rich sulfide precipitates inside the chromia layer. The weight gain of this alloy was slightly lower than that of alloy 2, however, it was still much higher than the other alloys. This can confirm our previously discussed hypothesis on the effect of increasing the Cr content of an alloy on its sulfidation resistance. As the reaction proceeds, the failure of the oxide scale causes the formation of Ni- and Co-rich sulfides. On the

other hand, in alloy 8 with both high Al and Cr concentrations, formation of an Al-rich oxide beneath the Cr-rich oxide scale gives better protection against sulfur and no sulfide formation was observed in the bulk of the alloy. However, even with 5% aluminum in its composition, formation of a protective external alumina scale was not observed and localized breakdown of the oxide scale and sulfide formation occurred around the edges of the sample. Aluminum still oxidizes internally (due to preferential oxidation of the Al-rich phase in substrate alloy) and sulfidation resistance is still much lower than the two Si-containing alloys.

5.4.2 Carburization

In the present chapter, the effects of both major and minor alloying elements on carburization resistance will be studied using the designed model alloys. The corrosion tests were carried out in a flowing Ar-H_2-C_3H_6 gas mixture (gas 5) in a tube furnace. In order to equilibrate the atmosphere, the pre-mixed gas was passed through a platinized catalyst. The carbon activity was calculated to be about 1. It is noteworthy that although the system was flushed with argon gas overnight, there still exists oxygen partial pressure at impurity levels. As will be shown, the existing oxygen potential is enough to form the most stable oxides, such as alumina and silica. The following sections will discuss the effect of different alloying elements on the carburization resistance of the model alloys.

5.4.2.1 Model alloys with minor alloying elements of Al, Ti, and Mo

The mass change versus time plots for alloys 1, 2, and 3 after exposure to gas 5 at 871 °C are shown in Figure 5-71. It is seen that the kinetics of carburization for alloys 1, 2, and 3 do not follow the parabolic behavior completely and slight deviations are observed. It should be noted

that (as will be discussed later in detail) throughout the test, these alloys go through an initial oxidation stage followed by transition of oxide to carbide (weight loss) and further internal carburization, which all affect the measured mass-change dynamics of the sample. However, comparison of the mass change data shows that the weight gain for all three alloys after 100 h are very close to each other, with alloy 3 (with less Ni content) slightly higher weight gain after 100 h compared to alloys 1 and 2.

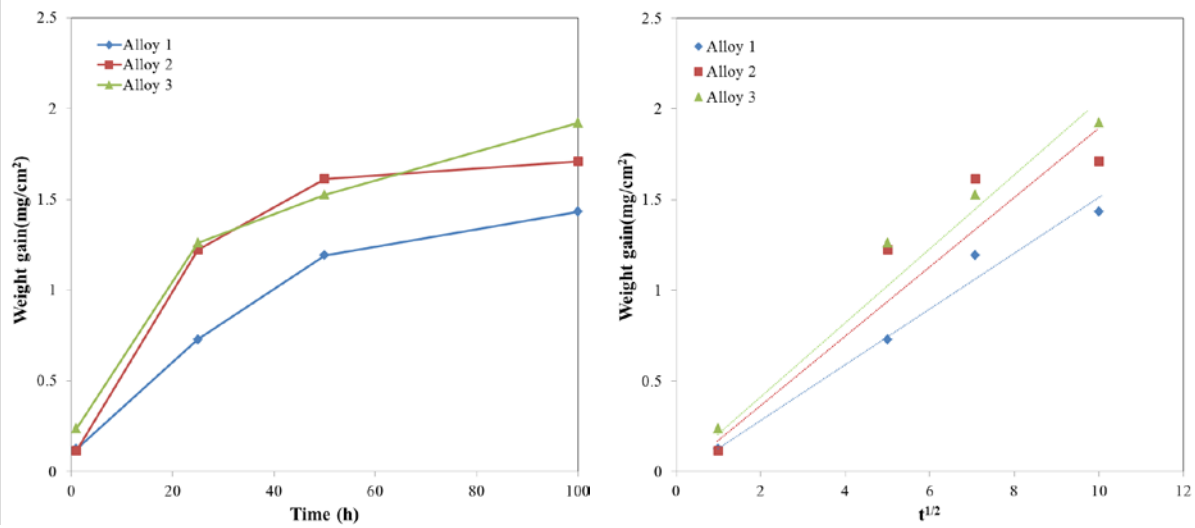

Figure 5-71 Mass change versus time for alloys 1, 2, and 3 after exposure to gas 5 (Ar-H_2-C_3H_6 with carbon activity of ~1) at 871 °C

Table 5-5 Parabolic rate constants and carbon penetration depths measured for alloys 1, 2, and 3 after 100 h exposure to gas 5

	Carbon Penetration Depth (μm)
Alloy 1	193 ± 24
Alloy 2	140 ± 15
Alloy 3	304 ± 27

Figure 5-72 presents the cross-sectional optical micrographs of these alloys after being stain-etched with Murakami solution [137], which helps to reveal the internal carbides. Based on these micrographs, the average carbon penetration depth in each sample was measured (average of 20 measurements based on the depth of intragranular carbides) and the results are reported in Table 5-5. The cross-sectional image of alloy 2 shows the presence of another phase in the form of thin linear plates in addition to the γ phase. Electron microprobe analysis (Figure 5-74) showed the enrichment of chromium and molybdenum in this phase. Subsequent phase stability calculations using the Thermo-Calc software (presented in Table 5-6) showed that σ-phase would be stable based on the chemical composition of alloy 2 with high Cr and Mo concentrations. The undesirable σ is a TCP phase composed of closed-packed layers of atoms forming in the shape of "basket weave" nets aligned with the octahedral planes of the FCC matrix. The presence of σ can have a detrimental effect on alloy properties, most importantly brittleness. The platelike morphology of this phase is an excellent source of crack initiation and propagation, leading to the low-temperature brittle failure. Sigma-phase also contains high content of refractory metals such as Mo in the case of alloy 2, which causes the loss of solution strengthening of the matrix. Formation of σ in the substrate alloy might affect the carburization behavior of the alloy since it ties-up the two most important carbide-former elements in the alloy (i.e., Cr and Mo). As can be seen in the SEM cross-sectional image of alloy 2 after 100 h exposure to gas 5 (Figure 5-73), carbides are following a similar pattern as the σ, which clearly shows that as the carbon diffuses into the substrate alloy, it carburizes the σ rich in Cr and Mo first. It should be noted that the $M_{23}C_6$ type of carbide has a very similar crystal structure to the σ-phase [138].

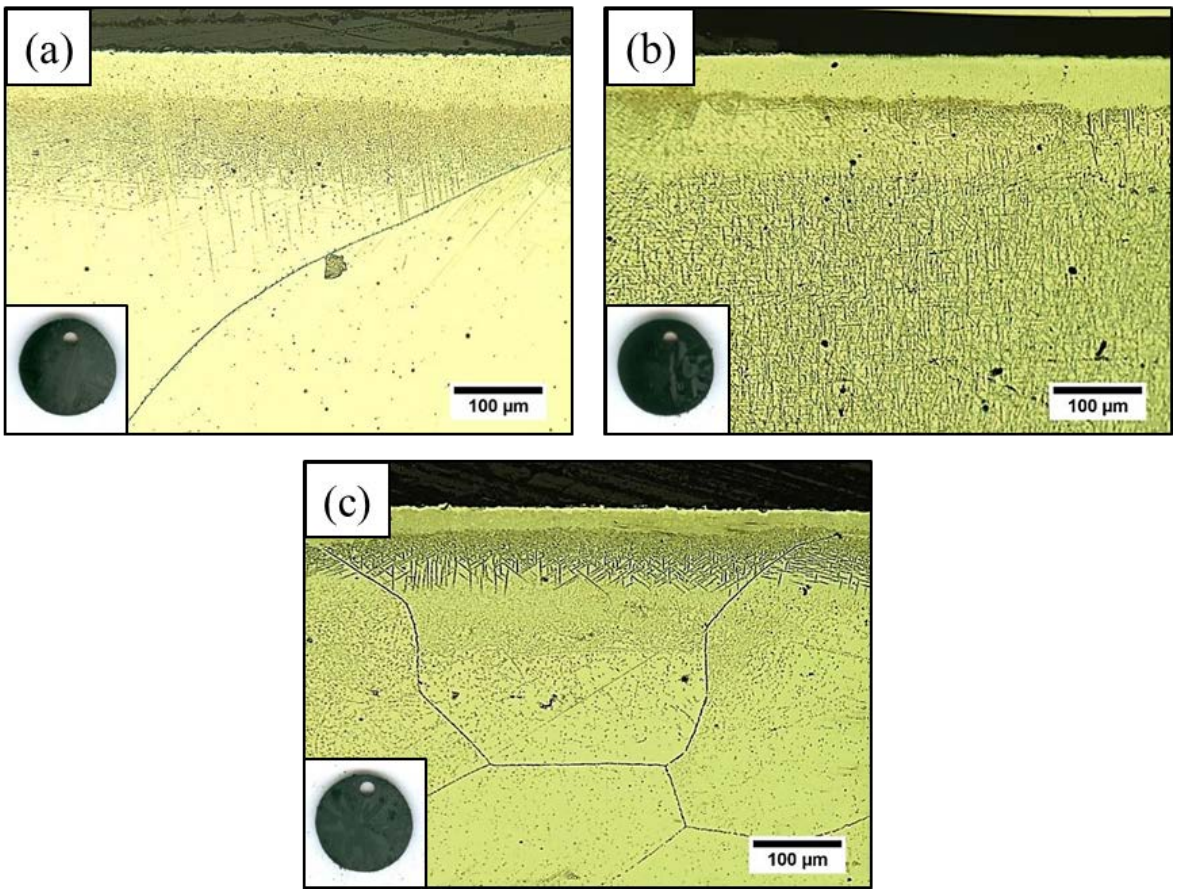

Figure 5-72 Optical micrographs of a) alloy 1, b) alloy 2 and c) alloy 3 after 100 h exposure to carburizing gas 5 at 871 °C, stain-etched using Murakami etchant

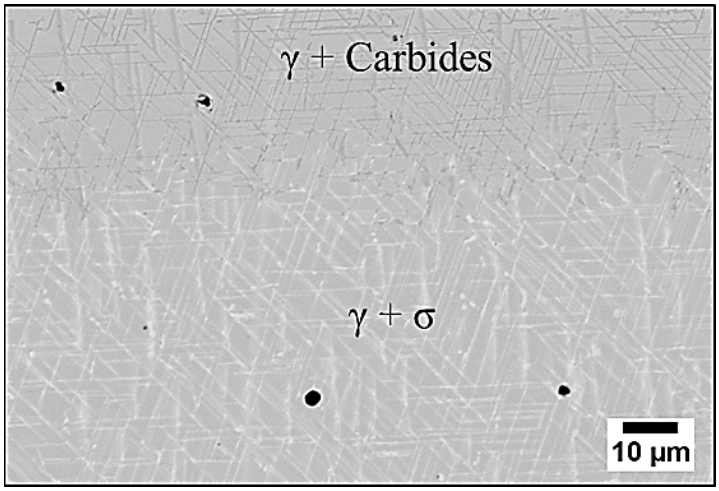

Figure 5-73 SEM cross-sectional micrograph of the reaction front in alloy 2 after 100 h exposure to carburizing gas 5 at 871 °C, transformation of the σ precipitates in alloy matrix to carbides can be observed

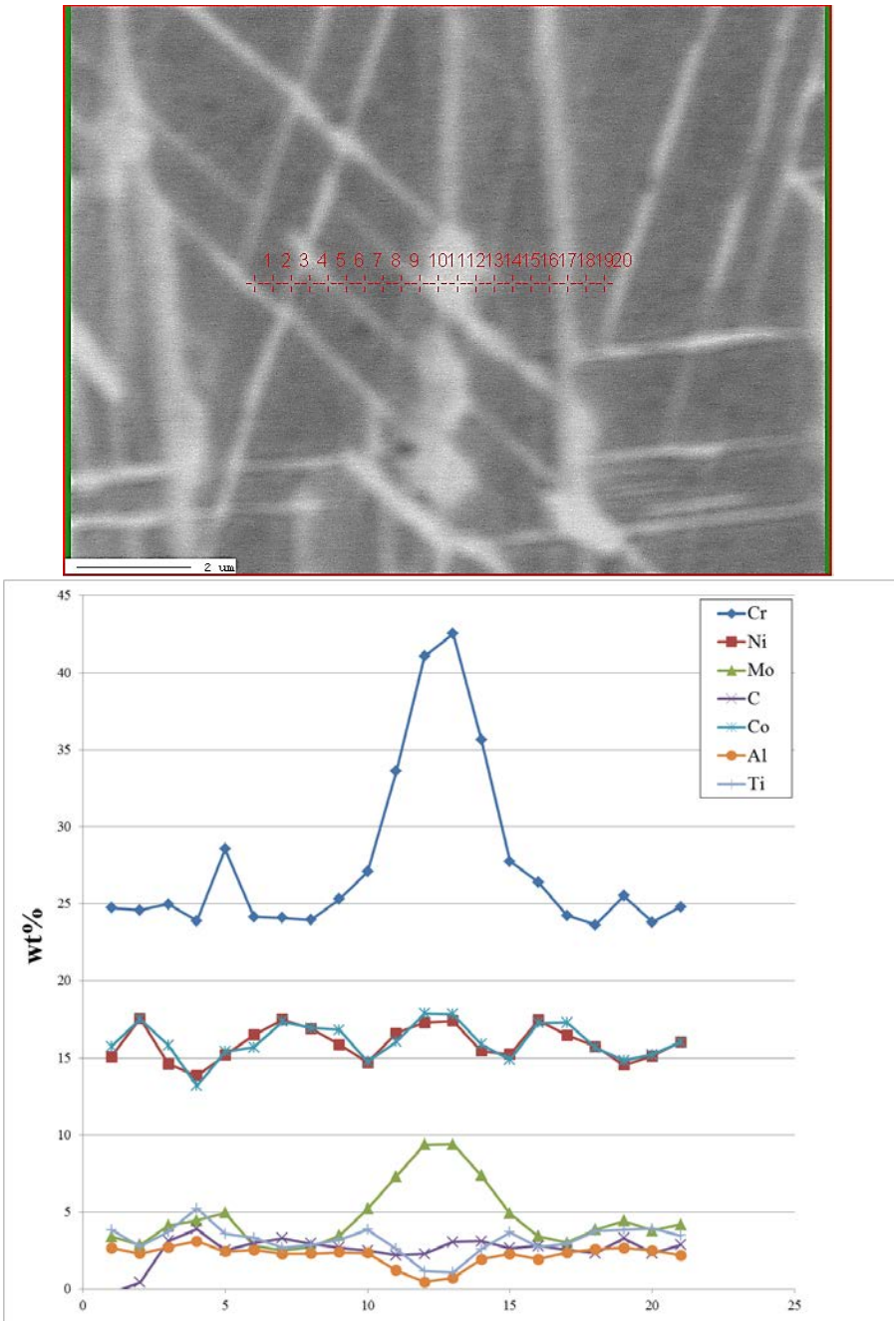

Figure 5-74 EPMA line scan of the Cr-Mo-rich precipitates in the bulk of alloy 2 prior to exposure to the carburizing gas 5

Table 5-6 Mole fraction of thermodynamically stable phases on alloys 1, 2, and 3 at 871 °C calculated using the Thermo-Calc software

Alloy	*Phase*	*Ni*	*Cr*	*Co*	*Al*	*Mole Fraction*
Alloy 1	γ	0.479	0.274	0.169	0.078	0.966
	γ′	0.648	0.072	0.075	0.206	0.034
Alloy 2	γ	0.442	0.313	0.168	0.078	0.812
	σ	0.125	0.666	0.200	0.009	0.105
	γ′	0.643	0.071	0.069	0.217	0.083
Alloy 3	γ	0.315	0.271	0.335	0.079	0.988
	B2	0.475	0.054	0.124	0.347	0.012

X-ray diffraction analysis of the external surfaces of samples after 100 h exposure revealed the presence of Cr_3S_2 and Cr_7C_3 in addition to peaks from the substrate γ phase. Electron microprobe analysis of the scale formed on alloy 2 (Figure 5-76) showed that the outer layer is mainly Cr-carbide and the inner layer is mainly Al-rich oxide with small amounts of Ti and Cr. The substrate metal is considerably depleted of Cr due to the formation of the Cr-carbide scale. The carbide scale on these alloys did not appear to affect the carburization resistance and alloys were carburized internally. In all cases, the internal carburization appeared in two zones, which based on their appearance after stain-etching might be the two different types of carbides, i.e., $Cr_{23}C_6$ in the inner zone and Cr_7C_3 in the outer zone.

Figure 5-77, Figure 5-78, and Figure 5-79 show SEM cross-sectional micrographs and corresponding EDS elemental maps of alloys 1, 2, and 3 after 100 h, 50 h, and 25 h exposure, respectively. According to these results, formation of a Cr-rich carbide layer followed by an Al-rich oxide sub-layer formed on all three alloys. In some cases, such as alloy 1, the Al-rich sub-layer is a thinner continuous layer and in other cases, such as alloy 2, it forms internally in the substrate alloy and it is thicker. The formation of the outer carbide scale above the oxide scale is of interest since Ni-Cr alloys are unlikely to form external carbide scales due to a high inward carbon flux [13]. Based on the behavior of these alloys at shorter exposure times, it can be seen

that this carbide scale and the subsequent Cr depleted region beneath are growing over time and form a continuous carbide scale at the surface after 100 h exposure.

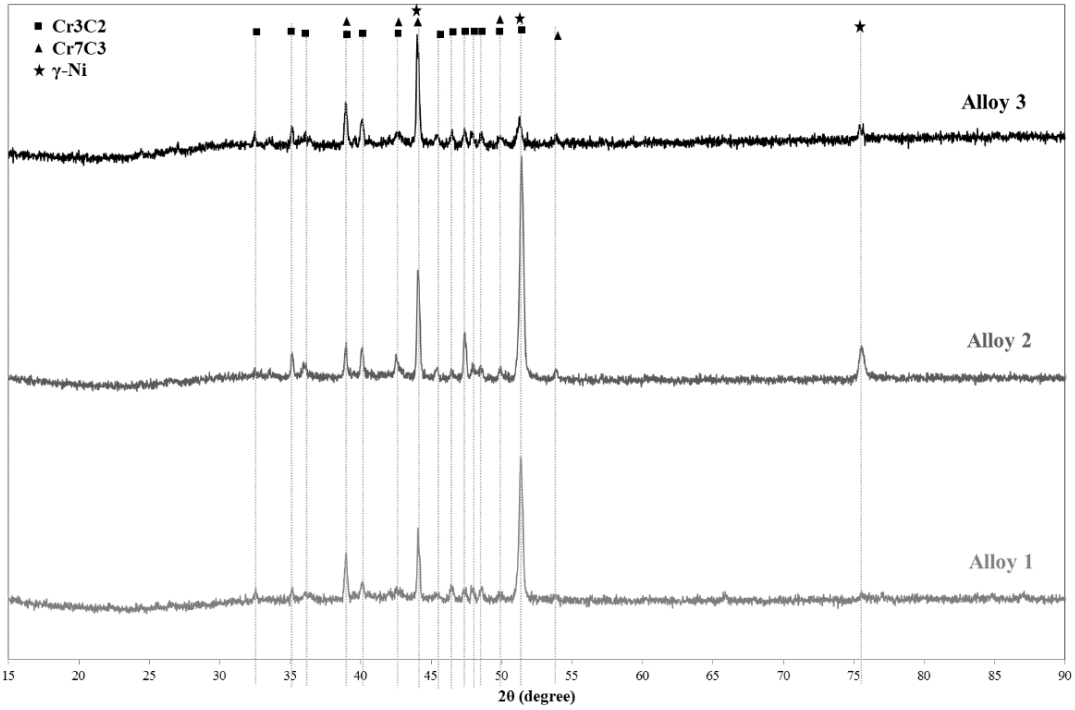

Figure 5-75 XRD spectra of the carburized surfaces of the tested model alloys

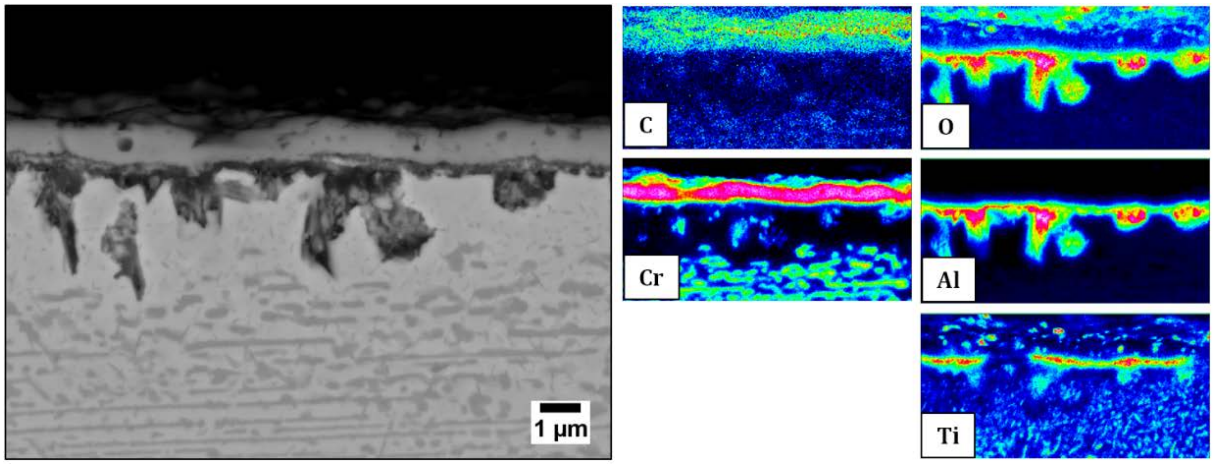

Figure 5-76 EPMA cross-sectional micrograph of alloy 2 after 100 h exposure to gas 5 at 871°C and WDS elemental mappings of the main alloying elements

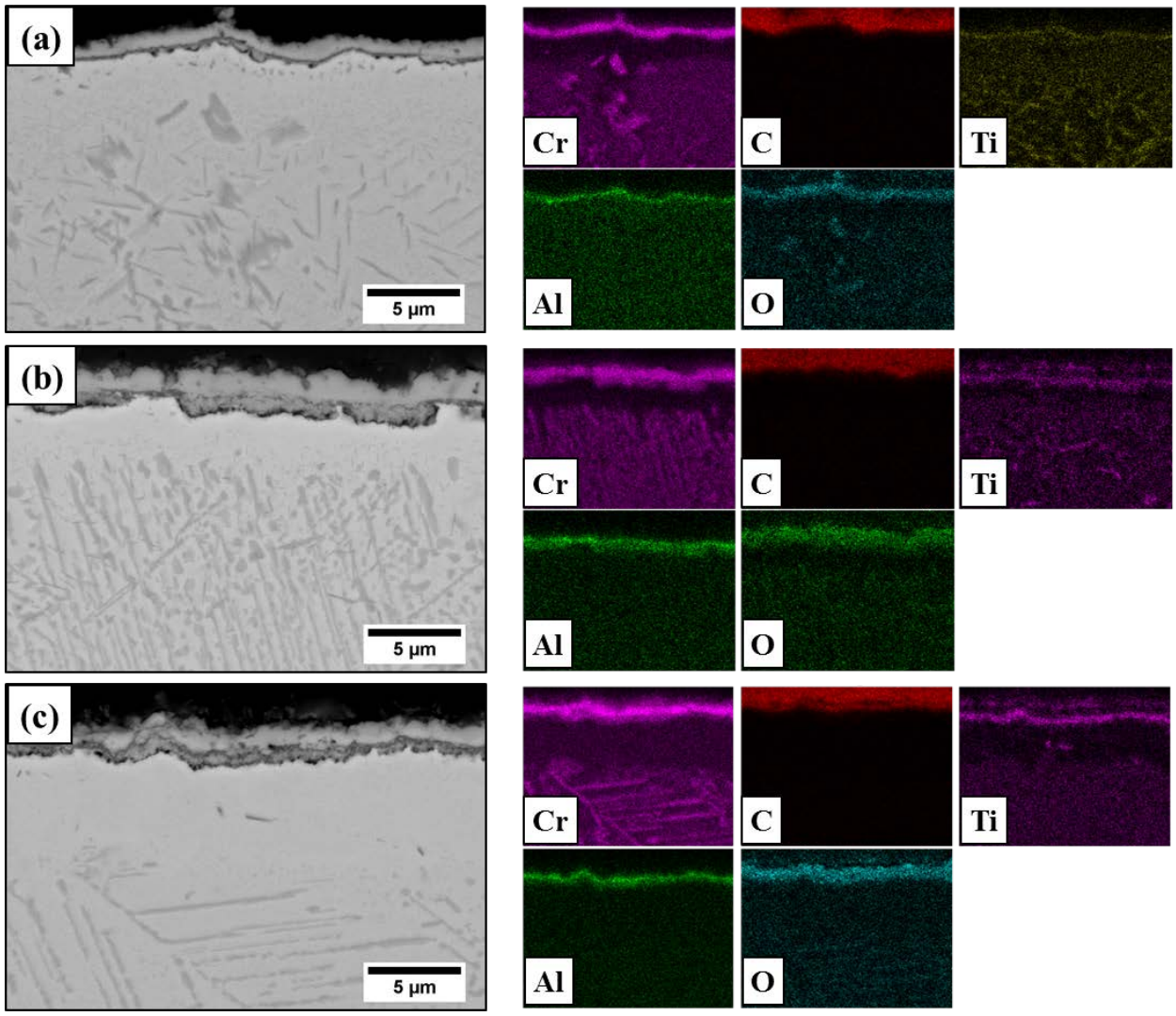

Figure 5-77 Scanning electron micrographs and EDS elemental maps of cross-sections of (a) alloy 1, (b) alloy 2, and (c) alloy 3 after 100 h exposure to gas 5

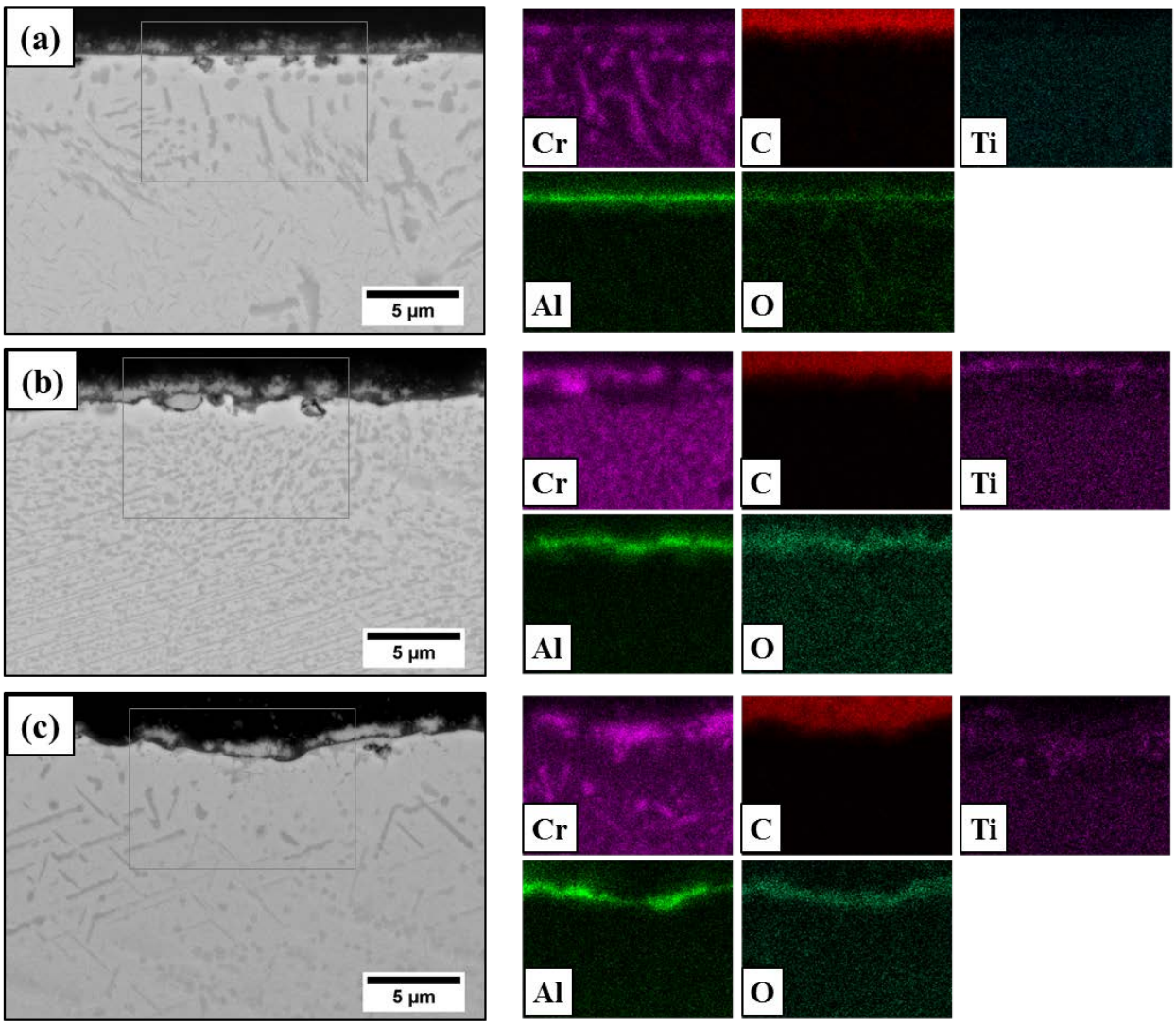

Figure 5-78 Scanning electron micrographs and EDS elemental maps of cross-sections of (a) alloy 1, (b) alloy 2, and (c) alloy 3 after 50 h exposure to gas 5

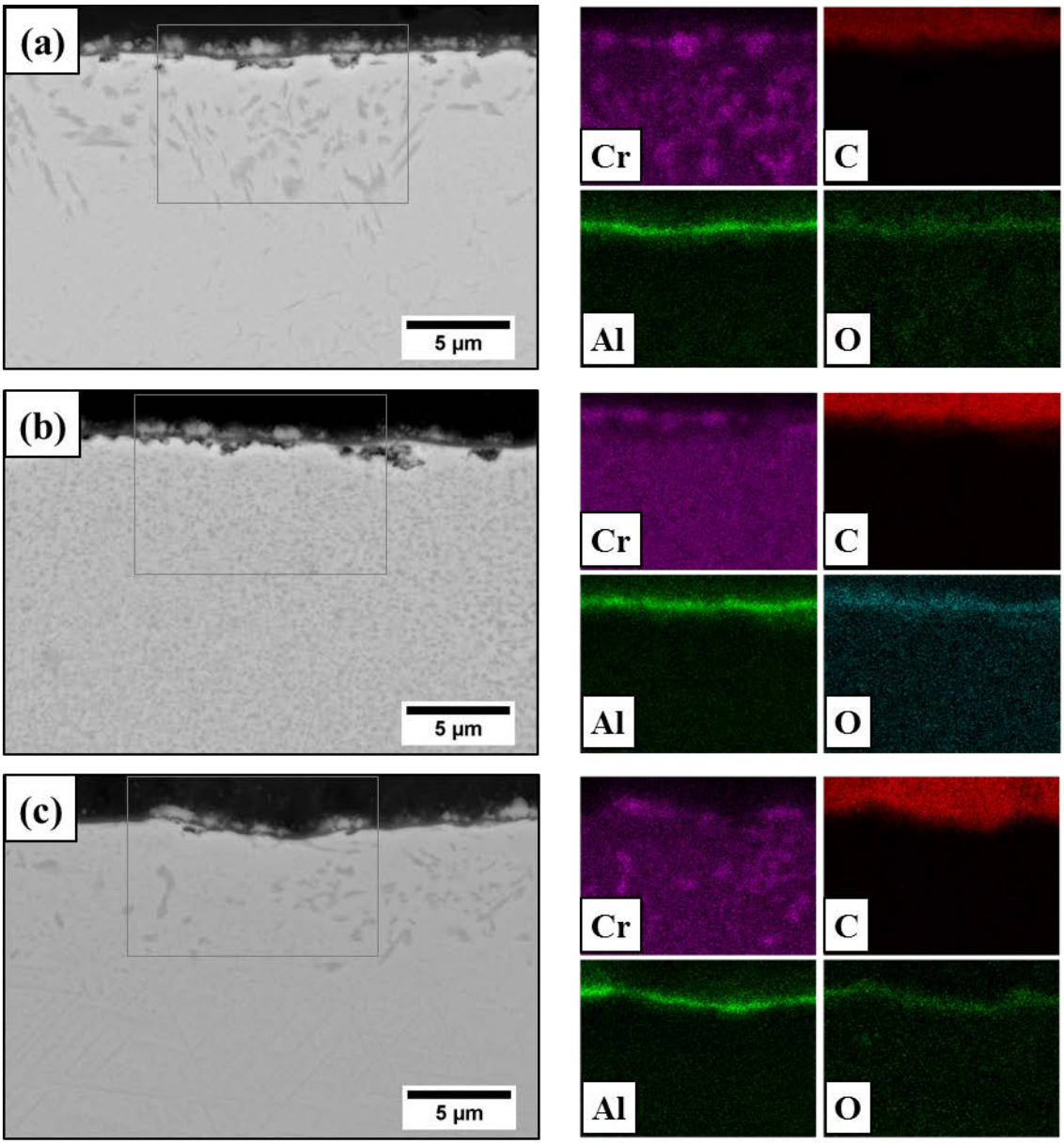

Figure 5-79 Scanning electron micrographs and EDS elemental maps of cross-sections of (a) alloy 1, (b) alloy 2, and (c) alloy 3 after 25 h exposure to gas 5 at 871 °C

In order to better understand the mechanism by which the external carbide layer is forming, alloy 2 after 1 h exposure to gas 5 was looked at more closely using XPS. Figure 5-80 shows the XPS narrow scan spectra of the Cr2p and C1s regions recorded on alloy 2 after 1 h exposure to gas 5 at 871 °C. At least three Cr-containing species were detected at the surface.

The spectra of Cr2p band represent a multicomponent structure. Peak deconvolution and analysis of literature data [139, 140, 141] on the binding energies of different chromium compounds revealed the existence of metallic chromium (574.3 eV) and chromium oxide (576.8 eV). The presence of Cr-carbide could not be confirmed since the binding energy of Cr_7C_3 (574.5 eV) is close to that of metallic Cr. However, the carbide-carbon peak for Cr_7C_3 at 283 eV was identified in addition to the strong carbon contamination peak at 285 eV. The C1s peak is unique and has energy of 283.3 eV, which is characteristic of carbidic carbon. According to these results, both Cr-oxide and Cr-carbide exists on the surface of alloy 2 at the initial stages. However, the EPMA results after 100 h exposure clearly showed the presence of a Cr-carbide scale only, followed by the alumina subscale.

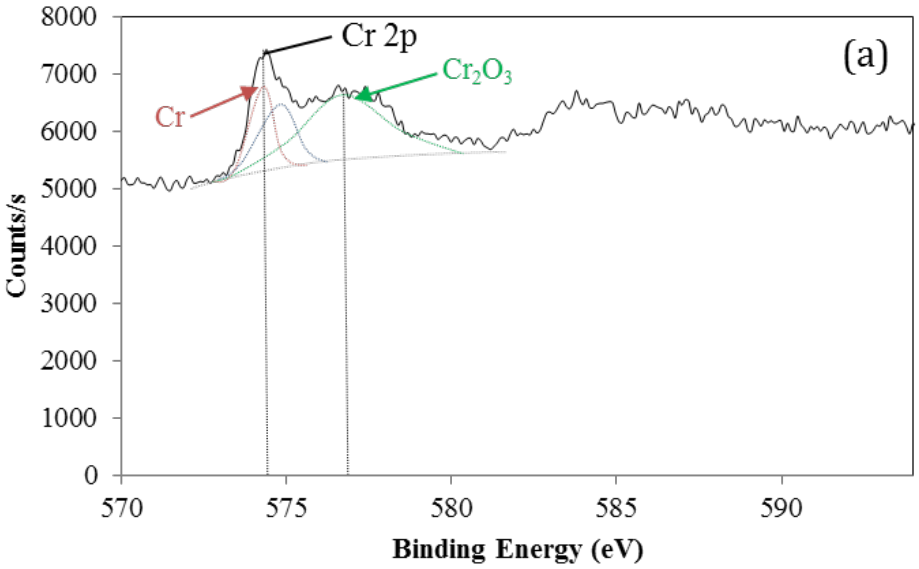

Continued.

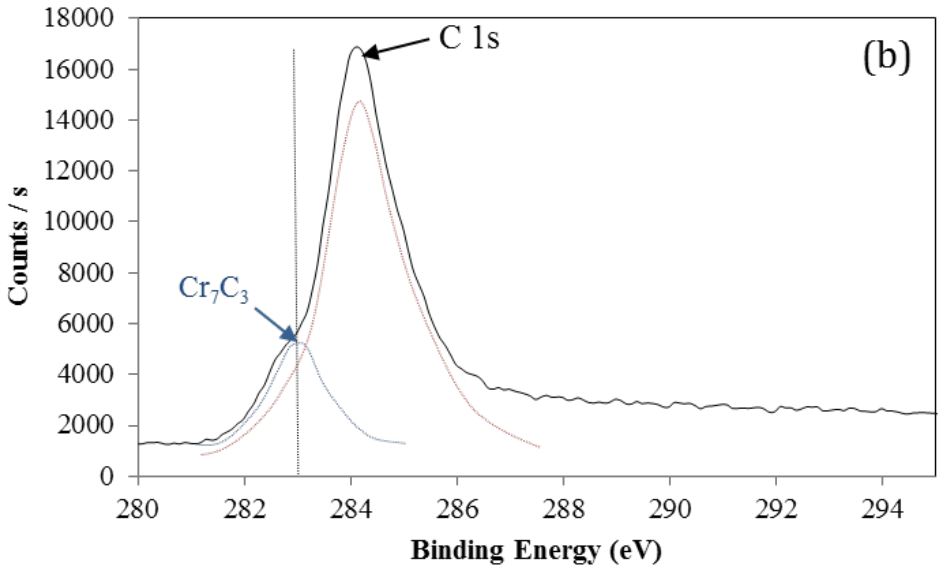

Figure 5-80 XPS spectra of (a) Cr2p and (b) C1s recorded from the surface alloy 2 after 1 h exposure in gas 5 at 871 °C

5.4.2.2 Model alloys modified with Si and higher Al contents

Modified model alloys with higher levels of Si (alloys 4 and 7) or Cr (alloy 5) or Al (alloys 6 and 8) showed that carburization behavior of these alloys could be highly improved under reducing conditions. In some cases, such as alloys 4, 6, and 7, carburization was almost completely prevented. This can be observed from the weight-gain results (Figure 5-81) obtained after 100 h exposure of these alloys to gas 5 in comparison with the first three model alloys. All modified model alloys showed weight gains less than 0.8 mg/cm^2, except for alloy 5, which has a composition similar to alloy 3 (28 wt. % Cr). The weight gain decreased considerably compared to alloy 3. However, it is still much higher than the other modified model alloys.

Figure 5-82 shows the stain-etched cross-sectional images of these alloys after 100 h exposure. Due to the multi-phase structure of these alloys, it is hard to distinguish between the internal carbides and different phases in the substrate alloy. However, there is a slightly different contrast between these phases near the surface (especially in alloy 5), which shows the internal

carburization zones. Based on these results, no significant internal attack could be observed on alloys 4 and 6. The depths of internal attack in alloys 7 and 8 are very low and approximately less than 50 µm. Alloy 5, however, shows an internal carburization zone of more than 100 µm. these results are in agreement with the observed mass gains. The as-received structures of these alloys before the exposure to gas 5 and chemical compositions of different phases in the as-received structure were previously reported in Figure 4-2. The main differences between these structures before and after exposure are the precipitation of the needle-shaped σ–phases in alloys 2, 6, and 8, which tend to precipitate during the service [138].

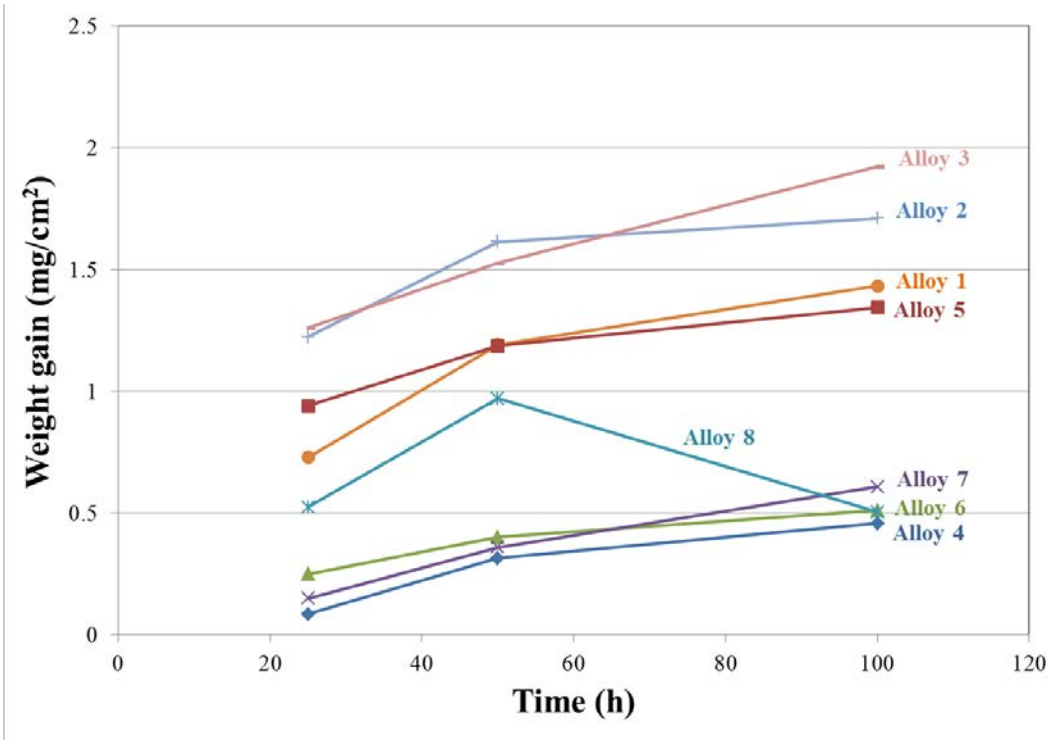

Figure 5-81 Mass change versus time for model alloys 1, 2, 3, 4, 5, 6, 7, and 8 after exposure to gas 5 at 871 °C

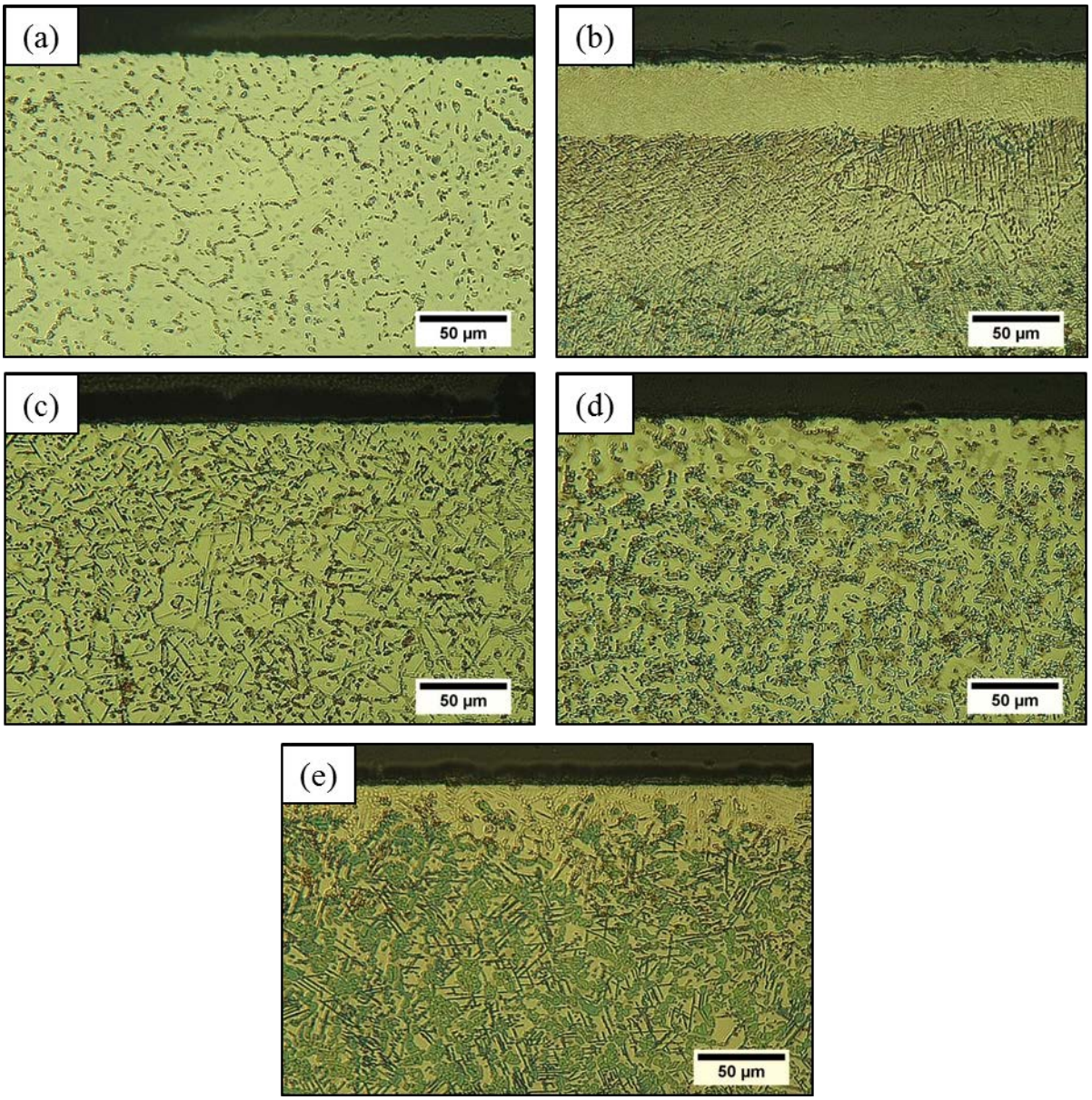

Figure 5-82 Optical micrographs of a) alloy 4, b) alloy 5, c) alloy 6, d) alloy 7, and e) alloy 8 after 100 h exposure to carburizing gas at 871 °C stain-etched using Murakami's etchant

Figure 5-83 shows electron microprobe cross-sectional images of selected systems: two Si-containing model alloys 4 and 7 with lowest weight gain after 100 h exposure and alloy 5 with the highest weight gain. It is seen that again a continuous and protective alumina layer formed on both alloys 4 and 7 (similar to what was observed after exposure to gas 2) and no internal or external carburization was observed even after 100 h exposure. By contrast, alloy 5 developed an

external Cr-carbide scale similar to alloys 1, 2, and 3, which was also followed by internal Al-rich oxide formation. Clearly, the scale was not protective enough to block the internal carbon diffusion and subsequent internal Cr-carbides were formed in the alloy.

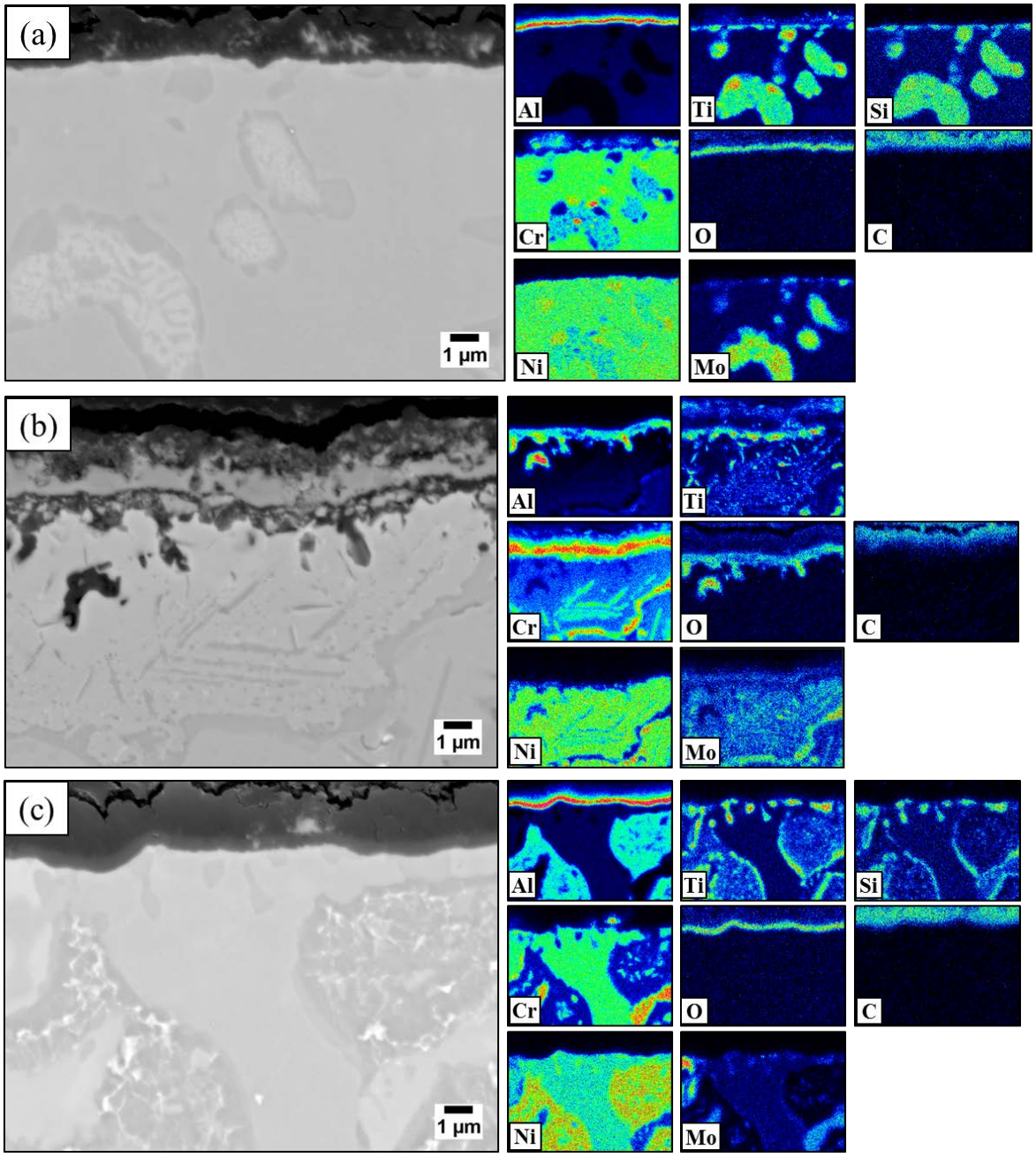

Figure 5-83 EPMA cross-sectional micrographs and WDS elemental maps of (a) alloy 4, (b) alloy 5, and (c) alloy 7 after 100 h exposure to gas 5

5.4.2.3 Discussion

According to the results observed for model alloys 1, 2, and 3, all three underwent some amount of carburization. The extent of carburization in alloy 1 was less than alloy 2 or 3. The reason might be the higher Ni content in alloy 1 causing a decrease in carbon permeability, as was discussed in Chapter 2.2. Although external scales formed on the surface of most of the alloys, formation of internal carbides showed that this scale does not provide very good protective behavior. Failure of this scale in providing protection against inward carbon diffusion is apparent from the internal carburization attack observed on alloys 1, 2, 3, and 5. Another interesting observation was the formation of the duplex scale on most of the alloys, in which an Al-rich oxide layer existed beneath an outer carbide layer. It has been reported [13, 45] that Al_2O_3 is thermodynamically stable at impurity levels of water vapor in the system, which is unavoidable in reaction gases. However, the formation of internal or external layer of alumina depends on the available flux of aluminum in the substrate alloy. Based on the thermodynamic stability of Cr-carbides and Al-oxide, it is always expected that the less stable phase (carbide in this case) should form beneath the highly stable oxide layer, as can be seen from the internal carburization zone. However, in this study it is seen that an external Cr-carbide layer forms at the surface and above the Al-rich oxide. The formation of this external carbide layer above an Al-rich oxide layer requires further explanation.

The XPS observations showed that these alloys undergo an initial oxidation during the heating stage, and for chromia forming alloys this leads to the formation of an initial layer of Cr_2O_3 on the surface. By selectively oxidizing Cr during this very early stage, Cr activity in the subsurface region of the alloy drops while Al activity should increase. As a result, Al-rich oxide can eventually nucleate at the scale/metal interface. As the temperature increases, the minimum

required oxygen potential for the formation of Cr_2O_3 increases. At the temperature of the reaction (871 °C), an oxygen potential of about 10^{-25} is needed for the formation of Cr_2O_3, which is unlikely for the existing impurity level of oxygen in the system (Figure 5-84). According to the Cr-O-C phase stability diagram in Figure 2-21 at 871 °C and comparison of the oxygen potential in the other gas mixtures used in this study, it is safe to say that the oxygen potential in gas 5 should be low enough for this gas to be in the carbide stable region. As a result, by increasing the temperature, the initially-formed chromium oxide (both during the flushing with Ar and heating stage) becomes unstable, as the minimum required oxygen potential for the formation of the Cr_2O_3 increases from 10^{-121} atm at room temperature to 10^{-25} atm at 871 °C (Figure 5-84). Therefore, conversion of the oxide film to carbide (thermodynamically more stable phase) will occur. Very little information is available on the mechanisms of the transformation of the initially formed oxide to carbide. According to Smith et al. [142], chromium carbide nucleates first on the outer surface of the oxide and then grows inward by consuming the oxide around it. When carbides make contact with the substrate metal, direct diffusion of base metal elements to the scale and inward carbon ingress could occur.

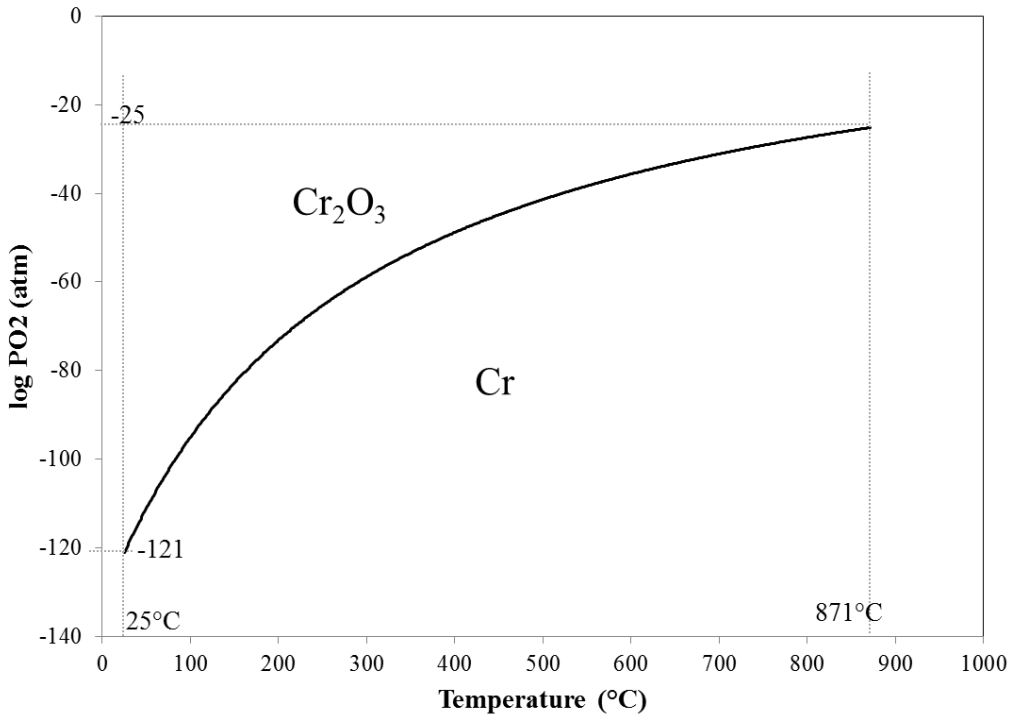

Figure 5-84 Dependence of the minimum required oxygen potential for Cr_2O_3 formation on temperature

In the case of Ni-based alloys and in the absence of iron, the thermodynamically stable carbide is Cr_3C_2. However, a previous study by Smith et al. [142] showed that on the binary Ni-Cr alloy after 400 min exposure, the thermodynamically stable Cr_3C_2 did not form and instead Cr_7C_3 was observed. The possible reasons for this occurrence were discussed as: first the structural compatibility of Cr_2O_3 with hexagonal Cr_7C_3 rather than orthorhombic Cr_3C_2 or secondly, lower activity of carbon since the alloy surface has not yet achieved full equilibrium with the gas mixture at this stage. The XPS analysis of alloy 2 after 1 h exposure to gas 5 showed the coexistence of Cr oxide and carbide in the scale, which clearly shows that the complete transformation of oxide to carbide is still in progress even after an hour into the reaction. Based on the XRD results after 25 h exposure, Cr_3C_2 exists at the surface of the sample which shows at least the partial conversion of the initially formed Cr_7C_3. The continued growth of this latter

carbide layer needs direct contact with the substrate metal in order to have chromium supply. When all the initially formed oxide transform to carbide, this contact will be achieved and the carbide scale will continue to grow outward.

It is important to compare the results observed on these alloys with the ternary alloys discussed before. Formation of an external carbide scale was not observed on the ternary Ni-Co-Cr alloys (Figure 5-42). These observations clearly show that the presence of Al, Ti and Mo play an important role in promoting the formation of this carbide scale. One plausible explanation is that the inward growth of the Al-rich oxide generates strain due to the lattice misfit between the oxide and substrate metal. As a result, the diffusivity in the sub-surface region is increased. This increase in diffusivity results in a more rapid outward diffusion of chromium to support the external carbide scale formation. Depletion of Cr in the subsurface layer could also be seen, which is due to the growth of the external carbide layer. However, it would be very difficult to argue the effect of stress on diffusion. One other possibility would be the interactive effect of minor elements on chromium diffusion. The presence of minor alloying elements such as Al, Ti and Si can promote the formation and stability of the initially formed Cr-oxide compared to Ni-Co-Cr alloys, as also discussed in previous Chapter 5.4.1. Li and Gleeson [143, 144] previously showed that the diffusive flux of a given element could be affected by the presence of other elements in the alloy. They showed that the effective diffusion coefficient of chromium were increased by a factor of 2 in the presence of silicon. No significant gradient in silicon developed, so no diffusional cross effects were involved. An alternative explanation is that the formation of a SiO_2. Therefore, the diffusion characteristics of chromium can be affected by concentrations and gradients of other elements in the substrate alloy. The multicomponent nature of these model alloys makes it very difficult to account for any cross-term effect. However, the experimental

results clearly show an increase in outward supply of Cr to the scale and supporting the continuous growth of the carbide layer compared to what was observed on ternary model alloys before and in the absence of minor alloying elements.

As discussed by other researchers [33, 34, 45], the carbide layer is not protective enough and both carbon and oxygen can diffuse through it. Thus, the subscale oxide layer continues to grow beneath this carbide layer. However, in none of the first three model alloys was the oxide scale continuous and protective; thus, both the carbide scale and internal carburization zone grew with time through outward diffusion of Cr and inward diffusion of carbon, respectively. When the external carbide scale forms, the carbon activity at metal/scale interface does not depend on the carbon activity of the environment, but rather is established through the carbide/alloy equilibrium via

$$Cr_3C_2 = 3\underline{Cr} + 2\underline{C} \tag{5-19}$$

$$\Delta G^{\circ} = \frac{a_{Cr}^3 \,.\, a_C^2}{a_{Cr_3C_2}} \tag{5-20}$$

However, the assumption that the carbide scale is continuous from the beginning is not valid since the shorter exposure times for these alloys showed that for up to 50 h exposure, the carbide scale is still not a continuous layer. Thus, substrate alloy is still in direct contact with the environment, unless it is covered by the alumina scale. Due to the relatively high atomic mobility within the carbide layer [45], carbon can easily penetrate into the alloy through this carbide layer and form a significant internal carbide precipitation zone, which may negatively affect the mechanical properties of the alloy.

Modification of these alloys with silicon in alloys 4 and 7 with 2.5% and 5% aluminum, respectively, almost completely blocked the carbon penetration into the substrate alloy by formation of a protective alumina scale. Increasing the chromium content up to 28% in alloy 5

compared to alloy 3 with 22% Cr, did not show a significant improvement on its carburization resistance and similar behavior to alloys 1, 2, and 3 was observed. This clearly shows that the only oxides which can apparently prevent carbon penetration in the alloy under carburizing environments are alumina and silica. Although alloys 6, 7, and 8 with 5%Al in their compositions were all alumina-forming alloys, alloy 4 with even less Al content of 2.5% showed the best resistance to carburization. Again, the excellent resistance of this alloy to corrosion is attributed to the formation of the alumina scale on top followed by the G-phase formation beneath.

5.4.3 Sulfidation-carburization-oxidation

5.4.3.1 Results

In this section, reactions in the more aggressive mixed gas 3 with high sulfur and carbon activities are considered. Figure 5-85 shows the mass change results up to 100 h exposure to gas 3 at 871 °C. The weight gains are much lower than the results obtained after exposure to gas 2. No sulfide formation was observed after 25 h exposure and only minor localized attack on the edges of the samples and on the casting defects in the middle was observed on alloys 1, 2, 3, 5 and 6 after 50 and 100 h exposures. Figure 5-86 shows the SEM surface images of these samples after exposure for 100 h to gas 3. Formation of sulfide nodules can be observed in a very small amount on alloys 1, 2, 3, 5, and 6. The cross-sectional micrographs of these alloys after 100 h exposure to gas 3 are shown in Figure 5-87. All alloys showed mostly protective behavior and no major sulfidation or carburization attack was observed.

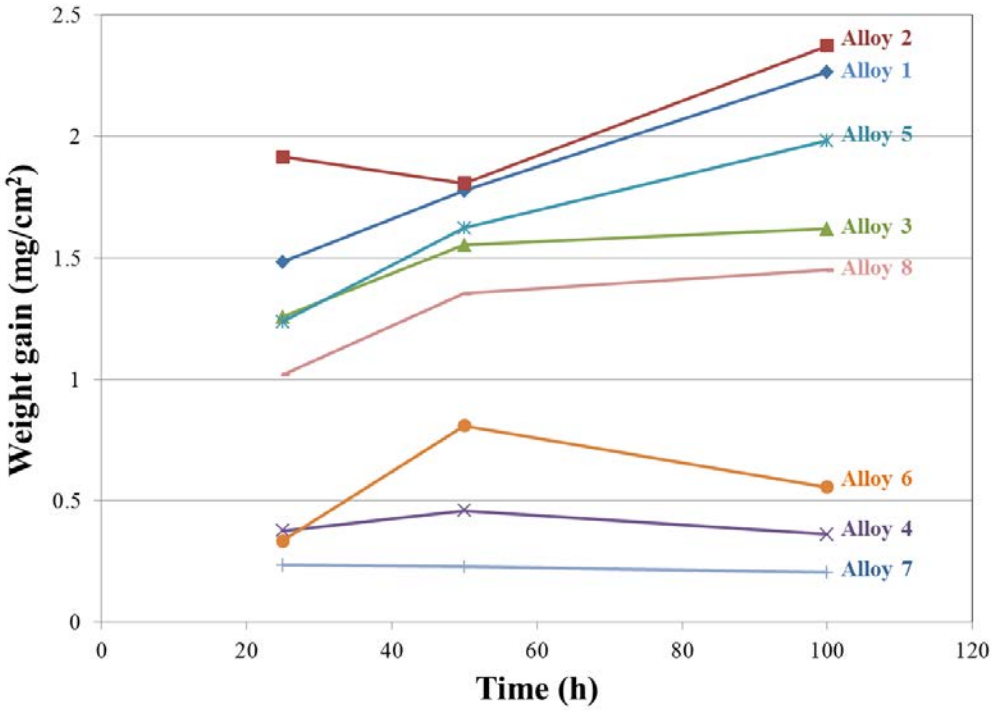

Figure 5-85 Mass change versus time for model alloys 1, 2, 3, 4, 5, 6, 7, and 8 after exposure to gas 3 at 871 °C

On the first three model alloys formation of a continuous chromia layer followed by internal Al-rich precipitates was observed. In addition, Ti enrichment was also observed on the outermost surface and at the alloy/scale interface. Formation of Cr-rich sulfide precipitates beneath the internal Al-rich precipitates shows that chromia layer was not impermeable to sulfur. It is noteworthy that the depth of the internal oxidation zone in alloy 3 was shallower after exposure in gas 3 compared to gas 2. Alloy 5, however, showed a slightly different behavior by formation of an outer chromia scale followed by a continuous alumina subscale, which was different from the internal oxidation of Al under gas 2 conditions. This suggest that by increasing the Co and decreasing the Ni content from the two alloys 1 and 2 to alloys 3 and 5, the depth of internal oxidation decreased under the conditions of gas 3 and alloy 5, to the extent that a continuous alumina layer could develop. Another important point is that even though pure

chromium and the Ni-Co-Cr model alloys showed a more aggressive type of attack in gas 3 compared to gas 2, addition of the minor alloying elements tends to dramatically change the resistance of these alloys, where they show a more protective behavior in the more aggressive environment of gas 3. Apart from minor sulfidation attack on the casting defects of some of these alloys, no additional sulfidation or carburization attack was observed even up to 100 h exposure. Formation of a continuous alumina layer was also observed on the two Si-containing alloys 4 (with 2.5% Al and 3% Si) and 7 (with 5% Al and 3% Si) and no Ni- or Co-sulfide nodules were observed at any location of these alloys. Alloys 6 and 8 (with high Al content of 5 wt. %) also formed an external alumina scale. However, some internal attack along the precipitates in the substrate alloy was detected.

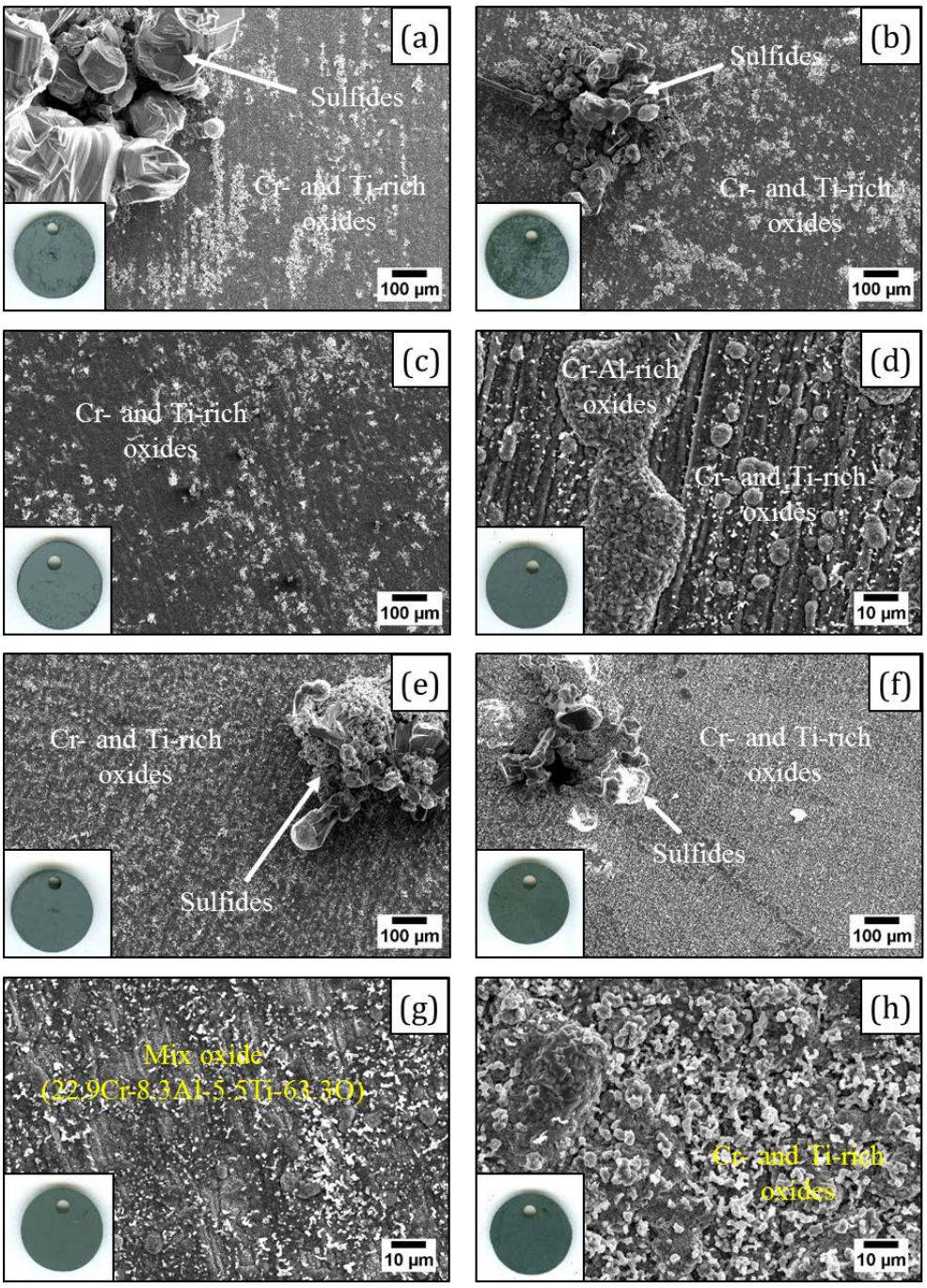

Figure 5-86 SEM surface images of: (a) alloy 1, (b) alloy 2, (c) alloy 3, (d) alloy 4, (e) alloy 5, (f) alloy 6, (g) alloy 7, and (h) alloy 8 after 100 h exposure to gas 3 at 871 °C

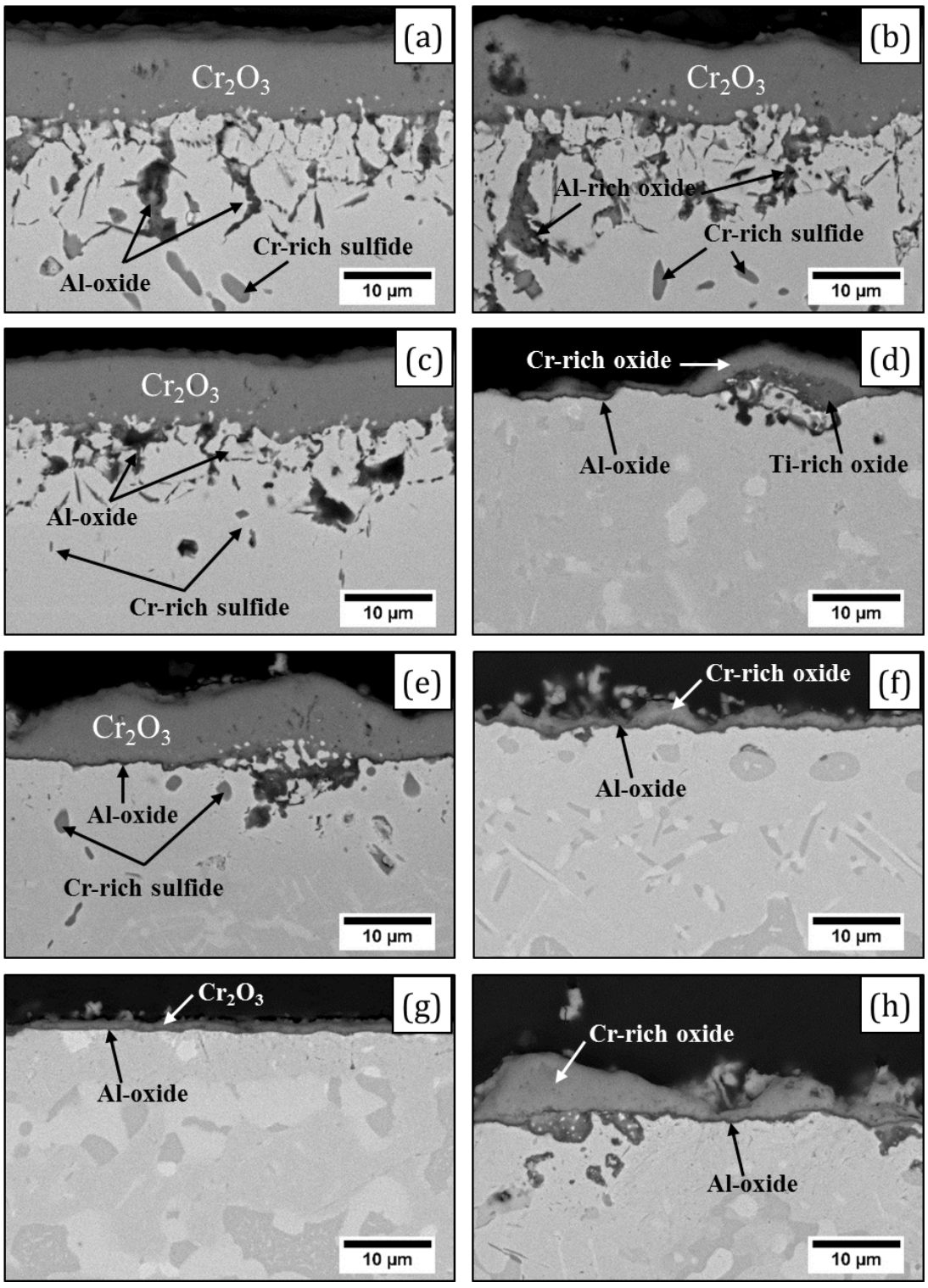

Figure 5-87 cross-sectional SEM micrographs of (a) alloy 1, (b) alloy 2, (c) alloy 3, (d) alloy 4, (e) alloy 5, (f) alloy 6, (g) alloy 7, and (c) alloy 8 after 100 h exposure to gas 3 at 871 °C

5.4.3.2 Discussion

The observed corrosion behavior of the model alloys in gas 3 were not anticipated. No major sulfidation or carburization attack was observed on any of the model alloys, even after 100 h exposure. In order to better understand the behavior of these alloys in the gas 3 environment, it is worthwhile to re-visit the observed corrosion mechanism of other systems in this environment, and also the behavior of these alloys in the previously discussed gas 2 environment with a lower carbon activity.

In Chapter 5.2, it was shown that gas 3 has higher H_2O and H_2S fluxes but lower oxygen and sulfur partial pressures compared to gas 2. However, the combination of higher carbon activity in this gas mixture and lower P_{H_2O}/P_{H_2S}, was inferred to be the main reason for the extreme attack observed on pure chromium. Under such conditions, sulfides and oxides can grow together and form a duplex-type scale, since the overgrowth of the metastable sulfide by the more stable oxide is inhibited. The co-formation of sulfide and oxide in the outer scale provides rapid transport paths for carbon toward the substrate alloy and it follows a rapid internal attack. Studying the behavior of ternary model alloys in this environment (Chapter 5.3) also confirmed that the formation of Cr-rich carbides at the initial stages of the reaction serves to decrease chromium availability for Cr_2O_3 formation and thus make the alloy susceptible to sulfidation. On the other hand, in Chapter 5.4.1, it was shown that addition of minor alloying elements of Al, Ti, and Mo could shift the Cr-sulfide/Cr-oxide kinetic boundary to the lower oxygen partial pressures and toward the thermodynamic boundary by stabilizing the oxide and increasing the incubation period for the partial occurrence of sulfidation attack under the conditions of gas 2. However, the question here is: Why do these model alloys show a more protective behavior in

the more aggressive environment of gas 3 (with higher carbon activity and lower oxygen potential) compared to gas 2?

The results after exposure to gas 3 clearly showed that none of the model alloys showed any type of oxide scale breakdown in the flat portions of the sample compared to what was observed after exposure to gas 2. The measured weight gains of most of the model alloys after 100 h exposure dropped dramatically from gas 2 to gas 3. The weight gains of alloys 4 and 7 after exposure to both environments of gas 2 and 3 were almost comparable, since these model alloys showed complete protection in both environments by formation of a continuous alumina scale. However, the difference between these two environments was more distinctive in the case of alloys 1, 2, 3, and 5. Figure 5-88 and Figure 5-89 show a comparison of the results obtained on these four model alloys (all with similar amounts of minor alloying elements of Al, Ti, and Mo but with different Ni:Co ratio and Cr contents) after exposure to gas 2 or 3. From Figure 5-88 it can easily be seen that the sulfidation attack and formation of sulfide nodules were decreased dramatically or, in some cases, almost completely prevented after exposure to gas 3. In addition, Figure 5-89 clearly shows that by decreasing the Ni:Co ratio to near unity, the total amount of degradation in these alloys (in both cases of gas 2 and 3) decreases. The reason for such behavior was discussed in Chapter 5.4. Previous studies [22, 23, 24, 73] had shown that increasing the cobalt content in nickel-base alloys reduces the rate of sulfur diffusion in the matrix and also, decreasing the Ni content of the alloy reduces the risk of formation of Ni-sulfide and Ni-Ni_3S_2 eutectic [70]. Thus, much less sulfidation attack and liquid sulfide formation was observed in the model alloys with lower Ni:Co ratio.

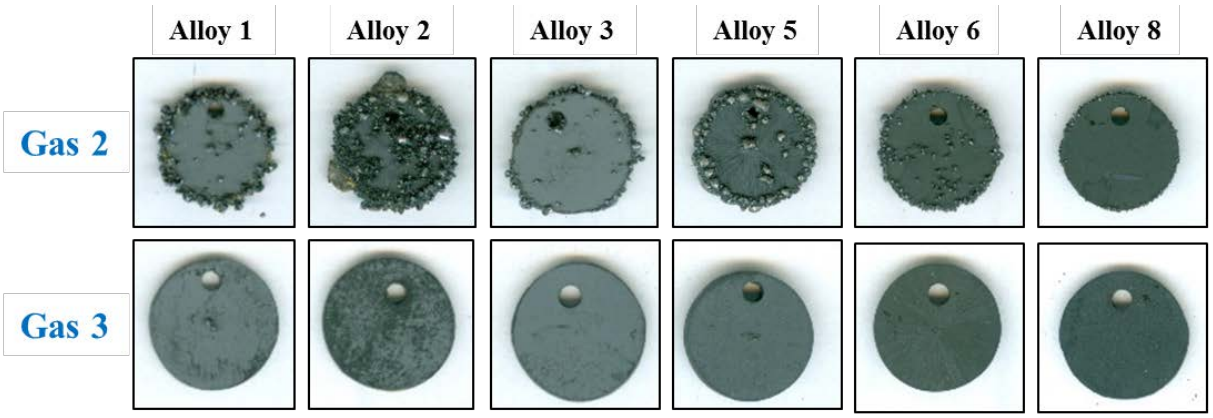

	Alloy 1	Alloy 2	Alloy 3	Alloy 5	Alloy 6	Alloy 8
Ni/Co	2.9	2.6	0.95	0.95	0.95	0.95
Cr	22	28	22	28	22	28
Al	2.5	2.5	2.5	2.5	5	5

Figure 5-88 Comparison of the behavior of selected model alloys in gas 2 and 3. Above surface images show that the sulfidation attack on alloys 1, 2, 3, 5, 6, and 8 was decreased from gas 2 to gas 3, where almost no sulfide nodules can be observed after exposure to gas 3

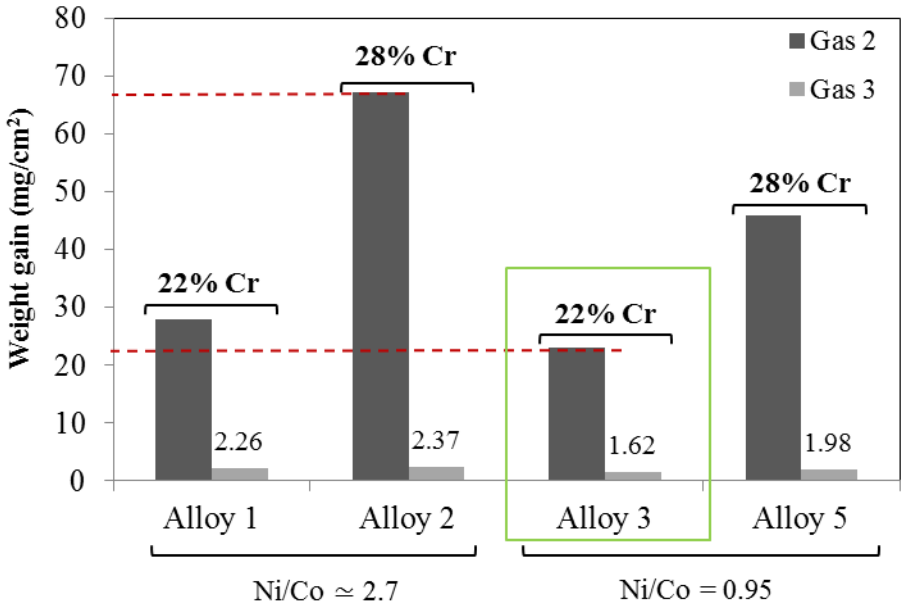

Figure 5-89 Comparison of the mass change results of alloys 1, 2, 3, and 5 in gas 2 and 3. This diagram shows the effect of gas composition, Ni:Co ratio and Cr content of the alloy on the total degradation observed after 100 h exposure at 871 °C for gas 2 and 3

Another important observation was the decrease in the extent of internal oxidation of Al in alloy 3 and complete transition from internal to external oxidation in alloy 5 when changing from gas 2 to gas 3. Figure 5-90 shows the cross-sectional micrographs of alloys 3 and 5 after exposure to gases 2 and 3 for comparison. Based on the Wagner's theory, the minimum value of Al concentration required for the formation of an external scale can be calculated using Eq. 2-29. Accordingly, this value is related to the oxygen solubility at the alloy surface and the diffusion coefficient of aluminum in the substrate alloy. Thus, a decrease of about two orders of magnitude in oxygen partial pressure from gas 2 to gas 3, can result in a decrease in oxygen solubility at the surface during the initial stages of the reaction, which results in a decrease of the minimum Al content necessary for formation of an external alumina layer. Initial formation of an external alumina scale on the sample surface can result in a decrease of the amount of transient oxides and sulfides (fast growing Ni and Co oxides and sulfides) and also Cr-rich carbides, thus, resulting in the formation of a more protective oxide scale compared to gas 2 environment.

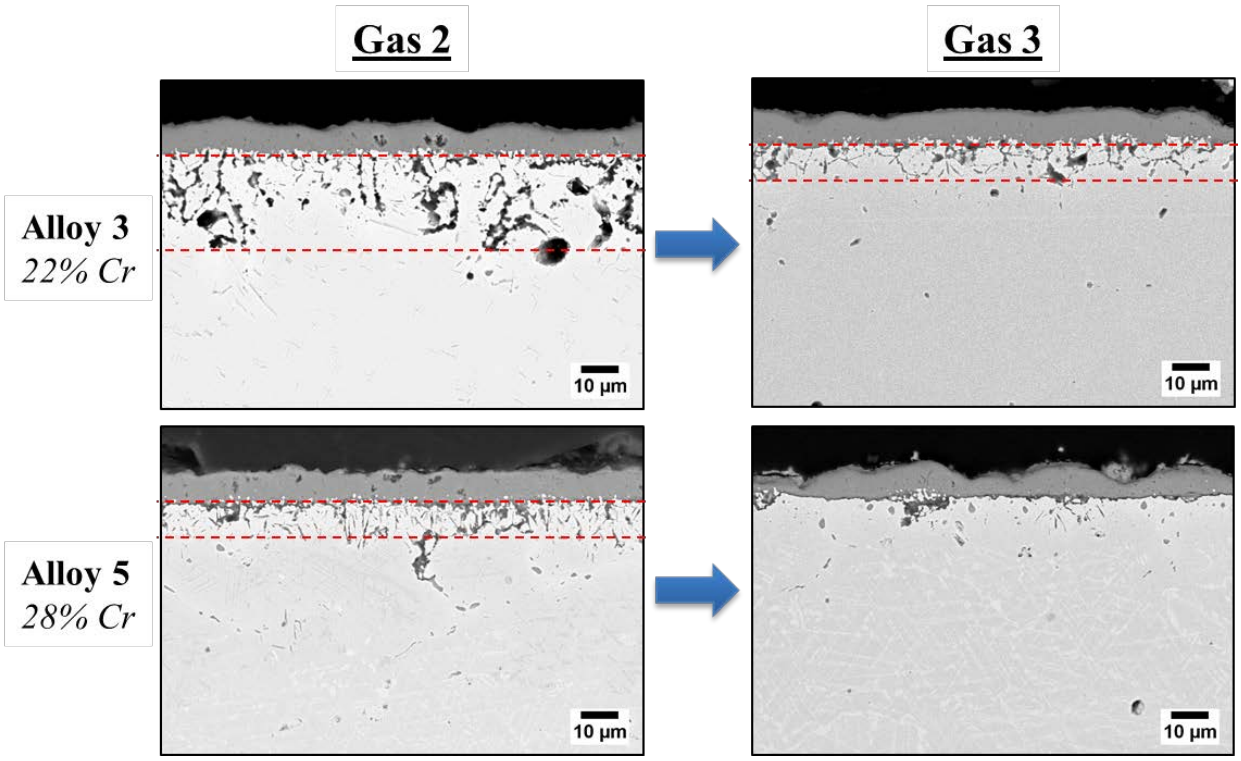

Figure 5-90 Comparison of the extent of internal oxidation of Al in alloys 3 and 5 after 100 h exposures in gas 2 and 3 at 871 °C using the SEM cross-sectional micrographs of these samples

In addition to the oxygen partial pressure, both major and minor alloying elements can also affect the transition between internal to external oxidation by affecting both the diffusion coefficient of aluminum in the substrate alloy, and the solubility of different gas species at the surface. Figure 5-91 shows a comparison of the scales formed on alloys 1, 2, 3, and 5 after exposure for 100 h to gas 3. It should be noted again that the aluminum content in all these four alloys are the same and it is about 5.1 at. %. The major differences are the Ni:Co ratio, which is lowered from about 2.7 in alloys 1 and 2 to about 0.95 in alloys 3 and 5, and the chromium contents, which is 22 wt. % in alloys 1 and 3 and 28 wt. % in alloys 2 and 5. Considering the abovementioned differences, Figure 5-91 shows that increasing the cobalt and chromium contents results in an effective decrease in the internal oxidation of aluminum, where in alloy 5 a

complete transition from internal to external oxidation was observed and a continuous alumina sub-scale was formed.

The effect of chromium content on aluminum oxidation has been studied previously by Guan and Smeltzer [145]. They showed that sufficient Cr addition reduces the oxygen solubility, and alters the oxygen distribution in the ternary Ni-Cr-Al alloys to avoid the oxygen supersaturation necessary for the onset of internal oxidation in the alloys. Thus, by increasing the Cr content from 22 wt. % in alloy 3 to 28 wt. % in alloy 5 the establishment of the external alumina scale can be easier. However, the effect of cobalt on transition from internal to external oxidation of aluminum was more pronounced in the results observed after exposure to gas 3. Thus, it is important to study the effect of Ni and Co concentrations on the mobility of Al in the substrate alloy. Figure 5-92 shows a CALPHAD-computed plot of Al mobility vs. Ni content for a $Ni_xCo_{1-x}CrAl$ alloy with a fixed Al and Cr contents of 5 at.% and 24 at.%, respectively, at 900 °C. It can clearly be seen that the Al mobility increases as the cobalt content of the alloy increases. Increasing the Al mobility, together with the lower oxygen partial pressure in the environment, enables aluminum to diffuse to the surface faster and to establish a complete layer of alumina at the alloy surface. Establishment of a more protective alumina scale can decrease the inward transport of carbon and sulfur and, thus, provides a better protection against sulfidation and carburization attack, which was previously observed in this environment on ternary model alloys. It also increases the time to breakaway corrosion in the modified model alloys (with addition of minor alloying elements) compared to gas 2. However, a more accurate analysis of the early stage reaction in these environments is needed in order to have a better understanding of how the interaction of minor alloying elements and different species in the gas phase can change the boundary conditions resulting in the observed protective behavior.

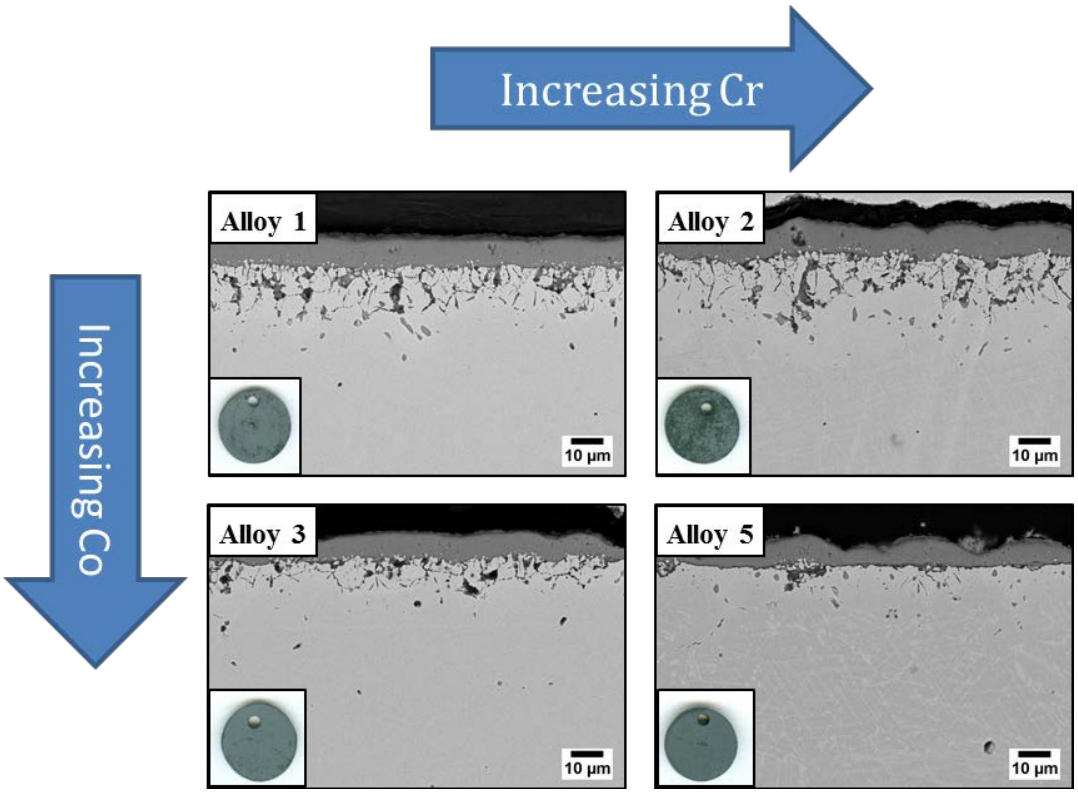

Figure 5-91 Effect of alloy composition on the extent of internal oxidation of Al in four alloys of 1, 2, 3 and 5 after 100 h exposure to gas 3 at 871 °C

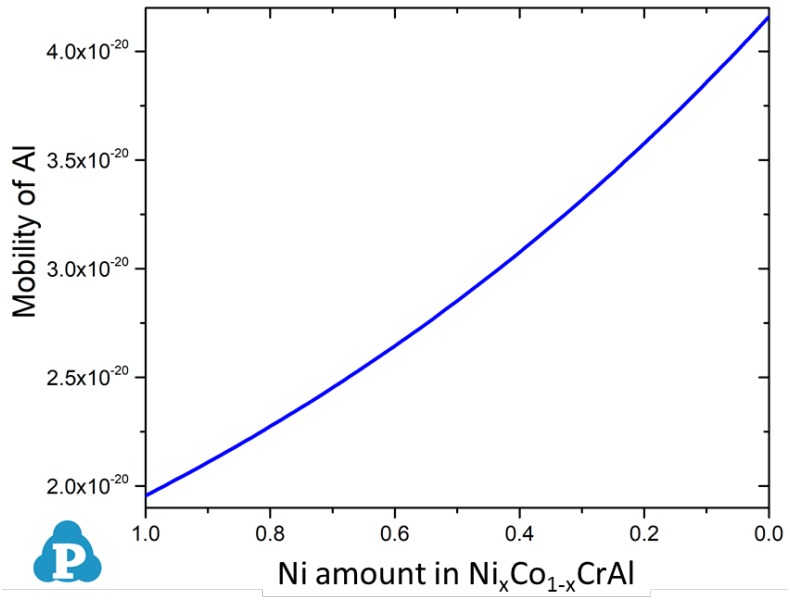

Figure 5-92 Calculated Al mobility vs Ni ratio for a $Ni_xCo_{1-x}CrAl$ alloy with a fixed Al and Cr contents of 5 at. % and 24 at.%, respectively, at 900 °C

6.0 CONCLUDING REMARKS

6.1 COMMERCIAL ALLOYS STUDY

Six commercial chromia- and alumina-scale forming alloys were tested at 871 °C (1600 °F) in three main environments of N_2-15%CO-3%H_2-0.6%CO_2-0.12%H_2S + 0.6% H_2O (gas 2), H_2-25%CH_4-14.8%N_2-4%CO-0.6%CO_2-0.6%H_2S + 3% H_2O (gas 3), and Ar-5%H_2-2%C_3H_6 (gas 5), all very reducing with different levels of oxygen, sulfur, and carbon potentials. The effects of both major and minor alloying elements on sulfidation and carburization resistance of these alloys were studied. The following conclusions can be drawn:

- As a general conclusion, Ni- and Ni-Co-based alloys showed much better corrosion resistance in all three environments compared to Fe-containing alloys (HR-120 and HR-224).
- Increasing the cobalt content in alloys 617 and HR-160 clearly increased the resistance of these alloys to sulfidation attack under conditions of gas 2. This is mainly due to the fact that decreasing the Ni content can decrease the risk of formation of Ni_3S_2 and, thus, the low temperature Ni-Ni_3S_2 eutectic (645 °C).
- It was also shown that protection is very dependent on the ability of a given alloy to form a continuous and tenacious oxide scale (Al_2O_3 is best). However, addition of higher concentrations of Cr, Al, or Si solely, cannot account for a good resistance to sulfidation and consideration of both major and minor alloying element effects is necessary.

- Alloys HR-120 and HR-224, with high Fe concentrations, both showed severe degradations by formation of the base-metal sulfides. It is deduced that the presence of carbon in all of the environments tested in this study makes the Fe-containing alloys susceptible to a more severe attack due to the intrinsically lower carburization resistance of these alloys. An increase in the carbide formation at the initial stages of the reaction can decrease the Cr available in the alloy (i.e., the “free Cr”) for the formation of a protective oxide and further resistance to sulfidation attack.
- Exposure of the commercial alloys to the predominantly carburizing environment clearly showed that all chromia-scale forming alloys undergo some extent of carburization attack. However, increasing the Cr-content of the alloys can decrease the depth of internal carburization.
- Alumina-scale forming Ni-base alloy 214 almost completely prevented any carburization attack due to formation of a continuous alumina scale. It was found that alumina is the only protective oxide scale that can prevent carbon penetration into the substrate alloy.
- Addition of silicon can decrease the carbon penetration depth by decreasing the solubility of carbon in the substrate alloy. Combination of Ni-Co-substrate and high Cr and Si contents in alloy HR-160 led to the good carburization resistance observed on this alloy.
- A combination of both good sulfidation and carburization resistance is needed for an alloy to withstand the conditions of the gas 3 environment. As a result, a Ni-Co-base alloy with high Cr concentration (similar to alloy HR-160) and possibly addition of other minor alloying elements (Al and Si) for reducing the carburization resistance is necessary for protection in mixed gas environments.

6.2 ENVIRONMENTAL EFFECTS

Due to the complicated effects of both environment and alloy composition at the same time, the direct effect of different gas species were first studied separately using the simple case of pure Cr and following conclusions were drawn:

- High-temperature exposure to mixed sulfidizing-carburizing-oxidizing environments is a complex and dynamic process that requires oxide-scale formation for protection. However, the mode of growth and kinetics of oxide formation is clearly affected in the presence of sulfur and carbon in the atmosphere.
- Gas 2 with the P_{H_2O}/P_{H_2S} ratio of 1.1 was located close to the kinetic boundary of Cr-oxide/Cr-sulfide at 871°C, but still in the oxide stable region. The formation of a relatively thick chromia scale was observed after 25 h exposure. Kinetic analysis that considered gas supply and consumption showed that under such conditions H_2O or CO_2 is the main reactant in the environment. The kinetically easier dissociation of H_2O leads to the inference that it is the principal reactant. The observed chromia scale was shown to form by a combination of both outward and inward growth, where the outer scale growth is dictated by cation diffusion and the inner zone, on the other hand, is the result of the oxide growth within the metal-consumption zone.
- It was shown that the fine-grain structure of the chromia scale formed in the gas 2 environment cannot solely account for fast oxidation kinetics observed in the mixed environments. The adsorbed sulfur affecting the grain boundary structure of the scale and the higher diffusion coefficient of the grain boundaries aligned in the growth direction of the scale are inferred to affect the grain-boundary diffusion.

- Void formation at the alloy/scale interface was observed due to the initial outward scale growth. Sulfur adsorption at the scale/metal interfacial voids and sulfur poisoning at the void surfaces is believed to be the main reason for an initial period of oxide formation inside the voids being impeded.
- Exposure of chromium to the gas mixture 3 with a relatively low P_{H_2O}/P_{H_2S} ratio of 0.5 resulted in a more aggressive attack than what was observed for gas mixture 2 with a P_{H_2O}/P_{H_2S} ratio of 1.1. Formation of a duplex Cr-oxide/Cr-sulfide outer scale indicates that the kinetic boundary of Cr-oxide/Cr-sulfide in Cr-O-S phase stability diagram is slightly shifted to the right, where gas 3 is located on this boundary. Increasing the carbon activity in addition to the lower P_{H_2O}/P_{H_2S} in gas 3 caused the co-formation of oxide and sulfide in the external scale and deep oxide-carbide-sulfide inner attack zones.

6.3 Ni-Co-Cr MODEL ALLOYS

Based on the observed results on commercial alloys, two ternary Ni-Co-Cr model alloys were designed to study the effect of major alloying elements under complex gas atmospheres. The corrosion behavior of these alloys was studied in all five environments with different oxygen, sulfur, and carbon potentials. The following conclusions can be drawn:

- Major sulfidation attack was observed on both alloys after exposure to mixed gases 2 and 3 by formation of liquid base-metal sulfides. The attack was more localized on both alloys under conditions of gas 2 with a lower carbon activity compared to gas 3.
- Increasing the Cr concentration from 22% to 28% in the Ni-Co-Cr model alloys is beneficial in providing a more protective barrier for substrate alloy against liquid sulfide attack in both

environments of gases 2 and 3. However, the degradation was still quite severe on both alloys.

- The effect of carbon in mixed gas atmospheres was studied in more detail by conducting a two-stage test in gases 5 and 2. In environments with a higher carbon activity, formation of Cr-carbides at the early stages of reaction serves to decrease Cr availability for Cr_2O_3 formation and, thus, make the alloy susceptible to sulfidation.
- When sulfur diffuses into the alloy, it tends to react with pre-existing Cr carbides to form Cr-sulfide and release carbon further into the alloy.

6.4 MINOR ALLOYING ELEMENT EFFECTS

The effects of minor alloying elements were studied using the designed model alloys with different levels of Cr, Al, Si, Ti, and Mo. These alloys were tested in the three environments of gas 2, 3, and 5. Based on the obtained results and using previous understandings from the commercial alloys, pure chromium, and ternary model alloys, the following conclusions were drawn:

- In Ni-Co-base alloys, increasing the Co content up to the level that the Ni:Co mass ratio is close to unity is highly beneficial in increasing the sulfidation resistance. At this ratio, the availability of both nickel and cobalt for sulfide formation is the lowest and, thus, an optimum sulfidation resistance can be achieved.
- Addition of minor alloying elements of Al+Ti+Mo provided much better resistance for these alloys than their parent ternary alloys without minor alloying addition. It was verified that

with the judicious addition of Al, Ti and Mo, better sulfidation resistance can be achieved even at relatively low Cr concentrations (22%).

- Higher Cr concentration is not necessarily better for sulfidation resistance. Combination of lower Cr and minor alloying elements can provide much better sulfidation resistance. Increasing the Cr concentration to 28% in the presence of minor alloying elements shortened the incubation period of the protective oxidation.
- The internal carburization depth decreased considerably by addition of the abovementioned minor alloying elements. Formation of an outer layer of Cr-carbide followed by an alumina sub-layer provided better protection against carbon penetration and internal carburization of the alloy.
- Formation of an external Cr-carbide scale was observed after addition of minor alloying elements. This scale, however, has no protective properties against inward diffusion of carbon and oxygen.
- Remarkable sufidation resistance was obtained by maintaining the Ni:Co base-metal mass ratio near unity and adding minor amounts of Al, Ti, Mo, and Si. Alloy 4 with composition of Ni-22Cr-33.4Co-2.5Al-2.5Ti-5Mo-3Si (in wt.%) showed the best sulfidation resistance in gas 2 environment by formation of a continuous alumina scale and the stable G-phase in the sub-scale region. This composition represents a major alloy-development result stemming from this study.
- Si additions in combination with Al+Ti+Mo showed to be the most effective in providing the sulfidation resistance, although in combination with high Al concentration can form a brittle structure.

- All model alloys showed protective behavior under the more reducing conditions gas 3. Formation of a protective alumina sub-layer in most of the model alloys provided much better resistance to both carburization and sulfidation attack.

APPENDIX A

GAS PHASE FLUX CALCULATIONS

A.1 DIFFUSION IN GASES

According to the kinetic theory of gases, the self-diffusivity of spherical A atoms diffusing in pure A can be written as:

$$D_{AA}^{*} = \frac{2}{3}\left[\frac{k_B^3}{\pi^3 m_A}\right]^{1/2} \frac{T^{3/2}}{Pd^2} \tag{A-1}$$

On the other hand, the interdiffusivity of two unequal size spherical atoms A and B can be written as:

$$D_{AB} = \frac{2}{3}\left[\frac{k_B^3}{\pi^3}\right]^{1/2} \left[\frac{1}{2m_A} + \frac{1}{2m_B}\right]^{1/2} \frac{T^{3/2}}{P\left[\frac{d_A + d_B}{2}\right]^2} \tag{A-2}$$

where k_B is Boltzmann's constant (1.38×10^{-16} ergs.molecule^{-1}.K^{-1}), d the molecular diameter (cm), m is the molecular mass (g.molecule^{-1}), P is the pressure (dyn.cm^{-2}), and T is the temperature (K). In order to predict D_{AB} more accurately, it is better to apply the Chapman-Enskog theory than the above equations. For monoatomic gases, which act ideally, we have

$$D_{AB} = \frac{0.0018583 T^{3/2}}{P(\sigma_{AB})^2 \Omega_{D,AB}} \left[\frac{1}{M_A} + \frac{1}{M_B}\right]^{1/2} \tag{A-3}$$

$$\sigma_{AB} = \frac{1}{2}(\sigma_A + \sigma_B) \tag{A-4}$$

where M_A and M_B are the molecular weights of species A and B, T the temperature (K), P the pressure (atm), σ_{AB} is the collision diameter (Å), $\Omega_{D,AB}$ collision integral for A-B mixture at dimensionless temperature, and T^*_{AB}, for the Lennard-Jones potential

$$T^*_{AB} = \left[\frac{k_B}{\varepsilon}\right]_{AB} T \tag{A-5}$$

$$\left[\frac{k_B}{\varepsilon}\right]_{AB} = \left[\left[\frac{\varepsilon}{k_B}\right]_A \left[\frac{\varepsilon}{k_B}\right]_B\right]^{1/2} = \text{average intermolecular force parameter, K} \tag{A-6}$$

Table 6-1 Intermolecular force parameters and critical properties [146]

Substance	Molecular weight, M	Lennard-Jones parameters*		Critical constants*	
		σ, Å	ε/κ_B, K	T_c, K	$\hat{V}_c$, cm³/mol
Light elements					
H_2	2.016	2.827	59.7	33.2	65.1
He	4.003	2.551	10.22	5.19	57.4
Noble gases					
Ne	20.183	2.820	32.8	44.4	41.6
Ar	39.948	3.542	93.3	150.8	74.9
Kr	83.80	3.655	178.9	209.4	91.2
Xe	131.3	4.047	231.0	289.7	118.4
Polyatomic gases					
Air	28.97	3.711	78.6	-	-
N_2	28.013	3.798	71.4	126.2	89.8
O_2	32.00	3.467	106.7	154.6	50.4
CO	28.01	3.690	91.7	132.9	93.2
CO_2	44.01	3.941	195.2	304.1	93.9
H_2O	18.02	2.641	809.1	647.3	57.1
SO_2	64.06	4.112	335.4	430.8	122.2
F_2	38.00	3.357	112.6	144.3	66.3
Cl_2	70.91	4.217	316.0	416.9	123.8
Br_2	159.81	4.296	507.9	588	127.2
CH_4	16.04	3.758	148.6	190.4	99.2

Note: The Angstrom, Å, equals 0.1 nm or 10^{-8} cm.

The values of the force parameters and the collision diameters for common gases are given in Table 6-1. The collision integral can also be calculated through:

$$\Omega_{D,AB} = \frac{A}{T_{AB}^{*B}} + \frac{C}{expDT_{AB}^{*}} + \frac{E}{expFT_{AB}^{*}} + \frac{G}{expHT_{AB}^{*}} \tag{A-7}$$

where A=1.06036, B=0.15610, C=0.19300, D=0.47635, E=1.03587, F=1.52996, G=1.76474, and H=3.89411.

A.2 MASS TRANSFER COEFFICIENT

As it was mentioned in Chapter 5.2.2.1, the maximum flux of a given gaseous species *i* to the alloy surface can be approximated by the expression [92, 93]

$$J_i = \frac{k_{m(i)} P_i}{RT} \tag{A-8}$$

where J is the flux and k_m is the mass transfer coefficient, which can be estimated from mass-transfer theory via

$$k_m = Sh \frac{D_{i(N_2)}}{L} \tag{A-9}$$

Here L is the sample length, $D_{i(N_2)}$ the diffusion coefficient of species *i* in nitrogen, and *Sh* is the Sherwood number. The diffusion coefficient can be calculated from the kinetic theory of gases as discussed in previous section A.1. For a flow parallel to a flat plate, Sherwood number is evaluated using

$$Sh = 0.664\, Sc^{0.343} Re_L^{1/2} \tag{A-10}$$

where the Reynolds number can be calculated via

$$Re_L = \frac{LV_\infty \rho}{\eta} \tag{A-11}$$

Using Lennard-Jones potential, Chapman and Enskog have developed the following equation for the viscosity of nonpolar gases at low pressures:

$$\eta = 2.67 \times 10^{-5} \frac{\sqrt{MT}}{\sigma^2 \Omega_\eta} \tag{A-12}$$

Here, M is the molecular weight (g), η is the viscosity (Poise), T the temperature (K), and σ is a characteristic diameter of the molecule (Å).

REFERENCES

[1] A. Aguero, M. Gutierrez, R. Muelas, D. Plana, A. Roman and M. Hernandez, "Laboratory corrosion testing of coatings and substrates simulating coal combustion under a low NOx burner atmosphere," *Materials and Corrosion,* vol. 65, no. 2, pp. 149-160, 2014.

[2] J. A. Urich and E. Kramer, "Designing Solutions for Low NOx-Related Water Wall Corrosion," in *ASME Joint Power Generation Conference,* 1996.

[3] R. M. Deacon, J. N. DuPont and A. R. Marder, "High temperature corrosion resistance of candidate nickel-based weld overlay alloys in a low NOx environment," *Materials Science and Engineering A,* vol. 460–461, pp. 392-402, 2007.

[4] S. C. Kung and W. T. Bakker, "Furnace Wall Corrosion in Reducing-sulfidizing Combustion Gas," *Materials At High Temperatures,* vol. 14, no. 2, pp. 175-182, 1997.

[5] B. Dooley, R. Tilley, T. P. Sherlock and C. H. Wells, "State of Knowledge Assessment for Waterwall Wastage," in *EPRI International Conference on Boiler Tube Failures in Fossil Plants*, Nashville, Tennessee, 1997.

[6] S. Mrowec, "The Problem of Sulfur in High-Temperature Corrosion," *Oxidation of Metals,* vol. 44, no. 1/2, pp. 177-209, 1995.

[7] B. Gleeson, "Alloy Degradation Under Oxidizing-Sulfidizing Conditions at Elevated Temperatures," *Materials Research,* vol. 7, no. 1, pp. 61-69, 2004.

[8] M. H. LaBranche and G. J. Yurek, "Kinetics and Mechanisms of the Oxidation of Chromium in H2-H2O-H2S Gas Mixtures," *Oxidation of Metals,* vol. 28, no. 1/2, pp. 73-97, 1987.

[9] S. Mrowec and K. Przybylski, "Transport Properties of Sulfide Scales and Sulfidation of Metals," *Oxidation of Metals,* vol. 23, no. 3/4, pp. 107-139, 1985.

[10] G. Y. Lai, High-Temperature corrosion and Materials Application, ASM International, 2007.

[11] C. Rao and K. Pisharody, "Transition Metal Sulfides," *Progress in Solid-State Chemistry,* vol. 10, p. 207, 1975.

[12] N. Birks, G. H. Meier and F. S. Pettit, Introduction to the High-Temperature Oxidation of Metals, Cambridge, UK: Cambridge University Press, 2006.

[13] D. J. Young, High Temperature Oxidation and Corrosion of Metals, Oxford: Elsevier Ltd., 2008.

[14] A. Atkinson, "Wagner Theory and Short Circuit Diffusion," *Materials Science and Technology,* vol. 4, pp. 1046-1051, 1988.

[15] C. Wagner, "The Theory of Warm-Up Process," *Zeitschrift Fur Physikalische Chemie-Abteilung B-Chemie Der Elementarprozesse Aufbau Der Materie,* vol. 25, no. 1/2, pp. 25-41, 1933.

[16] S. Mrowec and K. Przybylski, "Defect and Transport Properties of Sulfides and Sulfidation of Metals," *High Temperature Materials and Processes,* vol. 6, no. 1-2, pp. 1-79(32), 1984.

[17] S. Mrowec and J. Janowski, in *Selected Topics in High Temperature Chemistry,* New York, Elsevier, 1989, pp. 55-99.

[18] B. M. Gleeson, D. L. Douglass and F. Gesmundo, "A Comprehensive Investigation of the Sulfidation Behavior of Binary Co-Mo Alloys," *Oxidation of Metals,* vol. 33, no. 5/6, pp. 425-455, 1990.

[19] H. Rau, "Estimation of the homogeneity range of MoS2," *Journal of Physics and Chemistry of Solids,* vol. 41, no. 7, pp. 765-767, 1980.

[20] B. M. Gleeson, "Thermodynamics and Theory of External and Internal Oxidation of Alloys," *Richardson J. A. et al. (eds.) Shreir's Corrosion,* vol. 1, pp. 180-194, 2010.

[21] G. D. Smith, *Corrosion-NACE International,* vol. 53, no. 7, 1997.

[22] A. Davin, *Cobalt,* vol. 30, p. 19, 1966.

[23] A. Davin and D. Coutsouradis, "Dry Corrosion of Cobalt, Chromium, and Co-Cr, Ni-Cr and Fe-Cr Alloys in Hydrogen Sulphide Atmosphere," *Cobalt,* vol. 17, p. 23, 1962.

[24] S. Mrowec, S. Rusiecki and A. Wojtowicz, "The Kinetics of Cobalt Sulphidation at High Temperatures," *Bull. Pol. Acad. Chem.*, vol. 34, p. 411, 1986.

[25] G. Y. Lai, "High temperature Corrosion in Energy Systems," *The Metallorgical Society of AIME,* p. 227, 185.

[26] H. Rau, "The chromium-sulphur system between 873 K and 1364 K," *Journal of Less-Common Metals,* vol. 55, no. 2, p. 205–211, 1977.

[27] P. R. Roberge, Corrosion Basics—An Introduction, Houston, TX: NACE Internationa, 2006.

[28] J. A. Kneeshaw, "The corrosion behavior of Fe-Cr-Ni alloys in complex high temperature gaseous atmospheres containing the reactants oxygen, sulphur and carbon.," Doctoral Thesis, Loughborough University, Loughborough, UK, 1987.

[29] B. Gleeson, D. L. Douglass and F. Gesmundo, "Effect of Nb on the High-Temperature Sulfidation Behavior of Cobalt," *Oxidation of Metals, Vol. 31, Nos. 3/4, 1989,* vol. 31, no. 3/4, pp. 209-236, 1989.

[30] T. Biegun and A. Bruckman, *Bulletin of the Polish Academy of Sciences,* vol. 29, p. 69, 1981.

[31] G. Wang, D. L. Douglass and F. Gesmundo, "Effect of Al on the High-Temperature Sulfidation of Fe-30Nb," *Oxidation of Metals,* vol. 35, no. 3/4, pp. 279-294, 1991.

[32] H. Yakuwa, T. Narita, M. Kawasaki, M. Miyasaka, C. Fang, T. Go and S. Nakahama, "Development of A Sulfidation-Corrosion Resistant Nickel-Base Superalloy for FCC Power Recovery Turbine Rotors," in *Proceedings of the 27th Turbomachinery Symposium*, 1998.

[33] H. J. Grabke, "Nickel-Based Alloys in Carbonaceous Gases," *Corrosion Science,* vol. 56, no. 8, pp. 801-808, 2000.

[34] T. A. Ramanarayanan, R. A. Petrovic, J. D. Mumford and A. Ozekcin, "Carburization of high chromium alloys," *Materials and Corrosion,* vol. 49, pp. 226-230, 1998.

[35] A. Rahmel, H. J. Grabke and W. Steinkusch, "Carburization - Introductory Survey," *Materials and Corrosion,* vol. 49, pp. 221-225, 1998.

[36] A. Schneider and H. J. Grabke, "Effect of H2S on Metal Dusting of Iron," *Materials and Corrosion,* vol. 54, no. 10, pp. 793-798, 2003.

[37] J. Klower and U. Heubner, "Carburization of Nickel-Base Alloys and Its Effects on The Mechanical Properties," *Materials and Corrosion,* vol. 49, pp. 237-245, 1998.

[38] C. Wagner, "Reaktionstypen bei der Oxydation von Legierungen," *Z. Elektrochem.,* vol. 63, p. 772–782, 1959.

[39] S. Forseth and P. Kofstad, "Carburization of Fe-Ni-Cr Steels in CH4-H2 Mixtures at 850C-1000C," *Materials and corrosion,* vol. 49, pp. 266-271, 1998.

[40] D. J. Young and J. Zhang, "Carbon corrosion of alloys at high temperature," *The Journal of The Southern African Institute of Mining and Metallurgy,* vol. 113, pp. 149-154, 2013.

[41] R. Benz, J. F. Elliott and J. Chipman, "Thermodynamics of the Carbides in the System Fe-Cr-C," *Metallurgical Transactions,* vol. 5, pp. 2235-2240, 1974.

[42] G. M. Smith, D. J. Young and D. L. Trimm, "Carburization Kinetics of Heat-Resistant Steels," *Oxidation of Metals,* vol. 18, no. 5/6, pp. 229-243, 1982.

[43] H. J. Grabke, U. Gravenhorst and W. Steinkusch, "Carburization of chromium nickel steels in a carbon bed," *Materials and Corrosion,* vol. 27, no. 5, pp. 291-296, 1976.

[44] O. Demel, E. Keil and P. Kostecki, "Studiengesellschaft fur Atomnergie," SGAW Report No.2538, Osterreichische, 1970s.

[45] H. M. Tawancy and N. M. Abbas, "Mechanism of carburization of high-temperature alloys," *Journal of Materials Science,* vol. 27, pp. 1061-1069, 1992.

[46] S. K. Roy, H. J. Grabke and W. Wepner, "Diffusivity of Carbon in Austenitic Fe-Si-C Alloys," *Arch. Eisenhuttenwes.,* vol. 51, no. 3, pp. 91-96, 1980.

[47] D. R. G. Mitchell, D. J. Young and W. Kleemann, "Caburisation of heat-resistant steels," *Materials and Corrosion,* vol. 49, pp. 231-236, 1998.

[48] H. Ando, Y. Nakayama and H. Kimura, "Effect of Aluminum Oxide on Carbon Deposition of Fe–Al Alloys in Carburizing Gas," *ISIJ International,* vol. 29, no. 6P, pp. 511-516, 1989.

[49] D. R. G. Mitchell and D. J. Young, "The effect of molybdenum and aluminium additions on the carburization behaviour of high temperature steel.," *Journal of Materials Science Letters,* vol. 12, pp. 1076-1079, 1993.

[50] T. A. Ramanarayanan and D. J. Srolovitz, "Carburization Mechanisms of High Chromium Alloys," *J. Etectrochem. Soc.,* vol. 132, no. 9, pp. 2268-2274, 1985.

[51] P. L. Hemmings and R. A. Perkins, "Thermodynamic Phase Stability Diagrams for the Analysis of Corrosion Reactions in Coal Gasification/Combustion Atmospheres.," EPRI Report FP-539, Lockheed Palo Alto Research Laboratories, Palo Alto, CA, 1977.

[52] M. F. Stroosnijder and W. J. Quadakkers, "Review of High Temperature Corrosion of Metals and Alloys in Sulphidizing/Oxidizing Environments.," *High Temperature Technology,* vol. 4, pp. 141-151, 1986.

[53] B. Gleeson, "Thermodynamics and Theory of External and Internal Oxidation of Alloys," in *Shreir's Corrosion, Fourth Edition,* Mabchester, UK, Elsevier Science, 2010, pp. 180-194.

[54] X. G. Zheng and D. J. Young, "High Temperature Reaction of Chromium with Multi-Oxidant Atmospheres," *Materials Science Forum,* Vols. 251-254, pp. 567-574, 1997.

[55] D. J. Young and S. Watson, "High-Temperature Corrosion in Mixed Gas Environments," *Oxidation of Metals,* vol. 44, no. 1/2, pp. 239-264, 1995.

[56] J. Stringer and D. P. Whittle, "High temperature oxidation and corrosion of metals and alloys," *Rev. Int. Hautes Temp. Refract.,* vol. 14, no. 1, pp. 6-20, 1977.

[57] C. S. Giggins and F. S. Pettit, "Corrosion of Metals and Alloys in Mixed Gas Environments at Elevated Temperatures," *Oxidation of Metals,* vol. 14, no. 5, pp. 363-413, 1980.

[58] M. Howes, "High-temperature corrosion in coal-gasification systems. Final report.," Materials Properties Council, Inc., New York (USA), (October 1972-December 1985).

[59] M. Howes, "High Temperature Corrosion in Coal Gasification Systems," Gas Research Institute, Chicago, 1987.

[60] I. Wolf and H. J. Grabke, "A study on the solubility and distribution of carbon in oxides," *Solid State Communications,* vol. 54, no. 1, pp. 5-10, 1985.

[61] H. J. Grabke, K. Ohla, J. Peters and I. Wolf, "Radiotracer studies of carbon permeation through oxide scales on commercial high temperature alloys and model alloys," *Materials and Corrosion,* vol. 34, no. 10, pp. 495-500, 1983.

[62] X. G. Zheng and D. J. Young, "High-Temperature Corrosion of Cr2O3-Forming Alloys in CO–CO2–N2 Atmospheres," *Oxidation of Metals,* vol. 42, p. 163–190, 1994.

[63] T. D. Nguyen, J. Q. Zhang and D. J. Young, "Microstructures of chromia scales grown in CO2," *Materials at High Temperatures,* vol. 32, no. 1-2, pp. 16-21, 2015.

[64] R. H. Kane, "Effects of Silicon Content and Oxidation Potential on the Carburization of Centrifugally Cast HK-40," *Corrosion-NACE,* vol. 37, no. 4, pp. 187-199, 1981.

[65] K. Natesan, "High-Temperature Corrosion in Coal Gasification Systems," *Corrosion-NACE,* vol. 41, no. 11, pp. 646-655, 1985.

[66] A. Rahmel, M. Schorr, A. Velasco-Tellez and A. Pelton, "Transition from Oxidation to Sulfidation of Fe-Cr Alloys in Gases with Low Oxygen and High Sulfur Pressures," *Oxidation of Metals,* vol. 27, no. 3/4, pp. 199-220, 1987.

[67] C. D. Asmundis, F. Gesmundo and C. Bottino, "High-Temperature Corrosion of Pure Chromium in SO2 (700-1000C).," *Oxidation of Metals,* vol. 14, no. 4, pp. 351-361, 1980.

[68] F. Gesmundo, "Mechanism of the Simultaneous Formation of Oxide and Sulfide at the Scale Surface During the Oxidation of a Pure Metal in Mixed Atmospheres.," *Oxidation of Metals,* vol. 13, no. 3, pp. 237-244, 1979.

[69] M. A. Harper and J. P. Cotner, "Mixed Sulfidation/Carburization Attack on Several Heat-Resistant Alloys at 900C," *Oxidation of Metals,* vol. 53, no. 5/6, pp. 427-449, 2000.

[70] X. Wu, "High-Temperature Corrosion Behavior of Alloys in Gaseous Environments with Low-Oxygen and High-Sulfur Potentials," Doctoral Thesis, University of Pittsburgh, Pittsburgh, 2014.

[71] "The Ames Labpratory- Materials Preparation Center," Ames Labpratory, [Online]. Available: https://www.ameslab.gov/mpc.

[72] L. Paul, G. Clark, M. Eckhardt, R. Deacon, J. N. DuPont and A. R. Marder, "Alternate Alloys for Weld Overlay of Boiler Tubes in Low NOx Coal Fired Boilers," in *EPRI International Conference on Materials and Corrosion Experience for Fossil Power Plants,* Isle of Palms, South Carolina, 2003.

[73] G. Y. Lai, "Sulfidation-Resistant Co-Cr-Ni Alloy With Critical Contents of Silicon and Cobalt". U.S. Patent 4711763, Dec 1987.

[74] D. J. Young, W. W. Smeltzer and J. S. Kirkaldy, "The Effects of Molybdenum Addition to Nickel-Chromium Alloys on Their Sulfidation Properties," *Metallrugical Transactions A,* vol. 6, no. 6, pp. 1205-1215, 1975.

[75] X. Wu and B. Gleeson, "Compositional Factors Affecting the High-Temperature Degradation Behavior of Alloys Exposed to Relatively High PS2 – Low PO2 Atmospheres," in *NACE International* , Houston, Texas, 2013.

[76] R. P. Smith, *Transactions of the Metallurgical Society of AIME,* vol. 224, p. 10, 1962.

[77] G. Y. Lai, "High Temperature Corrosion in Energy Systems," in *TMS-AIME Symposium, M.F. Rothman (Ed.),* Warrendale, PA, p. 551, 1985.

[78] R. H. Kane, G. M. McColvin, T. J. Kelly and J. M. Davison, in *Corrosion/84, NACE, Paper No. 12,* 1984.

[79] A. W. Searcy, D. V. Ragone and U. Columbo, in *Chemical and Mechanical Behavior of Inorganic Materials,* New York, Wiley-Interscience, 1970, p. 33.

[80] D. J. Young, T. D. Nguyen, P. Felfer, J. Zhang and J. M. Cairney, "Penetration of protective chromia scales by carbon," *Scripta Materialia,* vol. 77, pp. 29-32, 2014.

[81] D. P. Whittle and J. Stringer, "Improvements in High Temperature Oxidation Resistance by Additions of Reactive Elements or Oxide Dispersions," *Philosophical Transactions of the Royal Society A,* vol. 295, no. 1413, 1980.

[82] D. Naumenko, B. A. Pint and W. J. Quadakkers, "Current Thoughts on Reactive Element Effects in Alumina-Forming Systems: In Memory of John Stringer," *Oxidation of Metals,* vol. 86, pp. 1-43, 2016.

[83] J. L. Smialek, "Maintaining Adhesion of Protective Al2O3 Scales," *JOM ,* pp. 22-25, 2000.

[84] B. A. Pint, "On the formation of interfacial and internal voids in α-Al2O3 scales," *Oxidation of Metals,* vol. 40, no. 3-4, pp. 303-328, 1997.

[85] S. P. Kinniard, D. J. Young and D. L. Trimm, "Effect of Scale Constitution on the Carburization of Heat Resistant Steels," *Oxidation of Metals,* vol. 26, no. 5/6, pp. 417-430, 1986.

[86] T. C. Tiearney and K. Natesan, "Sulfidation-Oxidation of Advanced Metallic Materials in Simulated Low-Btu Coal-Gasifier Environments," *Oxidation of Metals,* vol. 17, no. 1/2, pp. 1-26, 1982.

[87] R. A. Perkins, "High Temperature Corrosion of Metals and Alloys in Coal Conversion Atmospheres," in *DOE, EPRI, GRI, NBS, Third Annual Conference on Materials for Coal Conversion and Utilization,* October 10-12, 1978.

[88] M. F. Stroosnijder and W. J. Quadakkers, "Review of high temperature corrosion of metals and alloys in sulphidizing/oxidizing environments II. Corrosion of alloys," *High Temperature Technology,* vol. 4, no. 3, pp. 141-151, 1986.

[89] A. D. Smigelskas and E. O. Kirkendall, "Zinc Diffusion in Alpha Brass," *Transactions of AIME,* vol. 171, pp. 130-142, 1947.

[90] K. P. Lillerud and P. Kofstad, "On High Temperature Oxidation of Chromium- I.Oxidation of Annealed, Thermally Etched Chromium at 800C-1100C.," *Journal of Electrochemical Society,* vol. 127, no. 11, pp. 2397-2410, 1980.

[91] P. Kofstad and K. P. Lillerud, "On High Temperature Oxidation of Chromium-II.Properties of Cr2O3 and the Oxidation Mechanism of Chromium.," *Journal of Electrochemical Society,* vol. 127, no. 11, pp. 2410-2419, 1980.

[92] D. R. Gaskel, An introduction to Transport Phernomena in Materials Engineering, New York: Macmillan, 1992.

[93] D. R. Poirier and G. H. Geiger, Transport Phenomena in Materials Processing, Warrendale, Pennsylvania: The Minerals, Metals & Materials Society, 1994.

[94] J. Zurek, D. J. Young, E. Essuman, M. Hansel, H. J. Penkalla, L. Niewolak and W. J. Quadakkers, "Growth and adherence of chromia based surface scales on Ni-base alloys in high- and low-pO2 gases," *Materials Science and Engineering A,* vol. 477, p. 259–270, 2008.

[95] D. J. Young, "Effects of Water Vapour on the Oxidation of Chromia Formers," *Materials Science Forum,* Vols. 595-598, pp. 1189-1197, 2008.

[96] L. Latu-Romain, Y. Parsa, S. Mathieu, M. Vilasi, M. Ollivier, A. Galerie and Y. Wouters, "Duplex n- and p-Type Chromia Grown on Pure Chromium: A Photoelectrochemical and Microscopic Study," *Oxidation of Metals,* vol. 86, p. 497–509, 2016.

[97] M. Hänsel, L. Garcia-Fresnillo, S. L. Tobing and V. Shemet, "Effect of H2/H2O ratio on thermally grown chromia scales formed on Ni25Cr alloy in Ar–H2–H2O atmospheres at 1000°C," *Materials at High Temperatures* , vol. 29, no. 3, 2012.

[98] A. Rahmel and J. Tobolski, "Einfluss von wasserdampf und kohlendioxyd auf die oxydation von eisen in sauerstoff bei hohen temperaturen," *Corrosion Science,* vol. 5, no. 5, pp. 333-340, 1965.

[99] C. T. Fujii and R. A. Meussner, "The Mechanism of the High-Temperature Oxidation of Iron-Chromium Alloys in Water Vapor," *Journal of the Electrochemical Society* , vol. 111, no. 11, pp. 1215-1221, 1964.

[100] M. Michalik, M. Hänsel, J. Zurek, L. Singheiser and W. J. Quadakkers, "Effect of water vapour on growth and adherence of chromia scales formed on Cr in high and low pO2-environments at 1000 and 1050°C," *Materials at High Temperatures,* vol. 22, no. 3/4, p. 213–221, 2005.

[101] A. Galerie, Y. Wouters and M. Caillet, "The Kinetic Behaviour of Metals in Water Vapour at High Temperatures: Can General Rules Be Proposed?," *Materials Science Forum,* Vols. 369-372, pp. 231-238, 2001.

[102] H. J. Grabke, "Adsorption, segregation and reactions of non-metal atoms on iron surfaces," *Materials Science and Engineering,* vol. 42, pp. 91-99, 1980.

[103] R. G. Olsson and E. T. Turkdogan, "Catalytic effect of iron on decomposition of carbon monoxide: II. Effect of additions of H2, H2O, CO2, SO2 and H2S," *Metallurgical Transactions,* vol. 5, pp. 21-26, 1974 .

[104] T. A. Ramanarayanan, "The interaction of carbon and sulfur with iron-base alloys in predominantly carburizing environments," *Materials Science and Engineering,* vol. 87, pp. 113-118, 1987.

[105] J. Barnes, J. Corish and J. F. Norton, "Sulfur effects on the internal carburization of Fe-Ni-Cr alloys," *Oxidation of Metals,* vol. 26, no. 5-6, pp. 333-350, 1986.

[106] A. C. S. Sabioni, A. M. Huntz, J. Philibert and B. Lesage, "Relation between the oxidation growth rate of chromia scales and self-diffusion in Cr2O3," *Journal of Msterials Science,* vol. 27, pp. 4782-4790, 1992.

[107] R. E. Lobnig, H. P. Schmidt, K. Hennesen and H. J. Grabke, "Diffusion of Cations in Chromia Layers Grown on Iron-Base Alloys," *Oxidation of Metals,* vol. 37, no. 1/2, pp. 81-93, 1992.

[108] A. M. Huntz and S. C. Tsai, "Diffusion in oxide scales: application to Cr2O3 scales," *Journal of Materials Science Letters,* vol. 13, pp. 821-825, 1994.

[109] A. Atkinson, "Transport processes during the growth of oxide films at elevated temperature," *Reviews of Modern Physics, Vol. 57, No. 2, April 1985,* vol. 57, no. 2, pp. 437-470, 1985.

[110] A. H. Heuer, M. Zahiri Azar, H. Guhl, M. Foulkes, B. Gleeson, T. Nakagawa, Y. Ikuhara and M. W. Finnis, "The Band Structure of Polycrystalline Al2O3 and Its Influence on Transport Phenomena," *Journal of the American Ceramic Society,* vol. 99, no. 3, pp. 733-747, 2016.

[111] T. Nakagawa, H. Nishimura, I. Sakaguchi, N. Shibata, K. Matsunaga, T. Yamamoto and Y. Ikuhara, "Grain boundary character dependence of oxygen grain boundary diffusion in a-Al2O3 bicrystals," *Scripta Materialia,* vol. 65, no. 6, pp. 544-547, 2011.

[112] I. Sakaguchi, V. Srikanth, T. Ikegami and H. Haneda, "Grain Boundary Diffusion of Oxygen in Alumina Ceramics," *Journal of the American Ceramic Society,* vol. 78, no. 9, pp. 2557-2559, 1995.

[113] J. L. Meijering, Advances in Materials Research, 5th ed., H. Herman ed., New York: Wiley-Interscience, 1971.

[114] K. Bongartz, R. Schulten, W. J. Quadakkers and H. Nickel, "A Finite Difference Model Describing Carburization in High-Temperature Alloys," *Corrosion,* vol. 42, no. 7, pp. 390-397, 1986 .

[115] H. Xu, M. G. Hocking and P. S. Sidky, "Sulfidation-Oxidation Behavior of Alloy 800H in SO2 - 02 and H2 - H2S- CO- CO2 Atmospheres," *Omdation of Metals,* vol. 41, no. 1/2, pp. 81-101, 1994.

[116] D. J. Baxter and K. Natesan, "Breakdown of chromium oxide scales in sulfur-containing environments at elevated temperatures," *Oxidation of Metals,* vol. 31, no. 3-4, pp. 305-323, 1989.

[117] W. Ostwald, Lehrbuch der Allgemeinen Chemie, vol. 2, part 1, Leipzig, Germany: Leipzig, W. Engelmann, 1896.

[118] F. Jellinek, "The Structures of the Chromium Sulphides," *Acta Crystallographica,* vol. 10, pp. 620-628, 1957.

[119] S. Cruchley, H. E. Evans, M. P. Taylor, M. C. Hardy and S. Stekovic, "Chromia layer growth on a Ni-based superalloy: Sub-parabolic kinetics and the role of titanium," *Corrosion Science,* vol. 75, pp. 58-66, 2013.

[120] X. Hu, G. Chen, C. Ion and K. Ni, "The 1100 C Isothermal Section of the Ti-Ni-Si Ternary System," *Journal of Phase Equilibria,* vol. 20, no. 5, pp. 508-514, 1999.

[121] G. Böhm and M. Kahlweit, "On internal oxidation of metallic alloys," *Acta Metallurgica,* vol. 12, no. 5, pp. 641-648, 1964.

[122] F. H. Stott and F. I. Wei, "Comparison of the Effects of Small Additions of Silicon or Aluminum on the Oxidation of Iron-Chromium Alloys," *Oxidation of Metals,* vol. 31, no. 5/6, pp. 369-391, 1989.

[123] F. H. Stott, Y. Shida, D. P. Whittle, G. C. Wood and B. D. Bastow, "The morphological and structural development of internal oxides in nickel-aluminum alloys at high temperatures," *Oxidation of Metals,* vol. 18, no. 3, pp. 127-146 , 1982.

[124] S. Guruswamy, S. M. Park, J. P. Hirth and R. A. Rapp, "Internal Oxidation of Ag-In Alloys: Stress Relief and the Influence of Imposed Strain," *Oxidation of Metals,* vol. 26, no. 1/2, pp. 77-100, 1986.

[125] C. R. Wang, W. Q. Zhang and R. Z. Zhu, "High-Temperature Corrosion of Titanium-, Niobium-, and Manganese-Rich Fe-25Cr Alloys in H2-H20-H2S Gas Mixures," *Oxidation of Metals,* vol. 33, no. 1/2, pp. 55-78, 1990.

[126] P. Kofstad, "On the Formation of Porosity and Microchannels in Growing Scales," *Oxidation of Metals,* vol. 24, p. 265, 1985.

[127] A. Bruckman, "The Mechanism of Transport of Matter through the Scales during Oxidation of Metals and Alloys," *Corrosion Science,* vol. 7, p. 51, 1967.

[128] G. J. Yurek, M. H. LaBranche and Y. K. Kim, in *Proceedings of the Symposium on High Temperature Corrosion in Energy Systems, TMS-AIME/MSD-ASM Fall Meeting,* Detroit, Sept. 17-19, 1984.

[129] G. Y. Lai, *Corrosion 89/ NACE,* p. Paper No. 209, 1989.

[130] G. H. Meier, "A review of advances in high-temperature corrosion," *Materials Science and Engineering: A,* Vols. 120-121, no. Part 1, pp. 1-11, 1989.

[131] C. Leyens, K. Fritscher, M. Peters and A. Kaysser, "Phase Stability, Oxidation, and Interdiffusion of a Novel Ni-Cr-Al-Ti-Si Bond-Coating Alloy Between 900 and 1100 C," *Oxidation of Metals,* vol. 43, no. 3/4, pp. 329-352, 1995.

[132] L. S. Darken, "Diffusion of carbon in austenite with a discontinuity in composition," *Transactions of the American Institute of Mining and Metallurgical Engineers,* vol. 180, pp. 430-438, 1948.

[133] A. Chyrkin, P. Huczkowski, V. Shemet, L. Singheiser and W. J. Quadakkers, "Sub-Scale Depletion and Enrichment Processes During High Temperature Oxidation of Nickel Base Alloy 625 in the Temperature Range 900-1000C," *Oxid Met,* vol. 75, pp. 143-166, 2011.

[134] L. F. Garcia, A. Chyrkin, T. Huttel, C. Bohme, J. Barnikel, D. Gruner, F. Schmitz and W. J. Quadakkers, "Oxide Scale Formation and Subsuraface Phase Transformations During Long-Term Steam Exposure of the Cobalt Base Alloy 25," *Mater Corros,* vol. 63, pp. 878-888, 2012.

[135] L. Garcia-Fresnillo, A. Chyrkin, C. Bohme, J. Barnikel, F. Schmitz and W. J. Quadakkers, "Oxidation behaviour and microstructural stability of alloy 625 during long-term exposure in steam," *Journal of Materials Science,* vol. 49, no. 17, pp. 6127-6142, 2014.

[136] S. Jiang, F. Yin, M. Zhang, M. Zhao and Z. Li, "800 °C isothermal section of the Co-Cr-Mo-Si quaternary system," *International Journal of Materials Research,* vol. 105, no. 12, pp. 1191-1201, 2014.

[137] P. Walker and W. H. Tarn, Handbook of metal etchants, Boca Raton, Florida: CRC Press LLC, 1991.

[138] C. T. Sims, N. S. Stoloff and W. C. Hagel, Superalloys II, New York: John Wiley & Sons, Inc., 1987.

[139] M. Detroye, F. Reniers, C. Buess-Herman and J. Vereecken, "AES–XPS study of chromium carbides and chromium iron carbides," *Applied Surface Science,* Vols. 144-145, pp. 78-82, 1999.

[140] A. A. Edigaryan, V. A. Safonov, E. N. Lubnin, L. N. Vykhodtsev, G. E. Chusova and Y. M. Polukarov, "Properties and preparation of amorphous chromium carbide electroplates," *Electrochimica Acta,* vol. 47, pp. 2775-2786, 2002.

[141] Y. Chen, K. Ding, L. Yang, B. Xie, F. Song, J. Wan, G. Wang and M. Han, "Nanoscale ferromagnetic chromium oxide film from gas-phase nanocluster deposition," *Applied Physics Letters,* vol. 92, no. 17, p. 173112, 2008.

[142] P. J. Smith, O. Van der Biest and J. Corish, "The Initial Stages of High-Temperature Corrosion of Fe-Cr-Ni and Cr-Ni Alloys in a Carburizing Atmosphere of Low Oxygen Partial Pressure," *Oxidation of Metals,* vol. 24, no. 1/2, pp. 47-83, 1985.

[143] B. Li and B. Gleeson, "Effects of Minor Elements on the Cyclic-Oxidation Behavior of Commercial Fe-base 800-series Alloys," *Oxidation of Metals,* vol. 62, no. 1/2, pp. 45-69, 2004.

[144] B. Gleeson and B. Li, "Cyclic Osidation of Chromia-Scale Forming Alloys: Lifetime Prediction and Accounting for the Effects of Major and Minor Alloying Additions," *Materials Science Forum,* Vols. 461-464, pp. 427-438, 2004.

[145] S. W. Guan and W. W. Smeltzer, "Oxygen solubility and a criterion for the transition from internal to external oxidation of ternary alloys," *Oxidation of Metals,* vol. 42, no. 5-6, pp. 375-391, 1994.

[146] R. C. Reid, J. M. Pausnitz and B. E. Poling, The Properties of Gases and Liquids, Appendices A and B., New York, NY: McGraw-Hill Book Co., 4th edition, 1987.